MODELING SLIP GRADIENTS AND INTERNAL STRESSES IN CRYSTALLINE MICROSTRUCTURES WITH DISTRIBUTED DEFECTS

RAMIN AGHABABAEI

B.S. (Hons.), UNIVERSITY OF TEHRAN, 2006

A THESIS SUBMITTED

FOR THE DEGREE OF DOCTOR OF PHILOSOPHY

DEPARTMENT OF MECHANICAL ENGINEERING

NATIONAL UNIVERSITY OF SINGAPORE

2011

DEDICATION

To my dear parents

Mitra and Amir

who have supported and encouraged me from birth

To my beloved wife

Marjan

who has offered me unconditional love and happiness

ACKNOWLEDGEMENTS

This dissertation would not have been possible without the guidance and the support of several individuals who helped me with their valuable assistance in the preparation and completion of this study.

First and foremost, I would like express my deep gratitude to my supervisor Dr. Shailendra P. Joshi for his sound advice and careful guidance during my Ph.D. The innumerable discussions I had with him provided me a good understanding of the mechanics and physics together. Without his support, this work would never have been accomplished.

I would like to warmly thank Professor J.N. Reddy for his support and introducing me to the field of nonlocal theories. His profound understanding of the continuum mechanics and finite element theories helped me a lot in completing this work.

In addition, I would like to thank Professor R. Narasimhan from the Indian institute of Science for fruitful discussions I had with him. Among my peers, I greatly value the friendship I share with Hamidreza Mirkhani. I appreciate the help he extended during my PhD and many useful discussions we had on the topics in mechanics of materials. I also thank my friends and colleagues Dr. Jing Zhang and A.S. Abhilash for their comments and suggestions about my works. I also gratefully acknowledge the research scholarship provided to me by National University of Singapore.

I owe my special thanks to my lovely wife Marjan who has chosen to spend her life with me as my soul mate. Finally, this undertaking could never have been achieved without the encouragement of my wonderful father, mother and sister who have supported me from birth.

TABLE OF CONTENTS

DEDICATION ..... **I**

ACKNOWLEDGEMENTS ..... **II**

TABLE OF CONTENTS ..... **III**

SUMMARY ..... **VI**

LIST OF TABLES ..... **VII**

LIST OF FIGURES ..... **VIII**

LIST OF SYMBOLS ..... **XII**

1 INTRODUCTION **1**

1.1 Length-scale effects in response of materials 1

1.2 Length-scale Effects in Crystalline Microstructures 3

1.2.1 Plastic Deformation at Different Length-scales 4

1.2.2 A Brief Overview of Experimental Observations of Length-scale Effects in Plasticity: 10

1.2.3 Continuum descriptions of Dislocation-mediated Crystal Plasticity 13

1.2.3.1 Classical crystal plasticity 13

1.2.3.2 Continuum crystal plasticity with GNDs 15

1.3 Scope and Objectives of the Thesis 18

2 A Mechanism-Based Gradient Crystal Plasticity Investigation of Metal Matrix Composites **20**

2.1 Introduction 20

2.2 Computational Implementation of MSGCP Theory 24

2.2.1 Slip gradient calculation 27

2.2.2 Time integration scheme 28

2.3 Length-scale dependent MMC response induced by thermal residual stresses 29

2.3.1 Computational results for single crystals with inclusions 32

2.3.2 Crystal orientation and inclusion size effects on thermal GND density distribution 34

2.3.3 Size-dependent stress-strain response with pre-existing thermal GND density 43
2.3.4 Inclusion shape effect on stress-strain responses in the presence of thermal GND density 47
2.3.5 Thermal GND density distribution in polycrystalline MMC under thermal loading 52
2.4 Grain size-inclusion sizes interaction in MMC at moderate strain using MSGCP 54
2.4.1 Model Microstructures 58
2.4.2 Length-scale dependent polycrystalline response 61
2.4.3 Length-scale Dependent MMC Response 63
2.4.4 Grain orientation and mesh size effects 64
2.4.5 Grain size-inclusion Size Interaction strengthening 66
2.4.6 Analytical Model for Interaction Strengthening 70
2.5 Summary and Outlook 75

3 Length-scale Dependent Continuum Crystal Plasticity with Internal Stresses 77
3.1 Introduction 77
3.2 Background 80
3.3 Kinematics of Compatible and Incompatible Deformations 84
3.3.1 Compatibility of Lattice Curvature: 85
3.3.2 Relation between Incompatible Elastic Strain Tensor and the GND Density Tensor: 87
3.4 Internal Stress Tensor: Stress Function Approach 88
3.4.1 Internal Stress under Plane Strain Condition: Isotropic Elasticity 92
3.4.2 Internal Stress with Elastic Anisotropy 95
3.5 Thermodynamically Consistent Visco-plastic Constitutive Law 96
3.5.1 First law of thermodynamics: Power Balance 97
3.5.2 Second law of thermodynamics: Power imbalance 98
3.6 Results and Discussion 101
3.6.1 Tapered Single Crystal Specimen Subjected to Uniaxial Loading 101
3.6.2 Single Crystal Lamella Subjected to Simple Shear 110
3.7 Summary 115

4 A Crystal Plasticity Analysis of Length-scale Dependent Internal Stresses with Image Effects 117
4.1 Introduction 117

4.2 Nonlocal Continuum Theory with Internal Stress and Image Fields 120
4.3 Single Crystal Specimen under Plane-Strain Pure Bending: Role of Free Surfaces 125
4.4 Length-scale Dependent Pure Bending Response of Single Crystals 139
4.4.1 Monotonic response 143
4.4.2 Comparison with Experiment 146
4.4.3 Length-scale Dependent Bauschinger Effect 155
4.5 Summary and Outlook 161

5 Summary and Recommendations 163
5.1 Summary 163
5.2 Recommendations for future work 166

6 List of Publication 169

7 Bibliography 170

Appendix A. A Note on Continuum Descriptions of GND Density Tensor 189

Appendix B. Kernel functions 194

Appendix C. Numerical integration convergence study 200

SUMMARY

This thesis addresses a formulation, computational implementation and investigation of length-scale effects in the presence of heterogeneities and internal stresses in continuum crystal plasticity (CCP). First, we implement a gradient crystal plasticity theory in a finite element framework. Using this, we investigate the crystal orientation-dependent size effects due to thermal stresses on the overall mechanical behavior of composites. Then, through systematic simulations, we demonstrate additional Hall-Petch type coupling resulting from inclusion size-grain size interaction and propose an analytical model for the same. Since the continuum crystal plasticity augmented by short range interaction of dislocations fails to predict length-dependent strengthening at yielding point, a three-dimensional constitutive theory accounting for length-scale dependent internal residual stresses is developed. The second-order internal stress tensor is derived using the Beltrami stress function tensor that is related to the Nye dislocation density tensor. One of the common sources of these *internal residual* stresses is the presence of ensembles of excess (GN) dislocations which sometimes referred to as a *mesoscopic* continuum scale. The resulting internal stress is discussed in terms of the long-range dislocation-dislocation and dislocation-boundaries elastic interactions and physical and mathematical origins of corresponding length scales are argued. It will show that internal stress is a function of spatial variation of GND density in absence of finite boundaries where internal stress arises from GND – GND long range elastic interactions. However in presence of finite boundaries such as free surfaces or interfaces, additional source of internal stress is present due to long range interaction between GND and boundaries. Using these approaches, we investigate several important examples that mimic real problems where internal stresses play an important role in mediating the overall response under monotonic and cyclic loading.

LIST OF TABLES

Tables ***Page***

Table 2-2. Activated slip systems for two limiting crystal orientations 37

Table 2-3. Microstructural size combinations for MMC simulations 66

Table 2-4. Microstructural size combinations for MMC simulations 74

Table 3-1. Summary of governing equations 100

Table 3-2. Summary of constitutive equations 101

Table 3-3. Summary of unknown variables and available equations 101

Table 4-1. Parameters used in the analytical model for internal stress and prediction of beam behavior response 143

Table 4-2. Local and global coordinates of active slip system according to Motz et al., (2005) single crystal bending experiment 147

LIST OF FIGURES

Figures ***Page***

Figure 1.1. Plastic deformation and appropriate unit processes for modeling at different scales 7

Figure 1.2. Dislocation interactions at different length-scales 9

Figure 1.3. Schematic of geometrically necessary dislocations (GNDs) pile up at grain boundary in order to accommodate compatible plastic deformation. 11

Figure 1.4. Formation of GND in presence of strain gradient in (a) bending of single crystal (b) nano/micro indentation (c) metal matrix composite contains nano/micro inclusions. 12

Figure 2.1. Kinematics of single crystal deformation 24

Figure 2.2. (a) An Eight-node plane strain FE with four GPs and (b) a linear pseudo-element constructed from the GPs of the actual FE where ξ and η are the local isoparametric coordinates. The slip and normal directions (s and m) of a typical slip system α are also shown (b). 27

Figure 2.3. Metal matrix composite (MMC) with uniform arrangement of inclusions and unit cell comprising single crystal matrix and square inclusion. 33

Figure 2.4. Crystal orientation and inclusion size dependent distribution of effective GND density ρ_g^{th} ($|\Delta T| = 500,\ d_i = 1\ \mu m$) 35

Figure 2.5. (a) Distribution of effective GND density ρ_g^{th} along the diagonal line as shown in embedded figure. ($|\Delta T| = 500$) (b) evolution of average GND density ρ_g^{th} during cooling process ($d_i = 1\ \mu m$). 36

Figure 2.6. Distribution of normal stress σ_{11}^{th} under thermal loading for different crystal orientation of matrix ($d_i = 1\ \mu m$) 38

Figure 2.7. (a) Effective GND density ρgth distribution for different inclusion sizes , (b) average thermal GND density ρ_g^{th} evolution during thermal cooling for different inclusion sizes, (c) Inverse relation of average thermal GND density ρ_g^{th} and inclusion size ($|\Delta T| = 500, \theta = 45^o$). 41

Figure 2.8. Contributions of individual mismatch components under thermal loading ($d_i = 1\ \mu m$). 42

Figure 2.9. True stress-true strain response for MMC models under thermo mechanical loading. Bulk behavior is predicted by CCP while size dependent behavior is modeled using MSGCP for inclusion size $d_i = 1\ \mu m, \theta = 45°$. 44

Figure 2.10. Influence of the prior thermal loading on (a) true stress-true strain response and (b) hardening rate. ($d_i = 1\ \mu m, \theta = 45°$), obtained from MSGCP calculations. 45

Figure 2.11. Average GND density evolution under consequent thermal-mechanical loading. ($d_i = 1\ \mu m\ , \theta = 45°$).....47

Figure 2.12. Distribution of thermal GND density around square and circular inclusions embedded in single crystal with (a) $\theta = 0°$ and (b) $\theta = 45°$.....48

Figure 2.13. True stress-true strain response for MMC models comprising two different inclusion shapes. $\theta = 0°$.....49

Figure 2.14. Influence of inclusion shape on thermal residual stresses in MMC based on (a) CCP and (b) MSGCP. ($\theta = 0°$).....51

Figure 2.15. Schematic indicating an interaction between inclusion shape and size effects at the locations of stress concentrations.....51

Figure 2.16. Effective GND density distribution in polycrystalline MMC with random grain orientation for different grain size (a) $d_g = 0.5$ μm and (b) $d_g = 0.25$ μm. ($d_i = 1\ \mu m,\ |\Delta T| = 500$).....53

Figure 2.17. Average GND density distribution evolution in single crystalline and polycrystalline MMC.....54

Figure 2.18. MMC with micron-sized inclusions embedded in a nanocrystalline matrix (Joshi and Ramesh, 2007).....55

Figure 2.19. Representative models for (a, c) polyX and (b, d) MMC architectures..59

Figure 2.20. True stress-true strain responses for polyX models with different grain sizes.....62

Figure 2.21. Normalized grain size dependent flow stress at $\varepsilon = 2\%$ for polyX with identical grain orientations. The plot also includes the empirical Hall-Petch ($d_g^{-0.5}$) and inverse grain size (d_g^{-1}) fits.....62

Figure 2.22. Grain-size dependent true stress-true strain curves for MMC (solid lines) with $d_i = 2\ \mu m$. The corresponding polyX responses (Figure 2.20) are also included for comparison.....64

Figure 2.23. Standard deviation in $\Delta\sigma int$ arising for a given computational model with fixed d_g but different realizations of grain orientations. As expected, the variation is smaller for finer d_g.....65

Figure 2.24. Mesh convergence for the stress-strain curves of MMC $d_i = 2\mu m, d_g = 1\mu m$ with different mesh sizes d.....65

Figure 2.25. Flow stress $at\ \varepsilon = 2\%$ normalized by bulk polyX yield stress variation of MMCs as a function of grain size.....67

Figure 2.26. Inclusion size effect on the normalized flow stress (normalized by bulk polyX yield stress) for large grain sizes, $d_g = 3d_i$ (negligible grain size effect).....68

Figure 2.27. Distribution of the effective GND density (η/b) along path a-b $d_i = 2\ \mu m$ for different grain sizes.....69

Figure 2.28. Schematic of an inclusion embedded in a polycrystalline mass of finer grains.....71

Figure 2.29. Variation of the interaction strengthening with the product $d_g \times d_i$.....74

Figure 3.1. Examples illustrating the contributions of GND density to enhanced hardening in (a) pure beam bending - dissipative hardening, (b) non-uniform bending - dissipative and energetic hardening. 82

Figure 3.2. Schematic illustrating the non-locality arising from the presence of GND density at a continuum point and the distribution of the GND density around that point. 83

Figure 3.3. Variation of a typical component of the third gradient of the Green function in Eq (3.31) 91

Figure 3.4. A tapered bar under uniaxial loading. Dashed tapered edges indicate that they are sufficiently away from the centerline of the specimen 102

Figure 3.5. Plastic slip γ along bar axis y for various ratio of $\eta = L/l_b$ for tapered specimen under monotonic tension 105

Figure 3.6. Resolved shear stress versus plastic slip at $y = L$ for tapered bar under monotonic tension for various ratios (a) $\beta = L/l_g$, and (b) $\eta = L/l_b$. 106

Figure 3.7. Distribution of normalized internal shear stress τ^*/τ along the tapered specimen under monotonic tension for (a) $\lambda = 2.86°$, (b) $\lambda = 5.71°$. $\eta = 50$.....107

Figure 3.8. Resolved shear stress versus plastic slip at $y = L$ for tapered bar under cyclic loading (a) $\eta = 100$, (b) $\eta = 50$. 108

Figure 3.9. Resolved shear stress versus plastic slip at y=L for various tapered angle under cyclic loading (η=100) (a) $\lambda = 2.86°$, (b) $\lambda = 5.71°$. 109

Figure 3.10. A single lamella within a nano-twinned crystal under simple shear. .110

Figure 3.11. (a) Normalized resolved shear stress τ/g_0 versus average plastic slip as a function of η for $\theta = 90°$, (b) Normalized resolved shear stress τ/g_0 versus normalized lamella thickness at $\gamma = 0.2\%$. 112

Figure 3.12. (a) Distribution of plastic slip γ on a slip system as a function of η for $\theta = 90°$ versus distance normalized by lamella thickness λ (b) Normalized internal resolved shear stress τ^*/τ along the lamella thickness as a function of η for $\theta = 90°$, and (c) Normalized internal resolved shear stress τ^*/τ versus normalized lamella thickness. 114

Figure 4.1. Decomposition of the internal stress problem for a specimen hosting a general GND density distribution. See text for discussion. 123

Figure 4.2. Schematic showing effective GND arrangement in a specimen under uniform curvature. The specimen thickness is $t = 2h$ and the GND density is described by the global x, y and local ξ, η coordinates. 126

Figure 4.3. Internal stress components variation across thickness for $L = 0.2$ ($h = 5l_c$). 128

Figure 4.4. Variation of normalized internal stress Γ_{xx} along the normalized specimen thickness Y for different values of normalized internal length-scale L. 129

Figure 4.5. Variation of non-dimensional stresses in y direction ($\tilde{\Gamma}_{yy}$ and $\hat{\Gamma}_{yy}$) over beam thickness for a given normalized internal length-scale $L(=10)$ (Eq. 4.8a,b). Note that the components are equal and opposite resulting in overall $T^*_{yy} = 0$.....132

Figure 4.6. Variation of $\tilde{\Gamma}_{xx}$ with Y and L. (See Eq. 4.10a) 133

Figure 4.7. Variation of $\hat{\Gamma}_{xx}$ respect to (a) Y at *L=10* and (b) L at *Y=1.* (See Eq. 4.10b) 134

Figure 4.8. Variation of the normalized total internal stress Γ_{xx} with normalized internal length-scale L at specimen surface ($Y = 1$). 135

Figure 4.9. a) Normalized stress variation across normalized specimen thickness $Y = y/h$ at $E^s_{xx} = 0.05$, b) Stress-strain curves at specimen surfaces ($Y = 1$) for different values of $L = l_c/h$.....145

Figure 4.10. Contribution of short range GND interaction versus t/l_g and long range GND interactions versus. t/l_c on flow stress at 5% surface strain. 146

Figure 4.11. Schematic of single crystal specimen under pure bending, crystal orientation and corresponding active slip systems. 148

Figure 4.12. Comparison of the analytical results (Eq. 4.17) for different values of l_c with the experimental results of Motz, et al (2005).....150

Figure 4.13. Typical GND arrangement in double symmetric slip deformation under pure bending.....152

Figure 4.14. Bending-straightening cyclic response of single crystalline specimen oriented for double symmetric slip 156

Figure 4.15. Overall stress variation across specimen thickness at different strain shown in figure 4.14.....158

Figure 4.16. Length-scale dependent dissipative (isotropic) and energetic (kinematic) hardening components of pure bending responses for two different specimen thickness.....159

LIST OF SYMBOLS

In this dissertation, the following definitions are used and a Cartesian coordinate system with unit vector base $\{\mathbf{e_1}, \mathbf{e_2}, \mathbf{e_3}\}$ applies.

Quantities	***Notation***
Scalar	α, a, A
Vector	$\mathbf{a}, \mathbf{b}$
Second and higher order tensor	$\mathbf{A}, \mathbf{B}$
Kronecker delta	δ_{ij}
Permutation tensor	ϵ_{ijk}

Operators	***Notation***
Inner product	$\mathbf{a} \cdot \mathbf{b} = a_i b_i$
Cross product	$\mathbf{a} \times \mathbf{b} = \epsilon_{ijk} a_i b_j \mathbf{e}_k$
Tensor product	$\mathbf{a} \otimes \mathbf{b} = a_i b_j \mathbf{e}_i \mathbf{e}_j$
Trace	$tr(\mathbf{A}) = A_{ii}$
Vector differential operator	$\boldsymbol{\nabla} = \partial_i \mathbf{e_i}$
Gradient	$grad(.) = \nabla(.)$
Divergence	$div(.) = \nabla \cdot (.)$
Curl	$curl(.) = \nabla \times (.)$
Incompatibility	$inc(.) = curl\big(curl(.)\big)$

Nomenclature	*Notation*
Deformation gradient	$\mathbf{F}$
Displacement gradient	$\mathbf{B}$
Velocity gradient	$\mathbf{L}$
Compatible/Incompatible strain	$\mathbf{E}_c, \mathbf{E}_i$
Lattice curvature	$\mathbf{K}$
Rotation vector	$\mathbf{w}$
Spin tensor	$\mathbf{W}$
Incompatibility tensor	$\mathbf{N}$
GND density tensor	$\mathbf{A}$
Slip direction of α^{th} slip system	$\mathbf{s}^{\alpha}$
Normal direction	$\mathbf{m}^{\alpha}$
Effective GND density	ρ_g^{α}
Plastic slip	γ^{α}
Plastic slip rate	$\dot{\gamma}^{\alpha}$
Reference plastic slip	γ_0^{α}
Applied stress tensor	$\mathbf{T}^{app}$
Internal stress tensor	$\mathbf{T}^{*}$
Internal stress due to dislocation-dislocation interaction	$\tilde{\mathbf{T}}$
Internal stress due to dislocation-boundary interaction (Image stress)	$\hat{\mathbf{T}}$
Applied resolved shear stress	τ_{ext}^{α}
Internal resolved shear stress	$\tau^{*(\alpha)}$
Beltrami stress function tensor	$\boldsymbol{\psi}$
Slip resistance	g^{α}
Hardening modulus	$h_{\alpha\beta}$
Elastic modulus/Compliance tensor	$\mathbb{C}, \mathbb{S}$
Displacement	$\mathbf{u}$
Body force	$\mathbf{f}$
Traction force	$\mathbf{t}$

1 INTRODUCTION

1.1 Length-scale effects in response of materials

Nature relies on engineering its creations in a hierarchical manner in order to impart impressive properties for a range of applications (Endy, 2005; Fratzl, 2007; Gao et al., 2003). Intriguing examples of natural structural systems such as spider's silk (Vollrath, 2000) and nacre in abalone shells (Meyers, 2008) indicate impressive strengths resulting from strong, hierarchical architectures at small length-scales coupled with robust failure resistance mechanisms. Our singular quest to mimic nature has spawned tremendous excitement in synthesizing materials and constructing structures that are aimed at using some of the natural principles. The notion of the statement *Smaller is Stronger* has far-reaching implications in engineering the materials that push the limits of structural performance.

Length-scale effects on material properties, often termed as *size effects*, are of great importance in current engineering and scientific applications that range from large-scale structures that demand high strength at lower weight (e.g. automotive, aerospace systems) to miniaturized micro and nano-scaled systems that are being adopted in biomedical and electronics applications. In crystalline metals, size-effects are reported in a variety of material properties including elasticity (Agrawal et al., 2008; Wu et al., 2005), plasticity (Dehm, 2009; Greer and Hosson, 2011), thermal (Roh et al., 2010) and electrical conductivities (Boukai et al., 2008), as specimen dimensions and/ or microstructural features (e.g. diameter in nanowire, grain size in crystalline metals) are reduced. An understanding of these effects is especially important as our ability to design and manufacture structures at miniaturized length-scales and with nano-scaled

internal structures continues to acquire higher levels of sophistication (Zhu and Li, 2010).

In metallic microstructures, a general trend reported in artificial systems is that microstructures with smaller features exhibit stronger behaviors than those with coarser features (Greer and Hosson, 2011). For example, the yield strength of nanocrystalline pure aluminum with an average grain size of 40 nm is nearly 10 times more than that of a coarse-grained pure aluminum (Gianola et al., 2006). Nanotwinned copper with twin thickness of ~ 35 nm is nearly 7 times stronger than coarse-grained pure copper (Lu et al., 2009). For a fixed inclusion volume fraction the yield strength of a metal matrix composite (MMC) increases dramatically with decreasing inclusion size (Lloyd, 1994). Myriad examples pertaining to thin films (Haque and Saif, 2003), miniaturized beams (Motz et al., 2005), pillars (Greer and Nix, 2006), rods (Wong et al., 1997) unequivocally endorse the smaller is stronger phenomenon. In other words, with all other properties held constant, the smaller the geometrical or microstructural size the stronger a material is expected to be. Seen slightly differently, these examples suggest that the elastic and plastic properties of materials cease to be purely material parameters as the specimen dimensions or microstructural features approach characteristic microstructural length-scale (Greer and Hosson, 2011). All of these observations have a common message*: smaller is stronger*. In a broad sense, the size-dependent behaviors of micro and nano-scaled structures are associated with the high surface (or interface) area to volume ratio. This is in-turn based on the idea that the atomic interactions at boundaries tend to be different from those in the bulk of a material.

Rapid increase in computational power in the recent decades has enabled performing computational simulations that supplement, or at times enable, experimental investigations into the physics and mechanics at small length-scales. An

important question that arises is that of the choice of spatial and temporal resolutions. Atomistic provide a virtual experimental paradigm to capture the prevailing mechanisms at very high spatio-temporal resolution, but may become computationally prohibitive at larger structural length-scale (even beyond a few hundred nm). At the other extreme, continuum mechanics provides a strong theoretical construct that can be extremely useful if appropriately endowed with an ability to predict size-effects, albeit at the loss of sub-scale details. A third possibility is judiciously combining the atomistics and continuum mechanics to provide a concurrent multi-scale modeling approach. The choice of an approach is dictated by the details we are interested in and the scales that need to be bridged with the available computational power.

In this work, our focus is on a small subset within the vast expanse of length-scale dependent behaviors. We are interested in some of the size-effects that prevail in the mechanical behavior of crystalline metals. A particular category of size-effects covered in this thesis pertains to crystalline plasticity that arises from interacting effects between dislocations and their ambience. For example, dislocations get stopped by hard boundaries and get annihilated by free surfaces. In another scenario, dislocations *talk* to other dislocations in their neighborhood. All these events result in length-scale dependent macroscopic plastic responses that manifest as strengthening of a material. We probe some of these effects in heterogeneous crystalline microstructures of current interest through analytical and computational approaches.

To set the stage for the rest of the thesis, we briefly discuss dislocation plasticity in crystalline metals as it can be described at various length-scales.

1.2 Length-scale Effects in Crystalline Microstructures

During the last couple of decades, crystalline metallic materials especially Face-Centered-Cubic (FCC) metals are vastly used as the nano/micro structures for numerous

applications. Therefore, it is critically important to obtain fundamental insight into their length-scale dependent mechanical behavior at micro and nano scales. The experimental and theoretical aspects of these length-scale dependent behaviors are discussed in the following sections.

1.2.1 Plastic Deformation at Different Length-scales

In crystalline materials, the unit processes that are deemed relevant to describe plasticity must be identified based on the length and time-scales of interest. From a thermodynamic viewpoint, movement of the dislocations during plastic deformation is mediated by crystal lattice resistance. This crystal lattice resistance can or needs to be defined at different scales. At the finest length-scale (atomistic), it is an inherently dynamical process of atomic motions. In the development of an incrementally coarse-grained approach, some of the microstructural details at the finer scale are smeared out by making certain assumptions with regards the length- and time-scales at the sub-scale vis-à-vis the current scales of interest. This often provides a motivation to define a more relevant unit process at the coarser length-scale by coarsening the sub-scale defect dynamics. The review article by Zaiser and Seeger (2002) serves as a useful reference. A possible cascading flow of such a multi-scaling process (Fig. 1.1) that is deemed useful for this thesis is briefly discussed here:

Atomic scale – describes the individual atom in terms of its finer components such as electrons. *Density functional theory* (DFT) is the most popular method to investigate the total ground-level energy and properties of a system of interacting electrons in particular atoms and molecules (Sholl and Steckel, 2009). It uses the functional of the electron density, which provides the potential function as a basis for molecular dynamic simulations.

Nanoscopic scale – At this scale, the individual atoms and molecules are resolved where the information from the atomic scale that is coarse-grained is the interatomic interaction. *Molecular dynamics* (MD) is a powerful tool to computationally simulate the physical motions of atoms and molecules under external stimuli. In MD simulations, the Newton's equations of motion for a system of interacting particles are numerically solved where intermolecular interactions are described by a potential function provided by the atomic scale. A reasonably large ensemble of atoms is modeled, and the elastic and plastic properties emerge naturally through interatomic interactions. At this scale, the unit process that describes plastic deformation is the nucleation and mobility of individual dislocations within a crystalline lattice. Given the inherent dynamics of atomic motions, typical MD calculations need high temporal resolution in the order of femto to pico seconds. The interactive long- and short-range interactions between dislocations are naturally resolved at this scale and provide the essential physics that can be rationalized as constitutive descriptions at coarser scales. Nanoscopic lattice resistance is referred to as the Peierls stress. It depends strongly on the strain rate and can be thermally activated; hence, it is referred to as the *thermal lattice resistance*.

Microscopic scale – At this length-scale, the atomistic resolution is smeared out rendering an elastic continuum, but the discreteness of dislocations is retained. They are modeled as line singularities within an elastic continuum and their evolution is described through a set of constitutive rules that are formulated based on the subscale observations. The crystal lattice information is retained in the form of anisotropic elastic stiffness tensor and slip systems on which dislocations glide. The corresponding mathematical construct and numerical implementation is commonly referred to as *Discrete Dislocation Dynamics* (DDD), if inertial terms are retained (Cazacu and Fivel, 2010). Internal stresses around individual dislocations are accounted for at this length-scale and are inherently non-local, rendering a length-scale dependent *pseudo-continuum* framework. While DDD (and its static counterpart ignoring inertia) can

model relatively bigger computational domains compared to MD while accounting for short- and long-range dislocation interactions, the physical dimensions are still restrictive to a few microns making it somewhat difficult to apply to larger scale calculations that span several mm to m.

Mesoscopic scale – At this scale, the physical properties of a material are represented as continuous variables (continuum). As in the microscopic scale, the directional elasticity at the crystal lattice level is incorporated through anisotropic elasticity. However, instead of tracking plastic activity through motion of discrete dislocations, equivalent constitutive laws for plastic slip on individual slip planes are written in terms of dislocation densities on those slip planes (Asaro, 1983; Ma et al., 2005). In its conventional form, length-scale effects (Burger's vector information) in crystal plasticity are lost due to homogenization from discrete dislocations to dislocation density. However, some of these effects can be incorporated by appealing to non-local field theories (Evers et al., 2004; Gurtin, 2002; Han et al., 2005a). This scale can be considered as a bridge between the microscopic and macroscopic scale where the mechanics at finer length-scales is accounted for using appropriate constitutive relations.

Mesoscopic (and microscopic) internal stresses are usually referred to as *athermal lattice resistance* to dislocation motion, which are independent of temperature and strain rate except for its temperature dependence through the shear modulus (Hull and Bacon, 2001; Zaiser and Seeger, 2002).

Macroscopic scale –Bulk scale responses devoid of size-effects are well-described at this scale using classical continuum plasticity (Khan and Huang, 1995). Traditionally, the elastic and plastic behaviors are described by deterministic constitutive laws resulting from averaging the micro-structural information (e.g. dislocation cell structures and dislocation spacing) at finer scales over a representative volume that

comprises sufficient number of crystal orientations to render a homogenized continuum. Such averaging procedures naturally smear out much of the microstructural information and more importantly, the inherent microstructural features, giving length-scale independent frameworks. Again, this approach works well in many cases, but fails to capture size-effects that arise from microstructural differences. For example, such an approach essentially predicts the same (size-independent) yield strength and hardening response for a nanocrystalline material and a coarse-grained material. Recent attempts admit length-scale effects in such a macroscopic theory without resorting to crystal level slip details (Abu Al-Rub and Voyiadjis, 2006; Fleck and Hutchinson, 1997; Nix and Gao, 1998; Voyiadjis and Al-Rub, 2005).

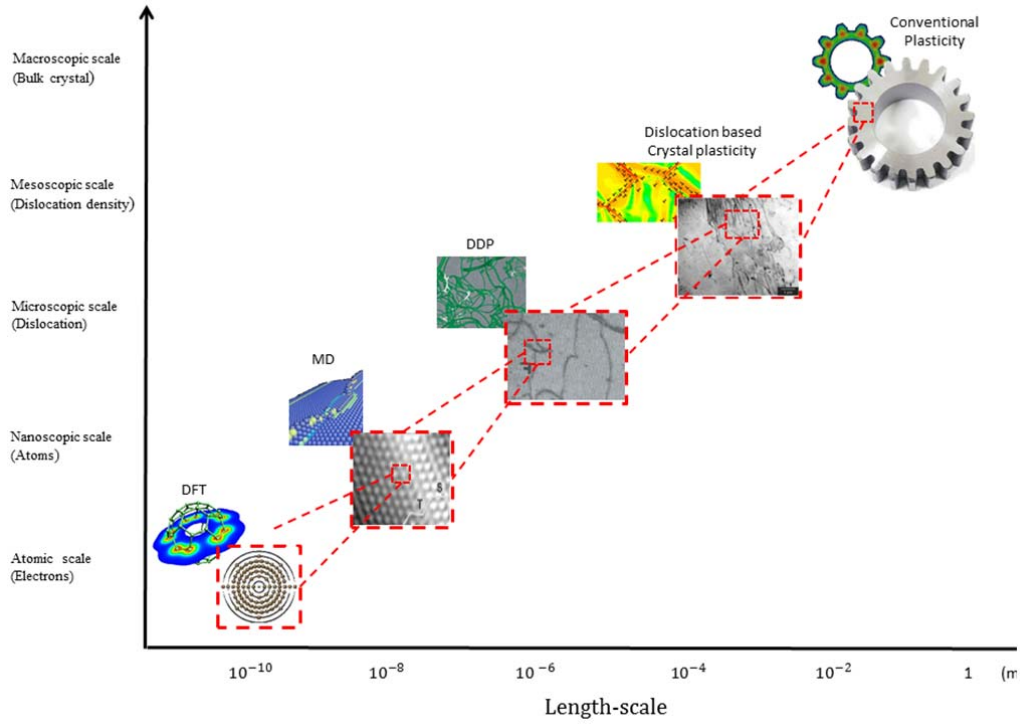

Figure 1.1. Plastic deformation and appropriate unit processes for modeling at different scales

At small length-scales, dislocation mechanisms are enriched by the presence of boundaries. For example, short-range interactions such as dislocation nucleation,

annihilation, and multiplication mechanisms and long-range interaction elastic interaction between dislocations may be influenced by interfaces such as grain or twin boundaries, and/or free surfaces. Therefore, additional interactions between dislocations and boundaries should be taken into account for nano/micro-scale structures where high surface (or interface) area to volume ratio is common. In single crystals under uniform loading conditions, length-scale dependent yield and flow strengths are observed with decreasing specimen dimensions and the underlying mechanisms are associated with dislocation activities that are modulated by free surfaces (Greer and Nix, 2006); (Shan et al., 2007). In nanostructured polycrystalline metals such as nanograined and nanotwinned metals (Haque, 2004; Lu et al., 2009), a Hall-Petch behavior arises from dislocation interaction with grain and twin boundaries in the form of dislocation pile-up.

At continuum scales, dislocation induced plasticity may be broadly classified into two groups based on the way they accumulate in during plastic deformation. Statistically stored dislocations (SSD) accumulate by statistical trapping of the dislocations to accommodate plastic slip (Ashby, 1970). At an atomistic scale, individual dislocations produce internal stresses in their vicinity, but at larger scales (meso and above), these are canceled in the process of averaging out, since SSDs by definition are randomly distributed. Another type of dislocations arises from the necessity to accommodate local lattice curvatures that arise due to non-uniform plastic deformation (Nye, 1953; Ashby, 1970). Ashby (1970) referred to these as the Geometrically Necessary Dislocations (GNDs). GNDs act as additional obstacles to the motion of SSDs, but themselves do not contribute to plastic strain (Gao and Huang, 2003). Incorporating GNDs within continuum frameworks endow them with an ability to predict a length-scale dependent macroscopic response under non-uniform plastic deformation (Acharya and Bassani, 2000; Ashby, 1970; Fleck et al., 2003; Nix and Gao, 1998).

The following GND related mechanisms could be identified in terms of stresses or resistance mechanisms at different scales (Figure 1.2):

- Short-range interactions of GNDs with SSDs as an additional thermal lattice resistance which occurs in nanoscopic scale (Acharya and Bassani, 2000; Nix and Gao, 1998).
- Long-range elastic GND-GND interaction described at the mesoscopic scale as athermal internal stresses that influence dislocation mobility (Kröner, 1967).
- Long-range elastic interaction between GNDs and boundaries such as free surfaces manifesting as athermal lattice resistance, which are described as image stress fields at the mesoscopic continuum scales

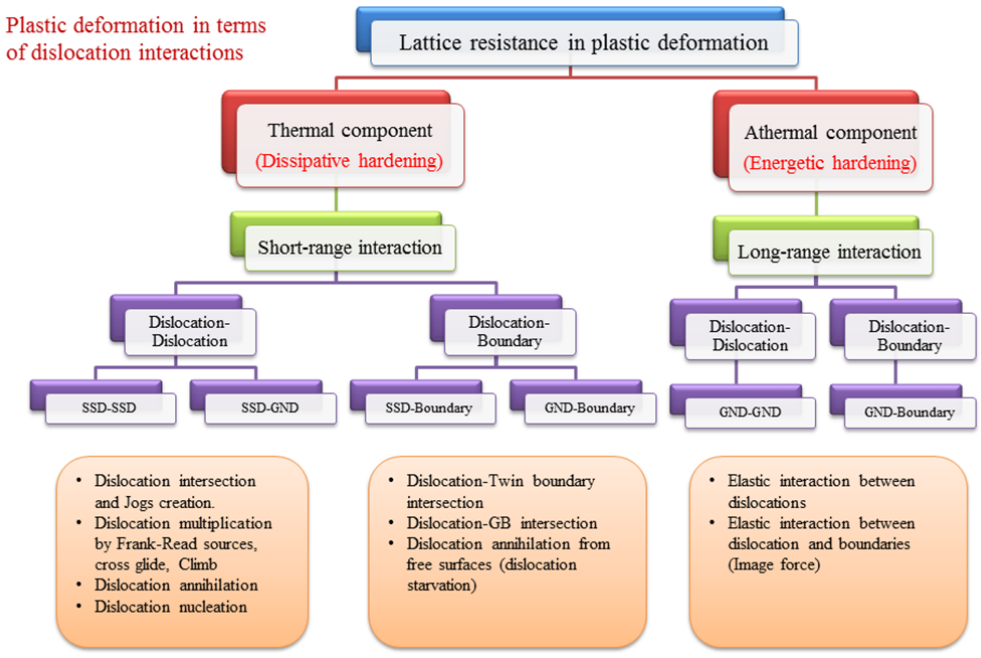

Figure 1.2. Dislocation interactions at different length-scales

Figure 1.2 also gives some examples of each of the interactions. The focus this work is modeling the plastic deformation in crystalline materials accounting for the length-scale effects that persist at the mesoscopic scale. While these effects are mainly ascribed to the presence of GNDs that are in-turn related to strain gradients, some dislocation mechanisms produce size-effects even in the absence of strain gradients and are briefly mentioned later in this chapter, for clarity. Each of these may possess an associated length-scale that must be compared with the length-scales of interest. Many a times, the length-scale are problem-dependent and may be determined by structure geometry, deformation profile, material microstructure, physical properties of boundaries and so on (Voyiadjis and Al-Rub, 2005).

1.2.2 A Brief Overview of Experimental Observations of Length-scale Effects in Plasticity:

Several similar observations are reported in micro-scaled specimens in a variety of heterogeneous deformation conditions including bending of single- and poly-crystalline beams and thin films (Haque and Saif, 2003; Huber et al., 2002; Motz et al., 2005; Stolken and Evans, 1998). Specifically, the observed trend is that the flow stress increases as the specimen thickness reduces. Furthermore, this size effect is enhanced in presence of substrate which causes additional pile-up of dislocations at the film-substrate interface. Similar behavior is observed in micro and nano indentation, which exhibit length-scale dependent hardness (Ma and Clarke, 1995; McElhaney et al., 1998; Nix and Gao, 1998). In metal matrix composites (MMCs), higher macroscopic strength and hardening is reported with decreasing inclusion size while keeping its volume fraction constant.

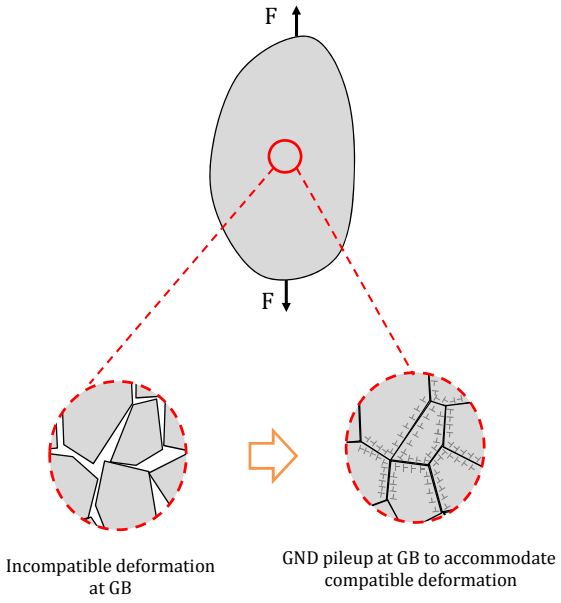

Figure 1.3. Schematic of geometrically necessary dislocations (GNDs) pile up at grain boundary in order to accommodate compatible plastic deformation.

In all the above-mentioned and similar scenarios, the length-scale effects are attributed to the presence of GNDs that accumulate in addition to SSDs in order to compensate incompatibilities in the plastic deformation (Figs. 1.3 and Figure 1.4) arising due to relevant reasons (e.g. elasto-plastic and thermal expansion mismatch between the inclusion and metal matrix in MMCs or incompatible plastic deformation, (Ashby, 1970; Fleck et al., 1994).

It is useful to mention here that although mechanics approaches relying GND-induced strengthening have gained popularity and is also the main topic of this thesis, these may not be the only or the most relevant mechanisms in strengthening.

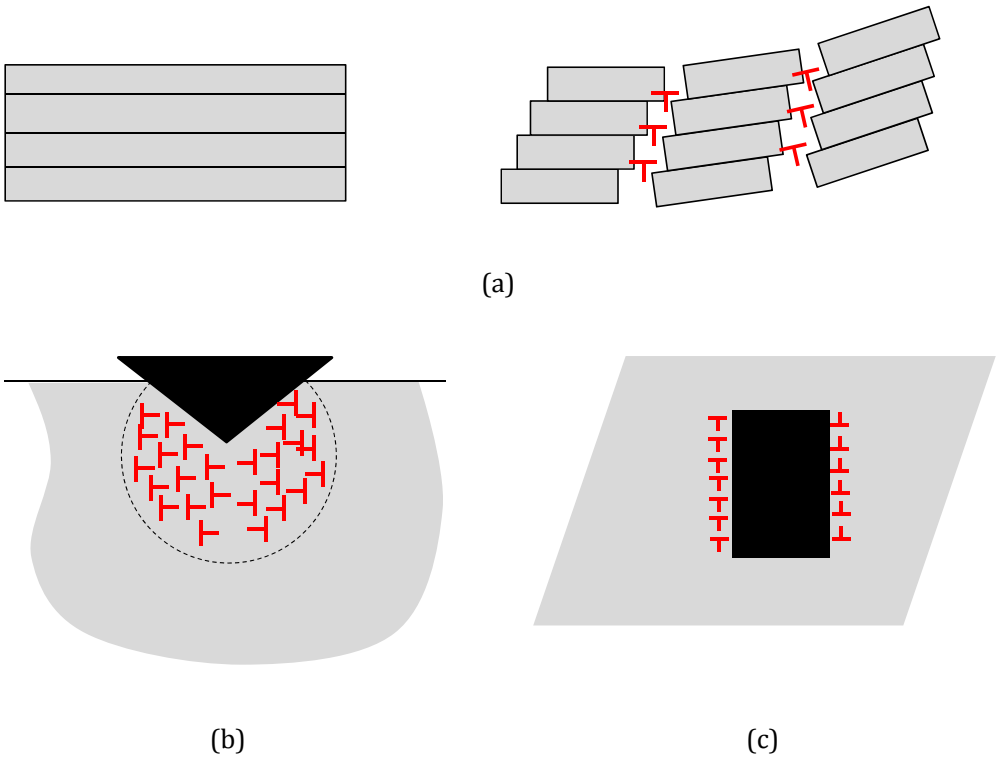

Figure 1.4. Formation of GND in presence of strain gradient in (a) bending of single crystal (b) nano/micro indentation (c) metal matrix composite contains nano/micro inclusions.

A somewhat disconnected result is the recently observed size-dependent strengthening of single crystalline materials under nominally uniform deformations (e.g. uniaxial tension or compression) at structural scales below a few microns (Uchic et al., 2004; Uchic et al., 2009). The GND mechanism is not expected to be operative or be a dominant mechanism in these cases due to the absence of lattice curvatures. This is a relatively nascent area of research and several postulates have been recently advocated. These include the *dislocation starvation* model (Dehm, 2009; Greer and Nix, 2006; Nix et al., 2007) which suggests that in a smaller specimen, dislocations readily escape from the free surfaces (aided by image stresses) in comparison to the rate of dislocation nucleation and multiplication, or the *source-limited dislocation plasticity* (Dehm, 2009; Uchic et al., 2009), which suggests that fewer dislocation sources in the case of smaller specimens compared to larger specimens is also likely to produce a similar size-effect. In general, many of the aforementioned mechanisms may operate in tandem and

contribute synergistically or compete with each other to produce overall plastic responses.

The spatial resolution that we focus on in this thesis is the single crystal. In the next section, we briefly summarize some of the proposed length-scale dependent continuum approaches that account for some of the GND effects described in Fig. 1.2.

1.2.3 Continuum descriptions of Dislocation-mediated Crystal Plasticity

1.2.3.1 Classical crystal plasticity

Classical continuum plasticity theories are generally based on macroscopic behaviors of materials in plastic region where materials are considered as a homogenized continuum body. The anisotropic plastic behavior of crystalline materials was pioneered by works of Taylor and coworkers (Taylor, 1934; Taylor and Elam, 1923), and Schmid, (1924) who proposed the movement of the dislocations in crystal lattice as a major source of plastic deformation. Based on these observations, Hill and Rice (1972) and Asaro and Rice (1977) developed a robust framework for single crystal plasticity. A comprehensive review of single crystal plasticity has been given by Asaro (1983). These theories explicitly account for anisotropic plasticity through slip system information in that the plastic slip can occur in certain directions, the slip directions and on certain atomic planes, the slip planes. The discreteness of atomistics is smeared out. Phenomenological hardening laws are prescribed that attempt to adhere to the physics of the hardening processes (Bassani and Wu, 1991; Peirce et al., 1983). The Taylor hardening model typically serves as a standard expression to describe the hardening induced by myriad short-range dislocation-dislocation interactions , for example, a generalized model proposed by Franciosi (1980)

$$\tau_f^\alpha = \tau_0^\alpha + \mu b \sqrt{\sum_\beta a_{\alpha\beta}\rho^\beta} \tag{1.1}$$

where τ_0^α is the critical resolved shear stress (CRSS) on α^{th} slip system, and μ and b are the shear modulus and Burgers vector, respectively. The coefficients $a_{\alpha\beta}$ apportion the hardening components that account for both, self and latent hardening and ρ^β is a continuum field variable describing the SSD density on β^{th} slip system. These coefficients implicitly accounted for macroscopic isotropic hardening behavior arises from short range dislocation interaction mechanisms in nanoscopic scale such as multiplication, annihilation, jog and dipole formation and cross slip.

In generalized dislocation based crystal plasticity individual dislocation mechanisms and their evolution laws incorporated into continuum framework in terms of continuum microstructural field variables (Prinz and Argon, 1984; Roters et al., 2000). Roters et. al. (2000) have proposed a dislocation based crystal plasticity for polycrystalline materials, which is mainly concern about SSD density while GND contributions are neglected. In their approach, plastic deformation is introduced in terms of three internal state variables as mobile and immobile dislocation density in the cell interiors and immobile dislocation density in the cell walls and their evolution laws.

The kinematic hardening in macroscopic continuum scale is addressed by Armstrong and Fredrick (1966; 2007) in terms of back stress tensor. Later, it has been extended into conventional crystal plasticity framework (Cailletaud, 1992). The evolution law for back stress tensor in crystal plasticity framework is sometimes written as (Voyiadjis and Huang, 1996; Xu and Jiang, 2004)

$$\dot{x}_b^\alpha = c\dot{\gamma}^\alpha - d|\dot{\gamma}^\alpha| x_b^\alpha \tag{1.2}$$

where $\dot{\gamma}^{\alpha}$ is the plastic slip rate on α^{th} slip system, and c and d are coefficients obtained from experiments. In microscopic scale, the back stress arises from long range elastic interaction between dislocations in cell structure and are responsible for classical Bauschinger effects (Mughrabi, 1983). In conventional crystalline materials with large grain sizes, the cell structure and average dislocation spacing are nearly independent of the specimen sizes and consequently internal stress is only function of plastic strain. However, as microstructural or specimen dimensions decrease, the dislocation arrangements and their interactions may be significantly affected.

1.2.3.2 Continuum crystal plasticity with GNDs

With increasing quest toward strong and ductile materials at low overall weight for large-scale structures on the one hand and the rapid development of miniaturized structures small scale devices on the other, predictive modeling of length-scale dependent material behavior has assumed a central role to analyze and design novel materials and structures. However, a robust understanding of length-scale dependent mechanisms is a challenging problem. Although, classical (i.e. length-scale independent) crystal plasticity theories capture the behaviors of bulk crystalline materials with good accuracy, they fail to predict length-scale effects since no explicit microstructural information is included. Furthermore, performing MD simulations on realistic time and length-scales for nano/micro structures are very costly. A logical recourse is to develop, continuum crystal plasticity theories that are endowed with GND information within.

Alongside the SSD interactions, the GND-SSD and GND-boundary interactions become important at small length-scales. Nix and Gao (1998) proposed that the GNDs act as the obstacles for movement of other dislocations and provide additional short-range interaction with other dislocations. Since the nature of these interactions is the same for both SSDs and GNDs, they reformulated the Taylor hardening model with an

additional term that arises from the presence of GNDs, which in-turn is related to the strain gradient. The associated length-scale is related to the Burgers vector that is scaled by elastic shear modulus and basic material strength. This approach has been extended into crystal plasticity framework (MSG-CP) by (Han et al., 2005a). Acharya and Bassani (2000) applied the same concept by introducing a hardening modulus as a function of both, strain and strain gradient to account for both SSDs and GNDs interactions. Since, these theories do not include higher-order stresses and boundary conditions, the generally referred to as the *lower-order gradient theories.* These theories have capability to capture size dependent flow stress at moderate strain where flow stress is dominated by short range interaction of dislocations (Acharya, 2003; Schwarz et al., 2008). However, they fail to predict size-dependent yield strength at initial stage of plasticity because they ignore the long-range elastic interaction effects.

This latter aspect that is related to small strains can be modeled by incorporating the internal stresses that arise due to the GNDs (Evans and Hutchinson, 2009; Fleck and Hutchinson, 1997). Unlike the SSD density, an average GND density over a mesoscopic volume result in net internal *residual* stresses through long-range elastic interactions between the GNDs. Kröner (1967) incorporated the long-range interaction of dislocations into continuum mechanics through the *nonlocal* constitutive equations using integral formulation. Later Aifantis (1984; 1987) accounted for this effect using constitutive equations that include plastic strain gradient terms. Fleck and Hutchinson (2001; 1993) proposed higher-order phenomenological strain gradient plasticity theories using reformulation of the yield function that included gradient terms and that introduce additional boundary conditions. Gurtin and coworkers (Anand et al., 2005; Gurtin, 2002, 2010; Gurtin and Anand, 2005) generalized this theory using thermodynamic framework by proposing an additional *defect energy* due to defects like dislocations. This additional energy is work-conjugate to the higher-order stresses that are related to the second gradients of plastic strain, requiring higher-order boundary

conditions. With the same concept, different approaches have been advocated to develop nonlocal theories (Abu Al-Rub et al., 2007; Anand et al., 2005; Gudmundson, 2004; Polizzotto, 2009; Voyiadjis and Deliktas, 2009). In all of these theories, length-scales enter into the continuum equations to be mathematically consistent, but their physical origin and connection with material microstructures are unclear.

To better understand the length-scale dependent behavior, underlying mechanisms and origin of length scale parameters, the defect energy and corresponding higher-order stress and boundary conditions need to be interpreted in terms of micro structural information. Recently, the long-range elastic interaction of GNDs at mesoscopic scale is modeled into continuum plasticity using dislocation theory of infinite medium where length-scales are defined in terms of the dislocation correlation distance (Evers et al., 2004; Gerken and Dawson, 2008; Mesarovic, 2005). This correlation distance relates to the collective behavior of dislocations statistical mechanics approach which explain the origin of strain gradient terms in size dependent continuum theories.

Summarizing, there are two main groups of strain gradient theories mostly accounting for short- and long-range interactions between dislocations: the lower-order and higher-order strain gradient theories. It has been shown that the short-range interaction is a major source of size dependency at moderate strain where dislocation density is large enough (Acharya, 2003; Schwarz et al., 2008). However, the higher-order strain gradient theories are successful in explaining the size-dependent response at yield and they tie it to the long-range interaction between GNDs (Borg, 2007; Evans and Hutchinson, 2009; Niordson, 2003a). The difficulty with higher-order b.c.'s is that it may not be always easy to identify appropriate descriptions for general interfaces (Voyiadjis and Deliktas, 2009) and typically, the computational effort is significantly large.

1.3 Scope and Objectives of the Thesis

In this dissertation, we investigate the length-scale dependent behaviors of microstructures due to the presence and non-homogeneous distribution of the GNDs. The formulation focuses on face-centered-cubic (FCC) materials and their size dependent behaviors under non-uniform plastic deformation. A broad objective here is to physically incorporate the GND related mechanisms into a continuum framework through the concept of kinematic incompatibility of the underlying lattice.

In Chapter 2, we focus our attention on the length-scale dependent behavior that arise from short-range interactions between the SSD and GND densities, which manifests as enhanced flow hardening at moderate strains. At such strains, the long-range elastic effects due to GNDs are expected to be negligible (Acharya, 2003; Schwarz et al., 2008). This GND induced hardening modeled through Taylor hardening (Nix and Gao, 1998) as extended to crystal plasticity (Han et al., 2005a). The resulting mechanism based strain gradient crystal plasticity is implemented within ABAQUS® via user-material subroutine (UMAT). First, we investigate the gradient-induced size-effects in single crystals with embedded inclusions under thermo-mechanical loading. The role of internal stresses due to prior thermal loading is probed as a function of crystal orientation, and inclusion shape and size. Then, we focus our attention on the length-scale dependent interaction effects in polycrystalline MMC due to the grain size and inclusion sizes. We propose a simple analytical model for this interaction effect.

Chapter 3 presents concerns the role of GNDs in producing long-range interactions that manifest as internal stresses. We develop a nonlocal crystal plasticity theory accounting for these long-range GND interactions using stress functions approach as applied to elastically isotropic materials. We systematically show that nonlocal internal stresses develop due to non-homogeneous spatial distribution of the GND density. Using

thermodynamic framework these internal stresses are incorporated into continuum crystal plasticity as an additional irreversible stored energy (defect energy). The internal stresses appear as additional resolved shear stress in the crystallographic visco-plastic constitutive law for individual slip systems. Using this formulation, we investigate boundary value problems involving isotropic single crystals subjected to monotonic and cyclic loading. The resulting length-scale dependent isotropic and kinematic hardening behaviors are investigated in terms of short-range and long-range GND interactions. Finally, we close the chapter by discussing the extension of this approach to crystalline materials with elastic anisotropy.

In the theory presented in Chapter 3 ignores the long-range elastic interactions between the GND density and boundaries, the so-called image stresses. These image stresses may have significant effects in miniaturized specimens and are therefore important. In Chapter 4, this additional long-range interaction is incorporated by augmenting the formulation in Chapter 3 with another kernel (Green) function that accounts for traction-free surfaces. The resulting additional internal stresses are introduced in terms of GND density-surface elastic interaction. While the basic approach is general, we choose thin film under pure bending as a model problem to investigate the length-scale dependent behavior. We show that these additional internal stresses produce a length-scale dependent macroscopic response even in the case of such a system that comprises a nominally uniform distribution of GND density. We compare our results with experiments and provide a physical interpretation of the underlying length-scale.

Finally, Chapter 5 summarizes the accomplishments of this PhD thesis and provides recommendations for future work.

2 A Mechanism-Based Gradient Crystal Plasticity Investigation of Metal Matrix Composites

2.1 Introduction

The advent of nanostructuring techniques has led to an unprecedented growth in the area of synthesizing metal matrix composites (MMC) with exceedingly superior strengths. It is possible to significantly enhance the strength of MMCs over that achieved by conventional strengthening from load transfer, by synthesizing microstructures with nanocrystalline matrices, incorporating small sized reinforcing inclusions, or a combination of both (Lloyd, 1994; Nan and Clarke, 1996; Sekine and Chent, 1995). Grain boundaries (gb's) create strong barriers to dislocations providing higher baseline matrix strength that can be further improved by the addition of reinforcing inclusions MMCs through a load-transfer mechanism. Thus, one may rely on synthesizing high-strength MMCs solely by using nanocrystalline matrices. Alternatively, the length-scale dependent strengthening from micron or sub-micron sized inclusions attributed to interaction of the geometrically necessary dislocations (GNDs) with matrix-inclusion interfaces may also provide another path to strength enhancement. However, both the strengthening strategies have to deal with one common caveat – the enhancement in the strength usually comes at the cost of precipitous reduction in the ductility. The latter alternative might be attractive, because it allows using smaller inclusion volume fractions (v.f.) that may help mitigate the strength-ductility dichotomy to some extent.

Recent experimental and analytical efforts have aimed at understanding the size-effects in MMCs (e.g. (Balint, 2005; Dai et al., 1999; Joshi and Ramesh, 2007; Kiser et al., 1996; Lloyd, 1994; Nan and Clarke, 1996))and have led to the development of novel

composite micro-architectures (Habibi et al., 2010; Joshi and Ramesh, 2007; Ye et al., 2005). These investigations indicate that one has to judiciously choose appropriate values for the microstructural design degrees of freedom in imparting optimal functional characteristics to an MMC. Analytical and computational investigations have focused on implementing length-scales in the conventional plasticity theory based on the GND argument as applied to MMCs (e.g. (Cleveringa et al., 1997; Joshi and Ramesh, 2007; Nan and Clarke, 1996; Niordson, 2003b; Xue et al., 2002; Zhou et al., 2010). From a mechanistic viewpoint there are several challenging aspects that need to be understood in the length-scale dependent MMC response. For example, the physics of plastic events at the inclusion-matrix interfaces (i-m) and at gb's (and triple junctions) due to thermal and mechanical loading, *communication* between the i-m interfaces and gb's, grain orientation effects, inclusion and grain size distributions, thermal and elastic mismatch between phases and several more. While it may be important to incorporate these mechanisms, a single mechanistic framework that is capable of resolving the microstructural details and concurrently also embeds appropriate physics for all the interfacial mechanisms is difficult to conceive at the moment. A comparatively tractable setting is possible if one chooses to simplify and/ or ignore some of the aspects. Crystal plasticity enriched with length-scale features can effectively handle the kind of resolution necessary for the problem.

In this chapter, we focus our attention on the length-scale effects in MMCs arising from short-range interaction between SSDs and GNDs, which is dominant at moderate strains where dislocation density is high (Acharya, 2003; Schwarz et al., 2008). To account for these interactions within a continuum framework, we resort to the Mechanism-based Slip Gradient Crystal Plasticity (MSG-CP) developed by Han, et al. (2005a) that has its roots in the pioneering work of the Nix and Gao (1999; 1998). The MSGCP framework accounts for length-scale effects in the slip system constitutive laws by including slip gradients on individual slip systems that are related to their GND

densities. Given that in the present work the grains and inclusions are explicitly resolved, slip gradients naturally arise at gb's and i-m interfaces due their elasto-plastic and thermal mismatch. However, the MSGCP approach is a lower-order theory compared to a higher-order framework[1], because it does not invoke additional boundary conditions (b.c.'s) at interfaces that are related to the gradient of the GND density, i.e. Laplacian of the plastic slip (Abu Al-Rub, 2009; Borg, 2007; Geers et al., 2007; Gurtin et al., 2007; Kuroda and Tvergaard, 2006; Kuroda and Tvergaard, 2008a, b; McDowell, 2008; Voyiadjis and Deliktas, 2009). Consequently, lower-order CP approaches cannot model some of the enhanced interactions between interfaces and dislocations that higher-order CP approaches are capable of handling. For example, (Borg, 2007) introduced a higher-order CP theory that includes a material parameter κ to tune the inter-granular interaction at gb's with impinging dislocations. Using this, he investigated the role of grain boundaries on the macroscopic behaviors of simulated polycrystals and demonstrated that $0 < \kappa < \infty$ determines the amount of strengthening at yield. Notably, the $\kappa = 0$ case (gb's fully transparent to dislocations) degenerates to a lower-order theory. As indicated by (Borg, 2007) these b.c.'s together with the choice of interface material parameters may have a profound effect on the nature of polycrystalline strengthening and hardening predicted by these theories. Although a higher-order theory would be suited for the present problem (Fredriksson et al., 2009), the difficulty with higher-order b.c.'s is that it may not be always easy to identify appropriate descriptions for general interfaces (Voyiadjis and Deliktas, 2009).

[1] Lower-order gradient theories introduce length-scale through first gradient of plastic slip that relates only to the presence of the GND density. On the other hand, higher-order gradient theories incorporate the GND density distribution effect too and relate to them to the second gradient of plastic slip. This leads to a constitutive law in the form of a partial differential equation that necessitates higher-order b.c.'s.

Moreover, the computational effort for higher-order CP is significantly larger than their lower-order counterparts. On the other hand, due to the inherent inability of the MSGCP in handling enhanced long-range interactions between dislocations and interface the length-scale effect appears only in the flow behavior rather than at yield (Evans and Hutchinson, 2009). However, despite some of its limitations, we choose the MSGCP theory keeping in view its simplicity in the numerical implementation within existing CP framework, computational expense for the present work and a relatively established physical understanding of the length–scale parameters.

In the following section, we first give a brief outline of the computational implementation of MSGCP (Han et al., 2005a) as user-material subroutine (UMAT) in ABAQUS/ STANDARD® finite element software. Using the implemented formulation, we first investigate size-effects in single crystal MMCs due to thermo-mechanical loading. This is a classic source of GND existence that arises due to thermal residual stresses that pre-exist in an MMC microstructure due to the mismatches in the thermal expansion coefficients (CTE) of the matrix and the inclusions together with elastic and plastic mismatches. The corresponding GND density is referred to here as the thermal GND density to distinguish it from the GND density that arises during mechanical loading. We simulate the role of pre-existing thermal GND density on the subsequent macroscopic and microscopic behaviors under mechanical loading as a two-step process. These thermo-mechanical simulations essentially restrict their attention to single crystal MMC in a bid to understand the local microscopic details that arise around the inclusions that are embedded within large grains. In section 2.4, we take a step further and model polycrystalline MMCs that include both, grain and inclusion size-effects under mechanical loading. The objective is to quantify the nature of the interaction between these two microstructural sizes on the overall response. Through these polycrystalline simulations, we propose a simple analytical model that can be easily integrated into

homogenized continuum calculations such as the Mori-Tanaka approach (Joshi and Ramesh, 2007).

2.2 Computational Implementation of MSGCP Theory

The kinematics and kinetics of MSGCP approach implemented in this work closely follow the conventional continuum crystal plasticity framework of Asaro and co-workers (Asaro, 1983; Peirce et al., 1983), except that a length-scale effect is introduced in the slip system hardening.

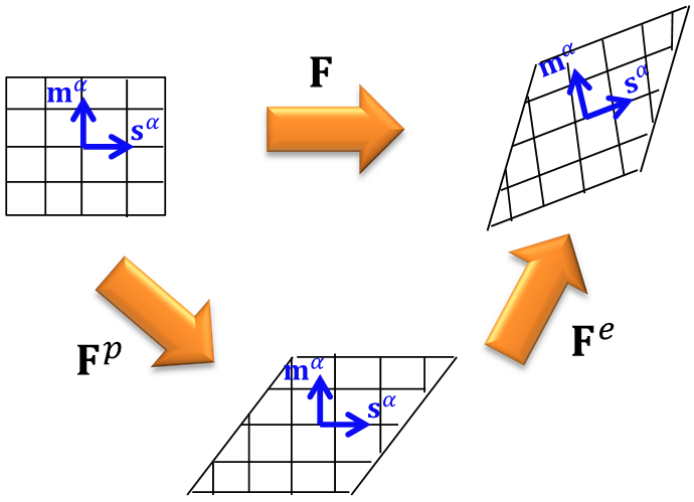

Figure 2.1. Kinematics of single crystal deformation

Based on the multiplicative decomposition of deformation gradient proposed by Lee (1966), in case of finite deformation, the total deformation gradient $\mathbf{F}$ is

$$\mathbf{F} = \mathbf{F^e F^p} \tag{2.1}$$

where $\mathbf{F^e}$ and $\mathbf{F^p}$ represent the elastic and plastic parts of the deformation gradient, respectively (Figure 2.1). The spatial velocity gradient in the current state is (Asaro, 1983)

$$\mathbf{L} = \mathbf{D} + \mathbf{W} = \mathbf{L^e} + \mathbf{F^e L^p F^{e-1}} \tag{2.2}$$

$$\begin{aligned} \mathbf{L^e} &= \mathbf{D^e} + \mathbf{W^e} = \dot{\mathbf{F}}^{\mathbf{e}}.\mathbf{F}^{\mathbf{e-1}} \\ \mathbf{L^p} &= \mathbf{D^p} + \mathbf{W^p} = \dot{\mathbf{F}}^{\mathbf{p}}.\mathbf{F}^{\mathbf{p-1}} = \sum_{\alpha} \dot{\gamma}^{\alpha} s^{\alpha} m^{\alpha} \end{aligned} \tag{2.3}$$

where **D** and **W** are the rate of deformation and spin tensors, respectively. The super scripts **e** and **p** signify the elastic and plastic parts, respectively. We assume that a single crystal deforms plastically solely by crystalline slip and the elastic behavior of the crystal is constant during plastic deformation. The lattice orientation is affected solely by elastic part of the total deformation gradient.

The elastic constitutive equation for a single crystal proposed by Hill and Rice (1972) is adopted in this code. The constitutive law for plastic slip rate $\dot{\gamma}^{\alpha}$ is assumed as

$$\dot{\gamma}^{\alpha} = \dot{\gamma}_0 . \left| \frac{\tau^{\alpha}}{g_T^{\alpha}} \right|^n . sign(\tau^{\alpha}) \tag{2.4}$$

where $\dot{\gamma}_0$ and τ^{α} are the reference plastic slip rate and resolved shear stress on slip system α and g_T^{α} is the overall hardening of lattice due to both SSD and GND densities. The evolution law for the SSD induced hardening for multiple slip deformation is given by

$$\dot{g}_{SSD}^{\alpha} = \sum_{\beta} h_{\alpha\beta} \dot{\gamma}^{\beta} \tag{2.5}$$

where $h_{\alpha\beta}$ is a matrix representing self and latent hardening coefficients given by (Asaro, 1983),

$$h_{\alpha\alpha}(\gamma) = h_0^\alpha sech^2 \left|\frac{h_0\gamma}{\tau_s^\alpha - \tau_0^\alpha}\right| \text{ (no sum on } \alpha)$$
$$h_{\alpha\beta}(\gamma) = q h_{\alpha\alpha}(\gamma), \qquad \alpha \neq \beta \tag{2.6}$$

In Eq. (2.6), h_0^α is initial hardening modulus, τ_s^α is the saturation value for the resolved shear stress, τ_0^α is the critical resolved shear stress, $\gamma = \sum_\alpha \gamma^\alpha$ is the total cumulative shear strain on all slip systems and q ($\sim$ 1-2) accounts for the interaction between different slip systems. In the MSGCP approach, the GND density ρ_g^α on α^{th} slip system is assumed to contribute to its overall hardening via Taylor hardening model. Consequently, g_T^α is (Han et al., 2005a)

$$g_T^\alpha = g_0^\alpha \sqrt{\left(\frac{g_{SSD}^\alpha}{g_0^\alpha}\right)^2 + l\eta_g^\alpha} \tag{2.7}$$

where the internal material length-scale $l = (a^2\mu^2\, b/\tau_0^{\alpha 2})$, with b as the magnitude of Burgers vector, μ as the overall shear modulus and a as an empirical material constant ranging between 0.1-0.5. In Eq. (2.7), η_g^α is an effective scalar measure of the GND density tensor on the slip system α

$$\eta_g^\alpha = |\mathbf{A} \times (\mathbf{s}^\alpha \times \mathbf{m}^\alpha)| \tag{2.8}$$

where $\mathbf{s}^\alpha$ and $\mathbf{m}^\alpha$ are respectively, the slip direction and slip-plane normal for α^{th} slip system. The effect of slip gradient is related to the GND density in each slip system via $\rho_{GND}^\alpha = \eta_g^\alpha / b$.

2.2.1 Slip gradient calculation

In implementing this length-scale feature within a UMAT, one needs to calculate the slip gradients at each Gauss point (GP). We exploit the concept of shape functions that is at the core of a typical finite element (FE) formulation for evaluating the slip gradients corresponding to each slip systems. For illustration purposes, we present the formulation applicable for an 8-node plane strain FE, but the approach can be extended to different types of FE's. As is widely known, the number of GP's in a FE determines the order of integration. The 8-node plane strain element that we adopt here (CPE8R) uses a reduced integration procedure in order to minimize the effects due to shear locking. Therefore, for each FE all the state variables (i.e. individual and total slip, slip gradients, etc.) and stresses are calculated at these GP's. To calculate the plastic slip gradients within an FE, we apply the approach similar to the one is used in calculating strains from displacements in a conventional FE formulation (Reddy, 2006). Within a FE, we consider a 4-node pseudo-element (Figure 2.2) constructed by joining the GP's describable by linear shape functions N_i' $(i = 1 - 4)$.

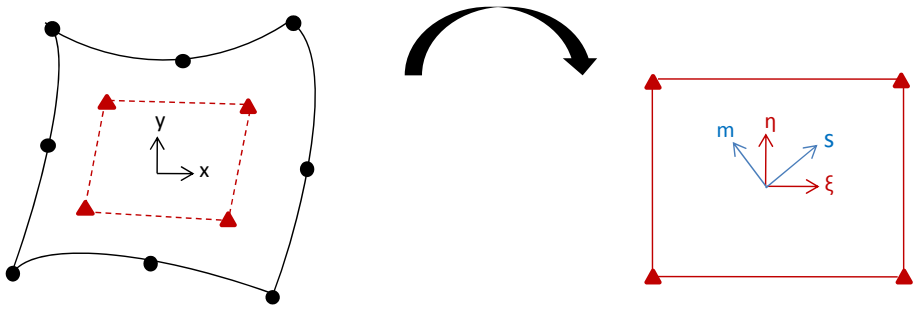

(a) (b)

Figure 2.2. (a) An Eight-node plane strain FE with four GPs and (b) a linear pseudo-element constructed from the GPs of the actual FE where ξ and η are the local isoparametric coordinates. The slip and normal directions (s and m) of a typical slip system α are also shown (b).

The local isoparametric coordinates (ζ and η) of the pseudo-element are related to the global coordinates x and y via the determinant J of the Jacobian matrix.

$$\begin{bmatrix} \frac{\partial}{\partial x} \\ \frac{\partial}{\partial y} \end{bmatrix} = J^{-1} \begin{bmatrix} \frac{\partial}{\partial \xi} \\ \frac{\partial}{\partial \eta} \end{bmatrix} \tag{2.9}$$

The slip gradient vector $\boldsymbol{\nabla}\gamma^{\alpha}$ in the slip direction s^{α} within each element is obtained using the chain rule of partial differentiation

$$\boldsymbol{\nabla}\gamma^{\alpha} = \frac{\partial \gamma^{\alpha}}{\partial x}\frac{\partial x}{\partial s^{\alpha}} + \frac{\partial \gamma^{\alpha}}{\partial y}\frac{\partial y}{\partial s^{\alpha}} \tag{2.10}$$

and the Cartesian slip gradients are related to the pseudo-element shape functions by

$$\frac{\partial \gamma^{\alpha}}{\partial x} = \sum_{i=1}^{4} \frac{\partial {N_i}'}{\partial x}\gamma_i^{\alpha}; \qquad \frac{\partial \gamma^{\alpha}}{\partial y} = \sum_{i=1}^{4} \frac{\partial {N_i}'}{\partial y}\gamma_i^{\alpha} \tag{2.11}$$

where γ_i^{α} is the plastic slip at i^{th} pseudo-node (i.e. GP of the actual FE) and on α^{th} slip system[2]. The Cartesian derivatives of N_i' (Eq. 2.8) are calculated using Eq. (2.9).

2.2.2 Time integration scheme

The time integration used in the UMAT is based on the implementation by Huang (1991), but contains augmented information about the GND effects. For completeness, we summarize the method here. The incremental slip on α^{th} slip system is

[2] This is similar to the one adopted in ABAQUS to calculate strain from nodal displacements u, e.g., $\varepsilon_{xx} = \frac{\partial u}{\partial x} = \sum_{i=1}^{4} \frac{\partial N_i}{\partial x} u_i$.

$$\Delta\gamma^{\alpha} = \Delta t[(1-\theta)\dot{\gamma}^{\alpha}(t) + \theta\dot{\gamma}^{\alpha}(t+\Delta t)] \tag{2.12}$$

where the parameter θ introduces a linear interpolation between value of slip rate $\dot{\gamma}^{\alpha}$ at the beginning and end of the time increment (Peirce et al., 1983). The $\theta = 0$ degenerates to Euler forward time integration scheme, but the recommended value is 0.5. Eq. (2.12) can be solved using Newton-Raphson technique

$$\Delta\gamma^{\alpha} - \Delta t(1-\theta)\dot{\gamma}^{\alpha}(t) - \Delta t\theta\dot{\gamma}^{\alpha}(t+\Delta t) = 0 \tag{2.13}$$

Then, the plastic slip rate is computed as

$$\dot{\gamma}^{\alpha}(t+\Delta t) = \dot{\gamma}_0 . \left|\frac{\tau^{\alpha} + \Delta\tau^{\alpha}}{g^{\alpha} + \Delta g^{\alpha}}\right|^{n} . sign(\tau^{\alpha} + \Delta\tau^{\alpha}) \tag{2.14}$$

Here, the values of stress and solution dependent state variables are evaluated at the end of each time increment and this allows using larger time increment. Further details on the basic implementation of the user subroutine UMAT and incremental formulations can be found in the report by Huang (1991).

2.3 Length-scale dependent MMC response induced by thermal residual stresses

Synthesis of metal matrix composites (MMCs) typically involve moderate to high temperature processing followed by cooling down to room temperature. Such thermal processes cause the internal residual stresses in MMCs due to high CTE and elastic mismatches between the matrix and inclusion. It is well-established that for conventional coarse-grained MMCs, the inclusion and matrix properties together with the volume fraction (v.f.), shape and arrangement of inclusions govern the overall stress-strain behavior (Christman et al., 1989; Corbin and Wilkinsona, 1994; Qiu and Weng, 1991; Shen et al., 1995). Arsenault and Taya (1987) experimentally investigated

the effects of thermal residual stress on the overall strengthening and hardening behavior of MMCs under monotonic tensile and compressive loading. They explained the tension-compression asymmetry through an analytical model based on Eshelby's equivalent inclusion approach. The strengthening and high hardening behavior of MMC occur due to high triaxiality in the stress state exists within the matrix region at the inclusion-matrix(i-m) interface (Christman et al., 1989; Li and Ramesh, 1998; Llorca et al., 1991; Shen et al., 1995). Most of these works employ inclusions that are several tens of microns in size. Lloyd (1994) observed that for a fixed inclusion v.f. the strength of the MMC increased with decreasing inclusion sizes (in the range of few microns). In other words, the MMC response becomes length-scale dependent- an effect that has been explained in terms of GNDs (Ashby, 1970; Nye, 1953). These are additional dislocations that arise due to the thermo-elastic mismatch between the inclusion and the matrix (Arsenault and Shi, 1986; Barlow and Hansen, 1995; Dai et al., 1999; Dai et al., 2001a; Dunand and Mortensen, 1990, 1991; Joshi and Ramesh, 2007). Several experimental observations indicate high dislocation density at reinforcement-matrix interface due to thermo-elastic mismatch between reinforcement material and matrix (Arsenault and Shi, 1986; Barlow and Hansen, 1995; Dunand and Mortensen, 1991).

A length-scale dependent metal plasticity framework becomes necessary in order to correctly predict size-effects in MMCs, including failure (Dai et al., 1999; Dai et al., 2001a). Recently, such a length-scale dependent behavior has been accounted for within finite element (FE) based computational works by introducing plastic strain gradients within the homogenized constitutive laws for continuum plasticity (Xue et al., 2002; Zhang et al., 2007; Zhou et al., 2011). Ohashi (2004) has explored the distribution of GND density around cuboidal and spherical inclusion embedded in the FCC crystalline matrix under uniaxial loading employing dislocation based crystal plasticity framework. However, these numerical approaches have not accounted for the effects due to initial GND density due to thermal processing. It is imperative to accounting for the (size-

dependent) thermal residual stresses within these frameworks, because they have important contributions to kinematic hardening. Analytical models have been proposed based on the idea of dislocation punching (Arsenault and Shi, 1986; Dai et al., 1999; Dunand and Mortensen, 1990, Taya et al., 1991; Qu et al., 2005) incorporated the contribution from the *thermal* GND density within FE-based strain gradient plasticity, but in a rather simplistic manner as an additional uniform background matrix strength. In comparison, underscoring the fact that these thermal GNDs may not be uniformly distributed in the matrix (Arsenault and Shi, 1986; Mukherjee et al., 1995; Suh et al., 2009). Suh et al., (2009) proposed an FE-based discrete punched zone approach that includes an additional region surrounding an inclusion whose strength is enhanced by the presence of thermal GNDs and investigated the length-scale dependent strengthening and interfacial failure of MMCs.

Common to all the aforementioned modeling approaches is the assumption of homogenized matrix plasticity in that they ignore specific crystallographic orientations, which are important in discerning the local deformation fields that affect global composite response (Schmitt et al., 1997; Barlow and Liu, 1998). One may envisage scenarios where crystallographic orientation effects are important in determining the inclusion-induced size effects (Barlow and Hansen, 1995; Shu, 2000). For example, in polycrystalline MMCs when inclusions are much smaller than the surrounding grains the local crystallography would be expected to decide the GND distribution. Likewise, in highly textured MMC architectures the overall crystallographic orientation would be expected to produce strong plastic anisotropy, which may also influence the GND induced size effect. Single crystal plasticity based approaches are valuable in such scenarios. Some works have been carried out to investigate the size-dependent MMC behaviors using crystal plasticity frameworks (Cleveringa et al., 1997; Shu and Barlow , 2000), but they ignore the presence of preexisting heterogeneously distributed thermally-induced GND density.

In the following, we address both these issues by adopting a Mechanism-based Slip-gradient Crystal Plasticity (MSGCP) approach and performing simulations of model MMC architectures under thermal and mechanical loads. We first elucidate the role of crystallographic orientation on the inclusion size dependent thermal GND density. We quantify the individual contributions therein from the thermal and elasto-plastic constituent mismatches. Then, for a given crystal with embedded inclusion, this crystallography mediated non-uniform thermal GND density is retained as a starting motif under subequent mechanical loading, which gets superposed on the mechanical GND density. The simulations not only resolve the inclusion size and shape-dependent distribution of the GND density, they also provide useful information about evolution of their averaged measures as a function of strain (Dai et al., 2001). We also model and discuss the size-dependent dependent tension-compression asymmetry under mechanical loading produced due to the pre-existing thermal GND density. Most of the results and discussions presented here pertain to single crystal matrices, but we also demonstrate the applicability of such an approach to polycrystal MMC architectures. The details of the slip-gradient crystal plasticity theory can be found in Han et al. (2005) and its computational implementation as a user-material subroutine within ABAQUS/ STANDARD as discussed in previous section.

2.3.1 Computational results for single crystals with inclusions

To enable consistent comparison of the size-effect across different parametric models, first we consider MMC unit cells comprising square inclusions embedded in single crystal matrix with plane-strain condition in the out-of-plane direction (Fig. 2.3).

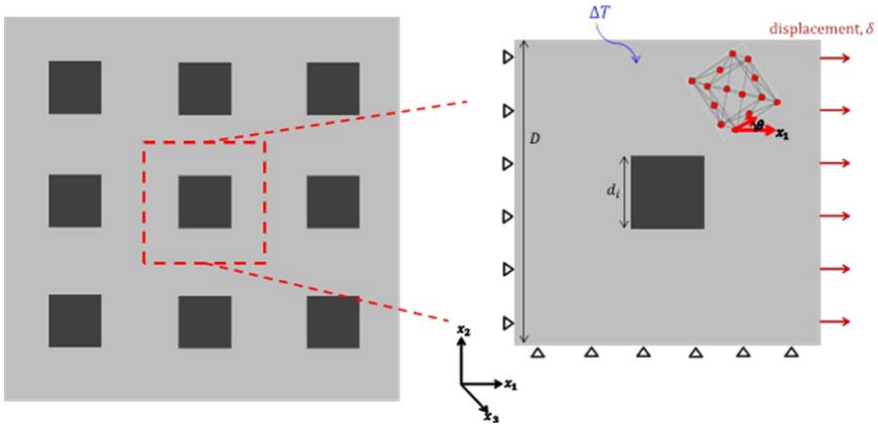

Figure 2.3. Metal matrix composite (MMC) with uniform arrangement of inclusions and unit cell comprising single crystal matrix and square inclusion.

As shown in the figure 2.3 the crystal orientation θ for an FCC structure is defined as the angle made by the [100] crystal direction with the global loading direction(x_1) and [001] crystal direction is taken to coincide with the global x_3 direction. For all the cases, the left and bottom edges are constrained along the x_1 and $x_2$directions, respectively; the top edge is allowed to move vertically, but constrained to remain straight during deformation. Table 2.1 gives the material properties used in the simulations, which are representative of pure Al (matrix) and SiC (inclusions). For simplicity, we assume isotropic elastic properties for the matrix, but anisotropic elasticity can be easily implemented.

Table 2-1. Constituent parameters used in single crystal MMC simulations

Parameter	Elastic Modulus	Poisson's ratio	Burgers vector	Initial hardening Modulus	CRSS	Saturation stress	Coefficient of thermal expansion
	E (GPa)	ν	b (nm)	$h_0\ (MPa)$	$\tau_0\ (MPa)$	$\tau_s\ (MPa)$	$\alpha(/K)$
Matrix (m)	70	0.33	0.25	510	60	109	23.6e-06
Inclusion (i)	190	0.19	-	-	-	-	4.3e-06

The thermo-mechanical loading condition is simulated as a two-step process that mimics the real scenario in that the thermal GND density arises due to thermal quenching as a part of processing, while the mechanical GND density accumulates during subsequent mechanical loading. A typical two-step thermo-mechanical simulation using MSGCP is performed as follows: in the first step, we apply a uniform temperature reduction $\Delta T = 500$ to the entire unit cell. This quenching effect results in a thermal GND density that is heterogeneously distributed within the matrix. The second step constitutes using this pre-existing GND density distribution as a background motif on the same starting microstructure and performing a new calculation under actual mechanical loading of interest. Thus, following the thermal loading step, a uniform displacement b.c. in the x_1-direction is applied to the right edge (Fig. 2.3) producing a nominal strain rate $\dot{\varepsilon} = 1 \times 10^{-5}$. We consider several crystal orientations $\theta = 0^o, 10^o, 30^o and\ 45^o$ and inclusion sizes $d_i = 1, 2, 5\ and\ 10\ \mu m$ to elucidate the crystallographically mediated size-effects. In all the simulations, the inclusion v.f. is kept constant ($f_i = 0.05$).

Under thermal and mechanical loads, size-dependent responses arise as a result of the plastic deformation carried by the GNDs due to the interfacial stresses arising from the thermo-elasto-plastic mismatch between the inclusion and the matrix. The *effective* GND density ρ_g under thermal/ mechanical loading condition is calculated using the constitutive laws provided in previous section (Eq. 2.8).

2.3.2 Crystal orientation and inclusion size effects on thermal GND density distribution

Figure 2.4a-d exhibit several interesting features pertaining to the distribution of the thermal GND density ρ_g^{th} for two $d_i = 1\mu m$ and $10\mu m$ as a function of different

crystal orientations θ, prior to the mechanical loading. Foremost, it can be validated that for a fixed θ the distribution of ρ_g^{th} is similar for different inclusion sizes; as expected, the magnitude is much larger for the finer inclusion (Dai et al., 2001b).

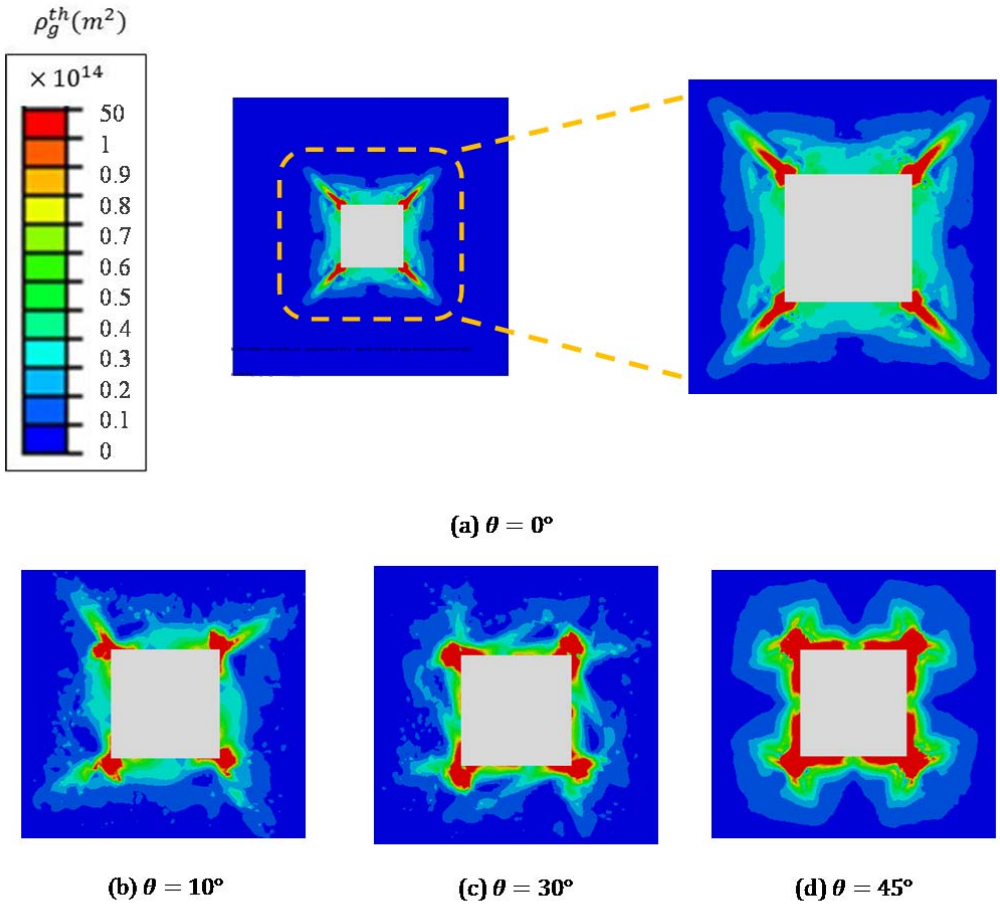

Figure 2.4. Crystal orientation and inclusion size dependent distribution of effective GND density ρ_g^{th} ($|\Delta T| = 500,\ d_i = 1\ \mu m$).

However, a key result is that the simulations quantify the heterogeneity in the distribution of ρ_g^{th}, which underscores the limitations that may arise from the assumption of uniform enhancement of matrix strength due to quenching (Dai et al., 2001b; Taya et al., 1991). Expectantly, the resulting matrix strengthening cannot be uniform and may be exacerbated by the heterogeneity of inclusion distribution.

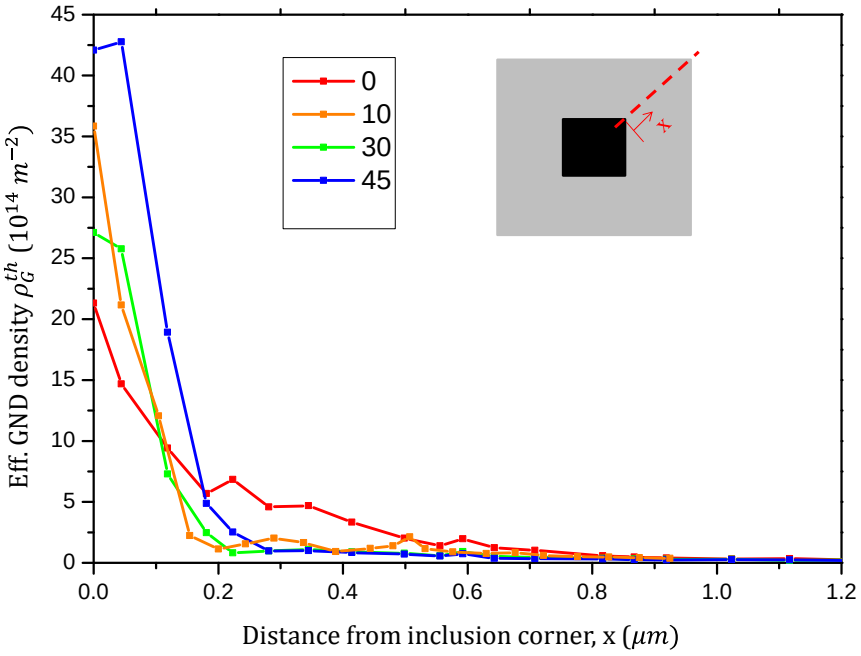

(a)

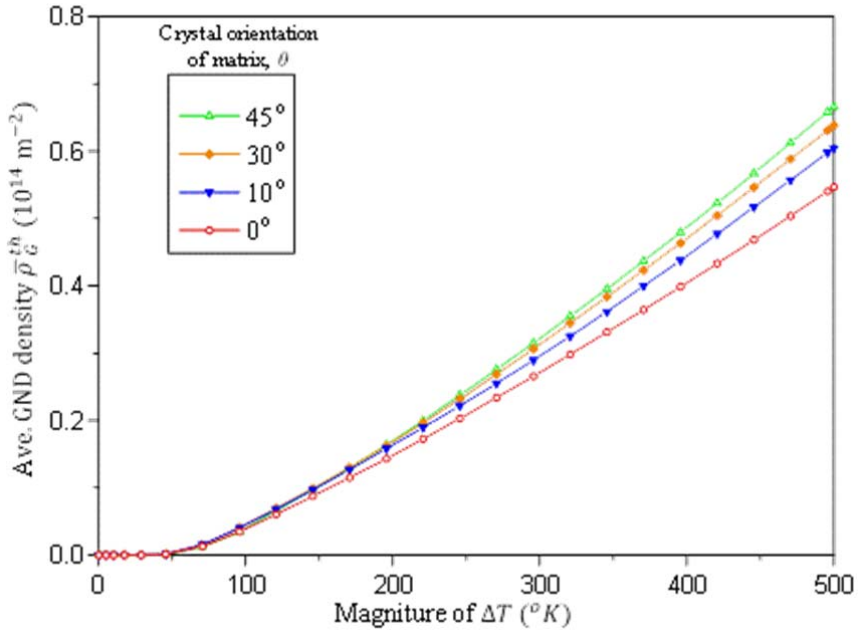

(b)

Figure 2.5. (a) Distribution of effective GND density ρ_g^{th} along the diagonal line as shown in embedded figure. ($|\Delta T| = 500$) (b) evolution of average GND density $\bar{\rho}_g^{th}$ during cooling process ($d_i = 1\ \mu m$).

This becomes especially critical when working with composites tend to host relatively dilute v.f.'s of micron or sub-micron sized reinforcements (Zhang and Wang, 2008) compared to conventional MMCs which usually host high v.f. of inclusions with sizes in the range of tens of microns. The GND density is mainly concentrated at the sharp inclusion corners to accommodate the strong lattice incompatibility that causes stress concentration. Table 2.2 shows the slip systems that contribute to the GND distribution for different crystal orientations. The distribution is determined by the number of active slip systems, which is function of θ. Figure 2.5a shows the magnitude of effective thermal GND density ρ_g^{th} along the line AB (see inset) with distance from the inclusion corner for different crystal orientation and $|\Delta T| = 500$, $d_i = 1\mu m$. It can be seen that the local GND density ρ_g^{th} near the matrix-inclusion interface is very high ($\sim 10^{15}\ m^{-2}$) while its magnitude rapidly decreases away from the interface. The local GND density magnitude at the interface is much higher for $\theta = 45$ where fewer slip systems actively participate (Table 2.2) and they are perpendicular to matrix/inclusion interface which cause the maximum thermo-elasto-plastic incompatibility at matrix/inclusion interface.

Table 2-2. Activated slip systems for two limiting crystal orientations

Slip Normal	Slip Direction	$\theta = 0^o$	$\theta = 45^o$
(1,1,1)	(0,-1,1)	-	X
(1,1,1)	(-1,0,1)	X	X
(1,1,1)	(-1,1,0)	X	-
(-1,1,1)	(0,-1,1)	-	-
(-1,1,1)	(1,0,1)	X	-
(-1,1,1)	(1,1,0)	X	-
(1,-1,1)	(0,1,1)	-	-
(1,-1,1)	(-1,0,1)	X	-
(1,-1,1)	(1,1,0)	X	-
(1,1,-1)	(0,1,1)	-	-
(1,1,-1)	(1,0,1)	X	X
(1,1,-1)	(-1,1,0)	X	X

Figure 2.5b shows the average thermal GND density $\overline{\rho}_g^{th} = \frac{1}{V_m}\int \rho_g^{th} dV_m$ in the matrix volume V_m for different $\theta's$ and fixed inclusion size ($d_i = 1\mu m$). Beyond the initial elastic deformation stage, $\overline{\rho}_g^{th}$ changes linearly with $|\Delta T|$, which is consistent with the analytical models (Arsenault and Taya, 1987; Dai et al., 1999; Dai and Bai, 2001). Notably, $\overline{\rho}_g^{th}$ is about : $10^{13}\ m^{-2}$ at $|\Delta T| = 500$, which is in the same range as evaluated in experiments (Barlow and Liu, 1998) and predicted from the dislocation punching model of (Arsenault and Shi, 1986). However, the additional information that we obtain from the figure is the effect of crystal orientation on $\overline{\rho}_g^{th}$. Even with isotropic elasticity as assumed here, higher lattice incompatibility produces higher GND density especially with increasing $|\Delta T|$.

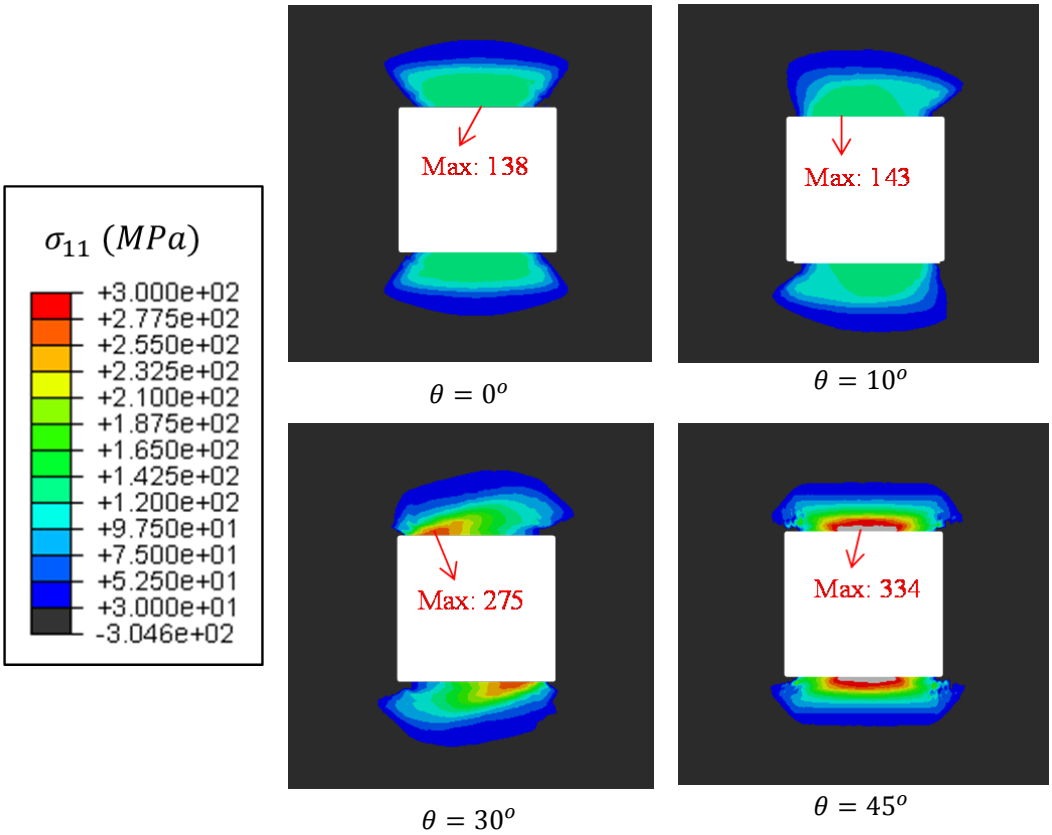

Figure 2.6. Distribution of normal stress σ_{11}^{th} under thermal loading for different crystal orientation of matrix ($d_i = 1\ \mu m$).

Figure 2.6 depicts the distribution of the normal residual stress σ_{11}^{th} around the inclusion for different θ. It is tensile in the vicinity of the top and bottom interfaces. Note that the maximum tensile stress is larger in the crystals with larger incompatibility and will be larger for smaller inclusions. A similar trend is also observed for σ_{22}^{th} (not shown), which is tensile along the vertical faces of the inclusion. Although not explored here, the likely implication on the matrix failure nucleation arising from the normal stresses due to thermal excursion is of interest. The results indicate that the with decreasing inclusion size and increasing incompatibility, the matrix may become susceptible to nucleating voids near the interface. Such a possibility may eventually lead to failure either through void growth in the matrix or one that culminates into interface failure.

Figure 2.7a presents thermal GND density distribution for different inclusion sizes for highest incompatible case ($\theta = 45$). It can be seen that for smaller inclusion size, the magnitude of thermal GND density and the area its distributed over are larger. Consistent with analytical models, figure 2.7b and 2.7c confirms the linear dependence of $\overline{\rho}_g^{th}$ on $|\Delta T|$ and its inverse dependence on the inclusion size for given $|\Delta T|$. While the trends broadly corroborate with analytical models, the simulations provide a deeper insight into the apportioning of $\overline{\rho}_g^{th}$ to the thermal mismatch and elasto-plastic mismatch, which is also influenced by crystal orientation.

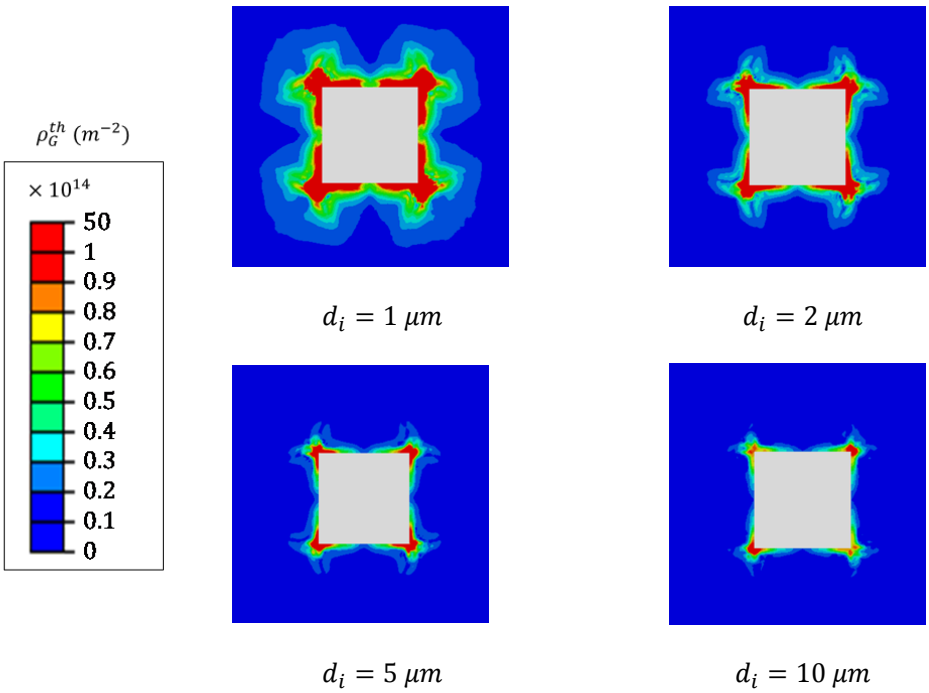
ρ_G^{th} (m^{-2})
$\times 10^{14}$
50
1
0.9
0.8
0.7
0.6
0.5
0.4
0.3
0.2
0.1
0
$d_i = 1\ \mu m$
$d_i = 2\ \mu m$
$d_i = 5\ \mu m$
$d_i = 10\ \mu m$

(a)

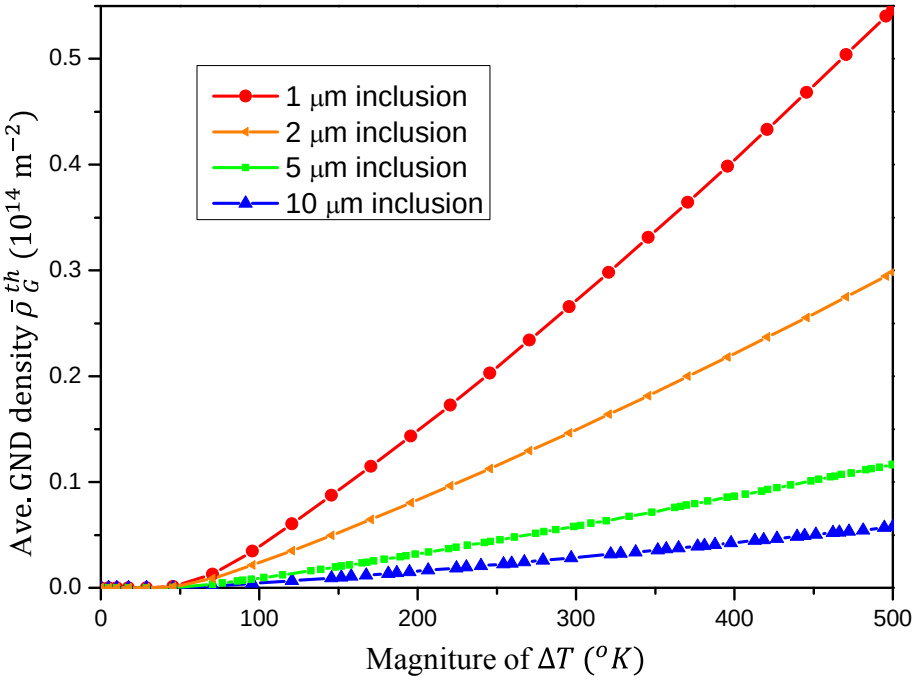
1 μm inclusion
2 μm inclusion
5 μm inclusion
10 μm inclusion
Ave. GND density $\bar{\rho}_G^{th}$ $(10^{14}\ m^{-2})$
Magniture of ΔT (^oK)
0.0
0.1
0.2
0.3
0.4
0.5
0
100
200
300
400
500

(b)

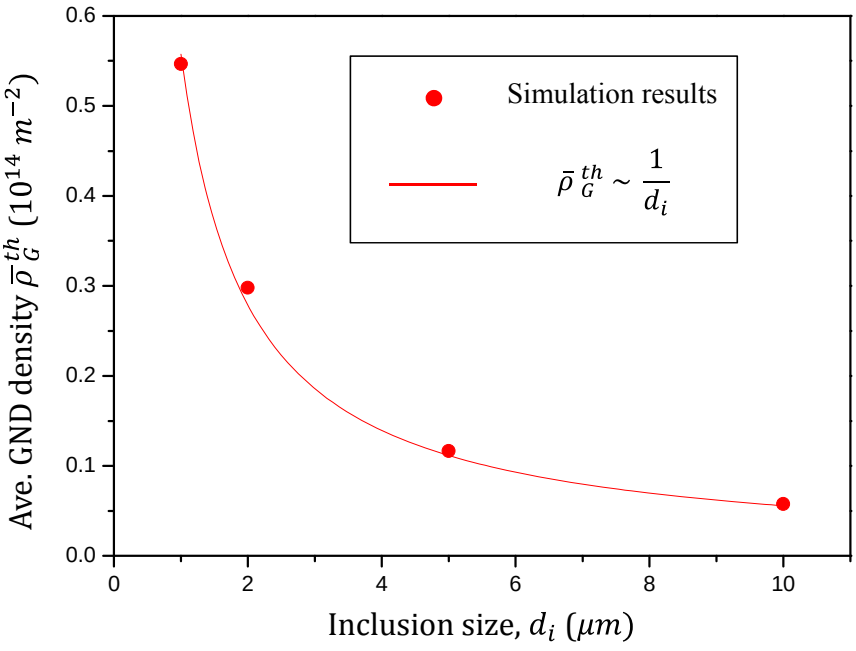

(c)

Figure 2.7. (a) Effective GND density ρ_g^{th} distribution for different inclusion sizes , (b) average thermal GND density $\bar{\rho}_g^{th}$ evolution during thermal cooling for different inclusion sizes, (c) Inverse relation of average thermal GND density $\bar{\rho}_g^{th}$ and inclusion size ($|\Delta T| = 500, \theta = 0^o$).

Note that in addition to the thermal mismatch that is commonly accounted for (e.g. (Arsenault and Shi, 1986; Dai et al., 1999; Dunand and Mortensen, 1990; Dai and Bai, 2001)), the elasto-plastic mismatch between the matrix and inclusion also contributes to the GND density under thermal loading. This latter contribution is not apparent in most of the analytical and numerical models. For example, Dai et al. (2001) provide an expression for the GND density that develops due to elastic mismatch under mechanically applied strain, but its application to the elastic mismatch strain developed during thermal loading is not accounted for. To isolate these individual contributions to thermal GND density, we performed additional simulations in that elasto-plastic mismatch is suppressed, but the thermal mismatch is retained. As can be seen in figure 2.8 for the particular case of $\theta = 0$ and $d_i = 1\mu m$, $\overline{\rho}_g^{th}$ is nearly 30% higher when the

elasto-plastic mismatch is accounted for. This difference is accentuated by increasing lattice incompatibility.

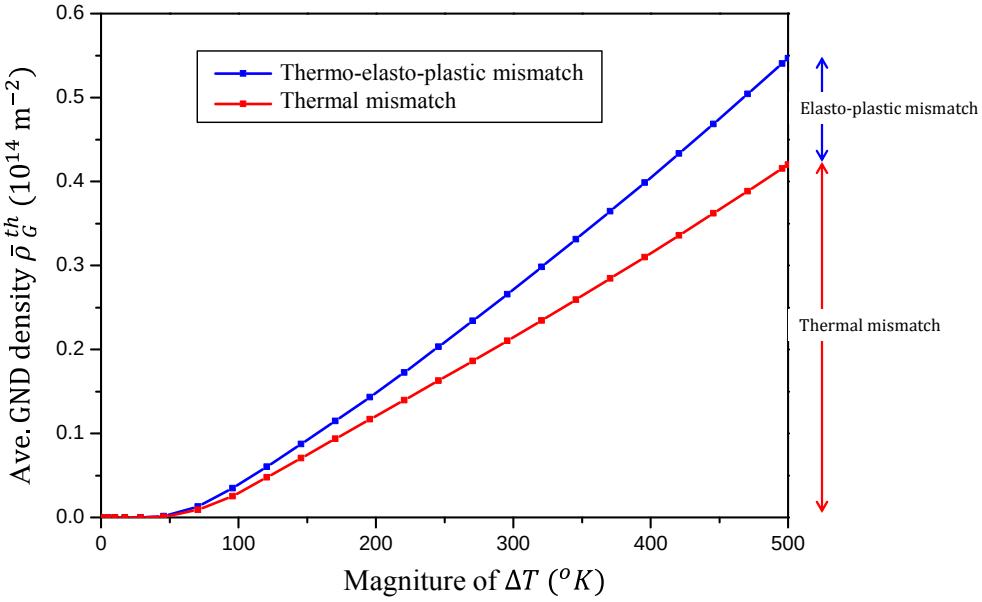

Figure 2.8. Contributions of individual mismatch components under thermal loading ($d_i = 1\ \mu m$).

Figures 2.5b and 2.7c together indicate an interesting interplay between the inclusion size and crystal orientation. We observe that an increase in the GND density due to a smaller inclusion could be compensated (at least partially) if the lattice is oriented in a manner that produces weak incompatibility. To first order, these effects due to thermal excursion may be accounted for in a manner similar to that derived analytically (Dunand and Mortensen, 1991; Dai et al., 2001)

$$\overline{\rho}_g^{th} = \frac{K\, f_i\, \Delta\alpha\, \Delta T}{b d_i} \tag{2.15}$$

where K is a pre-factor that embeds the information of the effects of crystallographically defined elastio-plastic properties of the matrix and the inclusion shape. For square inclusions, comparing Eq. 2.15 with the simulation results (Fig. 2.5b), $K \approx 30 - 40$, with

the lower bound delimited by the lowest lattice incompatibility (e.g. $\theta = 0^o$ in our simulations) and the upper bound by the highest lattice incompatibility (e.g. $\theta = 45^o$) with respect to the loading axis. Note that the pre-factor K is nearly thrice that of the analytically obtained coefficient (Dai et al., 2001).

2.3.3 Size-dependent stress-strain response with pre-existing thermal GND density

Following the thermal processing that produce residual stresses, the MMC behavior under compressive and tensile mechanical loads could differ significantly. For conventional coarse-grained MMCs with large inclusions, the thermal residual stresses provide a basis for the tension-compression asymmetry in the stress-strain response. This is also expected in MMCs with fine-scaled inclusions with an additional complexity arising from their size-dependency. As noted in the introductory part of this section, we subjected the same MMC unit cells to monotonic tension and compression (Fig. 2.9). The solid curves in figure 2.9 are the average true stress-true strain MMC responses in tension and compression in the presence of locked-in length-scale dependent thermal residual stresses ($d_i = 1\,\mu m,\ f_i = 0.05\,, \theta = 45°$). The classical crystal plasticity (CCP) results (i.e. ignoring the slip gradients) are shown by the dashed curves for the same f_i and θ. Note that the stress-strain curves are plotted up to 1 % strain only, in order to highlight the effect of prior thermal residual stresses on the initial strengthening and hardening. In both cases the thermal residual stresses lead to an asymmetry in the tensile and compressive responses, indicating their ubiquitous role irrespective of whether size-effects are accounted for or not. Specifically, the compressive response is stronger compared to the tensile response, because the

thermal residual stresses are tensile in nature (Arsenault and Taya , 1987; Dutta et al. ,1993).

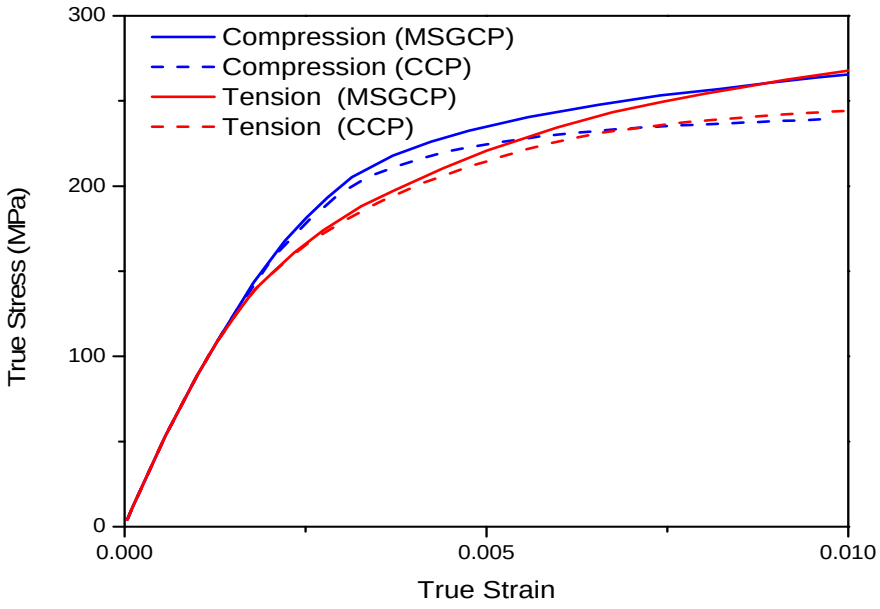

Figure 2.9. True stress-true strain response for MMC models under thermo mechanical loading. Bulk behavior is predicted by CCP while size dependent behavior is modeled using MSGCP for inclusion size $d_i = 1\ \mu m, \theta = 45°$.

Looking at different inclusion sizes and crystal orientation reveals that the thermal residual stress is tensile in the vicinity of the top and bottom interfaces and its magnitude is larger for smaller d_i for all θ. Likewise, for a fixed d_i the magnitude of the normal stress increases with increasing incompatibility, ($i.e.$ $\left(\sigma_{11}^{th}\right)_{\theta=45^o} > \left(\sigma_{11}^{th}\right)_{\theta=30^o} > \left(\sigma_{11}^{th}\right)_{\theta=10^o} > \left(\sigma_{11}^{th}\right)_{\theta=0^o}$). A comparison of the CCP and SGCP responses in Fig. 2.9 reveals that the thermal GND contribution in compression (difference between blue solid and dashed lines) is higher than in tension (difference between red solid and dashed lines). On the other words, under compressive loading, a higher overall load is required to overcome the initial tensile thermal residual stress and this causes higher overall stress compared to the tensile loading case where the initial tensile thermal residual stress augments the applied tension causing yielding at a smaller overall load.

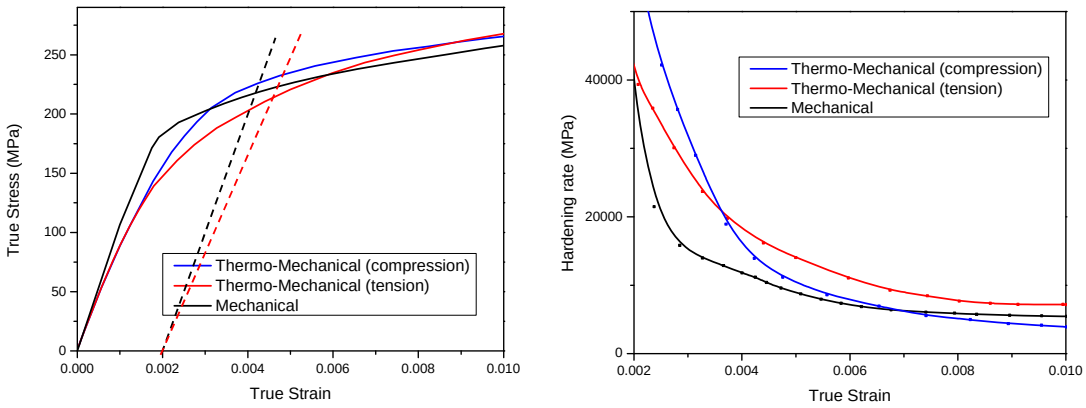

(a) (b)

Figure 2.10. Influence of the prior thermal loading on (a) true stress-true strain response and (b) hardening rate. ($d_i = 1\ \mu m, \theta = 45°$), obtained from MSGCP calculations.

Figure 2.10 indicates that the hardening rate in tension is higher than that in compression, at least in the initial stages of plasticity. To further study the evolution of hardening due to thermo-mechanically induced GND effects, we compare the hardening rates of the two-step thermo-mechanical loading for monotonic tension and compression with that of the mechanical-only loading case. Note that in the mechanical-only case the response is the same under tension and compression. Figure 2.10a shows influence of prior thermal loading on the subsequent stress-strain response under tensile and compressive mechanical loading when compared with the mechanical-only loading case and figure 2.10b shows the corresponding hardening rates $d\sigma/d\epsilon$. It can be seen that in the presence of initial thermal loading the subsequent tensile yield strength (measured at 0.2% strain) is lower, but the overall hardening rate is higher compared to the mechanical-only loading over the strain range considered. On the contrary, the compressive yield strength is higher and the hardening rate is also high in the incipient stage, but with increasing strain the latter quickly drops below the tensile response and asymptotes toward the hardening rate of the mechanical-only loading condition. These observations may be rationalized as follows: at the initial stages of

compressive loading, macroscopic compressive stresses at the inclusion-matrix interfaces are compensated by the initial tensile thermal residual stresses generated during the thermal loading at the interface (figure 2.11). Naturally, the net local stresses at the interface are lowered and therefore, the applied stress has to be increased for macroscopic yielding (Fig. 2.10a). Then, for the same strain the stress is higher in the thermal plus compressive loading case compared to the mechanical-only loading case and consequently, the initial hardening rate in the former is higher. The rapid drop in the compressive hardening rate indicates that the strengthening effect due to prior thermal residual stresses decreases with increasing strain. This may be construed as some of the initial thermal GND density being annihilated by the mechanical GND density accumulated during the subsequent mechanical loading.

Figure 2.11 shows the evolution of total (thermal+mechanical) GND density for the tensile and mechanical loading cases. In the initial stages the total GND density is nearly the same as that developed during prior thermal history. However, as deformation progresses we observe a drop in the GND density under compressive loading indicating partial annihilation of thermal GNDs; in comparison, under tensile loading the GND density increases much more rapidly. In other words, the lattice curvature generated at the inclusion-matrix interface due to thermal loading is compensated by that generated due to the mechanical loading. As the loading continues, the mechanically-induced lattice curvature (mechanical GND density) prevails over the initial thermal GND density and governs the macroscopic hardening. As mentioned in the preceding paragraph, in the case of tension, the external tensile stress arising from the mechanical loading adds to the initial tensile thermal residual stresses. This naturally causes the MMC to yield at a lower applied load, but as deformation progresses mechanical GND density adds to the initial thermal GND density producing an enhanced hardening rate.

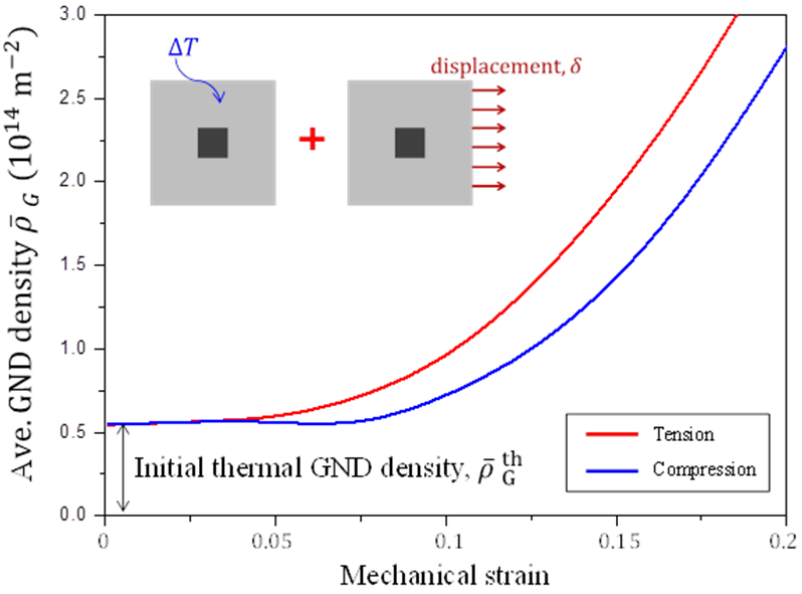

Figure 2.11. Average GND density evolution under consequent thermal-mechanical loading. ($d_i = 1\ \mu m$, $\theta = 45°$)

2.3.4 Inclusion shape effect on stress-strain responses in the presence of thermal GND density

Theoretical studies on MMC reveal that overall MMC response is strongly affected by inclusion shapes. (Meijer, 2000) used a cubic unit cell to investigate the residual thermal stress/strain in particulate reinforced metal matrix composites. They found that the sharp corners and edges of the cube shaped particles result in stress/strain localization and lead to a much larger initial hardening behavior than the spherical inclusions. (Chen et al., 1999) extensively studied effect of inclusion shape and its morphology on the MMC response. They showed that the plastic strain near the inclusion-matrix interface varies with inclusion shape. When the curvature at a corner increases the plastic strain gets more concentrated around it and has a significant effect on the thermal residual stress and strain distributions. (Xue et al., 2002) observed that there is a relatively weak interaction between inclusion size and shape for inclusion size larger than 7.5 μm when the thermal residual stresses are ignored. Here, we investigate

the coupling between the inclusion size and shape in the presence of initial thermal loading. To do so, we perform the two-step thermo-mechanical simulations for square and circular inclusions, with $f_i = 0.05$, which gives $d_i^{square} = 1\mu m$ and $d_i^{circular} = 1.13\mu m$.

Figure 2.12 shows the crystal orientation-dependent thermal GND distribution for the two inclusion shapes and corresponding active slip directions. For both the shapes, large incompatible deformations result in high GND density in the vicinity of i-m interface, which is distributed in the direction of slip systems. Quantitatively, the spatial extent of the GND affected zones are similar for both the inclusion shapes; however, the GND density is more concentrated near the sharp corners for the square inclusion.

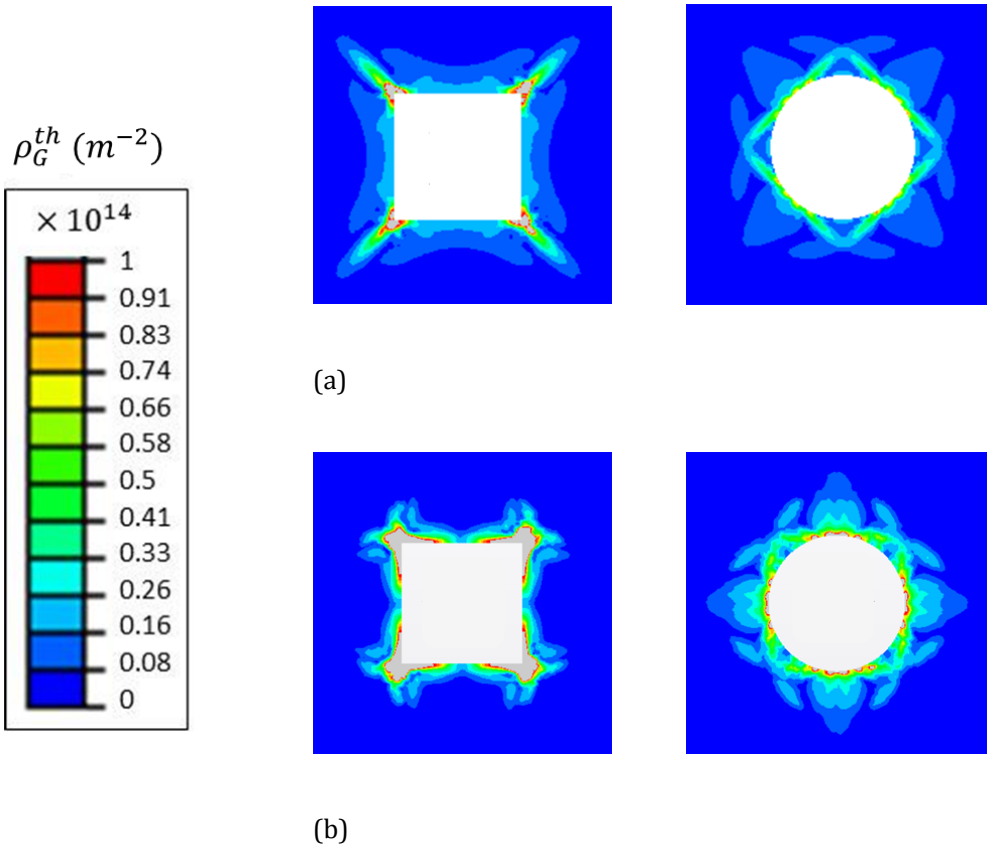

Figure 2.12. Distribution of thermal GND density around square and circular inclusions embedded in single crystal with (a) $\theta = 0°$ and (b) $\theta = 45°$.

Studies on the effect of inclusion shape using continuum plasticity have indicated that higher triaxiality of the stress-state exists at a sharp corner of a square inclusion compared to the stress state in the close proximity of a circular inclusion. This raises the overall stress-strain behavior of the MMCs with sharp-cornered inclusions compared to those with more rounded inclusions (Meijer, 2000). Interestingly, we find the situation to be somewhat different when the GND effects are included. Figure 2.13 shows the MSGCP true stress-true strain responses of MMC under thermo-mechanical loading for the square and circular inclusions embedded in single crystal with $f_i = 0.05$ and $\theta = 0°$). For comparison, the CCP results are also included in the same plot with same simulation parameters. The CCP results show that the shape of inclusion has an influence on the overall stress-strain behavior with the square inclusion providing a stronger response than its circular counterpart. This is qualitatively consistent with the trend indicated by (Meijer, 2000). However, the shape effect dramatically reduces in the presence of the thermal GND density.

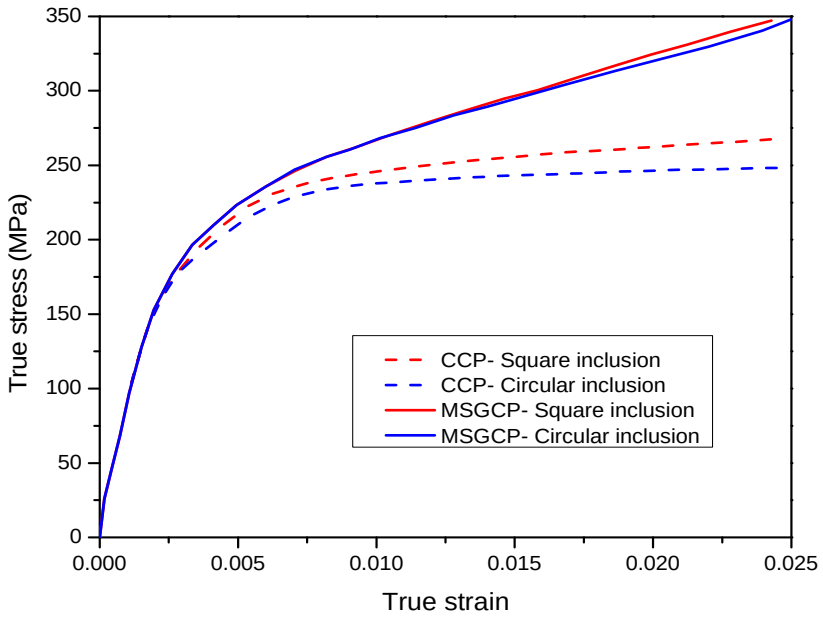

Figure 2.13. True stress-true strain response for MMC models comprising two different inclusion shapes ($\theta = 0°$).

The diminished shape effect in the presence of thermal GND density can be explained in terms of the interaction between the GND affected zone at i-m interface and the high triaxiality stress at a sharp corner. Figure 2.14 shows the von-Mises stress distributions around the square and circular inclusions as obtained from the CCP and MSGCP calculations. The CCP simulation, being length-scale independent, does not account for the thermal GND density and is akin to a large inclusion case where the GND effects are negligible. Note that the simulation results are for $\theta = 0°$, which possesses the lowest incompatibility amongst the cases evaluated here (see for example, Fig. 2.5a), which means that the thermal GND density would also be the lowest. Even in this case, as the inclusion size decreases the stress in the GND affected zone tends to overlay the regions of high triaxiality (sharp corners) so that the region around the square inclusion appears to have more distributed stress around it compared to the case where either the thermally induced GND density is not present or is negligible. Figure 2.15 further elaborates this idea schematically, indicating that the stress concentrations at the sharp corners tend to be engulfed by overall high stress around a square inclusion as the inclusion size decreases. This tempers the effect of inclusion shape on the macroscopic behavior, because the stress state around a sharp inclusion appears to be qualitatively closer to that of an inclusion with rounded corners, the limiting case being a circular inclusion. We note in passing that we observe qualitatively similar trends for the $\theta = 45°$ and are not repeated for brevity. In conclusion, the simulations reveal that in the presence of initial thermal GND density the inclusion shape effect on the overall MMC response diminishes at smaller inclusion sizes. In addition to this, although the stress around the inclusion is higher it is relatively more uniformly distributed compared to the case where the GND effect is absent and this is expected to shield such a material against fracture arising from locally high stresses.

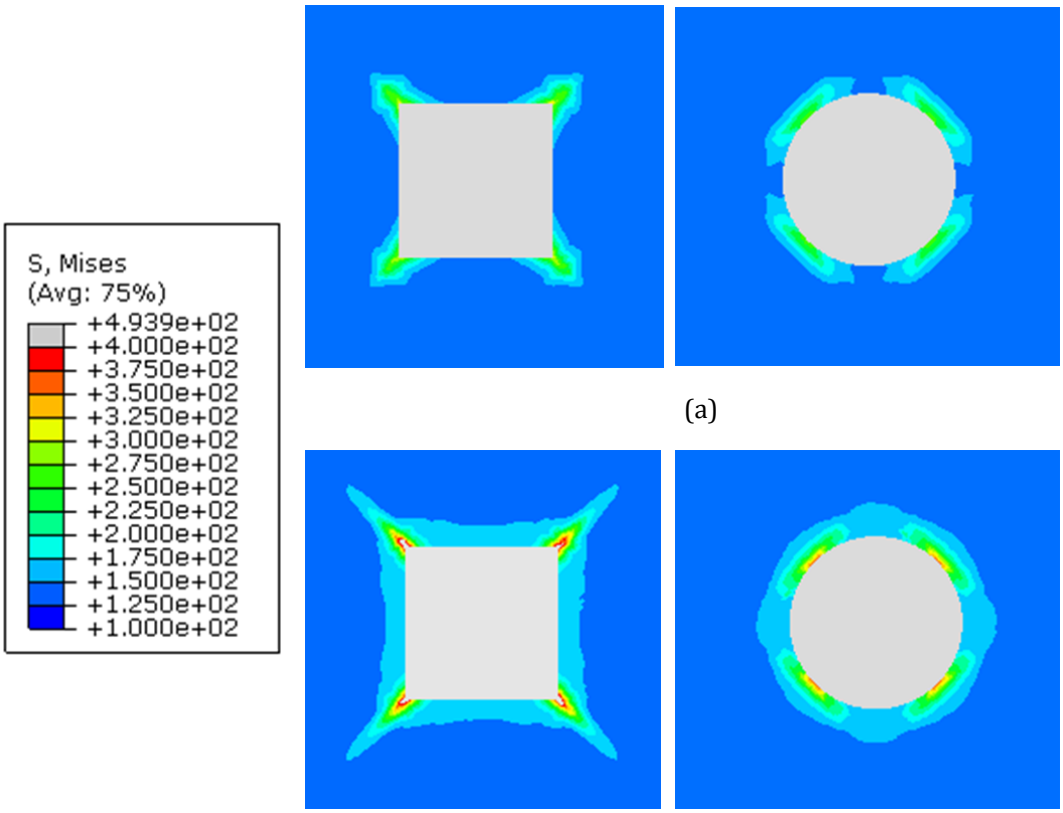

Figure 2.14. Influence of inclusion shape on thermal residual stresses in MMC based on (a) CCP and (b) MSGCP. ($\theta = 0°$)

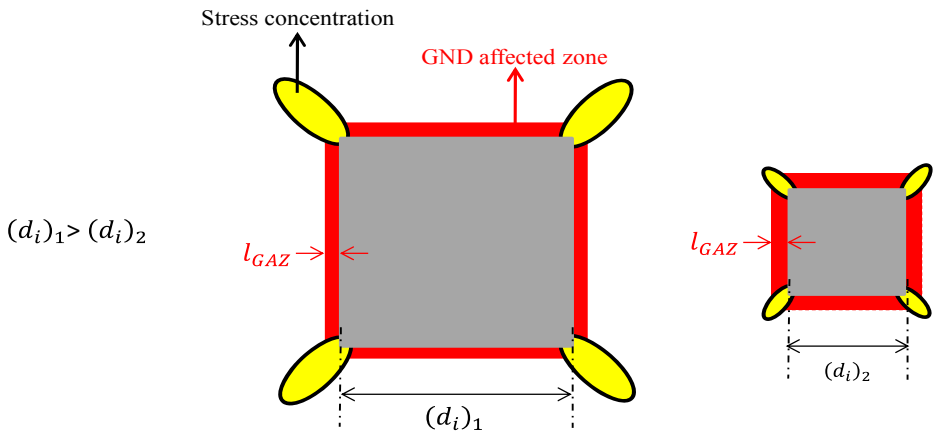

Figure 2.15. Schematic indicating an interaction between inclusion shape and size effects at the locations of stress concentrations.

2.3.5 Thermal GND density distribution in polycrystalline MMC under thermal loading

In the previous sections, the role of inclusion size and crystal orientation are investigated using unit cell model comprising a single inclusion embedded inside a single crystal matrix. In this section, we explore the applicability of the model on MMC with polycrystalline matrix where grain sizes are smaller than inclusion sizes. In the next section we will investigated the role of grain size, inclusion size and their interaction in MMC overall response under mechanical loading via mechanism based strain gradient theory. Here, we adopt unit cell approach including both the thermal and the elasto-plastic mismatches between the grains as well as the inclusion and the grains surrounding it (figure 2.16). The crystallographic elastic properties for the grains are $C_{11} = 168.4, C_{12} = 121.4$ and $C_{44} = 75.4\ GPa$ .The colors for individual grains represent their orientation as specified by the numerals within the grains surrounding the inclusion in Fig. 2.16. The contour plots in Figs. .....a and b respectively show the thermal GND density distribution grain sizes $d_g = 0.5\mu m$ and $0.25\mu m$. In both case, $f_i = 0.05$, and $d_i = 1\mu m$.

As a comparison, Fig. 2.17 shows the evolution of the average thermal GND densities in the polycrystalline MMC and its single crystal counterparts. First, it can be seen that the average GND density is higher in the case of polycrystalline MMCs as the grain boundaries act as additional sources of elasto-plastic incompatibility. Interestingly, this enhancement is only weakly dependent on the grain size. This indicates that the elastic anisotropy in polycrystalline matrices do not produce a significant coupling into the grain size-dependence of the thermal GND density. Second, we observe is that the finer grain size produces a more uniform distribution of the GND density, which is also important because it can help induce uniform strengthening around the inclusion. Finally, note that the single crystal cases give a lower GND density,

even that with the largest incompatibility ($\theta = 45^{o}$). From this, we may conjecture that for highly textured polycrystalline cases (a limiting case being a single crystal) the thermal GND density may be somewhat lower than a poylcrystal MMC with random texture. In other words, textured polycrystals may produce weaker initial strengthening due to thermal history compared to a randomly textured polycrystal MMC.

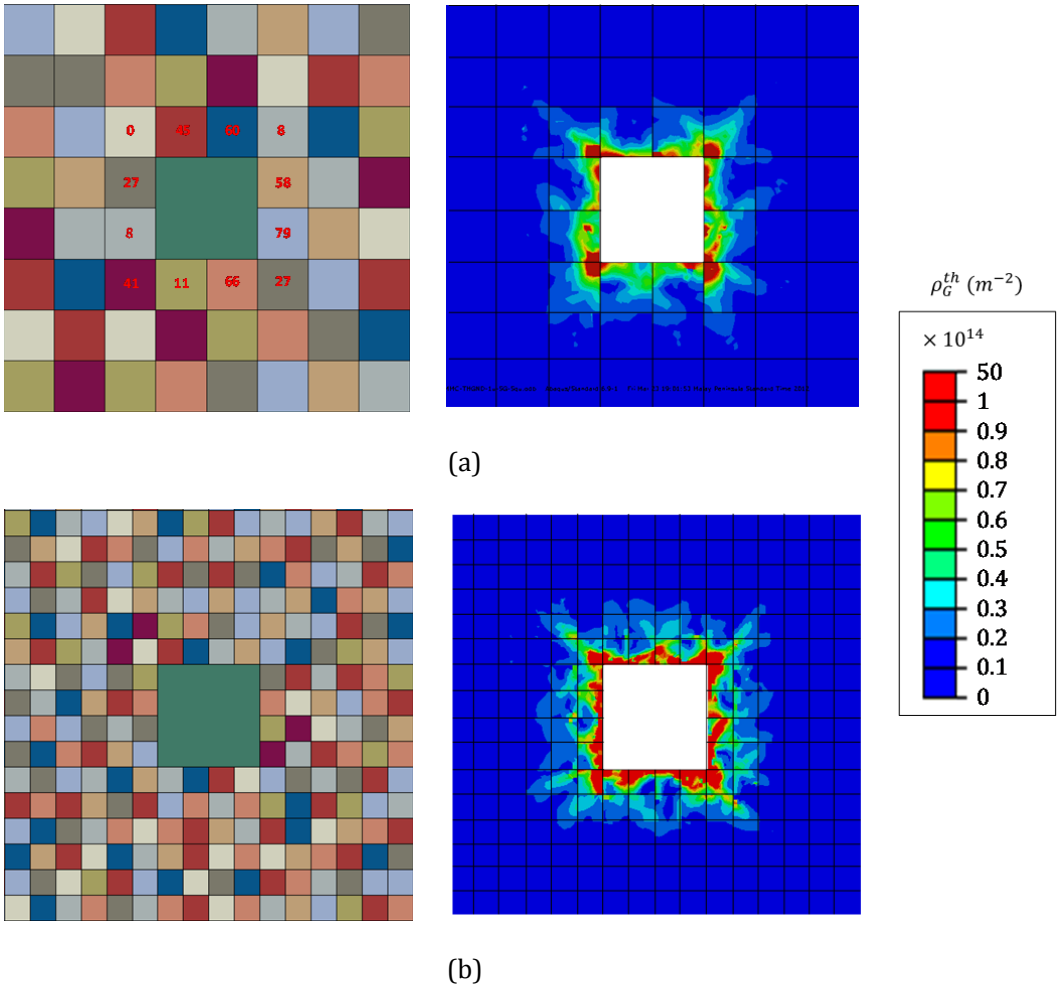

(a)

(b)

Figure 2.16. Effective GND density distribution in polycrystalline MMC with random grain orientation for different grain size (a) $d_g = 0.5$ μm and (b) $d_g = 0.25$ μm. ($d_i = 1\ \mu m$, $|\Delta T| = 500$)

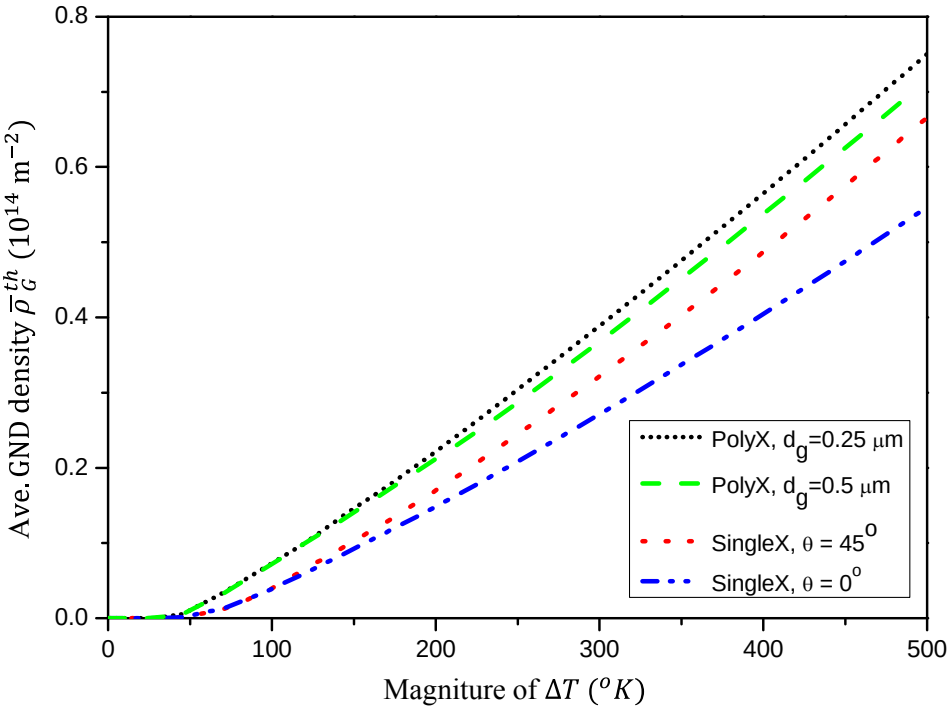

Figure 2.17. Average GND density distribution evolution in single crystalline and polycrystalline MMC

2.4 Grain size-inclusion sizes interaction in MMC at moderate strain using MSGCP

Most of the previous efforts on MMC behaviors and underlying mechanisms have been concentrated on the unit cell approaches where a single inclusion representing its v.f., is embedded in a single crystal or a homogenized matrix that is endowed with enriched plasticity descriptions. However, it is important to note the limitations of these models in terms of the microstructural characteristics: an inclusion embedded in a single crystal resembles a polycrystalline mass whose grains are much bigger than the particles (Cleveringa et al., 1997) so that the gb's do not interfere in the strengthening response (e.g. a sub-micron sized inclusion embedded within a large grain of a polycrystal). The other extreme is the assumption of a homogenized matrix with discrete inclusions (Nan and Clarke, 1996; Suh et al., 2009; Xue et al., 2002), which

resembles a polycrystalline mass with grains that are much finer (allowing homogenization of the matrix) than the inclusions. In practice, one may encounter important intermediate cases in addition to these two extremes, especially for nanostructured composites. For example, the *trimodal* Al-alloy composites (Joshi and Ramesh, 2007; Zhang et al., 2008) possess grain sizes that are in the same range as those of the reinforcing particles (Figure 2.18). In such situations it may not be appropriate to assume either a homogenized matrix model or a single crystal approximation. Rather one has to explicitly resolve both inclusion and its surrounding grains within the microstructure to capture the length-scale dependencies on the overall response.

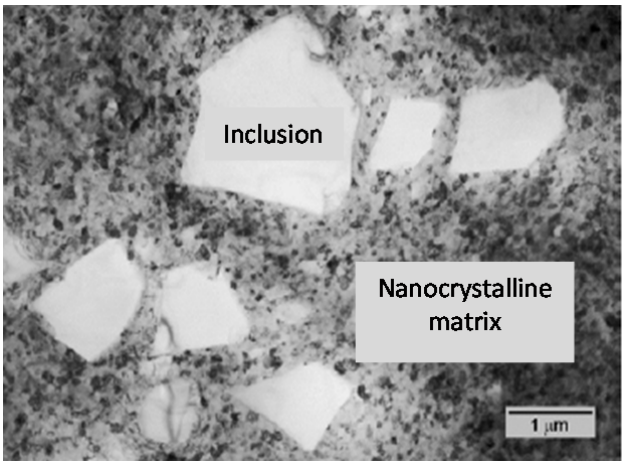

Figure 2.18. MMC with micron-sized inclusions embedded in a nanocrystalline matrix (Joshi and Ramesh, 2007)

This observation poses interesting questions – what roles do the grain size and the inclusion size play in the overall length-scale dependent response of an MMC? How does one account for or model the interaction between these microstructural features? Is there a range of grain size-inclusion size combinations that produces significant synergistic contributions? Is it possible to quantify this interaction, for example, as an additional hardening contribution? To our knowledge, these questions have not been addressed via either analytical or computational modeling at any length-scale.

From a mechanistic viewpoint this is a challenging problem as there are several aspects that one has to understand, for example, the physics of the plastic events at the inclusion-matrix (i-m) interfaces and at gb's (and triple junctions), *communication* between the i-m interfaces and gb's, grain orientation effects, inclusion and grain size distributions, and several more. While it may be important to incorporate these mechanisms, a single mechanistic framework that is capable of resolving the microstructural details and concurrently also embeds appropriate physics for all the interfacial mechanisms is difficult to conceive at the moment. A comparatively tractable setting is possible if one chooses to simplify and/ or ignore some of the aspects. Crystal plasticity enriched with length-scale features can effectively handle the kind of resolution necessary for the problem. In its simplest version, it is possible to model MMC microstructures using CP by explicitly resolving the grains and inclusions and accounting for some of the size-dependent mechanisms, but ignoring some of the intricate details such as size and spatial distributions of grains and inclusions, gb deformation processes and failure[3].

With this notion, we demonstrate a computational approach based on length-scale dependent crystal plasticity (CP) to answer the questions posed in the preceding paragraph. Specifically, this work resorts to the mechanism-based slip gradient crystal plasticity (MSGCP) (Han et al., 2005a) theory. MSGCP accounts for size-effects by incorporating slip gradients that are related to the GND densities within the constitutive description of individual slip systems. Given that both grains and inclusions are explicitly resolved in this approach, slip gradients naturally arise at gb's and i-m

[3] These details can be included within CP, but they complicate the problem by introducing several additional variables and understanding their effects on the overall behavior would require significant computational effort.

interfaces due their elasto-plastic mismatch and are accounted for in the MSGCP theory. However, this approach is essentially a lower-order theory compared to a higher-order framework, because it does not invoke additional boundary conditions (b.c.'s) at interfaces. Consequently, the lower-order CP approaches cannot model some of the enhanced interactions between interfaces and dislocations that the higher-order CP approaches are capable of handling. Although a higher-order theory would be suited for the present problem (Fredriksson et al., 2009), (Bardella and Giacomini, 2008), the difficulty with higher-order b.c.'s is that it may not be always easy to identify appropriate descriptions for general interfaces (Voyiadjis and Deliktas, 2009). Moreover, the computational effort for higher-order CP is significantly larger than their lower-order counterparts. On the other hand, due to the inherent inability of the MSGCP in handling enhanced interactions between interfaces and dislocations the length-scale effect appears only in the flow behavior rather than at yield (Evans and Hutchinson, 2009). However, despite some of its limitations, we choose the MSGCP theory keeping in view its simplicity in the numerical implementation within existing CP framework, computational expense for the present work and a relatively established physical understanding of the length–scale parameters. In this regard, the results presented here on the grain size-inclusion size interaction are applicable in the flow regime, i.e at moderate strains, rather than at yield (Acharya and Beaudoin, 2000). However, we also note the experimental observation of (Kouzeli and Mortensen, 2002) that the size effect in the flow regime of MMCs follows similar trends as at yield and return to this aspect in the closing section of this chapter.

In the next section, we describe the model microstructures adopted in the present work and the procedure to isolate the individual length-scale effects arising from the grain size, inclusion size effects and the grain size-inclusion size interactions.

2.4.1 Model Microstructures

To enable consistent comparison across different parametric models, we consider highly idealized MMC microstructures comprising square grains and inclusions. We also assume that the inclusions are regularly arranged, and the gb's and interfaces remain intact throughout the deformation. Figure 2.19 shows canonical polycrystal (Figure 2.19 a, c) and MMC (Figure 2.19 b, d) microstructures amongst several considered in the present work. One extreme case is where the inclusion is much smaller than the grain so that it effectively resides within the grain (Figure 2.19 b), and the other case is where the inclusion is much bigger than the grains (Figure 2.19 d) so that multiple grains share an inclusion interface. A grain orientation (Figure 2.19 a) for this FCC crystal structure is defined here as the angle made by the [100] crystal direction with the global loading direction (x_1) and [001] crystal direction is considered to coincide with the global x_3 direction. The associated color for each grain acts as a reference for the other microstructures[4]. Within each MMC configuration the grain size d_g and inclusion size d_i are constant. This enables organizing the microstructural arrangements into two broad categories: (a) $d_g > d_i$ (Figure 2.19 c), and (b) $d_g \leq d_i$ (Figure 2.19d).

[4] In section 2.4.6 we briefly discuss the statistical effect of the number of grains with random grain orientations on the stress-strain responses.

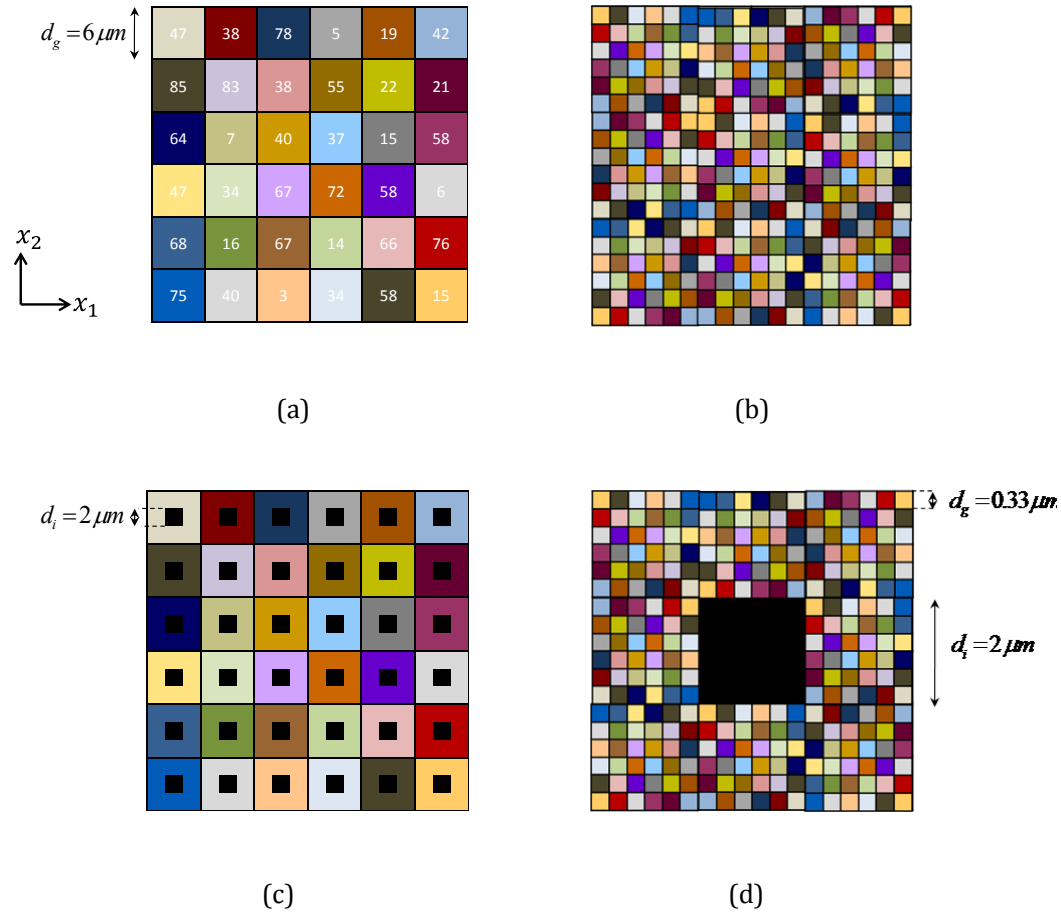

Figure 2.19. Representative models for (a, c) polyX and (b, d) MMC architectures.

For case (a) we construct a 36 grain polycrystal with random crystal orientations with each grain embedding one inclusion. For case (b) a single particle is surrounded by randomly oriented grains. Note that only when $d_g \gg d_i$ would a computational cell asymptote to a unit cell approximation that is commonly adopted (Dai et al., 2001a; Kouzeli and Mortensen, 2002; Nan and Clarke, 1996; Zhang et al., 2007) however, most works do not state the assumptions on the matrix microstructural details explicitly. In such cases, it is not obvious how the matrix strengthening due to grain size would couple with the contribution from inclusion size. To quantify the grain size and particle size effects:

(i) First, we model polycrystalline masses comprising a fixed number of grains of size d_g, without inclusions (c.f. Figure 2.19 a, c). These simulations are performed for microstructures with different grain sizes, but keeping the initial orientations between the different microstructures unchanged.

(ii) The same microstructures in (i) are again simulated with inclusions of fixed size d_i and volume fraction f (e.g. Figure 2.19 b and d).

Steps (i) and (ii) are applied to different inclusion sizes with fixed f, Based on (i), the flow stress σ_{polyX} of a bare polycrystalline mass at a fixed strain is

$$\sigma_{PolyX} = \sigma_0 + \Delta\sigma_g \tag{2.16}$$

where σ_0 is the size-independent flow stress of the polycrystalline mass with large grain sizes for a given set of crystallographic orientation, and $\Delta\sigma_g$ is the additional grain size-dependent flow stress derived from the slip gradients at gb's. Likewise, from step (ii) the flow stress for an MMC (σ_{MMC}) may be written as

$$\begin{aligned}\sigma_{MMC} &= \underbrace{\sigma_0 + \Delta\sigma_g}_{polyX} + \underbrace{\Delta\sigma_f + \Delta\sigma_i}_{inclusion} + \underbrace{\Delta\sigma_{int}}_{interaction} \\ &= \sigma_{polyX} + \Delta\sigma_f + \Delta\sigma_i + \Delta\sigma_{int}\end{aligned} \tag{2.17}$$

where $\Delta\sigma_f$ is the size-independent flow stress purely due to the inclusion v.f., $\Delta\sigma_i$ is the contribution due to inclusion size effect arising from the slip gradients (GNDs) at the i-m interface and $\Delta\sigma_{int}$ is an additional contribution that may exist due to the synergistic effects between d_g and d_i. Note that the grain size contribution is common to Eqs. (2.16) and (2.17).

For all the cases, the left and bottom edges are respectively constrained along x_1 and x_2 directions, the top edge is allowed to move vertically, but remain straight. A uniform velocity b.c. is applied to the right edge producing a nominal strain

rate $\dot{\bar{\varepsilon}} = 1 \times 10^{-2}\ s^{-1}$. In what follows, we refer to the polycrystalline microstructures sans inclusions as *PolyX* and those with inclusions as *MMC*. Table 1 gives the material properties used in the simulations. These properties are representative of pure Al as the matrix and SiC as the inclusions. For simplicity, we assume isotropic elastic properties for the Al, but anisotropic elasticity can be easily implemented.

2.4.2 Length-scale dependent polycrystalline response

Figure 2.20 shows the size-dependent polyX true stress-true strain responses with different grain sizes. The red dashed curve is the baseline calculation without gradient effects that represents a polyX with large grains. As noted earlier, the nature of the slip gradient model implemented here is such that the length-scale effect manifests itself in the hardening response rather than at yield (Evans and Hutchinson, 2009; Han et al., 2005a). Therefore, we measure the average flow stress at 2% nominal strain to demonstrate the size effects. Figure 2.21 shows the strong dependence of the flow stress on d_g. The plot also includes the popular Hall-Petch type empirical fit $\left(\sim d_g^{-0.5}\right)$ to the simulation results alongside the inverse grain size correlation (d_g^{-1}). (Acharya and Beaudoin, 2000) applied their version of the length-scale dependent CP theory to investigate grain size effects in polycrystals and obtained corroborations with experiments at moderate strains. Experimental evidences (Hommel and Kraft, 2001; Nix, 1989; Venkatraman and Bravman, 1992) and theoretical models (Ohno and Okumura, 2007; Sinclair et al., 2006; Zhang et al., 2007; Zhou et al., 2011) make cases for both the types of dependencies, but for consistent comparison here we adopt the Hall-Petch relation for subsequent discussions.

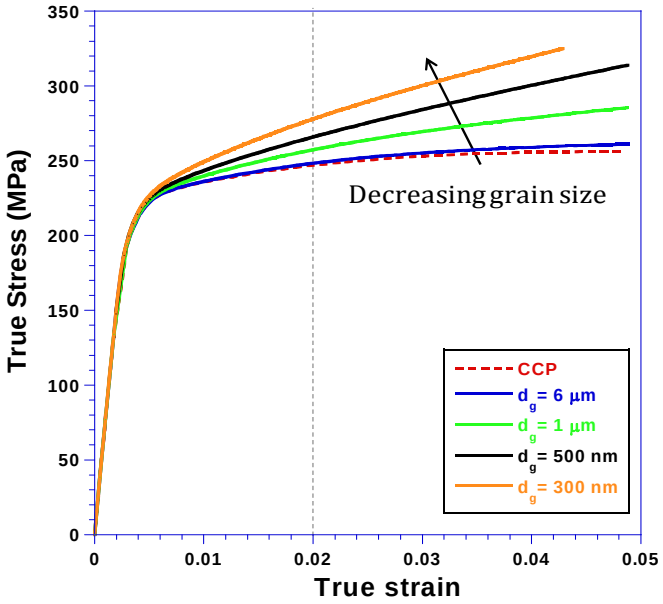

Figure 2.20. True stress-true strain responses for polyX models with different grain sizes.

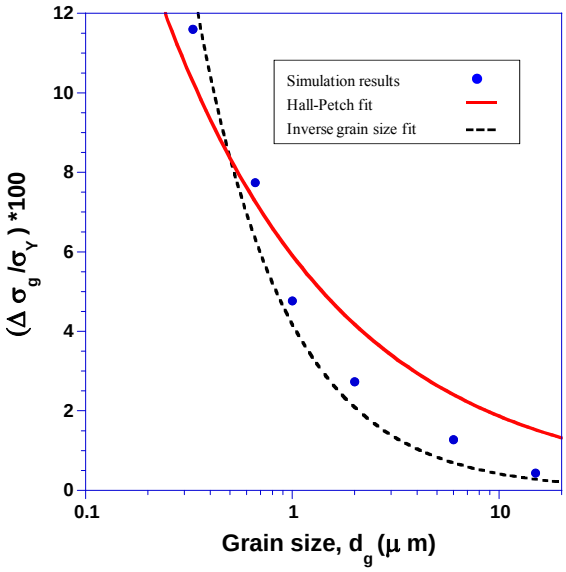

Figure 2.21. Normalized grain size dependent flow stress at $\bar{\varepsilon} = 2\%$ for polyX with identical grain orientations. The plot also includes the empirical Hall-Petch $(d_g^{-0.5})$ and inverse grain size (d_g^{-1}) fits.

2.4.3 Length-scale Dependent MMC Response

We now discuss the results obtained from the MMC simulations. For clarity, we focus initially on the case with fixed $d_i = 2\ \mu m$ and different $d_g's$ ($= 6\ \mu m$ and $1\mu m$), but subsequently also discuss the effect of inclusion size. Figure 2.22 shows the response of MMCs (solid curves) for different grain sizes. For comparison, the polyX results for the same grain sizes and orientations are also included in the figure (dashed curves). The red dashed and solid curves respectively denote the response of the polyX and MMC without the gradient effects (i.e. conventional crystal plasticity). As expected, irrespective of whether gradients are included or not the MMC flow stress is higher than its polyX counterpart due to the presence of inclusions in the former ($\Delta\sigma_f$). The blue solid curve is the response of an MMC with inclusions that are much smaller than the grains (e.g. Figure 2.19 b), whereas the green solid curve is for the case where the grains are smaller than the inclusions (e.g. Figure 2.19 d). Interestingly, in the presence of gradients, the latter exhibits a higher hardening rate over its polyX (dashed green curve) counterpart compared to the former (solid and dashed blue curves). This suggests that there exists an interaction between the gb's and the i-m interfaces when the grain sizes are comparable to or smaller than the inclusion sizes. In the following section, we quantify this interaction through systematic simulations with different grain and inclusion sizes. In the next section, we briefly discuss the mesh convergence studies performed on one $d_g - d_i$ combination.

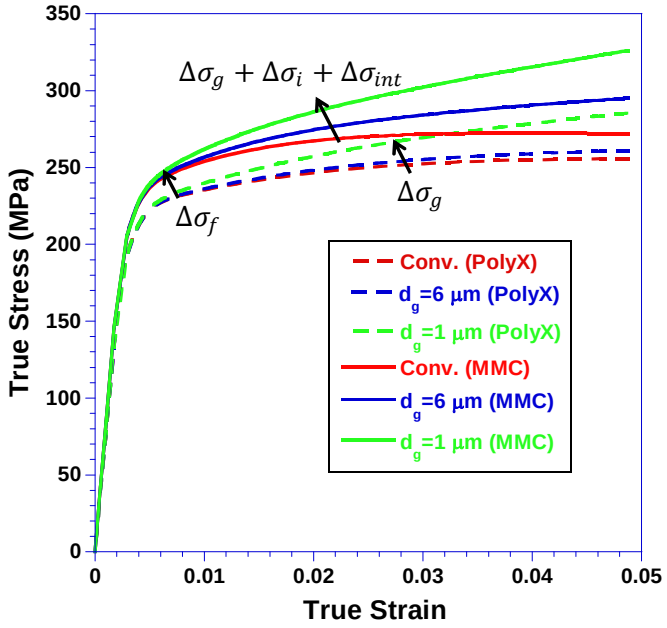

Figure 2.22. Grain-size dependent true stress-true strain curves for MMC (solid lines) with $d_i = 2\ \mu m$. The corresponding polyX responses (Figure 2.20) are also included for comparison.

2.4.4 Grain orientation and mesh size effects

Since the focus of this work is to capture the interaction effects, we investigate the influence of random grain orientations on $\Delta\sigma_{int}$ in $d_g < d_i$ regime for different d_g for fixed $f = 0.12$ and $d_i = 2\ \mu m$. Note that in the present 2D investigation the number of grains N_g in an RVE is then equal to $\frac{1}{f}\left(d_i/d_g\right)^2$. This indicates that by reducing the grain size, more grains with random orientations are modeled in the RVE and this should help reduce the statistical variation due to grain orientation. Figure 2.23 shows the variation in $\Delta\sigma_{int}$, shown by the error bars, for five different realizations per grain size. Indeed, the standard deviation in $\Delta\sigma_{int}$ arising from random choice of grain orientations reduces with decreasing grain size. We also investigated mesh dependency and convergence for a limited number of MMC simulations and present one such result for the case with $d_i = 2\mu m$ and $d_g = 1\mu m$.

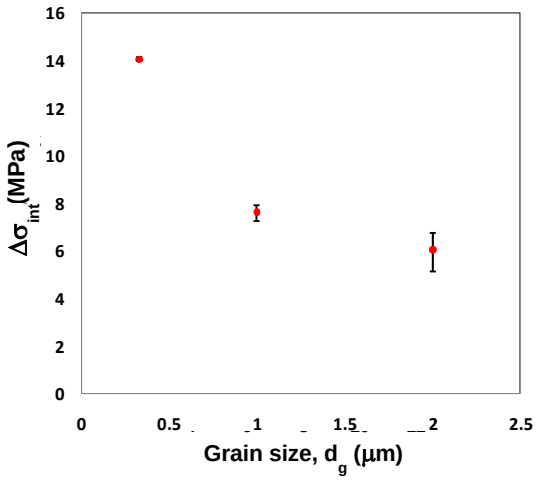

Figure 2.23. Standard deviation in $\Delta\sigma_{int}$ arising for a given computational model with fixed d_g but different realizations of grain orientations. As expected, the variation is smaller for finer d_g.

Figure 2.24a shows that the stress-strain curves converge with finer mesh size. In addition, the flow stress at a true strain of 0.04 is depicted versus total number of elements used in the model in Figure 2.24b.

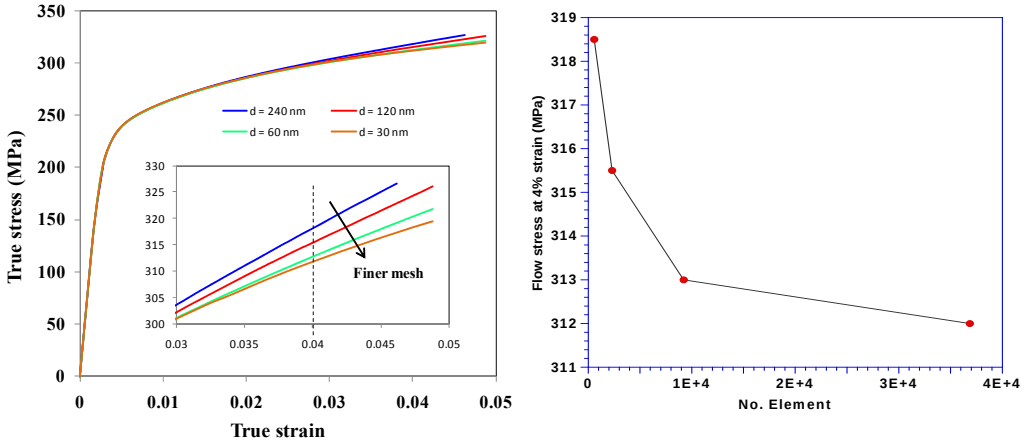

(a) (b)

Figure 2.24. Mesh convergence for the stress-strain curves of MMC $\left(d_i = 2\mu m, d_g = 1\mu m\right)$ with different mesh sizes d.

2.4.5 Grain size-inclusion Size Interaction strengthening

To systematically discern the interaction effect that exists when the inclusion size is in the same range or smaller than the grain size, we performed FE simulations of MMCs with various grain size-inclusion size combinations (see Table 2-3). The procedure adopted is discussed here briefly within the context of a fixed d_g, d_i and f. First, two simulations are performed for the MMC with both SGCP and conventional crystal plasticity (CCP). The algebraic difference between the overall stress-strain behaviors of these two gives the total MMC strengthening $\left(\Delta\sigma_{MMC} = \Delta\sigma_g + \Delta\sigma_i + \Delta\sigma_{int}\right)$ due to the grain size, inclusion size and interaction terms (Eq. (2.17). The grain size effect $\Delta\sigma_g$ is obtained as the difference between the polyX-SGCP and polyX-CCP response that possess the same grain sizes and orientations as the MMC. Subtracting the $(1-f)$ portion of the grain size effect $\Delta\sigma_g$ from the total MMC strengthening $\Delta\sigma_{MMC}$, the combined inclusion size and interaction effects are isolated, i.e. $\Delta\sigma_{it} = \Delta\sigma_i + \Delta\sigma_{int}$. This procedure is performed for different grain sizes and inclusion sizes with fixed f.

Table 2-3. Microstructural size combinations for MMC simulations

Inclusion Size (μm)	5	2	1
Grain Size (μm)	0.83, 1.6, 5, 15	0.33,0.66,1,2,6,15	0.33,0.5,1,3,15

Figure 2.25 shows the normalized $\Delta\sigma_{it}$ as a function of d_g at 2% nominal strain for $d_i = 1\ \mu m, 2\ \mu m$ and $5\ \mu m$. Note that strengthening behavior can be split up into two distinct regions. The first region is $d_g > d_i$, characterized by $\Delta\sigma_{it}$ that is larger for smaller inclusion sizes. In this regime, the curves remain horizontal and parallel to each other over the d_g range, meaning that the grain size does not play any major role in contributing to the overall MMC strengthening. In other words, for $d_g > d_i$ the inclusion

strengthening is grain-size independent and only inclusion size-effect prevails. To extract the inclusion size effect, we consider cases with $d_g = 3d_i$ where the interaction effect is negligible.

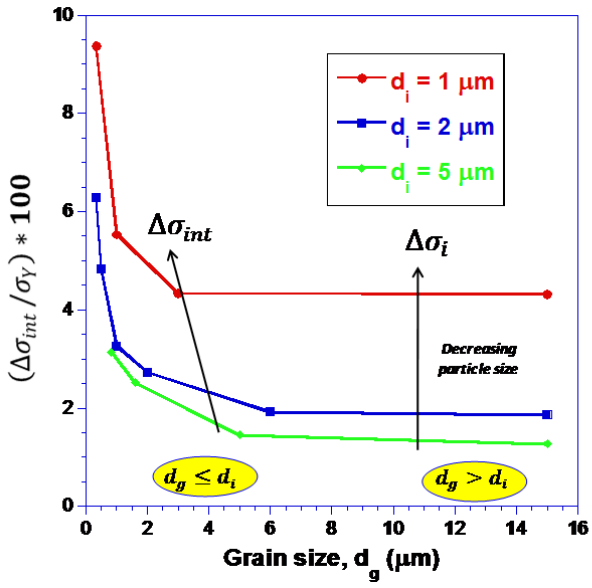

Figure 2.25. Flow stress ($at\ \bar{\varepsilon} = 2\%$) normalized by bulk polyX yield stress variation of MMCs as a function of grain size.

It can be seen that in Figure 2.26 that the flow stress varies as $d_i^{-0.5}$, which can be explained by Taylor hardening description that is embedded in the MSGCP (Dai et al., 2001a)

$$\Delta\,\sigma_i = \sqrt{3}\alpha_T\mu_m b\sqrt{\rho_{GND}^i} = \sqrt{3}\alpha_T\mu_m b\sqrt{\left(\frac{6f\varepsilon}{bd_i}\right)} \tag{2.18}$$

where α_T is the Taylor factor and μ_m is the matrix shear modulus and ε is the applied strain.

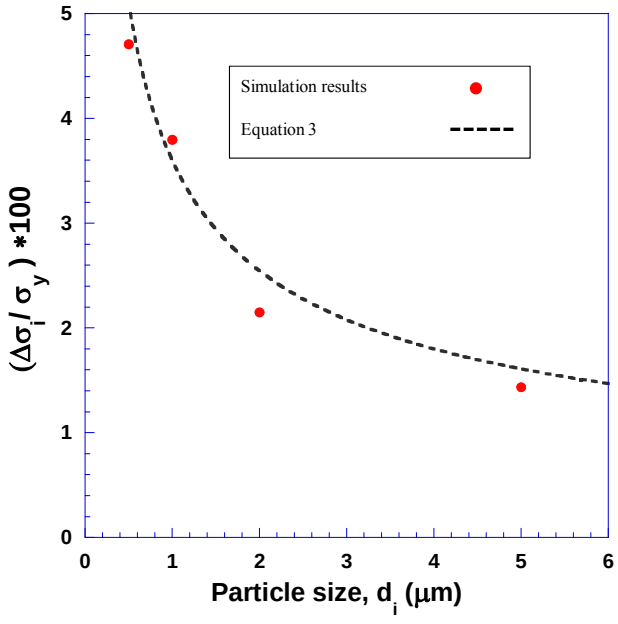

Figure 2.26. Inclusion size effect on the normalized flow stress (normalized by bulk polyX yield stress) for large grain sizes, $d_g = 3d_i$ (negligible grain size effect).

The second regime in Figure 2.25 corresponds to $d_g \leq d_i$ where a dramatic increase in strengthening is observed, which must be due to the interaction between the i-m interfaces and gb's. In this regime, the interaction effect for a given d_i is simply the deviation of the curve from its baseline inclusion strengthening at large grain sizes, i.e. $\Delta\sigma_{int} = \Delta\sigma_{it} - \Delta\sigma_i$. Note that for a fixed d_g the interaction effect is larger for smaller d_i. Further, for smaller inclusions the interaction effect kicks in at correspondingly smaller grain sizes. In other words, the inclusions do not *feel* their neighboring grains unless the characteristic microstructural wavelengths of the latter are comparable or smaller than the former.

The manner in which the GND density component of the total dislocation density is distributed depends strongly on the grain size and the inclusion size. As an example, Figure 2.27 shows the GND density distributions along a nodal segment staring from an i-m interface traversing through the matrix for three cases with different $d_g's$ and fixed d_i. Clearly, the presence of multiple gb's (smaller grains) around an inclusion leads

to a higher GND density at the i-m interface as well as GND accumulation at the gb's. This effect is further enhanced for smaller inclusion sizes (not shown here).

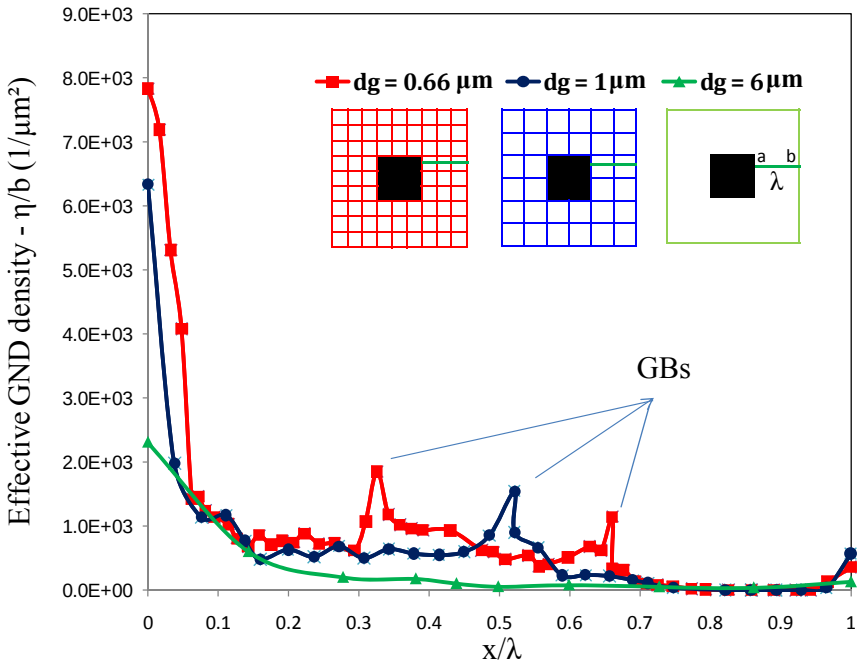

Figure 2.27. Distribution of the effective GND density (η/b) along path a-b $(d_i = 2\ \mu m)$ for different grain sizes.

We posit that the intersection of a gb and an inclusion interface can be considered as an additional source of dislocation activity that leads increasing dislocation density in its vicinity and contributes to the overall hardening as an interaction effect, $\Delta\sigma_{int}$. In the next section, we propose an analytical model based on this hypothesis to account for the dependence of $\Delta\sigma_{int}$ on both the grain size and the inclusion size.

Interaction effects discussed in the context of MMCs have also been observed in polycrystalline thin films on substrates. There, strong interactions exist between the gb's and the relatively rigid substrates. Although these effects have been addressed based on the grain sizes and film thickness, they have mostly been accounted for separately rather than as an interactive effect (Hommel and Kraft, 2001; Nix, 1989; Venkatraman and Bravman, 1992). Interestingly, (Hommel and Kraft, 2001) indicated

that the dislocation density measured in their film-substrate experiments was larger than the computed total dislocation density, which is summation of the SSD and GND densities. Furthermore, (Choi and Suresh, 2002; Nicola et al., 2005) pointed out that grain size and film thickness are coupled and not independent. Hence, a linear combination of grain size and film thickness may not adequately capture the overall size-dependent behavior of thin film structures, similar to the present scenario. The MMC architectures considered here bear microstructural resemblance with polycrystalline thin films on substrates, and it would be interesting to perform similar studies on these architectures.

2.4.6 Analytical Model for Interaction Strengthening

From Figure 2.27, we note that the GND density distribution arising from the kinematic incompatibilities within an MMC architecture is strongly affected by both the grain and the inclusion size. As shown, these in turn affect its flow stress. However, current homogenized micromechanical models do not account for the effect due to this synergistic interaction and it is useful to develop a simple analytical description for the same. Based on the notion that intersections of gb's with an inclusion serve as potential regions of enhanced dislocation generation, we propose a phenomenological model to quantify the dependence of the interaction effect on the grain size and inclusion size. The idea of intersections serving as dislocation sources has been recently laid out by (Forest and Aifantis, 2010) in the case of nano-twinned materials where gb-twin boundary intersections may nucleate dislocations. However, it is important to ascertain if indeed a gb-interface junction in an MMC could serve as a dislocation source. To our knowledge there are no explicit microscopic experimental evidences on MMCs to fortify this hypothesis. However, as discussed in the closing paragraphs of the preceding section the thin film-rigid substrate systems do exhibit similar coupling and we seek some guidance from experimental investigations on them. Indeed, there are evidences of

dislocations emanating from substrate-gb intersections (e.g. (Legros et al., 2009)), which indicates that such intersections can be potential sources. We use these experimental evidences to put forth our model for the MMC problem.

Figure 2.28 shows a computational cell of size $D \times D \times D$ considered for developing the analytical model. This cell comprises an inclusion of size $d_i \times d_i \times d_i$ and grains of size $d_g \times d_g \times d_g$.

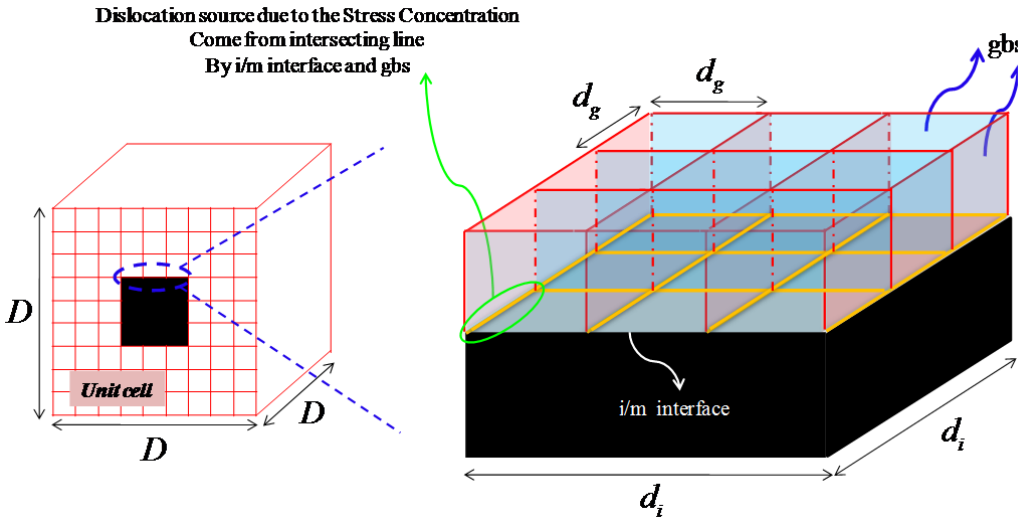

Figure 2.28. Schematic of an inclusion embedded in a polycrystalline mass of finer grains.

The number of special dislocation sources along a line formed by the intersection of the gb and inclusion face is

$$N_{s/l} = \frac{\alpha d_g}{b} \tag{2.19}$$

where α is a factor introduced to account for the fact that only a certain fraction of atomic positions may contribute as dislocation sources (Forest and Aifantis, 2010). Then, the total number of intersection lines along an inclusion surface is

$$N_l = \beta \left(\frac{d_i}{d_g}\right)^2 \tag{2.20}$$

where β is a geometrical factor that depending on the dimensionality of the problem and cross-sectional shape of the inclusion. From Eqs. (2.19) and (2.20) the number density of dislocation sources may be written as

$$\phi_{i-g} = \frac{N_l \times N_{s/l}}{V_{RVE}} = \frac{\alpha\beta \cdot (d_g/b) \cdot (d_i/d_g)^2}{D^3} \tag{2.21}$$

where $V_{RVE} = D^3$ is a representative volume (Figure 2.28). Noting that for a given RVE, $f = d_i^3/D^3$, we obtain

$$\phi_{i-g} = \frac{\alpha\beta f}{b d_i d_g} \tag{2.22}$$

Equation (2.22) indicates that the dislocation source density depends linearly on the inclusion v.f. and inversely on the inclusion and grain sizes. We propose that an additional dislocation density ρ_{int} emanates from these sources and can be quantified as

$$\rho_{int} = \frac{\overbrace{N_l \, N_{s/l}}^{N_{source}}}{V_{RVE}} n_{dis} \, l_{dis} = \phi_{i-g} \, n_{dis} \, l_{dis} \tag{2.23}$$

where l_{dis} is the average length of the nucleated dislocations and n_{dis} is the total number of the dislocation which is nucleated from one source. The plastic strain ε_{int}^p accommodated by these n_{dis} dislocations may be written as (von Blanckenhagen et al., 2004)

$$\varepsilon_{int}^p = \frac{b \, N_{s/l} \, n_{dis}}{d_g} \tag{2.24}$$

From Eq. (2.19), we may write $\varepsilon_{int}^p = \alpha n_{dis}$. Assuming that ε_{int}^p can be expressed as a fraction of the total plastic strain ε^p, the dislocations emanated from each source is

$$n_{dis} = \frac{\zeta}{\alpha}\,\varepsilon^{p} \tag{2.25}$$

where ζ is a ratio of the total plastic strain ε^{p} to ε_{int}^{p}. Substituting Eq. (2.25) into Eq. (2.24) we obtain

$$\rho_{int} = \frac{\zeta}{\alpha}\,\phi_{i-g}\,l_{dis}\,\varepsilon^{p} \tag{2.26}$$

Putting Eq. (2.22) in Eq. (2.27) and using Taylor hardening model, we write

$$\Delta\sigma_{int} = A\left(C\frac{f|\varepsilon^{p}|}{d_i d_g}\right)^{0.5} \tag{2.27}$$

where $A = \sqrt{3}\alpha_T\mu_m b$ and $C = \frac{\zeta\beta l_{dis}}{b}$. Through Eq. (2.27), the interaction effect exhibits a Hall-Petch type relation with both the grain size and the inclusion size. Figure 2.29 shows the $\Delta\sigma_{int}$ versus $d_g d_i$ relationship obtained from all the FE simulations performed in this work for different $d_g - d_i$ combinations. Notably, with appropriate parameters (Table 2-4) the trend from Eq. (2.27) corroborates well with the FE simulation result, indicating the precise nature of the interaction effect. Thus, in the analytical modeling of MMCs with size effects, one may account for the grain size-inclusion size interaction through Eq. (2.27).

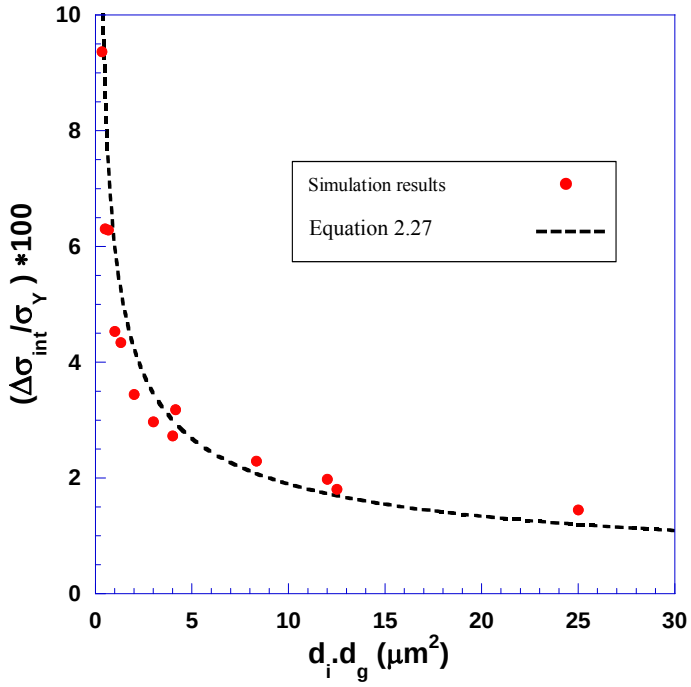

Figure 2.29. Variation of the interaction strengthening with the product $d_g \times d_i$.

Therefore, at moderate strains, the overall MMC flow strength remains independent of the grain size and depends only on the inclusion size for the $d_g > d_i$ cases, but shows a strong coupling between them for the $d_g \leq d_i$ cases. The transition from an uncoupled to a coupled (interaction effect) behavior occurs at $d_g \approx d_i$. Our detailed simulations enable isolating this interaction effect as a function of the two microstructural features.

Table 2-4. Microstructural size combinations for MMC simulations

Parameter	Value	Unit
Taylor factor (α_T)	0.3	-
Shear modulus of matrix (μ_m)	27×10^3	MPa
Burgers vector (b)	0.25	nm
Strain factor (C)	$\sim 5 \times 10^3$	-

2.5 Summary and Outlook

In this chapter, we developed an in-house UMAT for ABAQUS/ STANDARD® finite element code that implements the MSGCP theory to investigate the length-scale dependent responses of MMC architectures under thermal and mechanical loading.

We investigated the role of inclusion size and shape using unit cell model comprising a single inclusion embedded inside a single crystal matrix. The simulation results showed the length-scale dependent asymmetric responses under monotonic tension and compression loading, which are related to the prior thermal GND density due to thermo-elastic mismatch at the i-m interfaces. The pre-existing thermal GND density was shown to enhance the overall MMC hardening behavior in both tensile and compressive mechanical loading; however, the increase in hardening is higher in the case of tension.

Systematic computational simulations on bare polycrystalline and MMC architectures were performed in order to isolate the contributions due to grain size, inclusion size and the interaction thereof. We showed that at moderate strains, the overall MMC flow strength remains independent of the grain size and depends only on the inclusion size for the $d_g > d_i$ cases, but exhibits a strong coupling between them for the $d_g \leq d_i$ cases. The transition from an uncoupled to a coupled (interaction effect) behavior occurs at $d_g \approx d_i$. Based on the notion of enhanced dislocation source density, we proposed a phenomenological model that quantifies their relationship as a double Hall-Petch type behavior. Such an interaction term could be incorporated within length-scale dependent homogenized approaches to account for the interaction effect.

In this chapter, we mainly focused on the short-range interaction as arising from the thermal and mechanical GNDs. The length-scale dependent response at yield observed here was because of the length-scale dependent prior thermal residual stress

that was accounted for in the simulations. In the next chapter, we discuss another type of length-scale dependent internal residual stress that arises from the long-range elastic interactions between the GNDs. We present a theoretical formulation based on kinematic incompatibility and a stress function approach for this long-range effect that is incorporated into a continuum crystal plasticity framework.

3 Length-scale Dependent Continuum Crystal Plasticity with Internal Stresses

3.1 Introduction

Conventional continuum plasticity theories are size-independent and treat the plastic behavior of crystalline metals as a material response that does not depend on geometric or microstructural length-scales. However, there are compelling experimental evidences of strengthening in nanostructured materials compared to their coarse-grained counterparts. Experiments on miniaturized specimens also suggest that the yield strength ceases to be a purely material parameter as the specimen dimensions approach characteristic microstructural length-scales such as grain size, cell-wall spacing, dislocation spacing etc. At these length-scales, the mechanisms of plasticity may be significantly altered giving rise to macroscopic phenomena such as strong strengthening and modified hardening that are intimately tied to the microstructural and macrostructural details. To explain some of the experimentally observed length-scale effects, traditional continuum mechanics of plastic deformation is augmented with a variety of mechanisms such as strain gradients (Fleck and Hutchinson, 1993), dislocation starvation, limited dislocation sources (Dehm, 2009; Uchic et al., 2009) and so on. In practice, such effects may operate in tandem and may contribute synergistically or compete with each other to produce overall plastic responses. Of the different mechanism-based length-scale dependent plasticity theories, nonlocal approaches incorporating strain gradients have gained popularity. Such approaches invoke the existence of excess dislocations which are commonly referred to as the Geometrically Necessary Dislocations (GNDs), (Nye, 1953) and are necessary to maintain geometric

compatibility during plastic deformation. There are several versions of the gradient plasticity theories available in literature, but the core concept is the assumption that the local kinematics and kinetics of deformation at a continuum point are modulated by its surrounding points. The introduction of a gradient term introduces a length-scale into the conventional plasticity and endows it with an ability to predict length-scale dependent plastic behavior. In this work, we formulate a nonlocal approach based on continuum dislocation theory that augments the classical crystal plasticity theory with length-scale dependent internal residual stresses. First, we briefly summarize some of the strain gradient plasticity theories with reference to their salient features incorporating first and higher gradients of strain.

Fleck and Hutchinson (1993) introduced higher-order stresses corresponding to the first gradient of plastic strain in the classical plasticity theory to model the length-scale dependent responses in micro-beam bending, torsion of micro-wires and micro-indentation. Gao and co-workers (Gao, 2001; Nix and Gao, 1998) provided a physical basis for the microstructural length-scale in their Mechanism-Based Strain Gradient (MSG) plasticity theory that was based on the Taylor hardening model. Han and co-workers (Han et al., 2005a, b) extended the MSG theory to crystal plasticity. These approaches, requiring higher-order boundary conditions, have been further refined to include thermodynamically consistent descriptions of the dislocation density (e.g. (Abu Al-Rub et al., 2007)). On the other hand, lower order theories (Acharya and Bassani, 2000; Huang et al., 2004; Shu, 2001) avoid the complicating features of the higher-order theories by neglecting the higher-order stresses in the governing equations. Recently, Evans and Hutchinson, (2009) compared the lower-order and higher-order gradient theories and showed that even in the case of first-gradient theories the nature of the length-scale dependent formulation may exhibit either strengthening at yield or an enhancement in hardening after yield.

Recent approaches based on second gradients of plastic strains formulate the length-scale dependent plasticity in a thermodynamically consistent manner (Bardella, 2006, 2008; Gurtin, 2000, 2002; Gurtin et al., 2007) ascribing their presence to the distribution of defects. These approaches predict enhanced strengthening, hardening and the internal stress (aka back-stress) induced asymmetry in the tension-compression cyclic response (the Bauschinger effect) as a function of microstructural parameters. Acharya and Roy (2006) developed a phenomenological mesoscopic field dislocation mechanics approach (PMFDM) that accounts for GNDs in dissipative and energetic aspects based on incompatible elastic distortions. Ertürk, et al.,(2009); Evers, et al., (2004); Gerken and Dawson, (2008), and Kuroda and Tvergaard (2008a, b) developed physically based, crystal plasticity theories in that the back-stress that determines the effective (i.e. applied stress plus the size-dependent back stress) shear stress for plastic slip on a slip plane is derived using the Voltera dislocation theory. Concurrently, Yefimov, et al., (2004b) derived similar expressions for the effective shear stress on a slip plane corresponding to the edge dislocation density using a statistical-mechanics approach. These different approaches provide a similar computational construct and may be interpreted in terms of each other (Kuroda and Tvergaard, 2006).

In this chapter, we formulate a stress function based approach to derive length-scale dependent three-dimensional (3D) internal residual stress tensor arise from long range interaction among GNDS in the non-homogeneous spatial GND distribution density using continuum dislocation theory. Invoking the Beltrami stress function tensor $\boldsymbol{\varphi}$ Sadd, (2005), we systematically relate the length-scale dependent internal residual stress tensor $\mathbf{T}^{*}$ to the gradient of the Nye dislocation density tensor $\mathbf{A}$ via the constitutive equations for a bulk, linear elastic solid. This 3D internal stress tensor that automatically includes the effects of both edge and screw GNDs is described in terms of the incompatible parts of the continuum kinematic

variables, namely the elastic strain and curvature tensors. The definition of $\mathbf{T}^*$ via $\boldsymbol{\varphi}$ ensures its equilibrium and can naturally blend into the conventional equilibrium equation. The higher order derivatives of the Green function in $\mathbf{T}^*$ decay rapidly with distance introducing a length-scale that has to be related to the microstructural details of a boundary value problem (bvp). This length-scale dependent continuum framework is then extended to the crystal plasticity theory using the kinematics and kinetics of crystallographic slip, expressed in a thermodynamically consistent manner (Gurtin, 2002; Kuroda and Tvergaard, 2008b).

We consider two bvp involving single crystals under plane strain condition with symmetric double slip, namely, (i) a tapered specimen under uniaxial loading (ignoring the free surface effects), and (ii) constrained simple shear of a single lamella with impenetrable boundaries, from a layered microstructure that mimics a nano-twinned grain. The importance of the size-dependent hardening mechanisms is highlighted through these examples. The results are discussed within the context of the experimental/ computational investigations reported in the literature on the length-scale dependent single crystal plasticity under monotonic and cyclic loading.

3.2 Background

As an illustration to distinguish between the length-scale dependent mechanisms due to the GND density, we consider two examples of crystalline lattices subjected to curvatures. Here, we do not account for the free surfaces by implicitly assuming that the crystal lattice is embedded in an elastic region of same elastic properties (Mesarovic et al., 2010). Figure 3.1a shows the surrounding region of a continuum point wherein the crystal lattice is under pure bending resulting in constant lattice curvature (Fleck and Hutchinson, 1993). Noting the continuum description of GND used by Gurtin and coworkers (Cermellia and Gurtin, 2000;

Gurtin, 2002) and Gao and coworkers (Han et al., 2005a; Nix and Gao, 1998) (see appendix A) the non-uniform strain along the x_2 axis results in a non-zero GND density component A_{31} that is proportional to the curvature κ_{13} (Nye, 1953)[5]. However, at any section along the x_1 direction the curvature is a constant ($= \kappa$) and therefore, the GND density component is also homogeneously distributed along the x_1 axes. Consequently, at any continuum point the average stress fields due to the presence of the GNDs cancel out. In this problem, the size-dependent hardening mechanism is related to the presence of GND density and corresponding short range interaction between SSGs and GNDs which is the dissipative hardening mechanism and corresponds to the first gradient of plastic strain (e. g.(Acharya and Bassani, 2000; Nix and Gao, 1998)).

However, in the second case (Figure 3.1b) the lattice curvature varies linearly along the x_1 direction and correspondingly, the GND density also varies linearly (i.e. $A_{31} = ax_1 + b$, where a and b are constants characterized by the applied stimulus and material compliance). As demonstrated later, this leads to two contributions to hardening, one purely due to the presence of the GND density similar to the first illustration (short range dislocation interaction) and an additional term due to a net internal stress that exists owing to its non-homogeneous distribution, as their average stress fields at a continuum point may not cancel out (long range interaction among GNDs). The resulting hardening is sometimes referred to as energetic hardening. Therefore, this internal residual stress due to the non-zero gradient of the GND density as well as dissipative hardening mechanism must be accounted for to predict both the size-dependent hardening mechanisms.

[5]Based on continuum description of GND density by Nye (1953), non-uniform strain along the x_2 axis results in a non-zero GND density component A_{13}.

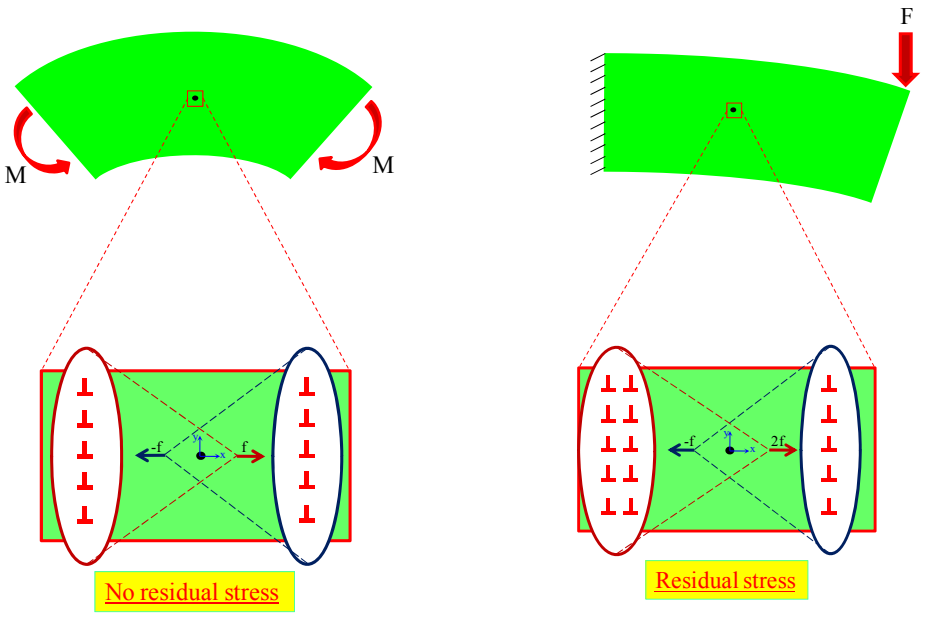

Figure 3.1. Examples illustrating the contributions of GND density to enhanced hardening in (a) pure beam bending - dissipative hardening, (b) non-uniform bending - dissipative and energetic hardening.

In discrete dislocation plasticity, the internal stress enters the formulation through the Peach-Koehler force acting on a dislocation (e.g.(Giessen and Needleman, 1995))

$$\mathbf{p}^i = -\mathbf{l}^i \times \left(\mathbf{T}^{ext} + \sum_{j \neq i} \mathbf{T}_j^* \right) \times \mathbf{b}^i \tag{3.1}$$

where $\mathbf{p}^i$ is the Peach-Koehler force vector on i^{th} dislocation, $\mathbf{b}^i$ is the Burgers vector for that dislocation, $\mathbf{l}^i$ is its unit tangent vector and $\mathbf{T}^{ext}$ is the applied stress. $\mathbf{T}_j^*$ is the internal stress field from the j^{th} on the i^{th} dislocation, which is superposed over all dislocations. While these length-scale dependent internal stresses may not play a big role in the response of conventional bulk crystalline materials, experiments show that it cannot be ignored in the regimes where the microstructural length-scales mediate the macroscopic response. For example, thin-

film tension and cyclic bending experiments by Xiang and Vlassak, (2006) exhibit length-scale mechanics of strengthening and the Bauschinger effect in passivated specimens compared to the unpassivated ones. In this case the passivation layers act as hard boundaries that obstruct dislocations escaping through the surfaces, leading to the accumulation of dislocations necessary to accommodate geometric incompatibilities. Very recently, Kiener, et al., (2010) experimentally observed the Bauschinger effect in single crystal Cu micro-beams under cantilever bending. Even under nominally homogeneous loading conditions such as uniaxial compression or tension the strain and curvature gradients may be induced in miniaturized specimens by virtue of geometric imperfections or fabrication defects that may play vital roles in the strengthening and hardening of single crystal specimens (El-Awady et al., 2009a; El-Awady et al., 2009b; Frick et al., 2008).

Unlike the discrete dislocation modeling where the superposition of the stress fields due to individual dislocations produces an inherently nonlocal theory (Giessen and Needleman, 1995), in homogenized approaches that smear out the discreteness of dislocations we must adopt a length-scale dependent approach to account for the internal stresses due to dislocation arrangement (Figure 3.2).

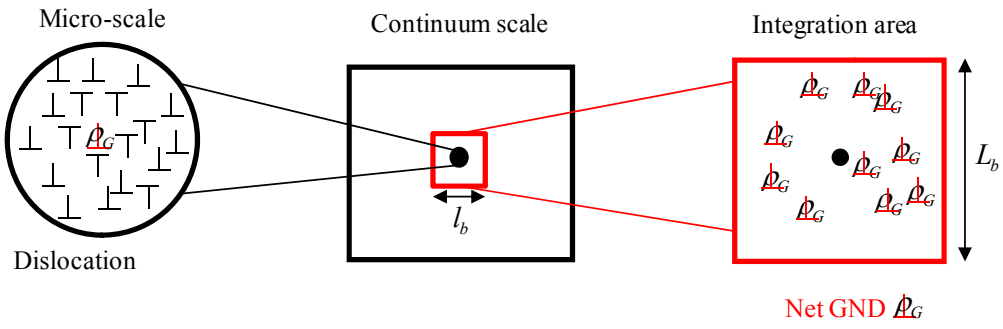

Figure 3.2. Schematic illustrating the non-locality arising from the presence of GND density at a continuum point and the distribution of the GND density around that point.

3.3 Kinematics of Compatible and Incompatible Deformations

In continuum mechanics the deformation gradient tensor ($\mathbf{F}$) is

$$\mathbf{F} = \mathbf{I} + \mathbf{B} \tag{3.2}$$

where $\mathbf{B} = \nabla\mathbf{u}$ is the total displacement gradient tensor. Under small deformation and small strain assumptions, the total displacement gradient tensor $\mathbf{B}$ may be additively decomposed into the elastic and plastic parts

$$\mathbf{B} = \mathbf{B}^e + \mathbf{B}^p \tag{3.3}$$[6]

Further, we have

$$\mathbf{B} = \underbrace{\frac{\mathbf{1}}{\mathbf{2}}(\mathbf{B} + \mathbf{B}^T)}_{\mathbf{E}} + \underbrace{\frac{\mathbf{1}}{\mathbf{2}}(\mathbf{B} - \mathbf{B}^T)}_{\mathbf{W}} \tag{3.4}$$

where $\mathbf{E}$ is the infinitesimal strain tensor and $\mathbf{W}$ is the infinitesimal rotation tensor. Further, we assume additive decomposition of the elastic and plastic strains into their compatible and incompatible parts [7]

$$\mathbf{E}^e = \mathbf{E}_C^e + \mathbf{E}_I^e \tag{3.5}$$

---

[6] In crystal plasticity, which we later relate to, $\mathbf{B}^P = \sum_\alpha \gamma^\alpha \ \mathbf{s}^\alpha \otimes \mathbf{m}^\alpha$ where γ^α is the plastic slip on slip system α comprising slip direction $\mathbf{s}^\alpha$ and slip normal $\mathbf{m}^\alpha$.

[7] Recently, Mesarovic et al. (2010) established the proof that for any strain field, there exists a unique orthogonal decomposition into compatible and incompatible strain fields.

and, $$\mathbf{E}^{p} = \mathbf{E}_{C}^{p} + \mathbf{E}_{I}^{\mathbf{p}} \tag{3.6}$$[8]

The incompatible part of the elastic strain tensor $\mathbf{E}_{I}^{e}$ may be obtained from the strain compatibility conditions. In the presence of internal defects such as dislocations the requirement of compatibility of the total strain introduces an incompatibility tensor **N** (Kröner, 1959)

$$\mathbf{N} = inc\,(\mathbf{E}_{I}^{e}) = -inc\left(\mathbf{E}_{I}^{p}\right) \tag{3.7}$$

where $\varepsilon_{kni}\varepsilon_{lmj}\,(\cdot)_{kl,nm} \overset{\text{def}}{=} inc\,(\cdot)_{ij}$. In Eq. (3.7) the incompatibility tensor, obtained as the second gradient of the elastic (or plastic) strain tensor, is a measure of the deviation of the elastic (or the plastic) strains from their compatible counterparts due to the presence of excess dislocations that result in internal stresses in addition to those due to the applied loads.

3.3.1 Compatibility of Lattice Curvature:

Under general loading conditions not only will the strains be non-uniform (leading to a strain gradient), but the curvatures (i.e. first gradient of strain) may also vary between two material points. The corresponding tensor is referred to as the Nye tensor (Nye, 1953). In what follows, we systematically relate the incompatibility tensor **N** to the first gradient of the elastic part of the lattice curvature tensor.

[8] Henceforth, the subscripts *C* and *I* indicate the compatible and incompatible parts, respectively, of the kinematic quantities.

The total lattice curvature tensor $\mathbf{K}$ is given as the gradient of the rotation vector $\mathbf{w}$ $(= \frac{1}{2}\ \varepsilon_{ijk} W_{ij}\ )$

$$K_{kl} = \frac{1}{2}\varepsilon_{ijk} W_{ij,l} = \frac{1}{2}\varepsilon_{ijk} u_{i,jl} \tag{3.8}$$

Noting that $\frac{1}{2}\varepsilon_{ijk} u_{l,ij} = 0$, we obtain

$$K_{kl} = \frac{1}{2}\varepsilon_{ijk}\left(u_{i,lj} + u_{l.ij}\right) = \varepsilon_{ijk} E_{li,j} \tag{3.9}$$

For convenience, we set $curl\ (.)_{kl} = \varepsilon_{ijk}(.)_{li,j}$. Then Eq. (3.9) may be rewritten as

$$\mathbf{K} = curl\ (\mathbf{E}) \tag{3.10}$$

Again, in the presence of internal defects the total lattice curvature is still compatible; however, its elastic ($\mathbf{K}^e$) and plastic ($\mathbf{K}^p$) parts may individually be incompatible. The incompatible part of $\mathbf{K}^e$ is

$$\mathbf{K}_I^e = curl(\mathbf{E}_I^e) \tag{3.11}$$[9]

The compatibility of the total lattice curvature tensor then gives[10]

$$curl\ (\mathbf{K}_I^e) = -curl\ (\mathbf{K}_I^p) \tag{3.12}$$

The compatible part of the curvature tensor $\mathbf{K}_C$ may be considered as the elastic lattice curvature due to the externally applied non-uniform stress, while the incompatible part of the curvature $\mathbf{K}_I$ is the additional lattice curvature due to the

---

[9] Note that Eq. (3.11) may be equivalently written in terms of the incompatible parts of the plastic strain ($\mathbf{E}_I^p$) and curvature ($\mathbf{K}_I^p$) tensors.

[10] The compatibility condition for the curvature tensor is $curl\ (\mathbf{K}) = \mathbf{0}$. Then, $curl(\mathbf{K}^e + \mathbf{K}^p) = curl\ (\mathbf{K}_C^e + \mathbf{K}_I^e) + curl\left(\mathbf{K}_C^p + \mathbf{K}_I^p\right) = \mathbf{0} \Rightarrow curl\ (\mathbf{K}_I^e) + curl\ (\mathbf{K}_I^p) = \mathbf{0}$.

atomic misfit in the presence of GNDs. Further, $\mathbf{K}_I$ may be conceptually decomposed into their plastic ($\mathbf{K}_I^p$) and elastic ($\mathbf{K}_I^e$) parts. The plastic part is the lattice curvature arising due to the presence of GND density (Nye, 1953) while the incompatible elastic curvature tensor $\mathbf{K}_I^e$ is the additional lattice curvature that corresponds to the internal residual stress field due to the surrounding excess dislocation density. These different parts of the total lattice curvature may be explained by resorting to the two illustrations in section 3.2. In the pure bending case, $\mathbf{K}_C^{\mathrm{e}}$ and $\mathbf{K}_I^p$ represent the elastic lattice curvature and additional lattice curvature due to the presence of the GND density, respectively, while the $\mathbf{K}_i^e$ vanishes. However, in the non-uniform curvature example the lattice curvature due to the atomic misfit $\mathbf{K}_I$ includes both the elastic and plastic parts. Taking the curl of $\mathbf{K}_I^e$, we obtain

$$\begin{aligned} curl\ (\mathbf{K}^e\ ) &= inc\ (\mathbf{E}_I^e) + \cancelto{0}{inc\ (\mathbf{E}_C^e)} \\ &= inc\ (\mathbf{E}_I^e) \end{aligned} \tag{3.13}$$

Equation (3.13) establishes that the gradient of the incompatible elastic curvature tensor is non-zero if a nonlinear strain (or stress) field exists due to an inhomogeneous GND density distribution in a given region.

3.3.2 Relation between Incompatible Elastic Strain Tensor and the GND Density Tensor:

Nye (1953) defined the GND density tensor **A** whose components are related to the plastic part of the incompatible lattice curvature tensor (See appendix A)

$$\mathbf{K}_I^p = -(\mathbf{A})^T + \frac{1}{2} tr(\mathbf{A}) \tag{3.14}$$

where $\mathbf{A} = curl\ (\mathbf{B}^p) = -curl\ (\mathbf{B}^e)$. Applying the curl operator to Eq. (3.14), we obtain

$$curl\left(\mathbf{K}_I^p\right) = -curl(\mathbf{A}^T) \tag{3.15}$$

Noting the compatibility conditions for the curvature [see Eq. (3.12) and Eq. (3.13)], we obtain the relation between the incompatible elastic strain and GND density tensors

$$curl(\mathbf{A}^T) = inc\ (\mathbf{E}_I^e) \tag{3.16}$$

Since, the right hand side of Eq. (3.16) is symmetric we rewrite this equation by considering the symmetric part of the left hand side as well

$$\mathbf{N} = inc\ (\mathbf{E}_I^e) = \ sym(curl(\mathbf{A}^T)) \tag{3.17}$$

i.e.
$$N_{kn} = \ \varepsilon_{ijk}\varepsilon_{lmn}(E_I^e)_{il,jm} = \frac{1}{2}\left(\varepsilon_{lmn}A_{lk,m} + \ \varepsilon_{lmk}A_{ln,m}\right) \tag{3.18}$$

Summarizing, we have established the relation between the gradient of the GND density tensor and the second gradient of the incompatible elastic strain tensor [Eq. (3.17)] in a continuum sense. This equation is central to deriving the expressions for the internal residual stress tensor, which is discussed in the next section.

3.4 Internal Stress Tensor: Stress Function Approach

In the preceding section, we introduced an incompatible elastic strain tensor $\mathbf{E}_i^e$ that is related to the GND density tensor [Eq. (3.17)]. Corresponding to this strain tensor, we introduce a work-conjugate internal stress tensor $\mathbf{T}^*$via Hooke's law

$$\mathbf{T}^* = \mathbb{C} : \mathbf{E}_I^e \tag{3.19}$$

where **C** is the fourth-order elastic stiffness tensor for the bulk material. Then, using superposition, the total stress is

$$\mathbf{T} = \mathbb{C} : \mathbf{E}^e = \mathbb{C} : \ (\mathbf{E}_C^e + \ \mathbf{E}_I^e) = \ \underbrace{\mathbb{C} : \mathbf{E}_C^e}_{\mathbf{T}^{ext}} + \ \underbrace{\mathbb{C} : \mathbf{E}_I^e}_{\mathbf{T}^*} \tag{3.20}$$

Inverting Eq. (3.19) we rewrite Eq. (3.17) as

$$\varepsilon_{ijk}\varepsilon_{lmn}\left(S_{pqil}T_{pq}^*\right)_{,jm} = \ -\frac{1}{2}(\varepsilon_{lmn}A_{lk,m} + \varepsilon_{lmk}A_{ln,m}) \tag{3.21}$$

where $\mathbb{S}\ (= \mathbb{C}^{-1})$ is the fourth-order compliance tensor.

Introduce a symmetric Beltrami stress function tensor $\boldsymbol{\varphi}$ (Sadd, 2005) to solve Eq. (3.21), such that

$$T_{ij}^* = \varepsilon_{kni}\varepsilon_{lmj}\varphi_{kl,nm} = inc\ (\boldsymbol{\varphi}) \tag{3.22}$$[11]

From Eqs. (3.7) and (3.22)

$$\mathbf{N} = inc\big(\mathbb{S} : \ inc(\boldsymbol{\varphi})\big) \tag{3.23}$$

For an isotropic medium, $\mathbb{S}$ depends only on the shear modulus μ and Poisson's ratio ν. Then, Eq. (3.23) simplifies to (Kröner, 1959)

$$\mathbf{N} = \nabla^4\boldsymbol{\psi} \tag{3.24}$$

where

$$\psi_{kl} = \frac{1}{2\mu}\left(\varphi_{kl} - \frac{\nu}{1+2\nu}\ \varphi_{mm}\delta_{kl}\right) \tag{3.25}$$

A fully three-dimensional solution of Eq. (3.24) for an infinite medium is obtained using Green's function $G(\mathbf{r} - \mathbf{r}')$ (Kröner, 1959)

$$\boldsymbol{\psi}(\mathbf{r}) = \int_V \ G(|\mathbf{r} - \mathbf{r}'|)\ \mathbf{N}(\mathbf{r}')d\mathbf{r}'^3 \tag{3.26}$$

---

[11] Eq. (3.22) satisfies stress equilibrium equation because $div\left(curl\left(curl\ (\cdot)\right)\right) = 0$

$$G(|\mathbf{r}-\mathbf{r}'|) = -\frac{|\mathbf{r}-\mathbf{r}'|}{8\pi} \tag{3.27}$$

where G is the Green function that depends on the dimensionality of the problem and the elastic stiffness of the material (i.e. isotropic or anisotropic). Substituting **N** from Eq. (3.17), components of $\boldsymbol{\psi}$ are

$$\begin{aligned}\psi(\mathbf{r})_{kl} = \frac{1}{2}\varepsilon_{lmn}\int_{V'} G(|\mathbf{r}-\mathbf{r}'|)A(\mathbf{r}')_{nk,m}d\mathbf{r}'^3 \\ + \frac{1}{2}\varepsilon_{kmn}\int_{V} G(|\mathbf{r}-\mathbf{r}'|)A(\mathbf{r}')_{nl,m}d\mathbf{r}'^3\end{aligned} \tag{3.28}$$

Using the Green-Gauss theorem and setting the surface term at infinity equal to zero, Eq. (3.28) can be rewritten in the form

$$\begin{aligned}\psi(\mathbf{r})_{kl} = \frac{1}{2}\varepsilon_{mnl}\int_{V'} G(|\mathbf{r}-\mathbf{r}'|)_{,m}A(\mathbf{r}')_{nk}d\mathbf{r}'^3 \\ + \frac{1}{2}\varepsilon_{mnk}\int_{V} G(|\mathbf{r}-\mathbf{r}'|)_{,m}A(\mathbf{r}')_{nl}d\mathbf{r}'^3\end{aligned} \tag{3.29}$$

We assume appropriate boundary conditions (Groma, 2003; Mesarovic, 2005) when solving the bvp's so that the surface effects due to image dislocation fields may be neglected.

Inverting Eq. (3.25) and substitute it in Eq. (3.22), we obtain

$$\begin{aligned}\mathbf{T}^* = inc\left(2\mu\left(\boldsymbol{\psi} + \frac{\nu}{1-\nu}(tr\boldsymbol{\psi})\mathbf{I}\right)\right) \\ T(\mathbf{r})^*_{ij} = \varepsilon_{kpi}\varepsilon_{lqj}\left[2\mu\left(\psi(\mathbf{r})_{kl,pq} + \frac{\nu}{1-\nu}\psi(\mathbf{r})_{mm,pq}\delta_{kl}\right)\right]\end{aligned} \tag{3.30}$$

where

$$\boldsymbol{\psi} = -\left(\int_V \mathbf{A}[curl\,(G\mathbf{I})]dV\right)_{symm}$$

$$\psi_{kl} = -\frac{1}{2}\int_V \varepsilon_{kns}G_{,n}(A^T)_{ls}dV \; -\frac{1}{2}\int_V \varepsilon_{lns}G_{,n}(A^T)_{ks}dV \tag{3.31}$$

Equation (3.30) is the 3D constitutive law for the internal stresses, which can be solved analytically or numerically once the distribution of **A** is known. If Eq. (3.30) were to be integrated exactly over the whole continuum domain, it would mean that the stress field due to the GND density at each point influences the stress field at every other point in the body. However, it can be seen that Eq. (3.31), and consequently, the internal stress constitutive relation (Eq. (3.30) are functions of the third gradient of G, which rapidly decays to zero (Figure 3.3).

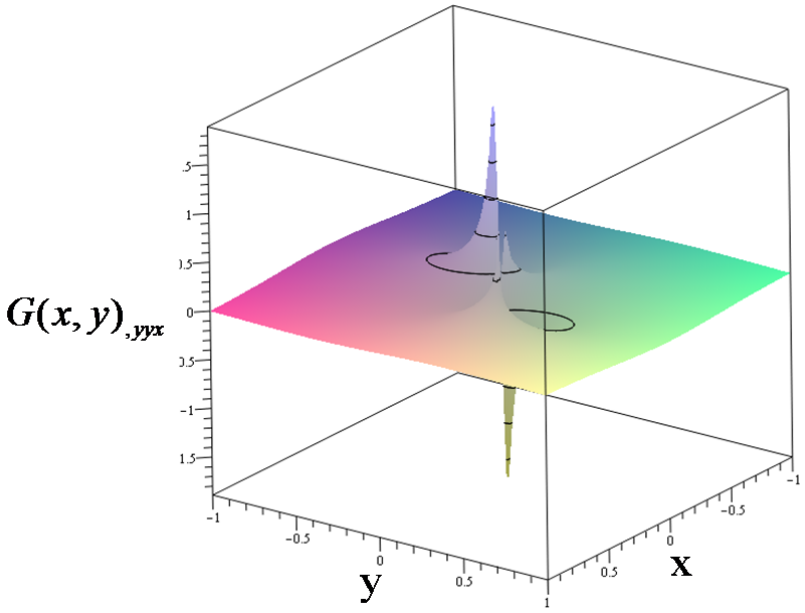

Figure 3.3. Variation of a typical component of the third gradient of the Green function in Eq (3.31)

Therefore, we may consider a small, but finite region (V') around a continuum point wherein the GND density distribution is accounted for (Evers et al., 2004; Gerken and Dawson, 2008; Groma, 1997; Mesarovic, 2005). Using the Taylor

expansion of $\mathbf{A}(\mathbf{r}')$ around the point $\mathbf{r}$ in the region V' and assuming that only the first gradient of this series is important (Groma, 2003), we obtain

$$\psi(\mathbf{r})_{kl,pq} = \frac{1}{2}\varepsilon_{mnl}A(\mathbf{r})_{nk,r}\int_{V'}(x_r - x_r')\cdot G(|\mathbf{r}-\mathbf{r}'|)_{,mpq}d\mathbf{r}'^3 + \frac{1}{2}\varepsilon_{mnk}A(\mathbf{r})_{nl,r}\int_{V'}(x_r - x_r')\cdot G(|\mathbf{r}-\mathbf{r}'|)_{,mpq}d\mathbf{r}'^3 \tag{3.32}$$

The only parameter which remains to be chosen is the integration volume, V', which defines a length scale in the problem that gives nonlocal $\mathbf{T}^*$(Eq. 3.32). Note that $\mathbf{T}^*$does not depend on $\mathbf{A}$ at a continuum point, but only on its gradient. Using the crystallographic definition of $\mathbf{A} = \sum_\alpha(\nabla\gamma^\alpha \times \mathbf{m}^\alpha)\otimes\mathbf{s}^\alpha$, the resolved components of $\mathbf{T}^*$ on a slip system α are obtained as the Laplacian of the plastic slip γ^α. For a slip system α the contributions from other slip systems to its internal stress automatically enters the formulation.

3.4.1 Internal Stress under Plane Strain Condition: Isotropic Elasticity

Although the result obtained in the preceding section gives a 3D internal stress tensor [Eq. (3.31)] we explicitly write its components for the simpler case of plane strain. Assuming a plane strain condition in the z-direction, the only non-zero components of the GND density tensor (i.e. containing dislocation lines in the z-direction) are A_{xz}, A_{yz}, A_{zz}. Then, the non-zero components of incompatibility tensor are [see Eq. (3.17)]

$$N_{zz} = -A_{zx,y} + A_{zy,x} \quad ; \quad N_{zx} = \frac{1}{2}A_{zz,y} \quad ; \quad N_{zy} = -\frac{1}{2}A_{zz,x} \tag{3.33}$$

From Eq. (3.22) the in-plane stresses can be obtained from the stress function tensor **φ**

$$T^*_{xx} = \varphi_{zz,yy} \quad ; \quad T^*_{yy} = \varphi_{zz,xx} \quad ; \quad T^*_{xy} = -\varphi_{zz,xy} \tag{3.34}$$

where φ_{zz} is similar to an Airy stress function. The out-of-plane stresses are

$$T^*_{zx} = \varphi_{zx,yy} - \varphi_{zy,xy} \quad ; \quad T^*_{zy} = \varphi_{zy,xx} - \varphi_{zx,yx} \tag{3.35}$$

Equation (3.24) can be solved in which $\psi_{zz} = ((1-\nu)/2\mu)\varphi_{zz}$ and then, the internal stress components are

$$\begin{aligned}
T^*_{xx} &= \frac{2\mu}{1-\nu}\Big[A_{zy,x}\int_s x'.G_{,y'y'x'}da' + A_{zy,y}\int_s y'.G_{,y'y'x'}da' \\
&\quad - A_{zx,x}\int_s x'.G_{,y'y'y'}da' - A_{zx,y}\int_s y'.G_{,y'y'y'}da'\Big] \\
T^*_{yy} &= \frac{2\mu}{1-\nu}\Big[A_{zy,x}\int_s x'.G_{,x'x'x'}da' + A_{zy,y}\int_s y'.G_{,x'x'x'}da' \\
&\quad - A_{zx,x}\int_s x'.G_{,x'x'y'}da' - A_{zx,y}\int_s y'.G_{,x'x'y'}da'\Big] \\
T^*_{xy} &= -\frac{2\mu}{1-\nu}\Big[A_{zy,x}\int_s x'.G_{,x'y'x'}da' + A_{zy,y}\int_s y'.G_{,x'y'x'}da' \\
&\quad - A_{zx,x}\int_s x'.G_{,x'y'y'}da' - A_{zx,y}\int_s y'.G_{,x'y'y'}da'\Big]
\end{aligned} \tag{3.36a-c}$$

where S is the integration area that defines a length-scale. For the plane strain condition the appropriate Green function is (Kröner, 1959)

$$G(|\mathbf{r}-\mathbf{r}'|) = -\frac{(\mathbf{r}-\mathbf{r}')(\mathbf{r}-\mathbf{r}')}{8\pi}\ln(|\mathbf{r}-\mathbf{r}'|) \tag{3.37}$$

choosing a square region $l_b \times l_b$ as the integration area, we obtain

$$T_{xx}^{*} = \frac{2\mu}{1-\nu} l_b^2 \left[-0.068 A_{zy,x} + 0.25 A_{zx,y}\right]$$

$$T_{yy}^{*} = \frac{2\mu}{1-\nu} l_b^2 \left[-0.25 A_{zy,x} + 0.068 A_{zx,y}\right] \qquad \text{(3.38 a-d)}$$

$$T_{xy}^{*} = -\frac{2\mu}{1-\nu} l_b^2 \left[-0.068 A_{zy,y} + 0.068 A_{zx,x}\right]$$

where $T_{xx}^{*}, T_{yy}^{*}, T_{zz}^{*}\ and\ T_{xy}^{*}$ are the internal stress components due to edge dislocations, while those due to the screw components ($T_{zx}^{*}\ and\ T_{zy}^{*}$) are zero. When described in terms of the crystal plasticity framework the resolved internal shear stress $\tau^{*(\alpha)}$ due to Eqs. (3.38 a-d) on α^{th}slip system is $\tau^{*(\alpha)} = \mathbf{s}^{\alpha} \cdot \mathbf{T}^{*}\mathbf{m}^{\alpha}$. These internal stresses bear close resemblance with those derived in the recent works (Geers et al., 2007; Gerken and Dawson, 2008; Yefimov et al., 2004b). Note that gradients in the dislocation densities may prevail in single crystal specimens due to a variety of reasons including geometric imperfections (Uchic et al., 2009), small misorientations, fabrication-induced defects (El-Awady et al., 2009b)etc. In polycrystalline materials, changes in crystal orientations across grain boundaries or twin boundaries may also set up regions with high GND density gradients in their vicinity. We highlight some of these aspects through the examples in the Results and Discussion section.

The length-scale in this theory is mathematically necessary, but it must also be physically meaningful. Recently, Mesarovic et al (2010) showed that a length-scale emerges from the thermodynamic coarsening error of the energies corresponding to the continuous and semi-discrete representations of stacked pile-ups, which is of the order of average slip plane spacing ($\sim 100b$) for each slip system. Depending on the

specific problem, microstructural length-scales may be related to, for example, average spacing of obstacles to dislocation motion in the form of grain boundaries (polycrystals), second-phase particles (heterogeneous alloys and composites), dislocation and cell-wall arrangements (single crystals). In other words the length-scale has to be determined by the microstructural details and may be problem-dependent. One interpretation of the length-scale emerges from the comparison of Eqs. (3.38 a-d) with that of Yefimov, et al. (2004) and relates to the average spacing of dislocations, i.e. $l_b \sim \frac{1}{\sqrt{\rho}}$ (also see, Groma, et al., 2003 and Bayley et al, 2006). With this interpretation the internal length-scale may range between few tens of *nm* (very high dislocation density, e.g. Dao, et al., 2006; Lu, et al., 2009) to a few μm (low dislocation density, e.g. miniaturized single crystals) and the length-scale itself may evolve with deformation. In the next section, we briefly discuss the extension of current stress function approach to account for elastic anisotropy.

3.4.2 Internal Stress with Elastic Anisotropy

In section 3.4, we derived the internal residual stress using Beltrami stress function for an elastically isotropic material. Here, the extension for anisotropic case is presented based on previous work by Kröner, (1955). For the anisotropic case the incompatibility equation is written as (compare Eq. (3.24))

$$f(\nabla)\boldsymbol{\psi} = \mathbf{N} \tag{3.39}$$

where $\boldsymbol{\psi}$ is fourth-order stress function tensor and $f(\nabla)$ is a scalar sixth-order differential operator which is given by

$$f(\nabla) = \varepsilon_{lpq}\varepsilon_{mrs}\, D_{lm}(\nabla) \cdot D_{pr}(\nabla) \cdot D_{qs}(\nabla) \tag{3.40}$$

In Eq. (3.40) $D_{ik} = C_{ijkl}(\cdot)_{,jl}$ is a second order tensor operator with C_{ijkl} as the elastic constant. The Green function solution of equation (3.39) is given by (compare Eq. (3.26))

$$\boldsymbol{\psi}(\mathbf{r}) = \int_V G(|\mathbf{r} - \mathbf{r}'|)\, \mathbf{N}(\mathbf{r}')dV \tag{3.41}$$

where G is the appropriate Green function for the anisotropic case. For cubic symmetry, the Green function is (Burger, 1939; Kröner, 1953)

$$G(|\mathbf{r} - \mathbf{r}'|) = a \cdot (|\mathbf{r} - \mathbf{r}'|^3), \qquad a = C_{11}C_{44}^2/96\pi \tag{3.42}$$

Further studies for the anisotropic cases can be found in the works of Leutz and Bauer, (1976) and Steeds and Willis(1979). Then, the internal stress $\mathbf{T}^*$ is given by Eq. (3.22) where the relation between Beltrami stress function tensor $\boldsymbol{\varphi}$ and fourth-order stress function tensor $\boldsymbol{\psi}$ is defined using a second-order differential operator X_{ijkl} as

$$\varphi_{kl} = X_{ijkl}\psi_{kl} \tag{3.43}$$

The explicit formulation for X_{ijkl} operator for cubic symmetry media has been derived by Kröner, (1955) and extended to fully anisotropic case by Michelitsch and Wunderlin(1996).

3.5 Thermodynamically Consistent Visco-plastic Constitutive Law

In this section, we derive the equilibrium and constitutive equations for crystal plasticity including the internal stress using the purely mechanical version of the thermodynamic laws.

3.5.1 First law of thermodynamics: Power Balance

Given a virtual displacement field $\tilde{\boldsymbol{u}}$, the virtual external power of any sub-body of volume V bounded by surface S is

$$\tilde{P}_{\text{ext}} = \int_{\text{S}} \mathbf{t}(\mathbf{n}) \cdot \dot{\tilde{\boldsymbol{u}}}\, dS + \int_{V} \mathbf{f} \cdot \dot{\tilde{\boldsymbol{u}}}\, dV \tag{3.44}$$

where $\mathbf{t}(\mathbf{n})$ is the traction vector on a plane whose unit normal is $\mathbf{n}$ and and $\mathbf{f}$ is the body force vector. The virtual internal power in the including the internal residual stress is

$$\tilde{P}_{\text{int}} = \int_{\text{V}} (\mathbf{T}^{ext} + \mathbf{T}^{*}) \cdot \nabla \dot{\tilde{\boldsymbol{u}}}\; dV \tag{3.45}$$

For any virtual displacement field, the internal and external powers should be balanced, so that

$$\int_{\text{S}} \mathbf{t}(\mathbf{n}) \cdot \dot{\tilde{\boldsymbol{u}}}\, dS + \int_{V} \mathbf{f} \cdot \dot{\tilde{\boldsymbol{u}}}\, dV = \int_{V} (\mathbf{T}^{ext} + \mathbf{T}^{*}) \cdot \nabla \dot{\tilde{\boldsymbol{u}}}\; dV \tag{3.46}$$

Using the divergence theorem, we obtain

$$\begin{aligned} \int_{\text{S}} (\mathbf{t}(\mathbf{n}) - (\mathbf{T}^{ext} + \mathbf{T}^{*})\mathbf{n}) \cdot \dot{\tilde{\boldsymbol{u}}}\, dS + \int_{V} (div(\mathbf{T}^{ext} + \mathbf{T}^{*}) + \mathbf{f}) \cdot \dot{\tilde{\boldsymbol{u}}}\, dV \\ = 0 \end{aligned} \tag{3.47}$$

Since this equation should be valid for all sub-body V and any arbitrary virtual displacement $\tilde{\boldsymbol{u}}$ **,** the nonlocal traction condition is

$$\mathbf{t}(\mathbf{n}) = (\mathbf{T}^{ext} + \mathbf{T}^{*})\mathbf{n} \tag{3.48}$$

and, the nonlocal force balance is

$$div(\mathbf{T}^{ext} + \mathbf{T}^{*}) + \mathbf{f} = 0 \tag{3.49}$$

Note that from Eq. (3.22), $div\ \mathbf{T}^{*}$ is always equal to zero. Then, Eq. (3.49) yields the classical force balance equation. Writing the plastic part of the total virtual

displacement gradient vector in terms of the crystal plasticity framework, in the absence of any macroscopic motion, we have

$$\nabla\dot{\tilde{\mathbf{u}}} = \dot{\tilde{\mathbf{B}}}^{e} + \sum_{\alpha} \dot{\gamma}^{\alpha} \left(\mathbf{s}^{\alpha} \otimes \mathbf{m}^{\alpha}\right) = \mathbf{0} \tag{3.50}$$

and the principle of virtual power [see Eq. (3.46)] yields

$$\begin{aligned} &\int_{S} \left(\mathbf{t}^{*}(\mathbf{n}) - (\mathbf{T}^{*})\mathbf{n}\right) \cdot \dot{\tilde{\boldsymbol{u}}}\, dS \\ &\qquad = \int_{V} \left[(\mathbf{T}^{ext} + \mathbf{T}^{*}) \cdot \dot{\tilde{\mathbf{B}}}^{e} + \sum_{\alpha} \tau^{\alpha} \cdot \dot{\tilde{\gamma}}^{\alpha} \right] dV \end{aligned} \tag{3.51}$$

where τ^{α} is the total shear stress on slip system α. Using Eq. (3.50), we obtain

$$-\tau^{\alpha}_{ext} - \tau^{*(\alpha)} + \tau^{\alpha} = 0 \tag{3.52}$$[12]

$$\mathbf{t}^{*}(\mathbf{n}) = \mathbf{T}^{*} \cdot \mathbf{n} \tag{3.53}$$

where $\tau^{\alpha}_{ext} = \mathbf{s}^{\alpha} \cdot \mathbf{T}^{ext}\mathbf{m}^{\alpha}$ is the resolved shear stress due to external loads and $\mathbf{t}^{*}(\mathbf{n})$ is the microscopic traction vector.

3.5.2 Second law of thermodynamics: Power imbalance

To derive the constitutive equation in the presence of the internal residual stress, we rewrite the second law of thermodynamics within the framework of crystal plasticity. The classical form of second law for isothermal condition is

[12] Equation (3.52) is the same as the micro-force balance equation of Gurtin (2002) where $\tau^{*(\alpha)} = div\, \xi^{\alpha}$ where $\xi^{\alpha}$is the micro-stress vector. In the present approach the internal stress is work-conjugate to the incompatible elastic strain tensor, akin to Gurtin's defect stress (Gurtin, 2002) that work-conjugates with the GND density tensor.

$$\mathbf{T} : \dot{\mathbf{E}} - \dot{\psi} \geq 0 \tag{3.54}$$

where ψ is the free energy. Noting the orthogonal decomposition of the total strain tensor (Mesarovic, et al., 2010), the total free energy may be decomposed as

$$\psi = \hat{\psi}(\mathbf{E}_C^e) + \tilde{\psi}(\mathbf{E}_I^e) \tag{3.55}$$

where $\hat{\psi}$ is the standard elastic strain energy corresponding to the compatible part of the elastic strain tensor and $\tilde{\psi}$ is the defect energy that corresponds to the incompatible part of the elastic strain tensor. Substituting Eq. (3.55) in Eq. (3.54) we obtain

$$\left(\mathbf{T}^{ext} - \frac{\partial \psi}{\partial \mathbf{E}_C^e}\right) \cdot \dot{\mathbf{E}}_C^e + \left(\mathbf{T}^* - \frac{\partial \psi}{\partial \mathbf{E}_I^e}\right) \cdot \dot{\mathbf{E}}_I^e + \sum_\alpha (\tau_{ext}^\alpha + \tau_*^\alpha)\dot{\gamma}^\alpha \geq 0 \tag{3.56}$$

This inequality should hold for all choices of $\dot{\mathbf{E}}_C^e$, $\dot{\mathbf{E}}_I^e$ and $\dot{\gamma}^\alpha$; the linearity of this inequality in $\dot{\mathbf{E}}_C^e$ *and* $\dot{\mathbf{E}}_I^e$ respectively provides the sufficient conditions for macroscopic and microscopic energetic constitutive equations

$$\mathbf{T}^{ext} = \frac{\partial \psi}{\partial \mathbf{E}_C^e} \tag{3.57}$$

$$\mathbf{T}^* = \frac{\partial \psi}{\partial \mathbf{E}_I^e} \tag{3.58}$$

and from the inequality, we obtain

$$(\tau_{ext}^\alpha + \tau^{*(\alpha)})\dot{\gamma}^\alpha \geq 0 \tag{3.59}$$

A visco-plastic constitutive law satisfying the inequality in Eq. (3.56) can be written as

$$\dot{\gamma}^\alpha = \dot{\gamma}_0^\alpha \left| \frac{\tau_{ext}^\alpha + \tau^{*(\alpha)}}{g_T^\alpha} \right|^n sign(\tau_{ext}^\alpha + \tau^{*(\alpha)}) \tag{3.60}$$

where g_T^α is the total crystallographic slip resistance due to the SSD density and the presence of the GND density (Han et al., 2005a). Writing the total internal power and

comparing with the theory of Gurtin, et al. (Gurtin et al., 2007) we identify the energetic and dissipative hardening terms

$$P_{\text{int}} = \int_V \left(\underbrace{\mathbf{T}^{ext} : \dot{\mathbf{E}}_C^e}_{\text{reversible stored power}} + \underbrace{\mathbf{T}^* : \dot{\mathbf{E}}_I^e}_{\text{irriversible stored power}} + \underbrace{\sum_\alpha (\tau_{ext}^\alpha + \tau^{*(\alpha)}) \dot{\gamma}^\alpha}_{\text{dissipative power}} \right) dV \tag{3.61}$$

The first term in Eq. (3.61) represents the length-scale independent stress power (reversible stored power) associated with externally applied loads. The second term is referred to as the length-scale dependent energetic power (irreversible stored power) as it is associated with the internal residual stress and incompatible elastic strain that will tend to reorganize the GND density from an energetically efficient configuration. The third term in Eq. (3.61) is the plastic dissipation due to the SSD (length-scale independent) and GND (length-scale dependent) densities.

Table)3-1)-)3-3) summarize key expressions developed in the present approach. Note that the internal stress tensor is blended into the continuum framework through ordinary equations of force balance and traction condition, and additional governing equations are not required.

Table 3-1. Summary of governing equations

Strain decomposition	$\mathbf{E}^e = \mathbf{E}_C^e + \mathbf{E}_I^e$
Kinematic relation	$\varepsilon_{ijk}\varepsilon_{lmn}(E_I^e)_{il,jm} = -\frac{1}{2}\left(\varepsilon_{lmn}A_{lk,m} + \varepsilon_{lmk}A_{ln,m}\right)$
Local force balance	$div(\mathbf{T}^{ext}) + \mathbf{f} = 0$
Non-local force balance	$div(\mathbf{T}^*) = 0$

Table 3-2. Summary of constitutive equations

Local elastic constitutive law	$\mathbf{T} = \mathbf{C} : \mathbf{E}_C^e$
Nonlocal internal stress constitutive law	$\mathbf{T}^* = \mathbf{C} : \mathbf{E}_I^e = \varepsilon_{kpi}\varepsilon_{lqj}\left[2\mu\left(\psi_{kl,pq} + \frac{\nu}{1-\nu}\,\psi_{mm,pq}\delta_{kl}\right)\right]$
Nonlocal visco-plastic constitutive law	$\dot{\gamma}^\alpha = \dot{\gamma}_0^\alpha \left\lvert \frac{\tau_{ext}^\alpha + \tau^{*(\alpha)}}{g_T^\alpha} \right\rvert^n sign(\tau_{ext}^\alpha + \tau_*^\alpha)$

Table 3-3. Summary of unknown variables and available equations

Unknown parameters	# unknowns	Governing equations	# equations
$\mathbf{T}^{ext}$	6	$div(\mathbf{T}^{ext} + \mathbf{T}^*) = 0$	3
$\mathbf{E}^e$	6	$(\mathbf{T}^{ext} + \mathbf{T}^*) = \mathbf{C} : \mathbf{E}^e$	6
$\mathbf{E}^p$	6	$\mathbf{E}^p = E^p(\mathbf{T}^{ext}, \mathbf{T}^*, \dots)$	6
$\mathbf{u}$	3	$\mathbf{E^e} + \mathbf{E}^p = (\boldsymbol{\nabla}\mathbf{u})_{sym}$	6
$\mathbf{T}^*$	6	$\mathbf{T}^* = T^*(curl\ \mathbf{A}, \dots)$	6
Total #	27	Total #	27

3.6 Results and Discussion

In this section, we investigate two problems involving single crystal specimens using the nonlocal visco-plastic constitutive relation (Eq. (3.60)). For simplicity we consider a two-dimensional plane strain setup with crystals oriented for symmetric double slip with respect to the loading direction.

3.6.1 Tapered Single Crystal Specimen Subjected to Uniaxial Loading

Figure 3.4 shows a tapered single crystal of length L in plane strain condition that is constrained against slip at one end and subjected to an axial force F at the

other end. The crystal is assumed to deform under symmetric double slip. The slip systems are oriented at an angle $\pm\theta$ giving

$$\left\{\begin{array}{l} s^1 = [\sin\theta, \cos\theta, 0], m^1 = [-\cos\theta, \sin\theta, 0], \\ s^2 = [-\sin\theta, \cos\theta, 0], m^2 = [-\cos\theta, -\sin\theta, 0] \end{array}\right\}$$

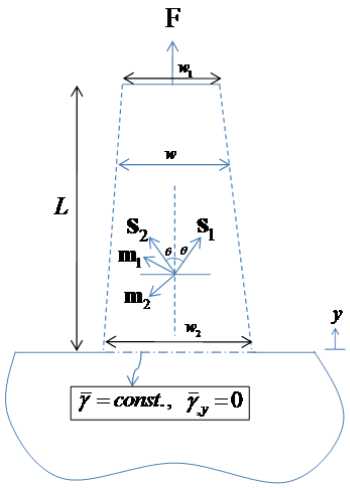

Figure 3.4. A tapered bar under uniaxial loading. Dashed tapered edges indicate that they are sufficiently away from the centerline of the specimen

Although this geometry is motivated by the recent micro-pillar experiments on single crystals, there are important differences that are discussed briefly before proceeding with the solution. First, the actual problem is essentially 3D, whereas we assume a plane strain condition. Further, as mentioned earlier, the present approach does not account for free surfaces that may give rise to image stresses and cause other mechanisms of strengthening. To circumvent the complexity associated with the free surface effects, we implicitly assume a quasi-1D situation in that the tapered boundaries are considered to be sufficiently away from the crystal center and their

presence is accounted for only through the stress variation along its length from an applied force[13].

We apply a uniaxial force F at the top and assume that at the base of the specimen ($y = 0$), $\gamma^{\alpha}(0) = const$ (specifically, zero, in this example) and $\nabla \gamma^{\alpha}(0) = 0$ so that the dislocations are free to move into the base, akin to a micro-pillar. The only non-vanishing stress component is then $\sigma_{yy} = F/w(y)$, where $w(y)$ is the width of the crystal at section y that changes linearly from w_1 at the loaded edge to w_2 at the constrained edge. Then, the resolved shear stress on each slip system is $\tau^{(1)} = -\tau^{(2)} = \sigma_{yy} \sin\theta \cos\theta$ and the corresponding plastic slip is $\gamma^1 = -\gamma^2 = \bar{\gamma}$. With the plastic strain tensor $\mathbf{E}^p = \sum_{\alpha} \gamma^{\alpha} (\mathbf{s}^{\alpha} \otimes \mathbf{m}^{\alpha})_{sym}$ the plastic slip gradient is $\nabla\bar{\gamma} = (0, \bar{\gamma}_{,y}, 0)$. In the crystallographic terms the GND density tensor is $\mathbf{A} = \sum_{\alpha} (\nabla\gamma^{\alpha} \times \mathbf{m}^{\alpha}) \otimes \mathbf{s}^{\alpha}$; therefore, we obtain

$$\mathbf{A} = \begin{bmatrix} 0 & 0 & 0 \\ 0 & 0 & 0 \\ 2cs\bar{\gamma}_{,y} & 0 & 0 \end{bmatrix}$$

where c and s denote $\cos\theta$ and $\sin\theta$, respectively. For this problem the only non-zero GND density component is the one with the Burgers vector in the $x-$direction and the dislocation line in the $z-$direction. For the total slip hardening we adopt the SSD and GND dependent hardening of the form (Han et al., 2005b)

[13] Alternatively, one may assume that the tapered edges are coated (i.e. no free surface for the dislocation to exit the specimen) with a sufficiently thick material of elastic properties same as that of the crystal so that they do not pile up along those edges. These are obviously highly idealized assumptions, but enable us to consider a simpler system to provide semi-analytical solutions.

$$g^{\alpha} = g_0 \left(\left(1 + \frac{C_h}{g_0} |\bar{\gamma}^{\alpha}| \right)^2 + l_g c |\bar{\gamma}_{,y}| \right)^{1/2} \tag{3.62}$$

The non-zero components of the internal stress tensor [see Eq. (3.38 a-d)] are

$$\begin{aligned} T^*_{xx} &= \frac{\mu}{1-\nu} \cdot l_b^2 cs \bar{\gamma}_{,yy} \\ T^*_{yy} &= \frac{0.27\mu}{1-\nu} \cdot l_b^2 cs \bar{\gamma}_{,yy} \\ T^*_{zz} &= -\nu (T^*_{xx} + T^*_{yy}) \\ T^*_{xy} &= 0 \end{aligned} \tag{3.63}$$

and the corresponding resolved internal residual shear stress on each slip system is

$$(\tau^*)^1 = -(\tau^*)^2 = -D l_b^2 c^2 s^2 \bar{\gamma}_{,yy}, \tag{3.64}$$

where $= \frac{0.73\mu}{1-\nu}$. Substituting Eqs. (3.62) and (3.64) into Eq. (3.60) and integrating with respect to time, we obtain

$$\bar{\gamma}^{\alpha} = \gamma_0^{\alpha} \left| \frac{cs \dfrac{F}{w_2 - \dfrac{w_2 - w_1}{L} y} - D l_b^2 c^2 s^2 \bar{\gamma}_{,yy}}{g_0 \sqrt{\left(1 + \dfrac{C_h}{g_0} |\bar{\gamma}^{\alpha}| \right)^2 + l_g c |\bar{\gamma}_{,y}|}} \right|^n sign(\tau^{\alpha}_{tot}) \tag{3.65}$$

Equation (3.65) is solved using the fourth-order Runge-Kutta method. The material and geometric parameters used are $\gamma_0^{\alpha} = 0.01$, $C_h = g_0/5$, $D = 1000 g_0$, $\theta = \pm 45^{\circ}$, $w_1 = 0.2L, w_2 = 0.4L$, $n = 10$. The results for monotonic and cyclic loading are discussed next.

a. Monotonic loading:

To begin with, we investigate the influence of l_b by setting $l_g = 0$. Figure 3.5 shows the variation of the magnitude of plastic slip along the length of the specimen for different $\eta = \left(\frac{L}{l_b} \right)$ ratios. As expected, the magnitude of the plastic slip decreases with decreasing η, that is for a smaller specimen size or larger l_b.

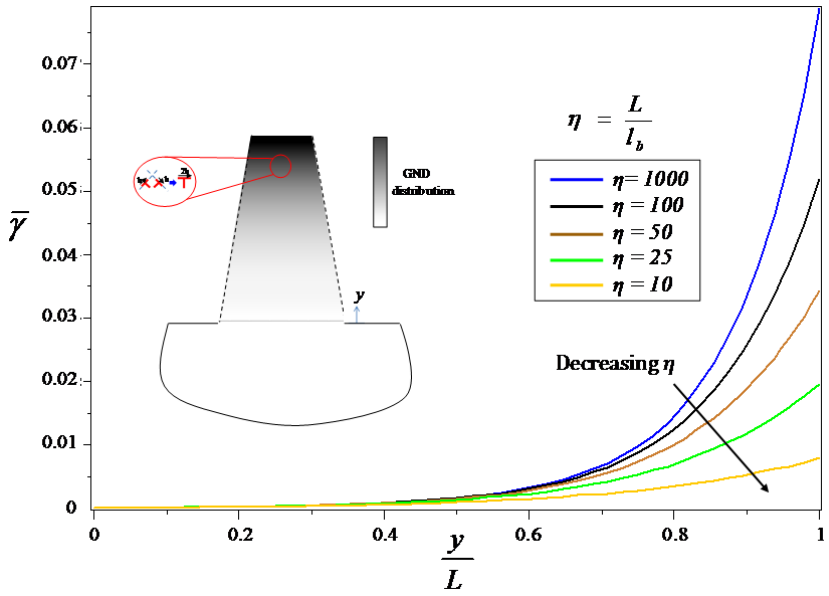

Figure 3.5. Plastic slip $\bar{\gamma}$ along bar axis y for various ratio of $\eta = L/l_b$ for tapered specimen under monotonic tension

With decreasing η the internal stress term in Eq. (3.65) becomes increasingly dominant and provides a strong resistance to plastic slip. The increasing internal stress with decreasing η tends to homogenize the plastic slip as observed from the trend of the plastic slip variation with decreasing η.

Next, we highlight the relative influence of the two length-scale dependent dissipative hardening mechanisms, i.e. the dissipative hardening due to the presence of GND (corresponding to l_g) and the one due to GND density gradient (corresponding to l_b) on the overall response of the crystal. Figures 3.6 a and b show the normalized resolved shear stress on a slip system versus the magnitude of plastic slip at $y = L$ for different values of η and β $\left(= \frac{L}{l_g}\right)$ ratios. Figure 3.6a shows that the length-scale dependent dissipative hardening due to the presence of GND influences the post-yield response, which has been previously reported by Han, et al. (2005b) in the context of MSG-CP theory.

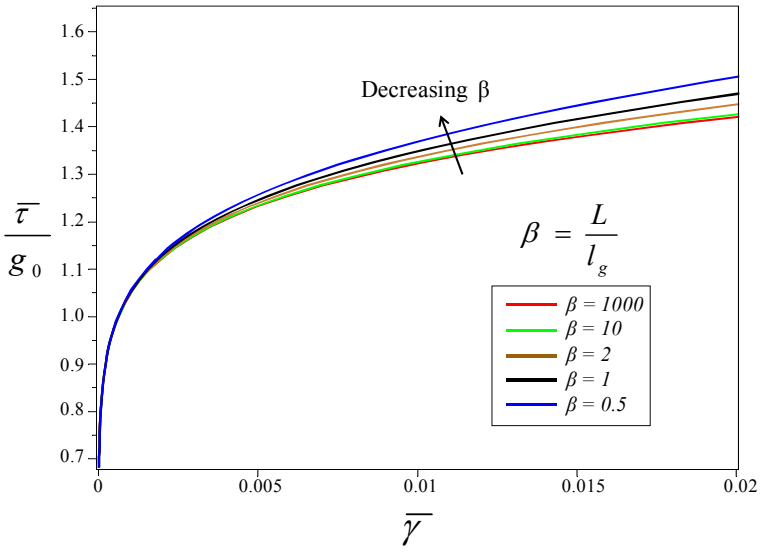

(a)

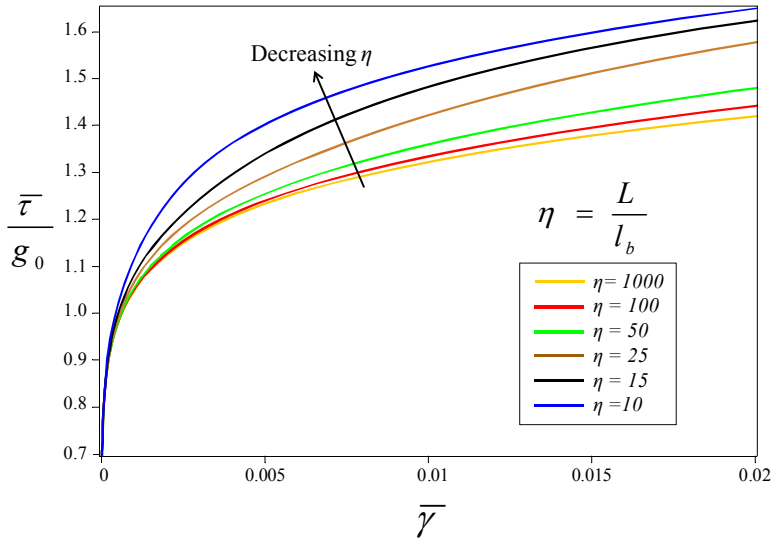

(b)

Figure 3.6. Resolved shear stress versus plastic slip at $y = L$ for tapered bar under monotonic tension for various ratios (a) $\beta = L/l_g$, and (b) $\eta = L/l_b$.

However, this enhanced hardening effect is discernable only when the slip is appreciably large, well beyond the initial yield. In comparison, Figure 3.6b shows that the internal stress significantly influences both the response at incipient slip as well as at relatively larger slip. That is, the length-scale dependence due to the gradient of the GND density has a stronger influence on both the strengthening and

hardening behavior of a crystal compared to that arising from the presence of the GND density. This is further exacerbated given that the range of η ratios considered here is relatively small compared to the range of β ratios. Figure 3.7 signifies the influence of geometric imperfection on the distribution of the internal stress along the specimen length. The larger the initial taper the more non-homogeneous is the GND density distribution that causes higher resolved internal shear stresses on individual slip systems. Consequently, the plastic slip on the slip systems would become harder giving an overall plastically stronger response.

The strong strengthening and hardening observed in this example is qualitatively similar to the specimen length-scale dependent strengthening behaviors reported in some of the recent experiments on miniaturized single crystals (e.g.(Frick et al., 2008)) that indicate presence of the GND density. While the actual mechanisms of strengthening in such miniaturized experiments have not been fully unraveled, the results from the present work correlate qualitatively with the experimentally observed size-dependent plasticity in the presence of strong gradients (Maaß et al., 2009).

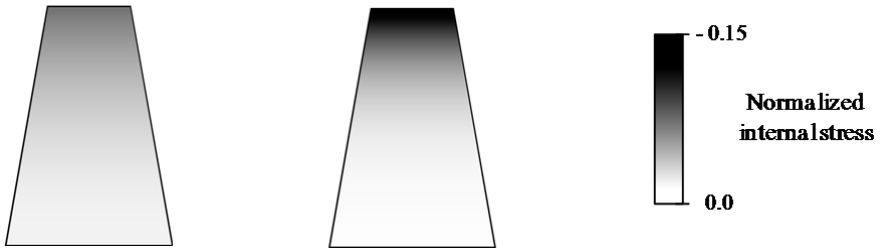

Figure 3.7. Distribution of normalized internal shear stress $\left(\frac{\bar{\tau}^*}{\bar{\tau}}\right)$ along the tapered specimen under monotonic tension for (a) $\lambda = 2.86^\circ$, (b) $\lambda = 5.71^\circ$. $\eta = 50$.

Although in the present case the gradient in the GND density is due to specimen taper, presence of fillets, low angle boundaries (Uchic et al., 2009) or surface damage layers due to fabrication may also produce significant gradients at small specimen

sizes (El-Awady et al., 2009b). Thus, the non-gradient based size-effects (e.g. source-limited dislocation plasticity, dislocation starvation) postulated in such experiments may be augmented by those due the internal stresses arising from the non-homogeneous distribution of the GND density.

b. Cyclic loading:

We now investigate the response of the tapered single crystal specimen under a single tension-compression cycle. Many metals exhibit the well-known Bauschinger effect under cyclic loading. In the present work, the internal stress tensor derived from the inhomogeneous GND density distribution produces a size-dependent Bauschinger effect. For simplicity, we suppress the contribution from the dissipative hardening by setting $l_g = 0$.

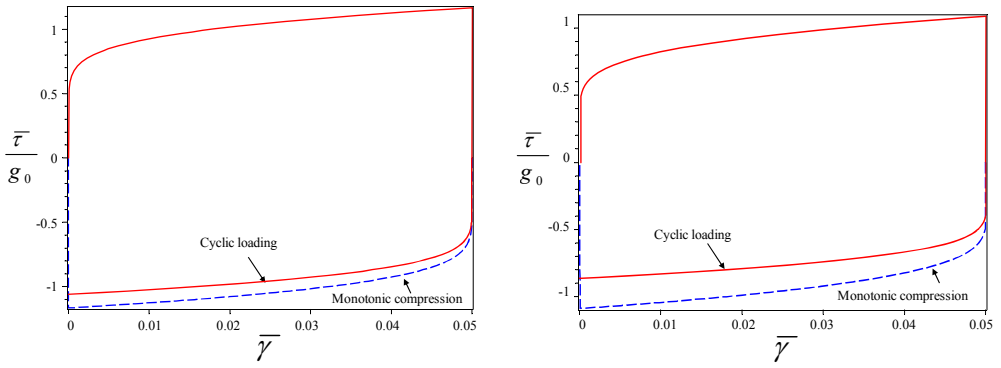

Figure 3.8. Resolved shear stress versus plastic slip at $y = L$ for tapered bar under cyclic loading (a) $\eta = 100$, (b) $\eta = 50$.

Figure 3.8 shows the resolved shear stress versus plastic slip curves at $y = L$ plotted for two different values of η. We also include the response of the same specimens under monotonic loading. For fixed η the monotonic compressive response is much stronger than if the specimen were loaded under a single tension-

compression cycle. The disparity between the monotonic and cyclic responses increases with decreasing η giving a length-scale dependent Bauschinger effect (Kiener et al., 2010; Xiang and Vlassak, 2006). However, upon reverse loading the direction of the resolved shear stress due to external load reverses, but that of the internal stress does not as the GND arrangement is unaffected. This causes the specimen to yield at a smaller load in the reverse loading. The hardening behavior is also weaker in the reverse loading compared to the initial forward response. In a realistic scenario with more than two slip systems, one may observe stronger hardening due to latent hardening that may accentuate the Bauschinger effect (Bayley et al., 2006). Figure 3.9 shows that geometric imperfections strongly influence the Bauschinger effect and it increases with increasing degree of imperfection. Such an asymmetric response cannot be predicted solely by a theory that does not account for the effect of distribution of the dislocation density. This is true irrespective of the particular nature of the strain gradient theory (Xiang and Vlassak, 2006).

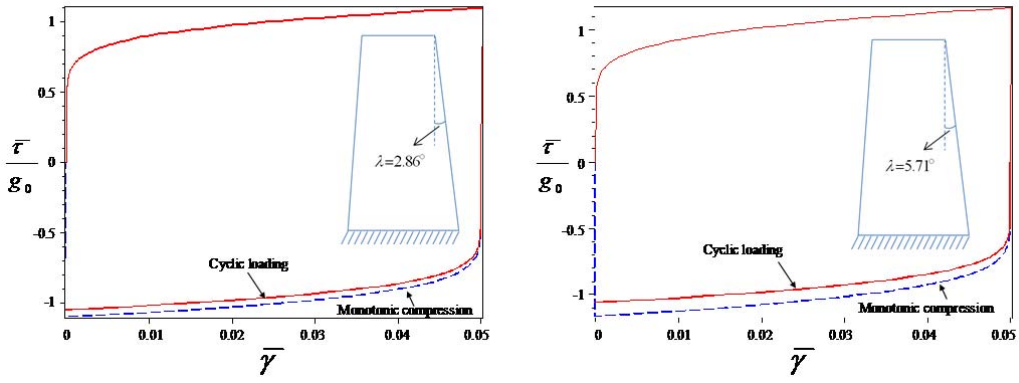

(a) (b)

Figure 3.9. Resolved shear stress versus plastic slip at y=L for various tapered angle under cyclic loading (η=100) (a) $\lambda = 2.86^{\circ}$, (b) $\lambda = 5.71^{\circ}$.

3.6.2 Single Crystal Lamella Subjected to Simple Shear

In the previous problem, the internal stress appeared because of non-homogeneous distribution of the stress due to geometric imperfections. Here, we consider the internal stress in a specimen with no geometric non-uniformities, but due to the pile-up of dislocations at impenetrable boundaries. Consider a layered crystal as shown in Figure 3.10. We isolate a single layer from this crystal and assume it to be a semi-infinite lamella of thickness 2λ with symmetric double planar slip subjected to simple shear. This geometry is reflective of a typical twin lamella within a grain of a nano-twinned polycrystal (Li et al., 2010).

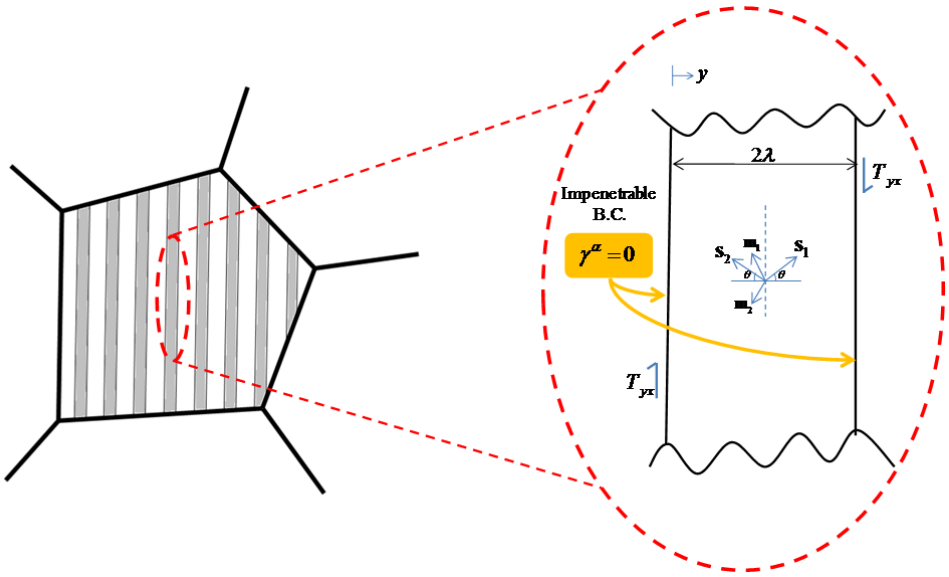

Figure 3.10. A single lamella within a nano-twinned crystal under simple shear.

We consider hard boundary conditions on the lamella boundaries such that

$$\gamma^{\alpha}(0) = 0, \quad \gamma^{\alpha}(2\lambda) = 0; \quad \alpha = 1,2 \tag{3.66}$$

These conditions ensure that no plastic slip occurs along a slip system at the boundaries causing dislocations to pile up there. The only non-zero component of macroscopic stress in this problem is T_{yx}. The corresponding resolved shear stress

and plastic slip due to the external load are, respectively, $\tau^1 = \tau^2 = -\bar{\tau} = T_{yx}\cos 2\theta$ and $\gamma^1 = -\gamma^2 = \bar{\gamma}$, where θ is the orientation of the slip systems with respect to the loading direction. The plastic slip gradient is $\nabla\bar{\gamma} = (0, \bar{\gamma}_{,y}, 0)$ and the continuum dislocation density tensor **A** for this case is

$$\mathbf{A} = \begin{bmatrix} 0 & 0 & 0 \\ 0 & 0 & 0 \\ 0 & -2s^2\bar{\gamma}_{,y} & 0 \end{bmatrix}$$

From Eq. (3.38 a-d) and using Schmid law, the resolved internal shear stress on each slip system is

$$(\tau^*)^1 = (\tau^*)^2 = -\bar{\tau}^* = -\frac{0.136\mu}{1-\nu} l_b^2 s^2 \bar{\gamma}_{,yy} \cos 2\theta \tag{3.67}$$

and the corresponding plastic slip is

$$\bar{\gamma}^\alpha = \gamma_0^\alpha \left| \frac{(T_{yx} - \frac{0.136\mu}{1-\nu} l_b^2 s^2 \bar{\gamma}_{,yy}) cos2\theta}{g_0 \sqrt{\left(1 + \frac{C_h}{g_0}|\bar{\gamma}^\alpha|\right)^2 + l_g c|\bar{\gamma}_{,y}|}} \right|^n sign(\tau_{tot}^\alpha) \tag{3.68}$$

The material parameters are the same as in the previous example, except θ, which is set equal to 90° providing the highest plastic incompatibility. Figure 3.11a shows the normalized shear stress-average plastic slip response for different $\eta = \frac{\lambda}{l_b}$. As expected, strong strengthening occurs with decreasing η. Figure 3.11b shows the normalized shear stress at $\bar{\gamma} = 0.002$ as a function of normalized lamella thickness. It is interesting to note that for the range of η values shown in the figure the strengthening trend compares well with Hall-Petch behavior.

For a given applied stress, Eq. (3.68) plastic slip variation along the lamella thickness can be obtained, subject to the boundary conditions in Eq. (3.66). For fixed applied loading ($T_{yx} = 1.5g_0$), Figures 3.12a and b respectively show the variation of plastic slip and normalized internal resolved shear stress on a slip system along the

normalized thickness ordinate for different values of η. As shown in figures 3.12, for fixed l_b (i.e. same material), when the lamella thickness is much larger compared to the internal length-scale ($\eta \gg 1$), only a very narrow region is affected by the boundary and away from it the effect decays rapidly.

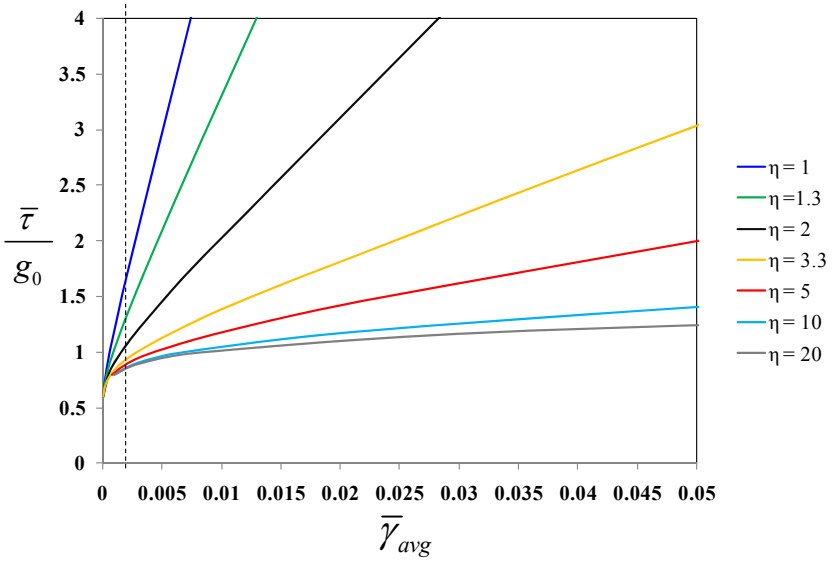

(a)

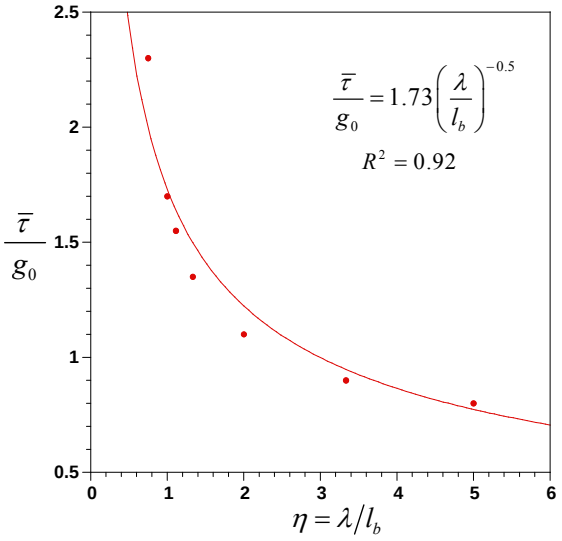

(b)

Figure 3.11. (a) Normalized resolved shear stress ($\bar{\tau}/g_0$) versus average plastic slip as a function of η for $\theta = 90^\circ$, (b) Normalized resolved shear stress ($\bar{\tau}/g_0$) versus normalized lamella thickness at $\bar{\gamma} =$ 0.2%.

The plastic slip away from the boundary reaches a constant value (Figure 3.12a), which corresponds to the absence of internal stress in that region (Figure 3.12b). However, as the lamella thickness approaches the internal length–scale ($\eta \to 1$) the *boundary affected zone (b.a.z.)* occupies a significant portion of the lamella. The magnitude of internal stress over the lamella thickness increases and at the same time it becomes more diffuse, i.e. it extends over the entire lamellar region. Correspondingly, it becomes increasingly difficult to produce plastic slip. With even further decrease in the lamella thickness ($\eta < 1$) the internal stress distribution within the lamella becomes nearly uniform (except at the boundary) and its magnitude tends to saturate. Figure 3.12c captures this aspect clearly in that it shows an initial strong increase in the normalized internal residual shear stress as η decreases, but a tendency to saturate at very small η. Although not shown in Figure 3.11b, the corresponding slip system strengthening also tends to saturate with the saturation of the internal residual shear stress.

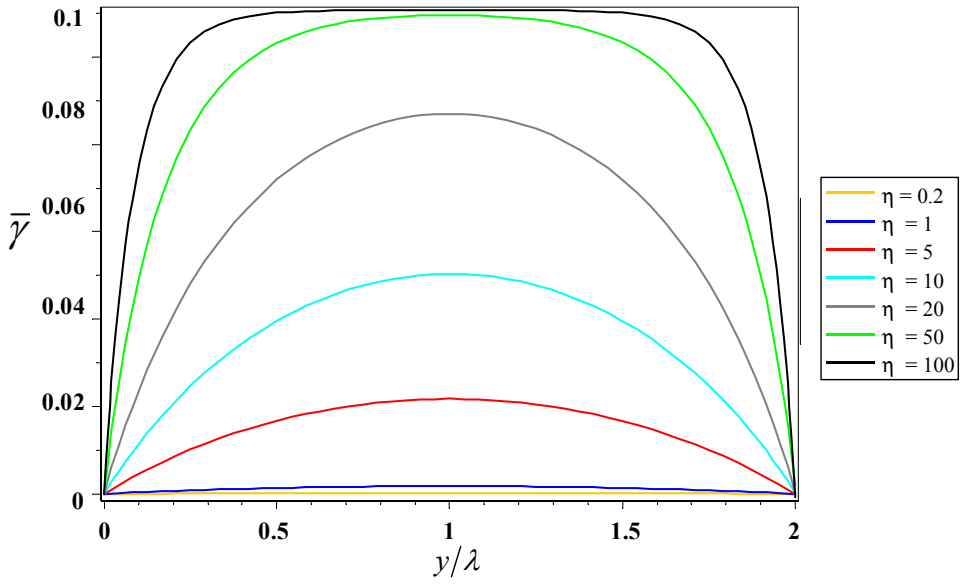

(a)

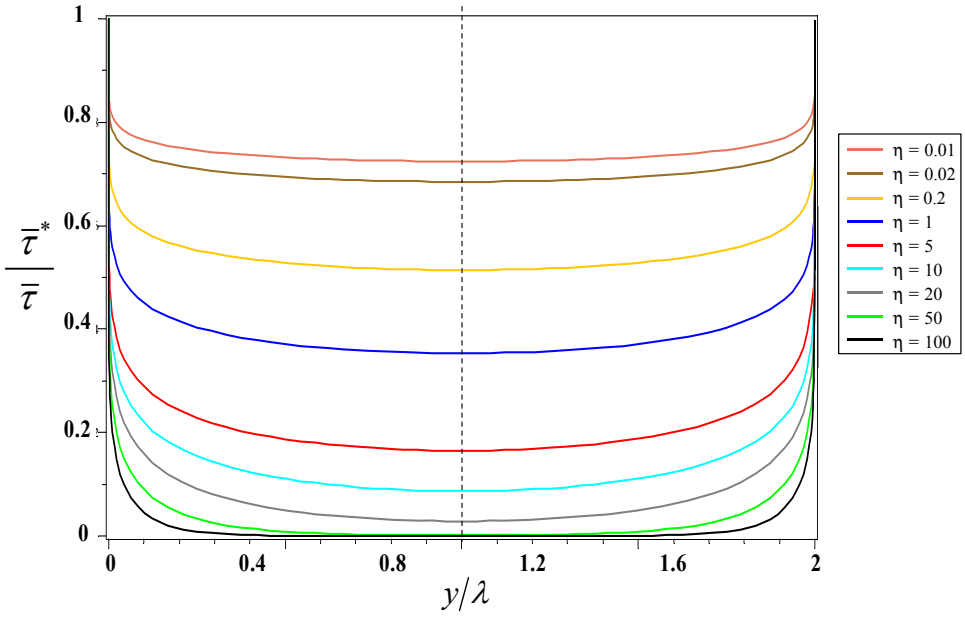

(b)

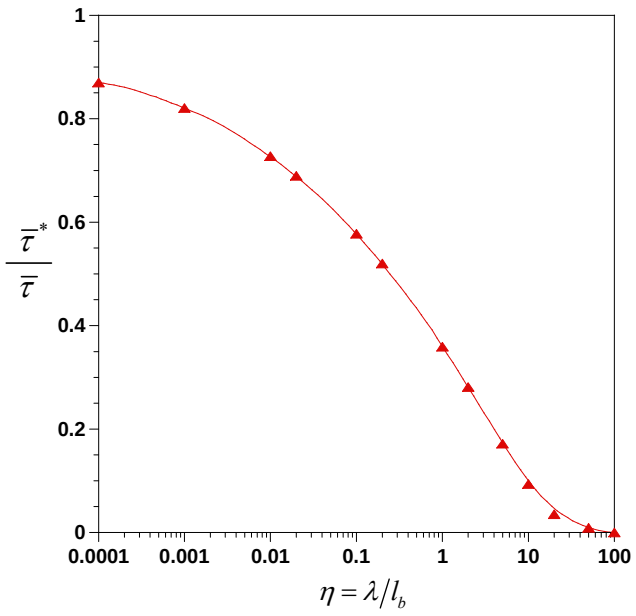

(c)

Figure 3.12. (a) Distribution of plastic slip ($\bar{\gamma}$) on a slip system as a function of η for $\theta = 90^{\circ}$ versus distance normalized by lamella thickness λ (b) Normalized internal resolved shear stress ($\bar{\tau}^*/\bar{\tau}$) along the lamella thickness as a function of η for $\theta = 90^{\circ}$, and (c) Normalized internal resolved shear stress ($\bar{\tau}^*/\bar{\tau}$) versus normalized lamella thickness.

3.7 Summary

In this chapter, we developed a nonlocal crystal plasticity approach enriched by internal residual stresses that arise due to the non-homogeneous distribution of GND densities. The salient feature of this work is the analytical derivation of the length-scale dependent 3D internal stress tensor using the stress function approach. This second order internal stress tensor blends into the conventional equilibrium equations and boundary conditions. In the crystal plasticity framework, the internal stresses appear as additional resolved shear stresses on each slip system alongside those due to the externally applied loads. The visco-plastic constitutive law for crystallographic slip that includes this effect is presented in a thermodynamically consistent manner. The connections between the continuum and crystallographic variables in this formulation render it useful for the development of computational framework for the $J_2 -$ deformation theory as well as small strain crystal plasticity theory.

The analytical examples highlight the importance of the internal stress on the size-dependent strengthening and hardening in single crystals. Geometric imperfections can cause strong gradients in the GND density and lead to a strengthening of the overall stress-strain response in specimens that are subjected to nominally uniaxial macroscopic loads. As evident from the second example, the internal stress-induced strengthening of a slip system is akin to the Hall-Petch behavior, but tends to saturate at small microstructural sizes.

As a closure, we briefly compare the present approach with some of the existing nonlocal theories that incorporate the internal residual stresses. The key equations derived here for internal stresses results bear close resemblance with the pioneering efforts of Groma and co-workers that use a statistical approach

mimicking the collective behavior of dislocations (Groma, 2003; Groma and Bakó, 1998; Zaiser et al., 2001). Recent versions of this approach by Yefimov et al (2004) have been developed for edge dislocations. The approach of Gerken and Dawson (2008) again restricts its focus on the internal stresses due to edge dislocations. In their theory, the average internal stress fields derived from Volterra dislocations are simplified assuming a bilinear variation of the GND density, but the motivation behind this choice is not obvious. Recently, Ertürk, et al (2009) presented a sophisticated crystal plasticity approach with back stresses accounting for the latent hardening effects due to both screw and edge GNDs. In comparison to these approaches, the present approach is based on a continuum theory of kinematic coarsening and also includes contributions from edge and screw components of the GNDs. The projection of the gradient of the GND density tensor on to a given slip system leads to the contribution from other slip systems providing a latent hardening effect. Further, it should be possible to extend this approach to anisotropic elastic cases using appropriate stress functions (See section 3.4.2). This aspect seems not well-outlined in most theories in that the development is restricted to elastically isotropic cases.

Our focus in this chapter was on interaction of GNDs in infinite medium where GND interaction with boundaries such as free surfaces and interfaces are neglected. It showed that internal stresses only present when GNDs are distributed non-uniformly and GND density gradient present. In the next chapter, we will account for GNDs-boundaries interaction in the finite region. It shows that even in presence of uniform GND density distribution, internal stresses arise due to GND-boundary interactions which affect overall behavior of small scale structures.

4 A Crystal Plasticity Analysis of Length-scale Dependent Internal Stresses with Image Effects

4.1 Introduction

Internal stresses arise in crystalline metals due to ensembles of geometrically necessary dislocations (GNDs) that accommodate lattice incompatibilities. An important macroscopic consequence of these internal stresses is that they produce length-scale dependent strengthening under forward loading and kinematic hardening under cyclic loading with decreasing microstructural and/ or specimen sizes (Kiener et al., 2010; Motz et al., 2005). These internal stresses appear because of the long-range dislocation-dislocation and dislocation-boundary interactions. Of particular interest are the long-range GND-GND and GND-free surface interactions. While molecular dynamics (MD) and discrete dislocation dynamics (DDD) account for these internal stresses as a length-scale dependent entity (e.g. Fivel et al. 1996; Yan et al. 2004), coarser realizations based on continuum approaches, e.g. crystal plasticity, rely on augmenting the traditional kinematics and kinetics with additional length-scale dependent features. A continuum crystal plasticity description of the internal stress due to long-range GND-GND interaction appears as the first gradient of the GND density ρ_{gnd} with respect to a slip direction (Evers et al., 2004; Gerken and Dawson, 2008; Gurtin, 2002; Kuroda and Tvergaard, 2008b). A natural requirement of this result is that the GND density ρ_{gnd} should be spatially non-uniform. Indeed in many cases, ρ_{gnd} varies along slip direction due to a variety of situations including geometric non-uniformity (see chapter 3), or deformation mapping leading to gradients, e.g. simple shear, (Evers et al., 2004; Gurtin et al., 2007; Yefimov et al., 2004b). However, in cases where ρ_{gnd} does not vary spatially

such an exposition predicts zero internal stress. For instance, a uniform curvature in the case of pure bending results in ρ_{gnd} also being constant (Han et al., 2005b). From a physical viewpoint however, internal stresses should exist even under uniform curvature conditions or even under homogeneous loading (Guruprasad and Benzerga, 2008), because of the additional long-range GND-surface interactions. These enhanced interactions are automatically resolved in a high resolution approach such as MD and are also modeled in DD frameworks through appropriate corrective traction boundary conditions (Cleveringa et al., 1999; Hou et al., 2008; Motz et al., 2008; Yefimov et al., 2004a). To our knowledge most length-scale dependent continuum crystal plasticity frameworks with internal stresses do not explicitly discuss image stress fields arising from the long-range elastic interactions between the GNDs and free surfaces. (Bayley et al., 2006; Evers et al., 2004; Gerken and Dawson, 2008; Gurtin, 2002; Kuroda and Tvergaard, 2008). Recently, Vinogradov and Willis (2008) and Cherednichenko (2010) derived a continuum crystal plasticity framework incorporating image stress fields using statistical mechanics based approach (Groma, 1997). They provided explicit solutions for image stresses in a strip under simple shear due to the presence of a hard boundary (causing dislocation pile up) rather than a traction-free boundary. Thermodynamically-based frameworks developed by Gurtin (2002) and Mesarovic (2005) provide pathways to introduce these additional effects. Mesarovic (2005) proposed a thermodynamic framework addressing the long-range GND-GND and GND-boundary interactions and discussed its applicability in the context of impenetrable and penetrable boundaries. Gurtin (2002) provided a basis to account for the image stresses through higher-order traction b.c. that can be adopted for traction-free surfaces. This *micro-traction* b.c. is sometimes reinterpreted in an equivalent null edge and screw dislocation densities at the free surfaces (Ertürk et al., 2009; Hayashi et al., 2011; Kuroda and Tvergaard, 2009; Yefimov et al., 2004a). However, such an equivalent null

GND prescription may not fully account for the long-range image effects produced by a traction-free surface.

Similar to the DD approaches (e.g. (Fivel et al., 1996; Lubarda et al., 1993; Van der Giessen and Needleman, 1995; Yan et al., 2004)), superposition of image stress fields due to dislocation ensembles described by a continuum density measure would be a natural way to satisfy the b.c.'s at free surfaces. There are some classic studies on obtaining image stress fields arising from a single dislocation hosted in a semi-infinite medium(Jagannadham and Marcinkowski, 1979; Lubarda and Kouris, 1996b), in the proximity of a bi-material interface (Chou et al., 1975; Jagannadham and Marcinkowski, 1980; Lubarda and Kouris, 1996a) and in a thin strip with two free surfaces (Fotuhi and Fariborz, 2008; Hartmaier et al., 1999; Ting, 2008). (Saada, 2008) provided a brief review on the image fields arising from planar dislocation arrays and their contribution to the plastic deformation. (Khanikar et al., 2011; Lubarda, 2006; Weinberger and Cai, 2007) investigated image effects in geometries mimicking micro-scale specimens.

In this chapter, we present a coarse-grained approach that accounts for image fields within continuum crystal plasticity arising from the long-range elastic interaction (LRI) between a GND density field **A** and bounding free surfaces of the specimen that hosts this GND field. The approach expands on our previous work (chapter 3) by introducing a generalized stress function that now incorporates appropriate boundary corrections through image fields. As a model system, we analyze a thin specimen experiencing uniform curvature under the action of an external bending moment. The analysis shows that even in the case of a uniform GND density distribution, internal stresses occur from two sources

I. LRI arising from finite spatial extent of the GND density (embedded in an infinite medium).

II. LRI between the GND density and free surfaces appearing as image fields.

The stress function corresponding to (i) is obtained via appropriate infinite medium Green's function (chapter 3) and the resulting stress fields are akin to the Volterra solution as applied to finite spatial extent of the GND density in an infinite medium. The solution to (ii) is incorporated by writing an available stress function for a single dislocation in a finite medium derived using complex Fourier transform approach (Fotuhi and Fariborz, 2008), equivalently in terms of the GND density. The formulation is applied to investigate length-scale dependent responses triggered by internal stresses – (a) strengthening under monotonic pure bending as a function of decreasing specimen thickness and (b) kinematic hardening under cyclic pure bending. We also compare our results with experiments and DD simulations and propose a likely origin of variable internal length-scale for internal stresses.

In the following section, we first provide key equations pertaining to our previous work based on stress functions (Chapter 3) and then extend the approach by including additional stress functions providing image fields.

4.2 Nonlocal Continuum Theory with Internal Stress and Image Fields

As discussed in the preceding Chapter, the total stress $\mathbf{T}$ comprises the stress due to externally applied loads $\mathbf{T}^{ext}$ and internal stress $\mathbf{T}^{*}$, given by

$$\mathbf{T} = \mathbf{C} : \mathbf{E}^{e} = \mathbf{C} : (\mathbf{E}_{C}^{e} + \mathbf{E}_{I}^{e}) = \underbrace{\mathbf{C} : \mathbf{E}_{C}^{e}}_{\mathbf{T}^{ext}} + \underbrace{\mathbf{C} : \mathbf{E}_{I}^{e}}_{\mathbf{T}^{*}} \tag{4.1}$$

where $\mathbf{E}^{e}$ is the total elastic strain tensor, $\mathbf{E}_{C}^{e}$ is the compatible elastic strain arising from lattice stretching due to external loading, $\mathbf{E}_{I}^{e}$ is the incompatible elastic strain tensor arising from internal stress due to distributed defects and $\mathbf{C}$ is the fourth-order elastic stiffness tensor. Internal stresses arise from the presence of defects that could span several orders of length-scales. One of the common sources of these internal *residual*

stresses is the presence of ensembles of excess dislocations (GNDs) and the relevant resolution is sometimes referred to as a *mesoscopic* continuum (Zaiser and Seeger, 2002). At this length-scale, it is appropriate to describe GNDs by equivalent density fields that could vary spatially. It has been well-established that these internal stresses occur due to the long-range dislocation-dislocation and dislocation-interface elastic interactions (Hull and Bacon, 2001; Mughrabi, 1983; Zaiser and Seeger, 2002). A special case of the latter is the dislocation- free surface interaction, which is the focus of this work.

The incompatible part of elastic strain $\mathbf{E}_I^e$ is given by the incompatibility condition (chapter 3),

$$\mathbf{N} = curl\ curl\ (\mathbf{E}_I^e) = -curl\ (\mathbf{A})_{symm} \tag{4.2}$$

where $\mathbf{N}$ is incompatibility tensor (Kröner, 1959) and $\mathbf{A}$ is the GND density tensor[14]. Then, from Eq. (4.1) and (4.2) can be written as

$$curl\ curl\ \left(\mathbb{C}^{-1} : \mathbf{T}^*\right) = -curl\ (\mathbf{A})_{symm} \tag{4.3}$$

A solution to Eq. (4.3) in terms of the internal stresses arising from $\mathbf{A}$ may be obtained by introducing a second-order Beltrami stress function tensor $\boldsymbol{\psi}$ (Kröner, 1959)

$$\mathbf{T}^* = curl\ curl\ \left[2\mu\ \left(\boldsymbol{\psi} + \frac{\nu}{1-\nu}\ (tr\ \boldsymbol{\psi})\mathbf{I}\right)\right] \tag{4.4a}$$

[14] The GND density tensor can be written as $\mathbf{A} = curl\ (\mathbf{H}^p)$ where $\mathbf{H}^p$ is plastic displacement gradient (Gurtin, 2002). The negative and transpose of GND density tensor $\mathbf{A}$ is often referred to as Nye's tensor. (Nye, 1953; Arsenlis and Park, 1999)

$$\boldsymbol{\psi} = -\left(\int_V curl\,(G\mathbf{I})\mathbf{A}^T dV \right)_{symm}$$

where $\mathbf{I}$ is the second order identity tensor and G is a Green's function. The component form of Eq. (4.4) is

$$T^*_{ij} = \varepsilon_{kpi}\varepsilon_{lqj}\left[2\mu\left(\psi_{kl,pq} + \frac{\nu}{1-\nu}\,\psi_{mm,pq}\delta_{kl}\right)\right]$$

$$\psi_{kl} = -\frac{1}{2}\int_V \varepsilon_{krn}G_{,r}(A^T)_{ln}dV \; -\frac{1}{2}\int_V \varepsilon_{lrn}G_{,r}(A)_{kn}dV \tag{4.4b}$$

The elastic Green's function G in Eq. (4.4) depends on the dimensionality and geometry of the problem and may include appropriate terms accounting for particular boundary conditions. Kröner (1959) proposed a solution based on a Green's function for an elastic infinite medium, which gives internal stress fields due to GND density that do not account for image effects. However, in systems with finite boundaries these internal stresses need a correction in order to properly account for the long range dislocation-boundary interaction. It is this latter correction termed as image stress that is a focus of this work.

To incorporate the image stresses due to dislocation-boundary interaction using GND density fields, the internal stress tensor in Eq. (4.1) may be conceptually decomposed as

$$\mathbf{T}^* = \widetilde{\mathbf{T}} + \widehat{\mathbf{T}} \tag{4.5}$$

Figure 4.1 illustrates this conceptually for a body whose boundary is a free surface. The full problem (Fig. 4.1a) comprises a body $\mathcal{B}$ bounded by a finite boundary Ω subjected to external tractions $\boldsymbol{t}^{app}$. It is assumed that $\mathcal{B}$ hosts a smoothly varying GND density field $\mathbf{A}(\boldsymbol{r})$ where $\boldsymbol{r}$ is the position vector. The problem may be conceptually decomposed into two auxiliary problems:

(i) *external* stress fields in $\mathcal{B}$ subjected to $\boldsymbol{t}^{app}$ (Fig. 4.1b), and

(ii) *internal* stress fields in $\mathcal{B}$ in the presence of $\mathbf{A}$ (Fig. 4.1c). This problem may be further considered to be a superposition of two sub-problems: (ii-a) internal stress field $\widetilde{\mathbf{T}}$ in a dislocated body $\mathcal{B}$ embedded within an infinite medium $\mathcal{B}_\infty$ that gives rise to a spurious tractions $\boldsymbol{t}^{dis}$ (Fig. 4.1d), and (ii-b) internal stress fields $\widehat{\mathbf{T}}$ produced by application of equal and opposite tractions at the boundary Ω to eliminate $\boldsymbol{t}^{dis}$ (Fig. 4.1e).

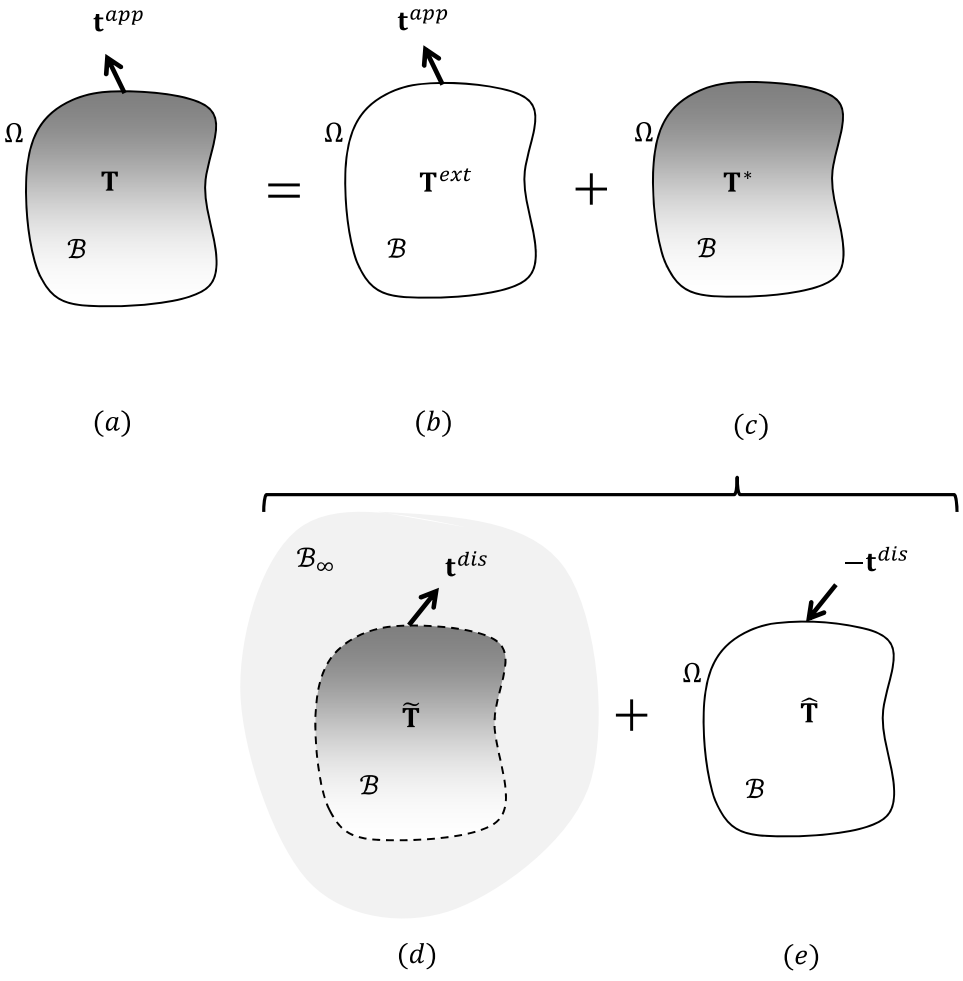

Figure 4.1. Decomposition of the internal stress problem for a specimen hosting a general GND density distribution. See text for discussion.

In accordance with the foregoing decomposition, here $\tilde{\mathbf{T}}$ is calculated using the elastic Green's function $\tilde{G}$ in the presence of defects (chapter 3) providing non-local stress fields due to GND density in an infinite medium, while the additional stress $\hat{\mathbf{T}}$ arising from the GND-boundary interaction needs an appropriate *corrective* kernel function $\hat{G}$. It is useful to mention that while $\tilde{G}$ is a function of only the spatial location of a point of interest in the medium from the dislocation, $\hat{G}$ is a function of both, the spatial position of a point from the dislocation and its proximity to the finite boundary. Further, the nature of $\hat{G}$ is expected to depend on the details of the boundary, e.g. a rigid/deformable interfaces, free surface and straight or arbitrary boundaries. Although a Green's function based treatment provides an elegant approach to such problems, at times it may be difficult to obtain an appropriate kernel function for $\hat{\mathbf{T}}$, e.g. an arbitrarily curved boundary. However, kernel functions have been derived for some fundamental cases accounting for finiteness of domains. Some of the examples involving single dislocations or dislocation arrays include geometries such as an elastic half-space (Head, 1953; Jagannadham and Marcinkowski, 1978; Lee and Dundurs, 1973; Lubarda and Kouris, 1996b; Ma and Lin, 2001) an infinitely long strip with two parallel free surfaces (Fotuhi and Fariborz, 2008; Moss and Hoover, 1978; Nabarro, 1978) , a straight, rigid interface separating two dissimilar half-spaces (Chou et al., 1975; Jagannadham and Marcinkowski, 1980). These kernel functions aim at providing fundamental solutions based on discrete dislocations to the problems of image fields, but may differ based on the conceptual appeal (e.g. image dislocation versus surface dislocations). In writing appropriate corrective stresses based on a continuum analog of dislocations (i.e. dislocation density), it is possible to use these fundamental solutions. The model problem discussed in this work is that of pure bending of a thin film, which is represented by a constant GND density tensor $\mathbf{A}$ and the corrective stress field $\hat{\mathbf{T}}$ is obtained by extending the basic construct developed by Fotuhi and Fariborz (2008) where the stress function is directly obtained using complex Fourier transformation

approach. Although the discussion is presented in detail for the model bending problem, it should be possible to construct similar solutions for other interfaces interacting with edge and screw GND densities using above-mentioned fundamental kernel functions or similar approaches (Cherednichenko, 2010; Vinogradov and Willis, 2008) .

4.3 Single Crystal Specimen under Plane-Strain Pure Bending: Role of Free Surfaces

This section presents an analytical formulation for the non-local internal stresses arising from GND density distribution including the effect of bounding surfaces through image stress fields. As mentioned in the preceding section, this is achieved by using the kernel functions derived by Fariborz and Fotuhi (2008) for a single dislocation in a bounded isotropic medium (Appendix A). We illustrate the problem as follows: consider an infinite domain of a crystal with a uniform GND density field **A**. A discrete equivalent of this problem is an infinite region containing infinitely long equally spaced arrays of dislocations with identical Burgers vector. It can be shown that for this arrangement the average stress field (integration of the stress fields arising from individual dislocations) over a given region that defines a mesoscopic length-scale is zero. This is because each individual dislocation *appears* to be at the center of the GND array and the individual stress fields cancel each other when integrated (Eq. (4.4)). On the other hand, if a part of such a *defective* (dislocated) region is embedded in a *pristine* (i.e. dislocation-free) material of same or different elastic properties, or is simply removed from the host material, a net internal stress must exist due to (a) finite spatial extent of the GND density, and (b) additional LRI between the GNDs and the boundaries. In the extreme situation of the region bounded by free surfaces, such a structure would represent a thin film that has been subjected to a uniform plastic curvature (Fig. 4.2). The extent over which the internal stress is felt away from the free boundaries should depend on the

internal length-scale corresponding to the long-range dislocation stress fields and the specimen dimensions.

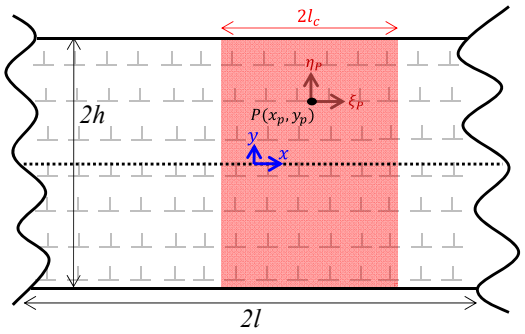

Figure 4.2. Schematic showing effective GND arrangement in a specimen under uniform curvature. The specimen thickness is $t = 2h$ and the GND density is described by the global (x, y) and local (ξ, η) coordinates.

For a plane strain condition in the z −direction, Eq. (4.5) can be written as (Fotuhi and Fariborz, 2008) in the component form as (see Appendix A)

$$
\begin{aligned}
T^*_{xx} &= \underbrace{\iint \left(A_{zx}\tilde{\chi}_{yyy} - A_{zy}\tilde{\chi}_{xyy}\right) d\eta d\xi}_{\tilde{T}_{xx}} + \underbrace{\iint \left(A_{zx}\hat{\chi}_{yyy} - A_{zy}\hat{\chi}_{xyy}\right) d\eta d\xi}_{\hat{T}_{xx}} \\
T^*_{yy} &= \underbrace{\iint \left(A_{zx}\tilde{\chi}_{yxx} - A_{zy}\tilde{\chi}_{xxx}\right) d\eta d\xi}_{\tilde{T}_{yy}} + \underbrace{\iint \left(A_{zx}\hat{\chi}_{yxx} - A_{zy}\hat{\chi}_{xxx}\right) d\eta d\xi}_{\hat{T}_{yy}} \\
T^*_{xy} &= \underbrace{\iint \left(A_{zx}\tilde{\chi}_{,yyx} - A_{zy}\tilde{\chi}_{xyx}\right) d\eta d\xi}_{\tilde{T}_{xy}} + \underbrace{\iint \left(A_{zx}\hat{\chi}_{yyx} - A_{zy}\hat{\chi}_{xyx}\right) d\eta d\xi}_{\hat{T}_{xy}}
\end{aligned}
\tag{4.6}
$$

where A_{zx} and A_{zy} are the components of **A** representing dislocations with line length in the z direction and Burgers vector along x and y directions, respectively. The $\tilde{\chi}$ and $\hat{\chi}$ are the kernel functions representing the stress fields of an edge dislocation with unit Burgers vector in an infinite medium and its corresponding correction due to traction-free boundaries, respectively (given in Appendix A). In Eq. (4.6), while the $\tilde{(\ )}$ field is translationally invariant, i.e. it does not carry the information about the absolute

position of a point from the free surface, this unaccounted feature is incorporated into the overall expression by the $\hat{(\,)}$ field which embeds the relevant spatial information.

Without losing the essential features in Eq. (4.6), we consider a thin film with uniform GND density subjected to external bending moment under plane strain condition as a model problem. Consider a structure of length $2l$ (x −direction) and thickness $t = 2h$ (y −direction) with a plane-strain condition in the z –direction. Assume that the structure is subjected to pure bending in the $x - y$ plane (Fig. 4.2). The x −axis lies at the neutral plane and the y −coordinate is measured from this neutral plane. A typical point P in the continuum is located at x_P, y_p from the neutral plane and carries a local coordinate system (ξ_P, η_P) with it. Further, the structure is assumed to be sufficiently long so that the x end faces (i.e. loaded faces) and the out-of-plane faces do not contribute to image stress fields. The y end faces constitute the thickness t of the structure. Since the structure is under pure bending, the in-plane internal shear stress T^*_{xy} must be zero and only the normal components of the internal stress tensor (Eq. (4.6)) exist. Assuming that the radius of curvature of the structure is much larger than its thickness, the GND density can be considered to be uniform over the entire thickness.

Note that in Eq. (4.6) the integration is performed over an area, which implies that the internal stress at a given point, say $P(x_p, y_p)$, is influenced by the GND densities and their stress-fields in its finite neighborhood. Such a non-local representation allows introducing an internal length-scale l_c into the problem (Evers et al., 2004; Gerken and Dawson, 2008). This length-scale is problem-dependent and requires some discussion. This length-scale is problem-dependent and requires some discussion. We return to the issue of the microscopic underpinnings of such an internal length-scale later when we compare our results with experiments, but briefly discuss it here within the context of the geometry under consideration. If h is much larger than l_c, then in the presence of a

uniform GND density the surfaces would influence regions only in its proximity $|h - l_c| \leq |y| \leq |h|$.[15] Therefore, in presence of uniform distribution of GNDs, $\tilde{T}_{xx}$ only felt in a thin surface layer with thickness of l_c due to the finiteness of dislocation distribution. Similarly $\hat{T}_{xx}$ significantly influence the internal stress in the surface layer due to image effect. Therefore, overall the internal stress variation remain zero away the neutral plane before becoming non-zero closer to the surfaces. Note that image field $\hat{T}_{xx}$ has small contribution in region $|y| \leq |h - l_c|$.). Each component of internal stresses is depicted in Figure 4.3 for $L = 0.2$.

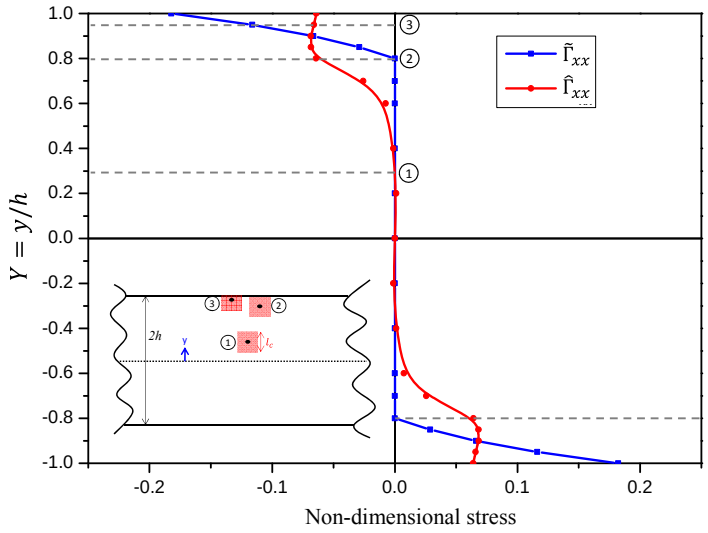

Figure 4.3. Internal stress components variation across thickness for $L = 0.2$ ($h = 5l_c$).

[15] Based on the DD simulations, from a dislocation-surface interaction viewpoint, perhaps it would be more appropriate to assume a dislocation-free zone (DFZ) of a fixed thickness in the proximity of a surface, irrespective of the specimen thickness (Cleveringa et al,. 1999). Such an assumption would introduce an additional length-scale into the formulation. However, we do not consider this aspect in the current work.

The overall internal stress variation across beam thickness is shown in Figure 4.4 for different value of L. It can be seen that internal stress decrease with decreasing L which means increasing specimen thickness where l_c is constant. In the current work, the internal stress arises from interaction of GNDs among themselves and with free surfaces which provide internal stresses even in case of uniform distribution of GNDs. Just recently, (Hayashi et al., 2011) presented similar internal stress profiles in relatively thick (compared to their chosen internal length-scale) beams under pure bending. They employed a higher-order slip gradient theory that induces GND density gradients owing to a null GND density b.c. at free surfaces.

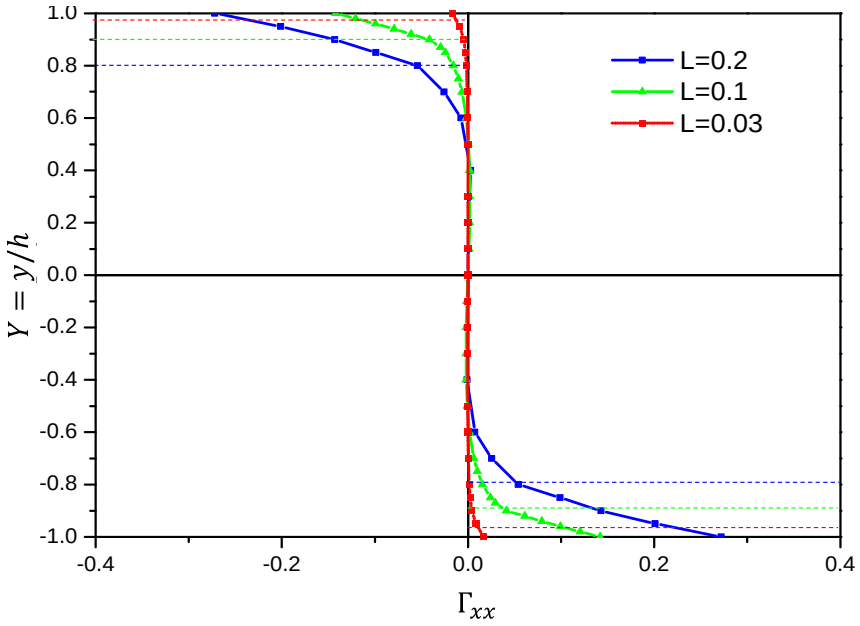

Figure 4.4. Variation of normalized internal stress Γ_{xx} along the normalized specimen thickness Y for different values of normalized internal length-scale L.

However, they did not explicitly account for the GND-surface LRI that cause image effects. However, this theory account for internal stress arise from GND interaction in an infinite medium in presence of non-uniform GND distribution and consequently image effects due to free surfaces are not taken into account. In addition, finite boundaries are not explicitly considered in this group of higher order theories and so they are not

capable to predict the internal stress for area near the finite boundaries. Therefore, for specimen which thickness is comparable or smaller than length scale parameter, finite boundaries effect and corresponding image effect have to be considered. As such, the effect of the internal stress on the overall response may be negligibly small. Very recently, (Hayashi et al., 2011) presented similar internal stress profiles in relatively thick (compared to their chosen internal length-scale) beams under pure bending. They employed a higher-order slip gradient theory that induces GND density gradients owing to a null GND density b.c. at the free surfaces. However, they did not explicitly account for the GND-surface LRI that cause image effects.

For cases with $h \leq l_c$ the entire thickness may participate in determining the stress field at every point along the thickness. It is this latter scenario that exhibits interesting length-scale dependent characteristics and is the main focus of this work. Consequently, we perform the integration (Eq. (4.6)) in the η direction over the entire thickness$t$. As for the $\xi -$ direction, at least in the present scenario of $l \gg h$, it would be reasonable to assume that $l_c \ll l$. Therefore, in the $\xi -$ direction, we may restrict our attention over a distance l_c on either sides of a typical point P (fig 4.2). As shown later, l_c may be related to the correlation distance between dislocations in a dislocated network (Zaiser and Seeger (2002) and Mughrabi (1975, 2004)). Note that if the structure has a finite length such that $l \approx h$ the effects due to x end faces must also be taken into account; this case is not considered here.

Returning to the case of pure bending about z-axis, A_{zx} is the only non-zero component of the GND density tensor and it is uniform over entire structure. The DDD simulations of Yefimov et al. (2004a) and Motz et al. (2008) also indicate a near-uniform distribution of dislocations over much of the beam thickness, except in the proximity of the surfaces where the spacing between individual dislocations on a slip-plane slightly increases. In this paper, the GND density is assumed to be uniform over entire beam

structure. Specializing Eq. (4.6) for pure bending, we obtain after re-arrangement and normalization

$$T_{xx}^{*} = h^2 \underbrace{\int_{-L}^{L}\int_{-1-Y}^{1-Y} \left(A_{zx}\tilde{\chi}_{yyy}\right) dMdN}_{\tilde{T}_{xx}} + h^2 \underbrace{\int_{-L}^{L}\int_{-1-Y}^{1-Y} \left(A_{zx}\hat{\chi}_{yyy}\right) dMdN}_{\hat{T}_{xx}}$$

$$T_{yy}^{*} = h^2 \underbrace{\int_{-L}^{L}\int_{-1-Y}^{1-Y} \left(A_{zx}\tilde{\chi}_{yxx}\right) dMdN}_{\tilde{T}_{yy}} + h^2 \underbrace{\int_{-L}^{L}\int_{-1-Y}^{1-Y} \left(A_{zx}\hat{\chi}_{yxx}\right) dMdN}_{\hat{T}_{yy}} \tag{4.7}$$

where $Y = y/h, M = \xi/h, N = \eta/h$ and $L = l_c/h$.

Since $\tilde{\chi}_{yyx}$ and $\hat{\chi}_{yyx}$ are odd functions of M (see Appendix A), T_{xy}^{*} vanishes automatically and consistently satisfies the shear traction boundary condition at $y = \pm h$. A similar condition for T_{yy}^{*} requires that it must also vanish at $y = \pm h$. From Eqs. (4.7b), the $\tilde{(\,)}$ and $\hat{(\,)}$ components of T_{yy}^{*} are

$$\tilde{T}_{yy} = \mu A_{zx} h \underbrace{\int_{-L}^{L}\int_{-1-Y}^{1-Y} \frac{1}{2\pi(1-\nu)}\left(\frac{N(M^2-N^2)}{(M^2+N^2)^2}\right) dMdN}_{\tilde{\Gamma}_{yy}}$$

$$\hat{T}_{yy} = \mu A_{zx} h \underbrace{\int_{-L}^{L}\int_{-1-Y}^{1-Y}\int_{0}^{\infty} \left[f_{yxx}(M,N,Y,\alpha) - g_{yxx}(M,N,\alpha)\right] d\alpha\, dMdN}_{\hat{\Gamma}_{yy}} \tag{4.8}$$

where $\tilde{\Gamma}_{yy}$ and $\hat{\Gamma}_{yy}$ are the non-dimensional stresses that depend on Y and L, and α is a non-dimensional spatial frequency coefficient that appears in the complex Fourier transform solution of the $(\hat{\ })$ stress function (Fotuhi and Fariborz, 2008). Appendix A gives detailed account of the functions involved in Eqs. 4.8b and 4.9b. Figure 4.5 shows the variation of $\tilde{\Gamma}_{yy}$ and $\hat{\Gamma}_{yy}$ over the beam thickness. It can be seen through these plots that not only does T_{yy}^{*} vanish at the boundaries, it also vanishes over the entire beam thickness as the magnitude as the distribution of $\hat{T}_{yy}$ exactly equal to and opposite of $\tilde{T}_{yy}$, independent of L.

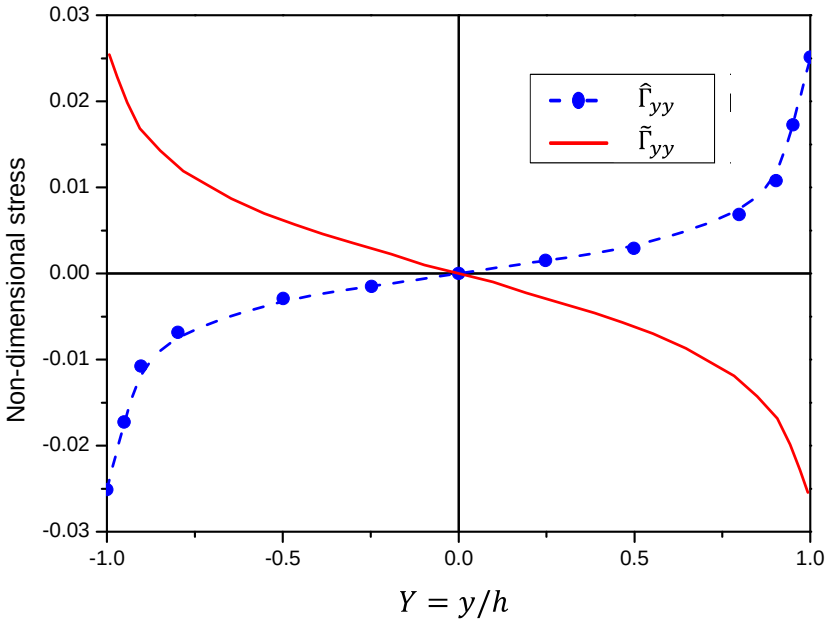

Figure 4.5. Variation of non-dimensional stresses in $\boldsymbol{y}$ direction ($\tilde{\Gamma}_{yy}$ and $\hat{\Gamma}_{yy}$) over beam thickness for a given normalized internal length-scale $L(=10)$ (Eq. 4.8a,b). Note that the components are equal and opposite resulting in overall $T^*_{yy} = 0$.

Therefore, the only non-zero internal stress is T^*_{xx} that reflects the curvature due to the uniform GND density distribution. From Eqs. (4.8), the $\tilde{(\cdot)}$ and $\hat{(\cdot)}$ components of T^*_{xx} read as follows

$$\begin{aligned} \tilde{T}_{xx} &= -\mu A_{zx} h \underbrace{\int_{-L}^{L}\int_{-1-Y}^{1-Y} \frac{1}{2\pi(1-\nu)}\left(\frac{N(3M^2+N^2)}{(M^2+N^2)^2}\right) dM dN}_{\tilde{\Gamma}_{xx}} \\ \hat{T}_{xx} &= \mu A_{zx} h \underbrace{\int_{-L}^{L}\int_{-1-Y}^{1-Y}\int_{0}^{\infty} \left[f_{yyy}(M,N,Y,\alpha) - g_{yyy}(M,N,\alpha)\right] d\alpha\, dM dN}_{\hat{\Gamma}_{xx}} \end{aligned} \tag{4.9}$$

In Eqs. (4.9) the non-zero GND density component A_{zx} pops out of the integral as it is independent of the spatial coordinates for the present problem. In general, the GND density components should be retained inside the integral if they vary spatially. In that case, the internal stresses would also be induced by smooth spatial GND density gradients.

It is informative to note that Eq. (4.8a) and (4.9a) are the averaged solutions of the Volterra-based result for a two-dimensional array of GNDs distributed over $h \times 2l_c$ embedded in an elastically isotropic medium. Thus, internal stress exists in this region that is delineated by the finite extent of the GND density field embedded in a medium (Eq. 4.9a). It is further modulated by the image stress fields due to dislocation - free surface interactions by the additional term (Eq. 4.9b). Equation (4.9a) can be integrated analytically and Fig. 4.6 shows the variation of $\tilde{\Gamma}_{xx}$ with Y and L. For a fixed Y, $\tilde{\Gamma}_{xx}$ varies nonlinearly with L. Specifically, $\tilde{\Gamma}_{xx} \to 0$ as $L \to 0$ and asymptotes to a constant value for $L \gg 1$.

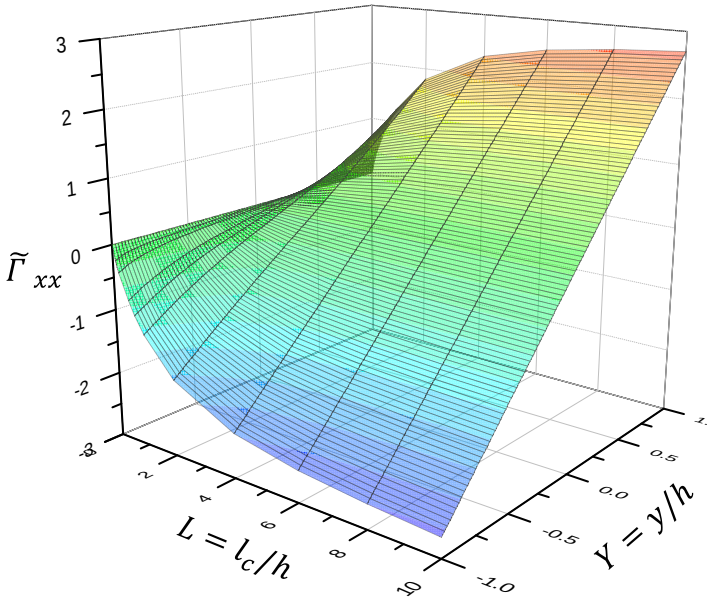

Figure 4.6. Variation of $\tilde{\Gamma}_{xx}$ with Y and L. (See Eq. 4.10a)

On the other hand, for a given L, $\tilde{\Gamma}_{xx}$ varies linearly over the thickness and changes from compressive to tensile about the neutral axis consistent with the notion of bending stresses. This latter variation compares well qualitatively and quantitatively with the DD

simulation results of (Cleveringa et al., 1999) for a single crystal under pure bending, which also shows a linear variation of the baseline stress field (i.e. before correcting for the image fields) across the beam thickness[16]. Unlike the $\tilde{\Gamma}_{xx}$ calculation, the $\hat{\Gamma}_{xx}$ variation (Eq. 4.9b) over the thickness requires numerical integration and is performed using Gauss-Laguerre quadrature (Press et al., 1992) [17]. Appendix B provides the detailed procedure of the numerical integration and related convergence study. As shown in Fig. 4.7a and b, $\hat{\Gamma}_{xx}$ variation with Y and L is qualitatively similar to that of $\tilde{\Gamma}_{xx}$.

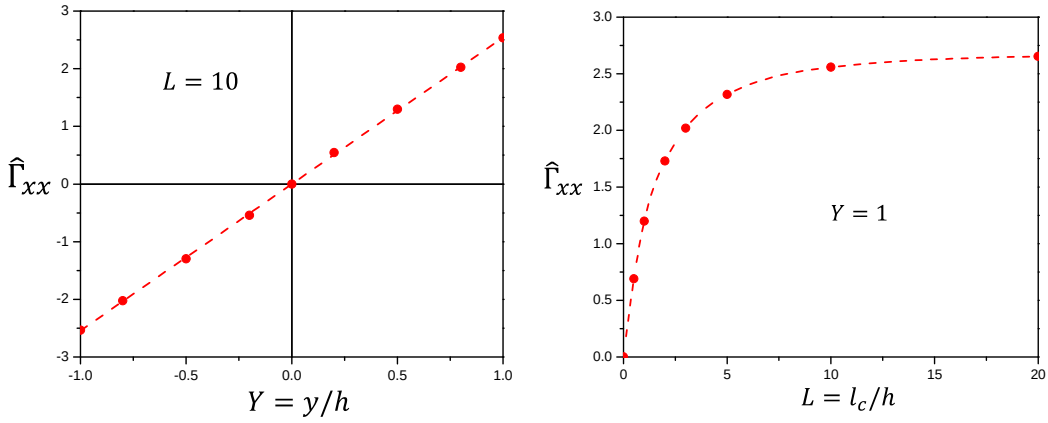

(a) (b)

Figure 4.7. Variation of $\hat{\Gamma}_{xx}$ respect to (a) Y at L=10 and (b) L at Y=1. (See Eq. 4.10b)

From Eqs. (4.9a,b), the overall internal stress T^*_{xx} can be written as

$$T^*_{xx} = -\mu A_{zx} h \Gamma_{xx} \tag{4.10}$$

---

[16] Fig 7 in Cleveringa's work (1999) shows that the $\tilde{(\,)}$ stress magnitude linearly varies from 0 MPa (neutral axis) to ± 600 MPa ($\pm h$) for a beam with $t = 4\ \mu m$ and $l = 12\ \mu m$ with $\mu = 27\ GPa$ subjected to a plastic rotation of 0.013 radians. We obtain the same values by substituting these parameters in Eq. (4.9a).

[17] Apart from this, in Eq. (4.9a, b), the Poisson's ratio ν cannot be isolated from $\hat{(\,)}$ components. We set $\nu = 0.33$ for all the calculations.

where $\Gamma_{xx} = \tilde{\Gamma}_{xx} - \hat{\Gamma}_{xx}$ (Fig 4.8). The value of Γ_{xx} asymptotes to ~1/3 as $L(= l_c/h)$ tends to infinity, which indicates that the internal stress saturates in the cases where the specimen thickness is much smaller compared to the internal length-scale. Note that L could vary because of changes in h, l_c, or both. An important question is: should L change with h, and if so, how? In other words, should l_c remain fixed, increase or decrease with h? If l_c changes linearly with h then $L =$ constant and therefore, $\Gamma_{xx} =$ constant (Fig. 4.8). In such a scenario, although the internal stress is non-zero it is not length-scale dependent. On the other hand, decreasing (increasing) l_c with increasing (decreasing) h indicates that the internal stress will also decrease (increase). This is also true if $l_c =$ constant. Thus, except for the constant L case the remaining possibilities provide the trend expected from a length-scale dependent internal stress theory. As we show later in the paper, comparing the predicted results with experiments suggests that the possibility of l_c increasing with decreasing h is a plausible scenario.

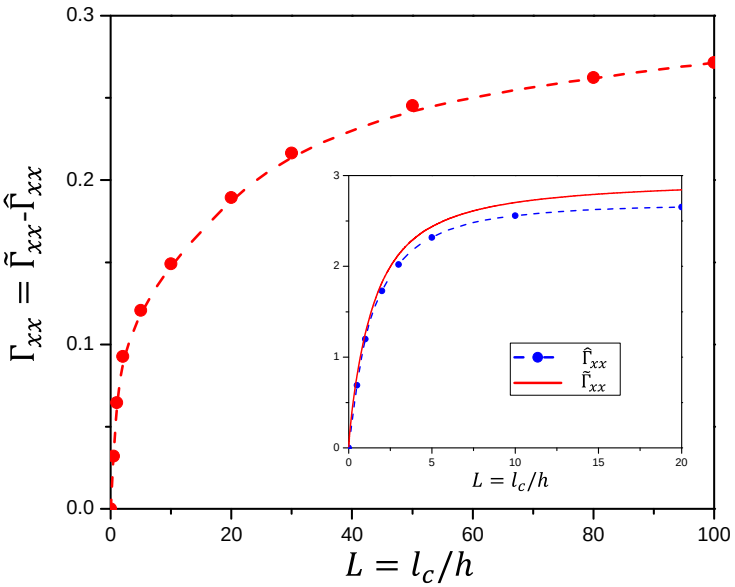

Figure 4.8. Variation of the normalized total internal stress Γ_{xx} with normalized internal length-scale L at specimen surface ($Y = 1$).

Equation (4.10) brings to fore a noteworthy feature in that the length-scale dependent internal stress shows an explicit dependence on the magnitude of GND density. This is in contrast to most continuum formulations for length-scale dependent internal stresses that predict a non-zero internal stress only if GND density gradient, rather than a non-zero GND density, is present (Evers et al., 2004; Gerken and Dawson, 2008; Gurtin, 2002). Thus, the length-scale dependent internal stresses may exist not only because of a non-uniform GND density but also because of the image fields and the latter may cause internal stresses even if the GND density is nominally uniform over a given finite region. From this viewpoint, the finite spatial extent of a uniform GND density field delineated by two free surfaces considered in this work serves as a simple, yet insightful example to further probe the internal stress characteristics in the presence of image fields.

Before discussing the results of the particular model problem, it is useful to note that the decomposition of the real problem in Fig. 4.1 and the treatment explicitly presented for the bending problem bears some semblance with the superposition technique used in DDP approaches (Van der Giessen and Needleman (1995)) (although there are some important differences, discussed as following). Using this broad analogy, the overall traction $\mathbf{t}(\mathbf{n})$ at a free boundary with unit normal $\mathbf{n}$ may be written as (Fig. 4.1)

$$\mathbf{t}(\mathbf{n}) = \left(\mathbf{T}^{ext} + \widetilde{\mathbf{T}} + \widehat{\mathbf{T}}\right)\mathbf{n} \tag{4.11}$$

with $\tilde{\mathbf{t}} = \widetilde{\mathbf{T}}\mathbf{n}$ being the *micro-traction* corresponding to the infinite medium solution (Fig. 4.1d) and $\hat{\mathbf{t}} = \widehat{\mathbf{T}}\mathbf{n}$ being the corrective traction applied to remove the spurious traction at the free surfaces arising from $\tilde{(\cdot)}$ fields (Fig. 4.1e). Thus, from a superposition viewpoint the following tractions b.c.'s conditions should be satisfied

$$\mathbf{t}^{ext}(\mathbf{n}) = \mathbf{T}^{ext}\mathbf{n}$$
$$\mathbf{t}^{*}(\mathbf{n}) = (\tilde{\mathbf{T}} + \hat{\mathbf{T}})\mathbf{n} \tag{4.12}$$

For a general geometry with prescribed *macroscopic* kinematic and traction b.c.'s, the distribution of $\mathbf{A}$ can be obtained from slip gradients. The tractions $\tilde{\mathbf{t}}(\mathbf{n})$ arising from the infinite medium assumption (Fig. 4.1d) may be calculated either analytically or numerically. Then, the stress fields arising from corrective image tractions $\hat{\mathbf{t}}(\mathbf{n}) = -\tilde{\mathbf{t}}(\mathbf{n})$ $(\because \mathbf{t}^{*}(\mathbf{n}) = \mathbf{0})$ applied at the free boundaries may be obtained by solving the corresponding boundary-value problem using FE method. The superposition of the two solutions (Fig. 4.1c) together with the stress fields from prescribed b.c.'s (Fig. 4.1b) would then provide the overall solution.

As shown in chapter 3, the internal stress $\mathbf{T}^{*}$may be compared to Gurtin's micro-stress $\boldsymbol{\xi}^{\alpha}$ that appears as an additional higher-order quantity on a slip system α that needs to be prescribed at the boundaries. On a traction-free boundary (Gurtin, 2002)

$$\boldsymbol{\xi}^{\alpha} \cdot \mathbf{n} = \mathbf{0} \tag{4.13}$$

which indicates that the component of the micro-stress along the normal to the boundary should be zero. Based on the present work, Eq. (4.13) may be expanded as

$$\boldsymbol{\xi}^{\boldsymbol{\alpha}} \cdot \mathbf{n} = (\tilde{\boldsymbol{\xi}}^{\alpha} + \hat{\boldsymbol{\xi}}^{\alpha}) \cdot \mathbf{n} = \mathbf{0} \tag{4.14}$$

where $\tilde{(\cdot)}$ and $\hat{(\cdot)}$ fields represent the appropriate micro-stress fields. The scalar components arising from the dot products $\tilde{\xi}^{\alpha} = \tilde{\boldsymbol{\xi}}^{\boldsymbol{\alpha}} \cdot \mathbf{n}$ and $\hat{\xi}^{\alpha} = \hat{\boldsymbol{\xi}}^{\boldsymbol{\alpha}} \cdot \mathbf{n}$ are the projections of the micro-traction acting normal to the boundary, so that we may obtain from all slip systems

$$\sum_{i=1}^{\alpha} \tilde{\xi}^{i} = -\sum_{i=1}^{\alpha} \hat{\xi}^{i} \tag{4.15}$$

Note that Eq. (4.15) is very similar to the one arising from Eq. (4.12). Thus, the micro-stress construed as net Peach-Koehler (P-K) force density (Gurtin, 2002)

manifests as image stress at a traction-free boundary. This can also be ascertained by noting the similarity between the internal stress due to a GND density and the P-K force acting on a discrete dislocation in the presence of external tractions, other dislocations and boundaries (Lubarda, 2006)

$$\mathbf{p}^i = -\mathbf{l}^i \times \left(\mathbf{T}^{ext} + \sum_j \widehat{\mathbf{T}}_j + \sum_{j \neq i} \widetilde{\mathbf{T}}_j \right) \mathbf{b}^i \tag{4.16}$$

where $\mathbf{p}^i$ is the Peach-Koehler force vector on i^{th} dislocation, $\mathbf{b}^i$ is the Burgers vector, $\mathbf{l}^i$ is its unit tangent vector and $\mathbf{T}^{ext}$ is the applied stress. $\widetilde{\mathbf{T}}_j$ is the internal stress tensor from the j^{th} on the i^{th} dislocation (dislocation-dislocation interaction) in an infinite medium and $\widehat{\mathbf{T}}_j$ is the image field contribution arising from the dislocation-boundary interaction of the j^{th} dislocation to the P-K force on the i^{th} dislocation. In our opinion, displacement-based formulations with slip gradients (or GND densities) as degrees of freedom (e.g. Kuroda and Tvergaard, 2009; Hayashi, et al, 2011) do not clearly connect the null GND density with the higher-order natural b.c.'s at free surfaces. Their equivalent representation as null GND density seems to account only for the $(\widetilde{\cdot})$ term in Eq. (4.14), because the internal stress expressions are based on infinite medium assumption that discount the $(\widehat{\cdot})$ contribution.

Although, the foregoing exposition is conceptually analogous to DDP approaches, it is useful to note at least a few important differences between the two approaches. First, unlike the DDP approach that models dislocations as discrete elastic singularities, the present setup treats them as a continuous density field. Consequently, the stress fields are expected to be smooth compared to the DDP results as they smear out fluctuations at a finer-scale. Second, by virtue of integration, only the information regarding the net Burgers vector is retained. This results in accounting only for the contributions from the GND density and the influence due to SSDs is lost. In comparison, the DDP approaches explicitly account for both LRI and SRI contributions arising from SSDs and GNDs

(Cleveringa et al., 1999; Guruprasad and Benzerga, 2008; Yefimov and Van der Giessen, 2005). The SRI interactions from SSDs must be incorporated via phenomenological constitutive prescription. Notwithstanding these differences, the present homogenized approach still enables making connections with its counterpart in the DDP approach. For example, it provides a possible description of the length-scale adopted in coarse-grained continuum approaches. Likewise, as just discussed it also enables interpreting the higher-order boundary conditions that appear in coarse-grained approaches (Bayley et al., 2006; Gurtin, 2002; Hayashi et al., 2011).

With this background, the model is extended to crystal plasticity framework to investigate the pure bending problem with reference to length-scale effects under monotonic and cyclic loading. The stresses due to the externally applied bending moment superpose with the internal stresses induced by the uniform GND density while accounting for the image stress fields arising from the GND-surface interaction to produce an overall length-scale dependent response. The results are compared with the micro-beam bending experiments and DD simulations (Cleveringa et al., 1999; Motz et al., 2005; Motz et al., 2008) and in doing so, an attempt is made to connect the internal material length-scale with microstructural underpinnings that define plastic deformation.

4.4 Length-scale Dependent Pure Bending Response of Single Crystals

In this section, we analyze the length-scale dependent behavior of an elastically isotropic single crystal beam under pure bending. We adopt a nonlocal plastic constitutive description for each slip system within the single crystal that is augmented by the GND effects. The GND-induced strengthening may be categorized as that arising from: (i) dislocation-dislocation intersections, termed as short-range interactions (SRI),

and is represented via Taylor hardening model for the slip system strengthening (Han et al., 2005a) and (ii) dislocation-dislocation and dislocation-boundary LRI that manifest as internal stresses, described in the preceding sections. For simplicity, we assume that the single crystal in this plane strain setup is oriented for symmetric double slip with an angle $\pm\theta$ respect to beam axis (Figure 4.2) and is subjected to total curvature κ. As mentioned earlier, we also assume $l/h \gg 1$ and therefore, ignore the image effects from the end faces in the x −direction. For a single crystal that is elastically isotropic and plastically incompressible, the relevant plastic strains under plane-strain pure bending may be written using the classical Kirchhoff beam theory (Han et al., 2005b)

$$E^p_{xx} = -E^p_{yy} = -\kappa^p y, \qquad E^p_{xy} = 0. \tag{4.17}$$

where $\kappa^p = \kappa - \kappa^e$ is mean plastic beam curvature and κ^e is the elastic curvature obtained as the current stress divided by the elastic modulus. In crystallographic terms, the plastic strain tensor $\mathbf{E}^p = \sum_\alpha \gamma^\alpha (\mathbf{s}^\alpha \otimes \mathbf{m}^\alpha)_{sym}$, where γ^α is the plastic slip on α^{th} slip system defined by the slip direction s^α and slip-plane normal m^α. For the symmetric double slip, the plastic slip on each slip system is

$$\gamma^1 = -\gamma^2 = \bar{\gamma} = \frac{-\kappa^p y}{2S} \tag{4.18}$$

where $S = \sin\theta \cos\theta$ is the Schmid factor. The crystallographic description of the GND density tensor is $\mathbf{A} = \sum_\alpha (\nabla\gamma^\alpha \times \mathbf{m}^\alpha) \otimes \mathbf{s}^\alpha$ where $\nabla(.) = \frac{\partial(.)}{\partial s^\alpha}$ (Han et al., 2005b). Therefore, GND density tensor is obtained as[18]

[18] The transpose of GND density tensor **A** is often referred to as Nye's tensor. (Nye, 1953; Arsenlis and Park, 1999)

$$\mathbf{A} = \begin{bmatrix} 0 & 0 & 0 \\ 0 & 0 & 0 \\ -\kappa^p & 0 & 0 \end{bmatrix} \tag{4.19}$$

It can be seen that the only non-zero GND density component is A_{zx}, which represents the density of GNDs with Burgers vector in the x −direction and dislocation line in the z −direction. In the rate-independent limit the following condition results in plastic flow

$$\tau^{ext} + \tau^* = g_t \tag{4.20}$$

where τ^{ext} and $\tau^* = 2\mu\bar{\gamma}\Gamma_{xx}S^2$are resolved shear components of the externally applied and internally developed stresses, respectively and g_t is the current total slip system hardness that develops through dislocation-dislocation SRI. Proposals to account for SSD and GND induced slip system hardening include Taylor model (Nix and Gao, 1998)and its variant e.g. $g_t \sim (f(\gamma)^r + l(\nabla\gamma)^r)^{1/r}$ (Fleck et al., 1994; Evans and Hutchinson, 2009) which has a more generalized form $g_t \sim (f(\gamma)^p + l(\nabla\gamma)^q)^{1/r}$ (Abu Al-Rub, 2004; Nix and Gao, 1998; Voyiadjis and Al-Rub, 2005) where γ is equivalently the total plastic strain, l is an appropriate length-scale parameter and p, q and r are fit parameters. The hardening function $f(\gamma)$ embeds information regarding the conventional size-independent strain hardening due to SSDs. Although not the focus of this paper, a notable point is that there seems to be no consensus in the precise range of l; it appears to depend on the details of the underlying formulation (Evans and Hutchinson, 2009; Hussein et al., 2008; Nix and Gao, 1998; Voyiadjis and Al-Rub, 2005). Note that with appropriate choice of parameters p, q and r (with $p = r = 2$ and $q = 1$) one retrieves the Taylor hardening model (Nix and Gao, 1998). Nonetheless, as our focus is primarily on the internal stresses arising from image effects due to free surfaces, we defer further the discussion on this matter to future investigations and choose a simple Taylor-like hardening approximation here

$$g_t^\alpha = g_0^\alpha \sqrt{\left(1 + \sum_{\alpha=1}^{n} C_0 |\gamma^\alpha|\right)^2 + \left(l_g \, \eta_g^\alpha\right)} \tag{4.21}$$

where g_0^α is the initial slip resistance for slip system α, C_0 is the ratio of hardening modulus over the initial resistance and $|.|$ indicates the magnitude of plastic slip. The second term inside the square root models the length-scale dependent SRI through slip gradients $\nabla\gamma^\alpha$ on individual slip systems that are associated an effective measure of the GND density on slip system α, $\eta_g^\alpha = |\mathbf{A} \times (\mathbf{m}^\alpha \otimes \mathbf{s}^\alpha)|$ (Han et al, 2005a). Substituting Eq. (4.21) into Eq. (4.20) and applying appropriate transformation, we obtain

$$T_{xx} = -\frac{1}{S}\left(g_0 + \underbrace{\left[\zeta \mu b \sqrt{2C\frac{|\kappa^p y|}{2S} + \frac{|\kappa^p \cos\theta|}{b}}\right]}_{SRI} \right) sgn(\kappa^p y) - \underbrace{\mu \kappa^p y \Gamma_{xx}}_{LRI} \tag{4.22}$$

Equation (4.22) gives the macroscopic stress-plastic strain relationship for the problem that accounts for length-scale effects owing to (a) SRI through slip hardening, and (b) LRI through the internal stress. Notably, the internal stress (the LRI term in Eq. (4.22)) now incorporates the image effects arising from the two bounding surfaces. The corresponding length-scale l_c is introduced through the non-dimensional internal stress Γ_{xx}.

In the subsequent sections, we present quantitative results and discuss the length-scale dependent strengthening arising from the LR and SR interactions in the presence of free surfaces under monotonic and cyclic pure bending. We also compare the predicted results with recent micro-beam bending experiments. Through this comparison, we postulate that the characteristic internal length-scale associated with internal stresses may not be a fixed parameter but could be related to a microstructural parameter that may itself vary with the characteristic structural dimension. Finally, we

discuss length-scale dependent Bauschinger effect in the presence of free surfaces. Unless otherwise mentioned, we set $C_0 = l_g = 0$.

4.4.1 Monotonic response

To begin with, we investigate the variation of length-scale dependent internal stress (Eq. (4.22)). To highlight its role in the overall response, we suppress both the SRI contributions, by setting $C = 0$ (no SSD hardening) and $l_g = 0$ (no GND-induced Taylor hardening), implying a non-hardening type material. With the parameters in Table 4-1, and symmetric double slip systems with angles = $\pm 45^{\circ}$ Figure 4.9a shows normalized overall stress Γ_{xx} variation across the normalized specimen thickness Y $(= y/h)$ for different values of normalized internal length-scale L $(= l_c/h)$.

Table 4-1. Parameters used in the analytical model for internal stress and prediction of beam behavior response.

Parameter	Value	Unit
Taylor factor (ζ)	0.3	-
Shear modulus (μ)	47×10^3	MPa
Burgers vector (b)	0.255	nm
Critical slip resistance (g_0)	60	MPa

The benchmark solution (blue dashed curve) is for the same problem but without the length-scale dependent internal stress (classical crystal plasticity – CCP). As expected the CCP response results in a constant stress over the specimen thickness because the only contribution comes from g_0, which is constant over the thickness (Eq. (4.22)). However, with LRI included (Eq. (4.22)) the overall stress varies linearly along the thickness. Further, this linear variation becomes stronger with increasing L, i.e. with increasing l_c and/ or decreasing h. An important aspect that should be highlighted is the

distribution of the internal stress over the specimen thickness. In Figure 4.9a, for a given L the internal stress is simply the difference between the inclined line for that L and the dashed line (Eq. 4.22). The plot indicates that the internal stress exists over the entire specimen thickness for the values considered in this example. This is a direct consequence of the assumption $h \leq l_c$ in writing the integration limits to obtain the internal stress (Eq. 4.7). In the case where $h > l_c$, one may expect the internal stress to decay to zero some distance away from the specimen surfaces. For $h \gg l_c$, the internal stress will exist only as a boundary layer effect and be zero over much of the specimen thickness as shown in previous sections. Very recently, (Hayashi et al., 2011) showed that non-zero internal stresses exist only close to the surface in their specimens with thicknesses in the range of 25-50 μm, whereas away from them the internal stresses decay to zero. This is expected given that the length-scale corresponding to the internal stresses is postulated to be in the range of few microns.

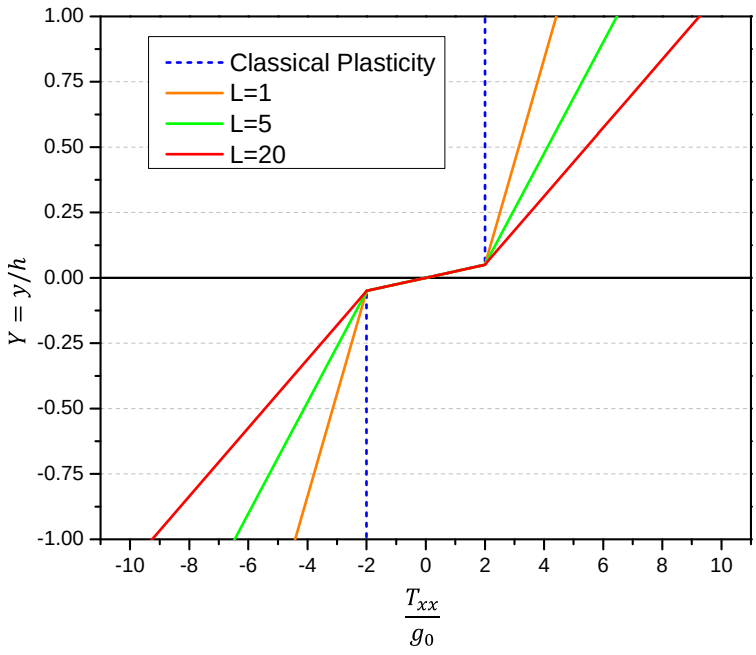

(a)

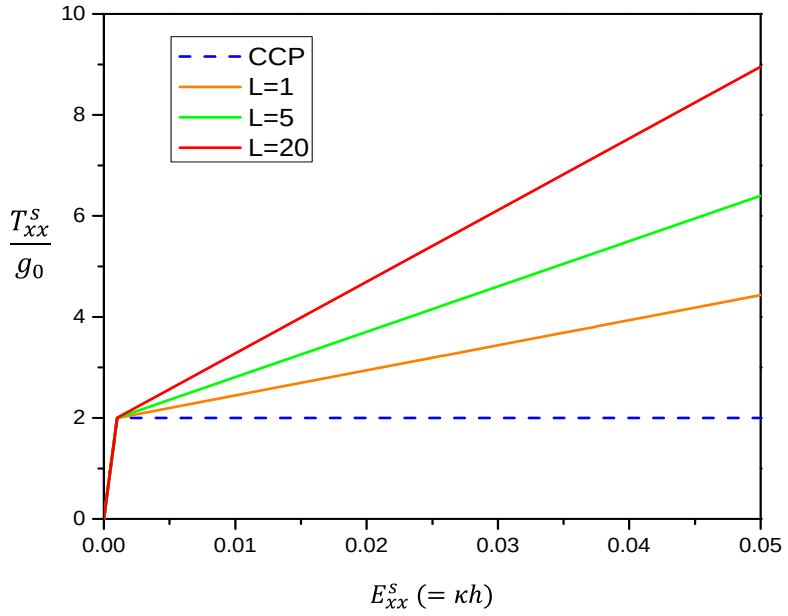

(b)

Figure 4.9. a) Normalized stress variation across normalized specimen thickness $Y = y/h$ at $E^s_{xx} = 0.05$, b) Stress-strain curves at specimen surfaces ($Y = 1$) for different values of $L = l_c/h$.

Since the overall stress varies across the specimen thickness, we consider the stress-strain relationship at the beam surface ($y = h$) (Eq. (4.22)) to describe the overall response. Figure 4.9b depicts the length-scale dependent $T^s_{xx} - E^s_{xx}$ relationship where $E^s_{xx} = (E^s_{xx})_e + \kappa^p h$ is the total surface strain and $(E^s_{xx})_e = T^s_{xx}/2\mu\ (1+\nu)$ is the surface elastic strain. For a fixed l_c the internal stress induces increasingly stronger hardening as specimen thickness t decreases even under pure curvature conditions.

Conversely, for a fixed t, the internal stress increases with increasing l_c. From the figure 4.10 it can be seen that the LRI contribution increases as $\sim 1/t$, which is a natural outcome of the present internal stress formulation.

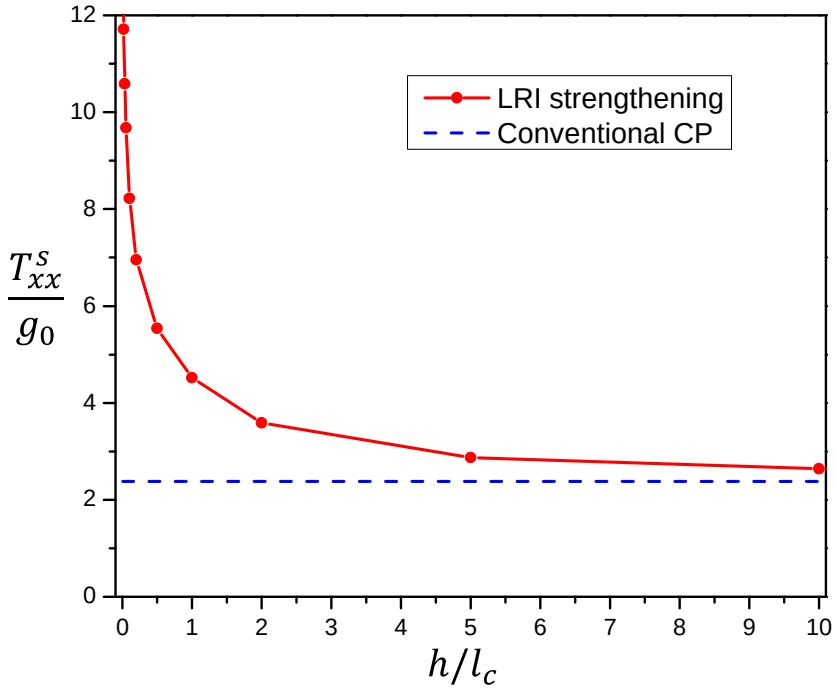

Figure 4.10. Contribution of short range GND interaction versus t/l_g and long range GND interactions versus. t/l_c on flow stress at 5% surface strain.

Having investigated the role of image fields on the length-scale dependent internal stresses, in the following section we make attempt to connect the present results with a recent experimental result. In the process, we also discuss the nature of the internal length-scale l_c.

4.4.2 Comparison with Experiment

(Motz et al., 2005) performed bending tests on copper single crystal specimens with an <110> {111} orientation where the beam axis is collinear with the crystal <110> direction and neutral plane is along the {111} plane (Fig. 4.11). For this crystal orientation, there are four active slip systems with Schmid factor 0.408, while it is zero on the remaining slip systems (Table 4.2). Their experiments show that the flow stress $\sigma_f - t$ relationship for monotonic bending of single crystal copper micro-beams

roughly follows $\sigma_f \propto t^{-1}$. We compare our model predictions with these experimental observations[19].

Table 4-2. Local and global coordinates of active slip system according to Motz et al., (2005) single crystal bending experiment

Slip system No.	Slip direction $\mathbf{s}^\alpha$		Normal direction $\mathbf{m}^\alpha$	
	Local coordinate	Global coordinate	Local coordinate	Global coordinate
1	(0,-1,1)	(0.5,0,-0.86)	(-1,1,1)	(-0.81,0.33,-0.47)
2	(-1,0,1)	(-0.5,0,-0.86)	(1,-1,1)	(0.81,0.33,-0.47)
3	(1,0,1)	(0.5,0.81,-0.28)	(-1,1,1)	(-0.81,0.33,-0.47)
4	(0,1,1)	(-0.5,0.81,-0.28)	(1,-1,1)	(0.81,0.33,-0.47)

For this, we consider the specimen geometry to be the same as in the preceding section, but model two sets of conjugate slip systems as observed in the Motz et al's experiments (See Figure 4.11).

Noting Eq. (4.17) and the crystallographic description of plastic strain $\mathbf{E}^p = \sum_\alpha \gamma^\alpha (\mathbf{s}^\alpha \otimes \mathbf{m}^\alpha)_{sym}$ we obtain

$$\gamma^1 = \gamma^2 = \frac{\gamma^3}{3} = \frac{\gamma^4}{3} = \frac{-\kappa^p y}{4S} \tag{4.23}$$

[19] The experimental setup (Motz et al., (2005)) is that of cantilever bending subjected to a concentrated force at the free end. Therefore, the curvature and GND density vary along beam axis. However, most of the plastic deformation is concentrated near the cantilever root, and in this work, we assume a uniform curvature condition to mimic this region (see fig. 7 of Motz et al., (2005)).

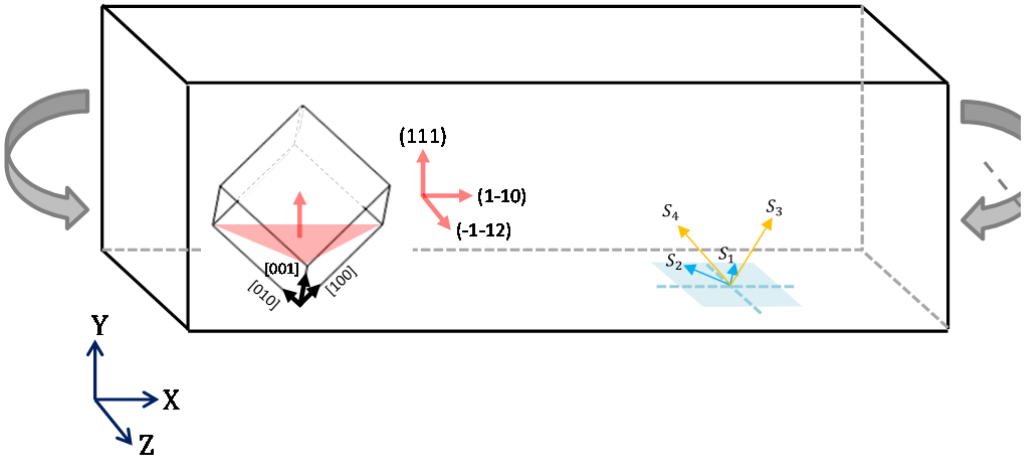

Figure 4.11. Schematic of single crystal specimen under pure bending, crystal orientation and corresponding active slip systems.

The crystal orientation in the experimental set up satisfies the plane strain conditions for plasticity, which is in agreement with our previous assumption in deriving internal stress constitutive equation.

Figure 4.12 compares the experimental $\sigma_f - t$ variation (green curve and circles) together with the theoretical predictions (dashed curves and symbols) with the parameter values provided in Table 4-1[20]. The different dashed curves signify the predicted $\sigma_f - t$ variation for different values of l_c. The blue dashed curve is the predicted $\sigma_f - t$ variation accounting for only the GND-SRI term in Eq. (4.22). Over the entire range of beam thicknesses investigated by Motz et al (2005) the predicted SRI contribution to the overall strengthening falls short of the experimentally reported strengthening indicating that there should be an additional contribution to strengthening. Further, the discrepancy is accentuated with decreasing t. That this

[20] For comparison with the experiment, we set $C_0 = 4$ so as to produce the same amount of SSD hardening (~ 70 MPa at 5% total strain) in order to obtain the size-independent limit of the macroscopic flow stress for bulk specimens (Motz et. al, 2005).

additional contribution should arise from internal stresses is substantiated by bending experiments (Kiener et al., 2010) and (Demir and Raabe, 2010) at similar length-scales, but under cyclic loading, which exhibit pronounced length-scale dependent kinematic hardening (Bauschinger effect) during load reversal, also predicted by (Hou et al., 2008) in the DDP analysis of pure bending of miniaturized beams. An interesting source of deviation from the classic Taylor hardening model was recently highlighted by Guruprasad and Benzerga (2008). They indicated that even under nominally homogeneous loading (tension or compression), presence of local GND structures at the micro-scale may cause additional hardening at small length-scales, especially over moderate to large strains. They also proposed an augmented hardening model to account for such higher-order effects.

Note that for the values of l_c considered in Figure 4.12, each curve compares well with the experiment only in a particular regime of beam thickness. For example, with $l_c = 1\ \mu m$ (red curve) the predicted σ_f corroborates well with experimental values for large beam thickness ($t > 3.5\ \mu m$). However, for thinner beams the predicted strengthening is much lower than the actual value. Interestingly, for beams with $t \leq 3.5\ \mu m$ one observes better corroboration with the experiment for larger values of l_c such that at the smallest t ($= 1\ \mu m$) the predictions with $l_c = 10\ \mu m$ corroborate very well with the experiments. Based on this comparison, it may be postulated that the evolution of internal length-scale changes with decreasing specimen thickness. It becomes imperative to seek a plausible explanation for such a dependency, which is discussed in the subsequent paragraphs.

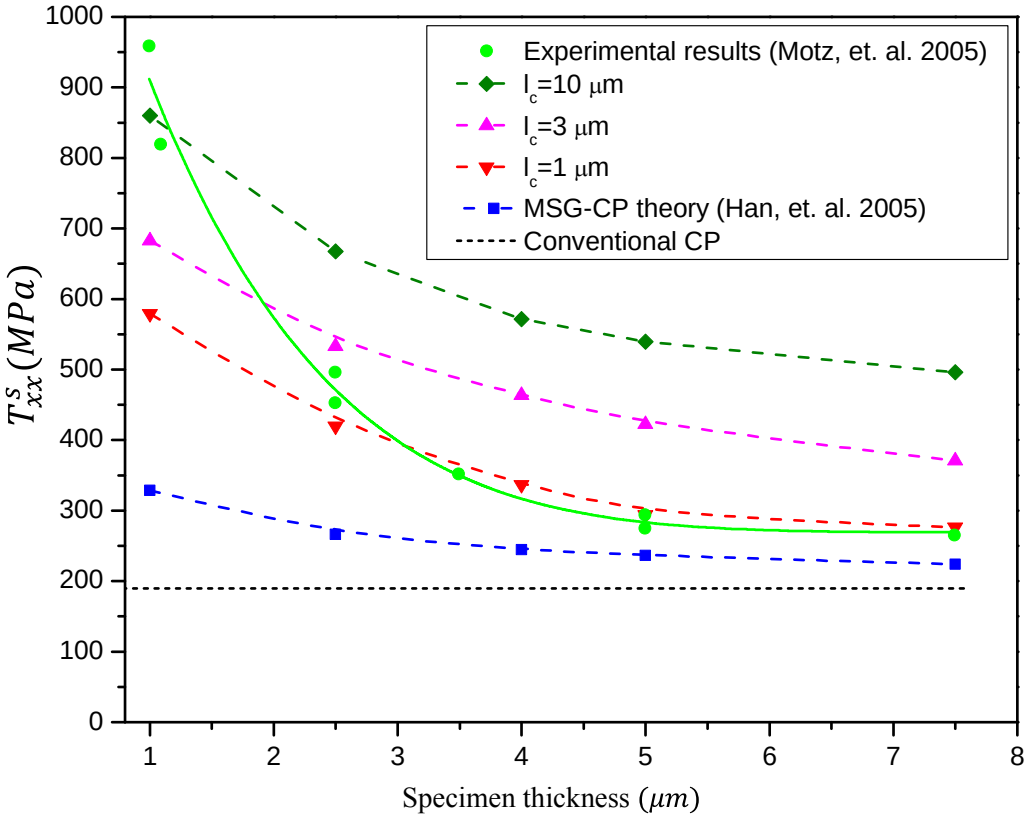

Figure 4.12. Comparison of the analytical results (Eq. 4.17) for different values of l_c with the experimental results of Motz, et al (2005).

Based on this comparison, it may be postulated that the internal length-scale itself increases with decreasing specimen thickness. It becomes imperative to seek a plausible explanation for such a dependency, which is discussed in the subsequent paragraphs. One physical interpretation of the internal length-scale l_c that governs internal stresses in a mesoscopic continuum is a correlation length-scale emerging from the collective behavior of dislocations[21]. (Groma, 1997, 2003; Groma and Bako, 2000; Groma and

[21] Zaiser and Seeger (2002) introduced *mesoscopic* internal stresses arising from long-range interactions of dislocation ensembles, which vary on the characteristic scale of the dislocation density variation in comparison to *microscopic* internal stresses in the vicinity of a single dislocation. Based on this definition, the internal length-scale associated with the mesoscopic

Bakó, 1998; Zaiser and Aifantis, 2003; Zaiser et al., 2001; Zaiser and Seeger, 2002). (Hahner and Zaiser, 1997) proposed a scaling law for correlation length, which gives a correlation length around $1\,\mu m$ for deformed Cu in stage-II hardening at room temperature. For a given specimen, the initial l_c may be defined by the starting dislocation substructure or the initial dislocation source distribution. It may evolve as the dislocation substructure evolves during deformation. Based on these ideas, we may consider the relevant length-scale l_c to be the correlation distance over which dislocation ensembles interact through their stress-fields. Conventionally l_c is described in terms of multiples of the average dislocation spacing λ, i.e. $\sim (\rho)^{-1/2}$, where ρ is the overall dislocation density (Weiss and Montagnat, 2007; Zaiser and Seeger, 2002). Mughrabi (1975, 1983, 2001) suggested that l_c should be in the range of 10-100 times the average dislocation spacing λ. On a given slip-plane with dislocations arranged in parallel (Figure 4.13), the average λ on that particular slip-plane can be obtained directly from their arrangement. However, normal to the slip-plane the dislocation spacing is set by another length-scale l_s, which is the distance between two adjacent slip-planes. The existence of such an *effective slip-plane spacing* l_s stems from the fact that not all the planes in a particular slip system are activated during initial stages of deformation. Indeed, this natural length-scale emerges from activation of dislocation sources (e.g. Frank-Read sources) on a few of the potential slip-planes – a process that is statistical in nature (Yefimov et al., 2004b).

---

continuum was suggested to be of the order of few microns (also see Weiss and Montagnat (2007)).

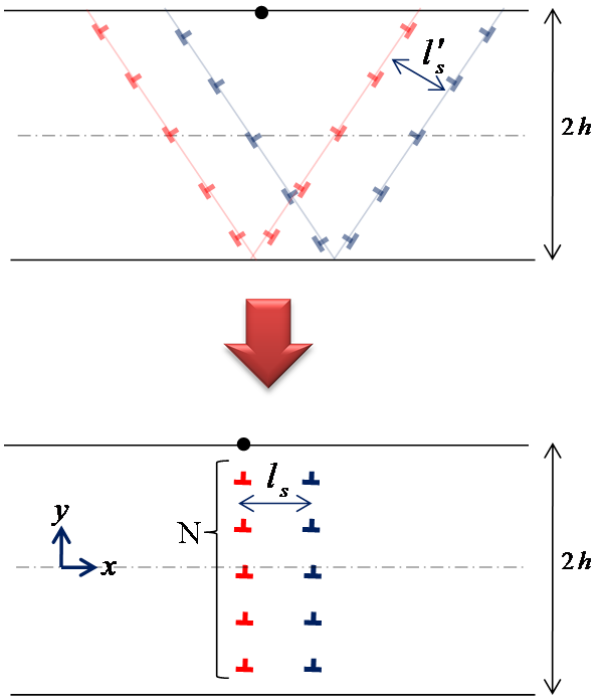

Figure 4.13. Typical GND arrangement in double symmetric slip deformation under pure bending.

Assuming for our current problem (Figure 4.13) that there exist N_d dislocations in an area $t \times \bar{l}_s$ where $\bar{l}_s$ is the projected slip-plane spacing, the GND density component A_{zx} can be written in a discrete sense as

$$A_{zx} = \left(\frac{N_d}{t\bar{l}_s}\right) b \tag{4.24}$$

where $(t/N_d) = \lambda$ on a given slip plane. For crystalline materials, $\bar{l}_s$ (or l_s) is in the range of tens of nanometers[22] (Deshpande et al., 2005). Mesarovic et al (2010) showed that $\bar{l}_s$ appears as a natural internal length-scale in the continuum description of internal stress by invoking the thermodynamic coarsening error between the discrete and

[22] $\bar{l}_s = l_s/\cos\theta$ is the projection of the actual slip-plane spacing l_s, which is ~$100b$.

continuum descriptions of a GND density field. From a kinematic coarsening perspective, if we smear out the dislocation arrangement along the slip-plane by adopting the notion of continuously distributed dislocations, but retain the discrete nature of distribution across it, then the correlation length-scale may be described as (Mughrabi, (1975), Zaiser and Seeger (2002) and Mesarovic, et al (2010))

$$l_c = \beta \overline{l_s} \tag{4.25}$$

where $\beta \sim 10 - 100$ (Mugharbi, 1975) may be viewed as the number of slip planes around a given point that influence the stress field at that point. For example, if $\overline{l_s} = 30nm$, we obtain $l_c \sim 300\, nm - 3\, \mu m$ from Eq. (4.25), which is in the range suggested by various continuum and DDP approaches (Deshpande et al., 2005; Hahner and Zaiser, 1997; Weiss and Montagnat, 2007; Zaiser et al., 2001). Note that the assumption of discreteness of slip-planes may be relevant in a scenario where a specimen initially hosts sparsely distributed dislocation sources, which would also indicate activation of fewer slip-planes giving a larger l_s. Recent explorations in small scale crystal plasticity have resulted in proposals for scale-dependent plasticity that rely on novel mechanisms such as dislocation starvation (Greer and Nix, 2006; Greer et al., 2005), exhaustion hardening (Benzerga, 2009) and source truncation (El-Awady et al., 2011; Kiener and Minor, 2011; Parthasarathya et al., 2007). It is likely that these mechanisms may couple into the description of internal stresses through the notion of internal length-scale. Although we do not explicitly account for such mechanisms, comparison of our calculations with experiments provides an interesting perspective from the viewpoint of internal stresses that may connect to these proposals.

Now, based on our postulate that l_c increases with decreasing t (Figure 4.12), a larger l_c for smaller specimen means that either $\overline{l_s}$ is larger for fixed β,or that more number of slip-planes participate in determining the internal stress at a point. Three-dimensional DDD simulations of single crystalline beam under bending for both single

and double-symmetric slip (Motz, et. al. (2008)) show that for smaller beam thicknesses, fewer dislocation sources are activated giving a lower initial dislocation source density than for a thicker beam. In the same simulations, plastic slip in thinner beams occurs in localized slip bands that are spaced much wider apart compared to those in the thicker beams where slip bands are close enough to resemble a relatively homogeneous plastic slip. As mentioned in the preceding paragraph, from the viewpoint of Eq. (4.24) and Figure 4.12, this suggests that below a certain value of t, for a fixed GND density a reduction in the average density of dislocation sources should indeed lead to the slip-planes being spaced wider apart, i.e. larger $\overline{l_s}$ with smaller t. This observation is also consistent with the notion of source-limited plasticity in geometrically confined systems (El-Awady et al., 2009a; Espinosa, 2005; Parthasarathy et al., 2007); Shi, et. al. (2004)). From Figure 4.12, $\overline{l_s}$ (and therefore, l_c) remains nearly constant above $t > \sim 4\,\mu m$, but increases dramatically below that value.

It is interesting to consider an allied length-scale dependency from the perspective introduced by Chakravarthy and Curtin (2010). For specimen under uniaxial tension, their DD and continuum analysis showed that the amount of strengthening increases with increasing ratio of the obstacle to dislocation source density ($r = \rho_{obs}/\rho_s$) for a fixed specimen thickness. In the present context, this may be viewed as follows: For a fixed t, Eq. (4.24) requires that for a fixed A_{zx} (i.e. fixed curvature) the number of dislocations N_d in the pile-up over the region ($\overline{l_s} \times t$) must increase for a larger $\overline{l_s}$. In other words, there should be more dislocations per slip-plane to accommodate the same curvature. This is also akin to saying that the density of obstacles (ρ_{obs}) to dislocation nucleation or motion per slip-plane is higher, because each new dislocation must overcome the back stress produced by existing obstacles. Further, higher $\overline{l_s}$ means more widely spaced slip-planes concomitant to fewer dislocation sources, i.e. lower ρ_s. With this, it can be postulated that the argument of higher $\overline{l_s}$ producing larger strengthening due to enhanced internal stress is also

consistent with the results of Chakravarthy and Curtin (2010). In the context of the present problem, we obtain that for two specimens experiencing same curvature, the specimen with the smaller thickness exhibits higher overall internal stress due to wider slip-plane spacing that couples with more number of dislocations per slip-plane acting as obstacles to dislocation motion.

In summary, we posit that the proposed origin of the inverse dependence of the internal length-scale l_c corresponding to the internal stresses on the specimen size t stems from the paucity of active slip planes (arising from lack of sufficient number of sources and/ or truncated sources) that determine their average spacing $\overline{l_s}$. We note in passing that from Figure 4.8, this also means that the internal stress increases non-linearly with decreasing t.

4.4.3 Length-scale Dependent Bauschinger Effect

Finally, we investigate the cyclic pure bending behavior of the single crystal specimen using developed continuum framework in the previous section. In particular, we mimic a single cycle comprising forward bending leading a prescribed plastic curvature followed by straightening to original undeformed geometry, which has been experimentally reported to exhibit a length-scale dependent Bauschinger effect (Demir and Raabe, 2010). In Eq. (4.22) we set $C = 0$ during the forward loading.

Figure 4.14 shows bending- strengthening responses of the single crystal specimens under double symmetric slip condition for two thicknesses, $t = 1\ \mu m$ and $10\ \mu m$. There are several interesting features that can be extracted from this figure. Firstly, it can be seen that the length-scale dependent internal stresses cause more severe Bauschinger effect (yield asymmetry) for the thinner specimen than for the thicker specimen (Kiener,(2010); Demir and Raabe (2010); Hayashi, et. al. (2011); Hou et. al (2008) and Kuroda and Tvergaard (2008)). During forward loading, the internal stress acts as back-

stress that resists plastic deformation and manifests as macroscopic strengthening, while during straightening the same internal stress assists plastic deformation causing a decrease in the yield strength. Demir and Raabe (2010) referred to this as a mechanical Bauschinger effect, which is due to internal stresses that arise from polarized dislocation (GNDs) arrangement during forward bending. Secondly, the hardening rate in the reverse plasticity is higher for thinner specimen. Finally, for a given thickness the hardening rate in reverse plasticity is lower than in its forward counterpart. This last aspect can be explained as a consequence of the idealized scenario of no SSD hardening and vanishing GND density with decreasing curvature as assumed in our analysis.

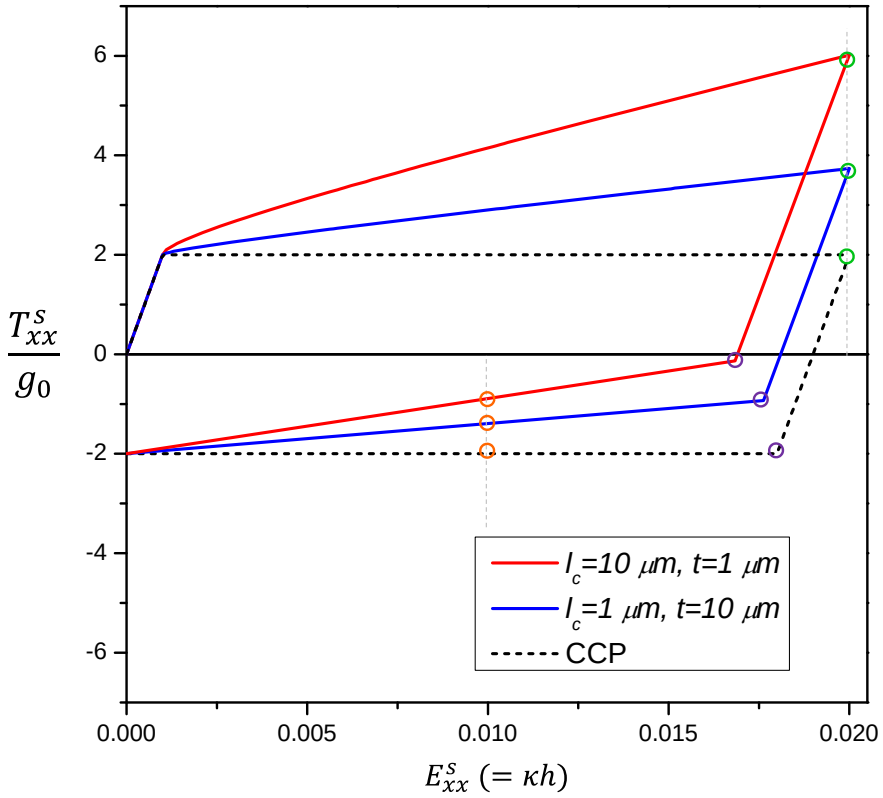

Figure 4.14. Bending-straightening cyclic response of single crystalline specimen oriented for double symmetric slip

Corresponding to Fig. 4.14, the GND-induced SRI and LRI terms are nonzero at the point of reverse yield and are equal to those at the strain at which unloading begins.

These contributions gradually decrease with decreasing curvature until they vanish when the specimen attains its original shape. Consequently, the overall stress also becomes equal to the yield stress determined by g_0 (Eq. 4.22). In reality however, the presence of SSD density and the remobilization of GNDs as SSDs due to decreasing curvature (Demir and Raabe, 2010) may produce a higher hardening rate in the straightening stage, which is not captured here. In addition they observed an enhanced hardening during straightening with decreasing specimen thickness. This likely arises because the GND density that evolves to accommodate increasing curvature during forward loading progressively decreases during the straightening phase and this accumulated density manifests itself as increased mobile dislocation density that may in turn enhance the overall hardening in the flow regime. In Figure 4.14, this effect is accounted for in the straightening phase within the Taylor hardening term in a simple way by assuming that the fractional reduction in the GND density is the same as that of the fractional increase in the SSD density. The GND-induced SRI and internal stress terms are nonzero at initial stages of unloading, but gradually decrease with decreasing curvature until it reaches zero when the specimen attains its original shape. Concurrently, the hardening due to remobilized GND density term is zero at initial stage of unloading, but evolves with stress reversal.

Figure 4.15 shows the overall stress variation across specimen thickness at different levels of surface strain indicated by the open circles in Fig. 4.14. While CCP (Figure 4.15a) exhibits identical variation over the thickness under forward and reverse loading (no Bauschinger effect), the length-scale dependent results (Figure 4.15b and c) show increasingly stronger asymmetry with decreased specimen thickness. As expected, for the latter cases the stress distribution under forward loading shows increasingly higher surface stress with decreasing thickness and a lower surface stress under reverse loading.

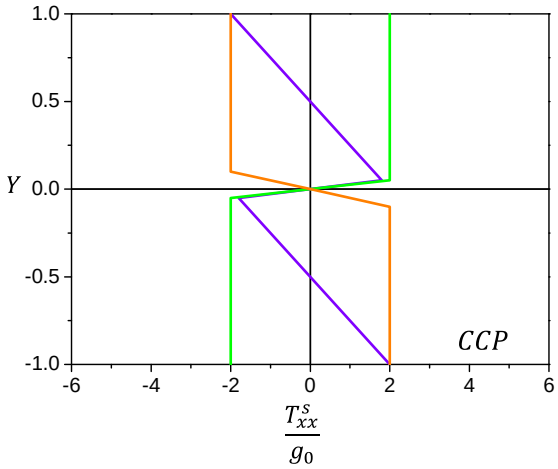

(a)

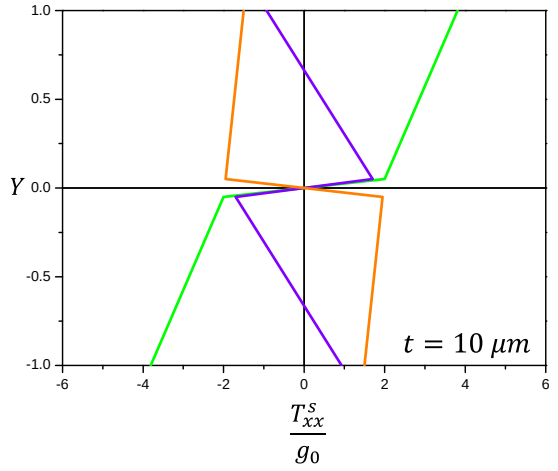

(b)

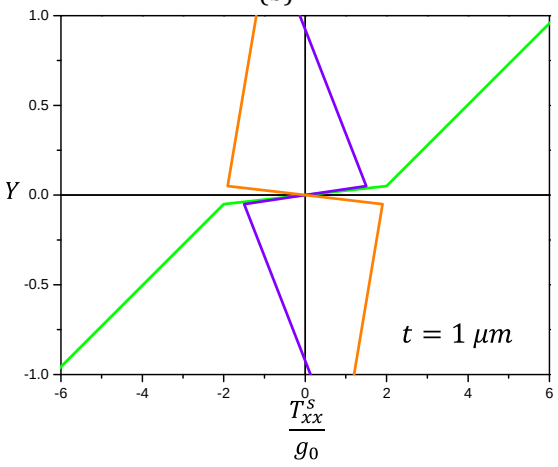

(c)

Figure 4.15. Overall stress variation across specimen thickness at different strain shown in figure 4.14.

Further, the stress distribution over the specimen thickness at the point of reverse yielding strongly depends on t and l_c (blue curves). Note that at the point of reverse

yielding, the CCP result shows a linear tension to compression transition between the neutral axis and the free surface. With decreasing l_c and concurrently higher l_c the inflection point moves toward the surface to the extent that it may even disappear. Figure 4.14 and 4.15 reveal that surfaces may deform plastically upon reversal loading even with a positive stress. Figure 4.16 displays the contributions from length-scale dependent isotropic (dissipative) and kinematic (energetic) hardening mechanisms for two different specimen thicknesses in cyclic bending-straightening.

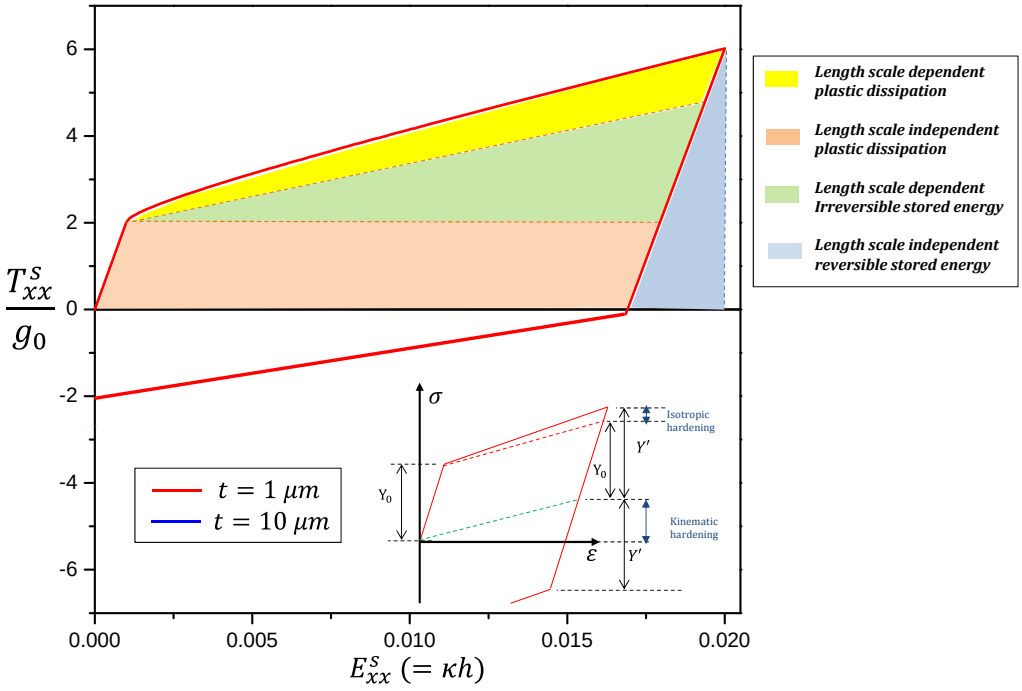

Figure 4.16. Length-scale dependent dissipative (isotropic) and energetic (kinematic) hardening components of pure bending responses for two different specimen thickness

Since the SSD hardening is ignored here, the length-scale independent plastic dissipation is only due to perfect plasticity. Therefore, the hardening behavior observed in the figure is fully ascribed to the length-scale dependent dissipative and energetic components of GNDs. Inset in Fig. 4.14 shows that the isotropic hardening can be obtained by deducting the initial yield stress Y_0 (OA) from subsequent yield stress

Y'(BC/2). The kinematic hardening contribution is obtained by deducting Y' from the stress at the point where the load is reversed (point B on the curve).

From a thermodynamic viewpoint, writing the total internal energy (see chapter 3) identify the different components of energy involved in plastic deformation as

$$W_{\text{int}} = \int_V \left(\underbrace{\mathbf{T}^{ext} : \mathbf{E}_C^e}_{\substack{\text{reversible stored} \\ \text{energy}}} + \underbrace{\mathbf{T}^* : \mathbf{E}_I^e}_{\substack{\text{irriversible stored} \\ \text{energy}}} + \underbrace{\sum_\alpha (\tau_{ext}^\alpha + \tau^{*(\alpha)}) \gamma^\alpha}_{\substack{\text{dissipative} \\ \text{energy}}} \right) dV \qquad (4.26)$$

The first term in Eq. (4.26) represents the length-scale independent reversible stored energy associated with externally applied loads. The second term is referred to as the length-scale dependent irreversible stored energy as it is associated with the internal residual stress and incompatible elastic strain that will tend to reorganize the GND density from an energetically efficient configuration. The third term in Eq. (4.26) is the plastic dissipation due to the SSD[23] (length-scale independent isotropic hardening) and GND (length-scale dependent isotropic hardening) densities.

It can be seen than regardless of beam thickness, the contribution of energetic hardening is higher than the dissipative one which is depicted in figure 4.10 as well. Furthermore, higher irreversible energy store and dissipate in thinner beam due to polarized GND distribution which provide the length-scale dependent responses. Note that length scale dissipative energy arises from short-range interaction of GNDs with SSD and causes isotropic hardening, while long-range elastic GND-GND and GND-

[23] In the results presented in figure 4.14 and 4.15, the SSD hardening is neglected by setting C=0 in Eq. (4.17) and plastic energy is dissipated only because of short range interaction of GNDs with SSDs

boundary interactions cause irreversible energy, sometimes referred to as *defect energy* (Gurtin, 2002) and cause kinematic hardening (Bauschinger effect).

4.5 Summary and Outlook

This chapter presents an elasticity based approach to account for image effects due to GND-free surface interaction producing length-scale dependent internal stresses in crystal plasticity. The approach developed here is generic in that the internal stresses from GND density in an infinite medium is corrected by an additional term that accounts for GND-boundary long-range interaction. The latter explicitly depends on the nature of the boundary and the particular case treated here is that of a free surface. It should be possible to apply the concept to other continuum analogs based on fundamental solutions such as elastic half-spaces and interfaces between dissimilar materials under homogeneous or non-homogeneous deformations.

The pure bending example shows that finite spatial extent of the GND density produces net long-range elastic interaction when image fields are taken into account that manifest as internal stresses even when the GND density is uniformly distributed. The results show that these effects become increasingly important as the characteristic specimen size approaches the internal material length-scale. If the specimen size is much larger than the internal length-scale the internal stresses are still non-zero, but only in the proximity of the free surfaces. A proposal that stems from the present work is the nature of the internal length-scale contributing toward internal stresses. This is expressed in terms of the average slip-plane spacing through the dislocation density argument. A comparison of the model predictions with experimental results on monotonic micro-beam bending suggests that the initial internal length-scale should increase with decreasing characteristic specimen size. This proposal is rationalized by appealing to recent experimental and computational results on miniaturized specimens

subjected to homogeneous or non-homogeneous loading. Cyclic responses of the specimens under pure bending and straightening are also explored and the experimentally observed length-scale dependent Bauschinger effect is captured. Again, it is important to note that this effect stems from the GND-free surface long-range interaction. The resulting contributions of the isotropic and kinematic hardening are quantified in the stress-strain responses.

In closing, we would like to mention the recent work by Cherednichenko (2010) that introduces the idea of continuum representation of image fields, although the underlying mathematical representation is different from ours. In comparison to the present work that relies on the theory of elasticity and kinematic incompatibility, that work constructs image fields through statistical-mechanics based ensemble averaging of dislocations (Groma, 1997; Groma and Balogh, 1999; Yefimov et al., 2004), similar to that of Vinogradov and Willis (2008). The resulting elegant formulation embeds an enriched nonlocal constitutive law that tracks plasticity through dislocation density evolution including nucleation, while accounting for image effects. Although the image fields constructed there are for a different boundary value problem (simple shear of a constrained thin strip arising where dislocations pile-up at the hard boundary), it would be interesting to draw broad correlations between these two approaches.

5 Summary and Recommendations

In this chapter, we summarize the key contributions of this thesis and provide an outlook into the future developments along the chosen direction.

5.1 Summary

Classical continuum crystal plasticity theories are successful to predict inelastic behavior of material in macroscopic scale while it fails to capture size dependency of the material when sub structural counterparts or specimen sizes are comparable with microstructural characteristic length. Therefore, to explain some of the experimentally observed length-scale responses in crystalline materials, traditional continuum mechanics of plastic deformation is augmented with a variety of dislocation related mechanisms. In this thesis, we explore the length-scale dependent behaviors of FCC crystalline materials in terms of GND interaction mechanisms at different scales. The three GND related mechanisms investigated in this thesis are summarized as follows:

(i) Short-range interaction between GNDs and SSDs is considered in chapter 2 in terms of length-scale dependent Taylor hardening model. This phenomenon is modeled using the Mechanism-based Slip Gradient Crystal Plasticity (MSG-CP), which is implemented by the author as a user-material subroutine (UMAT) within ABAQUS/STANDARD®. Using this implementation, the length-scale dependent behavior of model single crystal MMC architectures under thermal and mechanical loading are investigated. Specifically, role of initial thermal GND density on the subsequent response under mechanical loading is investigated for certain crystal orientations. The length-scale dependent thermo-mechanical response is modeled as a two-step procedure within finite element analysis that closely follows the actual synthesis route. The results

exhibit the characteristic tension-compression asymmetry arising from pre-existing internal (thermally-induced) residual stresses that is now length-scale dependent.

(ii) Another important result that emanates from the MSGCP-MMC investigations is the negligible effect of inclusion shape (whether round or sharp-cornered) at small sizes. This is because the high triaxiality that exists in the matrix surrounding the sharp corners is smeared out by the hardened GND zone around the inclusions that is about the same spatial extent as the stress concentration at corners.

(iii) The MSGCP implementation is also used in systematic simulations of polycrystalline MMC architecture to delineate the interaction strengthening contribution as arising from the grain size and the inclusion size interaction. This effect has been traditionally ignored in MMC simulations to-date. Our simulations predict that the interaction term appears as Hall-Petch type contribution. Based on this observation, we propose an analytical solution for this interaction effect based on the idea that the inclusion-grain intersections act as special sources that emit additional GNDs and these GNDs pile-up at grain boundaries resulting in additional strengthening. . The proposed analytical model is deemed amenable to homogenized approaches.

(iv) The thesis then expands its scope to address the length-scale dependent internal stress arising from long-range GND-GND interaction. A nonlocal continuum crystal plasticity is developed to account for these *residual* stresses arising from a non-homogeneous distribution of GND density. The thesis proposes a stress functions approach to analytically derive the length-scale dependent 3D internal stress tensor. This internal stress tensor is incorporated into continuum framework using thermodynamic laws.

(v) The model examples treated semi-analytically with the aforementioned formulation highlight the importance of the internal stress on the length-scale dependent strengthening and hardening in single crystals. The tapered single crystal

example that approximately mimics a micro-pillar subjected uniaxial loading substantiates that of geometric imperfections in such structures cause strong gradients in the GND density and lead to a strengthening of the overall stress-strain response in specimens that are subjected to nominally uniaxial macroscopic loads. The simple shear of a single crystal lamella mimics a nano-twin within a grain that undergoes shearing deformation and the internal stress-induced strengthening of a slip system exhibits Hall-Petch type behavior. Interestingly, at small structural sizes the strengthening tends to saturate.

(vi) Finally, the thesis addresses the long-range interaction between the GND density and traction-free boundaries. Building up on the stress functions approach, the internal stress formulation incorporates additional image stresses due to this contribution through an additional stress function. The resulting internal stress tensor representing image fields is length-scale dependent. In analyzing a model micro-architecture comprising a single crystal thin film under pure bending, it is shown that internal stresses also occur under nominally uniform curvatures. The formalism reveals that the micro-traction boundary conditions in the form of Peach-Koehler force density due to GND density invoked in the work of Gurtin (2002) can be construed as image stresses imposed due to GND-surface long-range interaction. A comparison with the experimental results suggests that internal length-scale is a function of structural and microstructural dimensions and may increase with decreasing specimen dimensions. The structurally dependent internal length-scale is explained in terms of the recent proposals of paucity of dislocation sources and enhancement of obstacle density with decreasing structural dimensions.

5.2 Recommendations for future work

The work compiled in this thesis may serve to provide a basis to variety of problems in the mechanics and physics of length-scale dependent plasticity. Some of these are identified and discussed here:

(i) In the MMC modeling, we have assumed highly idealized microstructures in the form of grain shapes and inclusion arrangement. Further, it may be useful to mimic microstructures that are closer to the real microstructures. A simple, yet plausible approximation could be that of hexagonally-shaped grains rather than the square-shaped approximations chosen in this work. The former would be a better approximation, because typically one finds triple junctions in real microstructures unlike the quad-junctions in the microstructure with square grains.

(ii) The length-scale dependent MMC behaviors including thermo-mechanical loading conditions may be extended to polycrystalline microstructures. This would require invoking the elastic anisotropy of the crystals to render differential stresses across grain boundaries, which is already present in the MSGCP UMAT developed here but was not used for simplicity.

(iii) The area of hierarchical MMCs (Joshi and Ramesh, 2007) is an exciting direction to use the MSGCP approach. Several local and global features of such composite-within-composite architectures can be investigated with high resolution as a function of judiciously arranged topologies with varying grain sizes.

(iv) Our MMC investigations do not invoke higher-order boundary conditions, which would be necessary to capture enhanced interactions between the dislocations and interfaces. Therefore, it would be worthwhile to endow the current crystal plasticity code with higher-order gradients. Within ABAQUS, this would entail developing a full-fledged user-element (UEL) that would enable calculating second

gradients of plastic slip (i.e. first gradient of the GND density), of which the current UMAT would be a part.

(v) The stress functions approach to account for internal stresses while attractive and insightful, has limitations that explicit solutions are possible only for a limited number of cases such as those with regular geometry, ideal boundary conditions, elastic isotropy. Although, we have provided a brief outline of the extension of this approach to elastically anisotropic materials, a complete solution to a boundary value problem is expected to be quite complicated. Hence, it may be useful, or perhaps necessary, to develop a finite element approach that calculates these internal stresses.

(vi) In the context of stress function approach which has developed in this thesis, some fundamental cases which are interesting for large mechanics community can be investigated where appropriate Green functions are available or can be derived. For instance,

- Torsion of single crystalline micro wire comprising uniform distribution of screw dislocation.
- MMC unit cell comprising circular inclusion and crystalline matrix where internal stresses develop at the inclusion/matrix interface due to dislocation piles up.
- Micro compression of tapered pillar accounting for image effects.

(viii) Alternatively, the surface dislocation model proposed by Jagannadham and Marcinkowski (1978) can be incorporated to account for image effect while simple infinite medium green functions are used.

(viii) In the case of complicated topologies and non-ideal higher-order traction boundary conditions, the stress function approach is not a very useful approach to

obtain image fields. A brief discussion and a possible approach are outlined in the closing section of Chapter 4, which should provide a direction for future work.

6 List of Publication

Articles published in Journals:

Aghababaei, R and Joshi, SP (2011) Grain size–inclusion size interaction in metal matrix composites using mechanism-based gradient crystal plasticity. *International Journal of Solids and Structures,* 48 (18) 2585-2594.

Aghababaei, R, Joshi, SP and Reddy, JN (2011) Nonlocal continuum crystal plasticity with internal residual stresses. *Journal of the Mechanics and Physics of Solids,* 59, 713–731.

Aghababaei, R and Reddy, JN (2009), Nonlocal Third-Order Shear Deformation Plate Theory with Application to Bending and Vibration of Plates. *Journal of Sound and Vibration,* 326, 277-289.

Articles in preparation/submission:

Aghababaei, R and Joshi, SP. A Crystal Plasticity Analysis of Length-scale Dependent Internal Stresses with Image Effects (under review in *Journal of the Mechanics and Physics of Solids*).

Aghababaei, R and Joshi, SP. Length-scale dependent composite response induced by thermal residual stresses (manuscript in preparation)

Conference presentations:

Aghababaei, R and Joshi, SP (2011) Grain Size-Inclusion Size Interaction in Metal Matrix Composites at Moderate Strains. *International Conference on Materials for Advanced Technologies, ICMAT*, (June 26-July 1, 2010), Singapore.

Aghababaei, R, Joshi, SP and Reddy, JN (2010) A Nonlocal Continuum Theory Accounting for Size Dependent Bauschinger Effect. *9th World Congress on Computational Mechanics and 4th Asian Pacific Congress on Computational Mechanics,* WCCM/APCOM 2010 (19 – 23 July 2010), Sydney, Australia

Aghababaei, R and Joshi, SP (2010) A Nonlocal Continuum Theory Accounting for Size Dependent Bauschinger Effect. *16th US National Congress on Theoretical and Applied Mechanics*, USNCTAM (June 27-July 2, 2010), Penn State University, Pennsylvania, USA

Aghababaei R, Joshi, SP and Zhang, J (2010) Length-Scale Dependent Response of Hierarchical Composites using Enriched Polycrystal Plasticity. 16th US National Con Congress on Theoretical and Applied Mechanics (June 27-July 2, 2010), Penn State University, Pennsylvania, USA.

7 Bibliography

Abu Al-Rub, R.K., 2009. Modeling the particle size and interfacial hardening effects in metal matrix composites with dispersed particles at decreasing microstructural length scales. International Journal for Multiscale Computational Engineering 7, 329-350.

Abu Al-Rub, R.K., Voyiadjis, G.Z., 2006. A physically based gradient plasticity theory. International Journal of Plasticity 22, 654-684.

Abu Al-Rub, R.K., Voyiadjis, G.Z., Bammann, D., 2007. A thermodynamic based higher-order gradient theory for size dependent plasticity. International Journal of Solids and Structures 44, 2888-2923.

Acharya, A., 2003. Geometrically necessary dislocations, hardening, and a simple gradient theory of crystal plasticity. Scripta Materialia 48, 167-172.

Acharya, A., Bassani, J.L., 2000. Lattice incompatibility and a gradient theory of crystal plasticity. Journal of mechanics and physics of solids 48, 1565-1595.

Acharya, A., Beaudoin, A.J., 2000. Grain-size effect in viscoplastic polycrystals at moderate strains. J. Mech. Phys. Solids 48, 2213-2230.

Acharya, A., Roy, A., 2006. Size effects and idealized dislocation microstructure at small scales: Predictions of a Phenomenological model of Mesoscopic Field Dislocation Mechanics: Part I. Journal of the Mechanics and Physics of Solids 54, 1687-1710.

Agrawal, R., Peng, B., Gdoutos, E.E., Espinosa, H., 2008. Elasticity size effects in ZnO nanowires--a combined experimental-computational approach. Nano Letters 8, 3668-3674.

Aifantis, E.C., 1984. On the Microstructural Origin of Certain Inelastic Models. Journal of Engineering Materials and Technology 106, 326-330.

Aifantis, E.C., 1987. The physics of plastic deformation. International Journal of Plasticity 3, 211-247.

Anand, L., Gurtin, M.E., Lele, S.P., Gething, C., 2005. A one-dimensional theory of strain-gradient plasticity: Formulation, analysis, numerical results. Journal of the Mechanics and Physics of Solids 53, 1789-1826.

Armstrong, P.J., Frederick, C.O., 1966. A mathematical representation of multiaxial Bauschinger effect., GEGB report RD/B/N731. Berkeley Nuclear Laboratories.

Arsenault, R.J., Shi, N., 1986. Dislocation generation due to differences between the coefficients of thermal expansion. Materials Science and Engineering 81, 175-187.

Arsenault, R.J., Taya, M., 1987. Thermal residual stress in metal matrix composite. Acta Metallurgica et Materialia 35, 651-659.

Arsenlis, A., Parks, D.M., 1999. Crystallographic aspects of geometrically-necessary and statistically-stored dislocation density. Acta Materialia 47, 1597-1611.

Asaro, R.J., 1983. Micromechanics of crystals and polycrystals. Advances in Applied Mechanics 23, 1-115.

Asaro, R.J., Rice, J.R., 1977. Strain localization in ductile single crystals. Journal of the Mechanics and Physics of Solids 25, 309-338.

Ashby, M.F., 1970. The deformation of plastically non-homogeneous materials. Philosophical Magazine 21, 399-424.

Balint, D.S., Deshpande, V.S., Needleman, A., Van der Giessen, E., 2005. A discrete dislocation plasticity analysis of grain-size strengthening. Materials Science and Engineering A, 186–190.

Bardella, L., 2006. A deformation theory of strain gradient crystal plasticity that accounts for geometrically necessary dislocations. Journal of Mechanics and Physics of Solids 54, 128-160.

Bardella, L., 2008. Influence of material parameters and crystallography on the size effects describable by means of strain gradient plasticity. Journal of Mechanics and Physics of Solids 56, 2906-2934.

Bardella, L., Giacomini, A., 2008. Influence of material parameters and crystallography on the size effects describable by means of strain gradient plasticity. J. Mech. Phys. Solids 56, 2906-2934.

Barlow, C.Y., Hansen, N., 1995. Dislocation configurations in metal-matrix composites correlated with numerical predictions. Acta Metallurgica et Materialia 43, 3633-3648.

Barlow, C.Y., Liu, Y.L., 1998. Microstructure, strain fields and flow stress in deformed metal matrix composites. Acta Materialia 46, 5807-5817.

Bassani, J.L., Wu, T.Y., 1991. Latent hardening in single crystals ii. Analytical characterization and predictions. Proceedings of the Royal Society A 435, 21-41.

Bayley, C., Brekelmans, W., Geers, M., 2006. A comparison of dislocation induced back stress formulations in strain gradient crystal plasticity. International Journal of Solids and Structures 43, 7268-7286.

Benzerga, A., 2009. Micro-pillar plasticity: 2.5D mesoscopic simulations. Journal of Mechanics and Physics of Solids 57, 1459-1469.

Borg, U., 2007. A strain gradient crystal plasticity analysis of grain size effects in polycrystals. European Journal of Mechanics - A/Solids 26, 313-324.

Boukai, A.I., Bunimovich, Y., Tahir-Kheli, J., Yu, J.K.G., W. A., Heath, J.R., 2008. Silicon nanowires as efficient thermoelectric materials. Nature 451, 168-171.

Burger, J.M., 1939. Some Considerations on the Fields of Stress Connected with Dislocations in a Regular Crystal Lattice. I. Koninklijke Nederlandse Akademie van Wetenschappen.

Cailletaud, G., 1992. A micromechanical approach to inelastic behaviour of metals. International Journal of Plasticity 8, 55-73.

Cazacu, O., Fivel, M., 2010. Discrete Dislocation Dynamics: Principles and Recent Applications, in: Cazacu, O. (Ed.), Multiscale Modeling of Heterogenous Materials: From Microstructure to Macro-scale Properties. wiley.

Cermellia, P., Gurtin, M.E., 2000. On the characterization of geometrically necessary dislocations in finite plasticity. Journal of Mechanics and Physics of Solids 49, 1539-1568.

Chakravarthy, S.S., Curtin, W.a., 2010. Effect of source and obstacle strengths on yield stress: A discrete dislocation study. Journal of the Mechanics and Physics of Solids 58, 625-635.

Chen, C.R., Qin, S.Y., Li, S.X., Wen, J.L., 1999. Finite element analysis about effects of particle morphology on mechanical response of composites materials science and Engineering A 278, 96-105.

Cherednichenko, K.D., 2010. An approach to constitutive modelling of elasto-plasticity via ensemble averaging of the dislocation transport. Journal of the Mechanics and Physics of Solids 58, 798-809.

Choi, Y., Suresh, S., 2002. Size effects on the mechanical properties of thin polycrystalline metal films on substrates. Acta Materialia 50, 1881-1893.

Chou, Y.T., Pande, C.S., Yang, H.C., 1975. Interfacial edge dislocations and dislocation walls in anisotropic two-phase media. Journal of Applied Physics 46, 5-10.

Christman, T., Needleman, A., Suresh, S., 1989. An experimental and numerical study of deformation in metal-ceramic. Acta Metallurgica et Materialia 37, 3029–3050.

Cleveringa, H.H.M., Van der Giessen, E., Needleman, A., 1997. Comparison of discrete dislocation and continuum plasticity predictions for a composite material. Acta Materialia 45, 3136-3179.

Cleveringa, H.H.M., Van der Giessen, E., Needleman, A., 1999. A discrete dislocation analysis of bending. International Journal of Plasticity 15, 837-868.

Corbin, S.F., Wilkinsona, D.S., 1994. The influence of particle distribution on the mechanical response of a particulate metal matrix composite. Acta Metallurgica et Materialia 42, 1311-1318.

Dai, L.H., Ling, Z., Bai, Y.L., 1999. A strain gradient-strengthening law for particle reinforced metal matrix composites. Scripta Materialia 41, 245-251.

Dai, L.H., Ling, Z., Bai, Y.L., 2001a. Size-dependent inelastic behavior of particle-reinforced metal-matrix composites. Composites Science and Technology 61, 1057-1063.

Dai, L.H., Ling, Z., Bai, Y.L., 2001b. Size-dependent inelastic behavior of particle-reinforced metal–matrix composites. Composites Science and Technology 61, 1057-1063.

Dai, L.H.L., Z., Bai, Y.L., 2001. Size-dependent inelastic behavior of particle-reinforced metal–matrix composites. Composites Science and Technology 61, 1057-1063.

Dehm, G., 2009. Miniaturized single-crystalline fcc metals deformed in tension: New insights in size-dependent plasticity. Progress in Materials Science 54, 664-688.

Demir, E., Raabe, D., 2010. Mechanical and microstructural single-crystal Bauschinger effects: Observation of reversible plasticity in copper during bending. Acta Materialia 58, 6055-6063.

Deshpande, V.S., Needleman, A., Van der Giessen, E., 2005. Plasticity size effects in tension and compression of single crystals. Journal of the Mechanics and Physics of Solids 53, 2661-2691.

Dunand, D.C., Mortensen, A., 1990. On plastic relaxation of thermal stresses in reinforced metals. Acta Metallurgica et Materialia 39, 127-139.

Dunand, D.C., Mortensen, A., 1991. Dislocation emission at fibers—II. Experiments and microstructure of thermal punching. Acta Metallurgica et Materialia 39, 1417-1429.

El-Awady, J.a., Rao, S.I., Woodward, C., Dimiduk, D.M., Uchic, M.D., 2011. Trapping and escape of dislocations in micro-crystals with external and internal barriers. International Journal of Plasticity 27, 372-387.

El-Awady, J.A., Wen, M., Ghoniem, N.M., 2009a. The role of the weakest-link mechanism in controlling the plasticity of micropillars. Journal of the Mechanics and Physics of Solids 57, 32-50.

El-Awady, J.A., Woodward, C., Dimiduk, D.M., Ghoniem, N.M., 2009b. Effects of focused ion beam induced damage on the plasticity of micropillars. Physical Review B 80, 104-109.

Endy, D., 2005. Foundations for engineering biology. Nature 438, 449-453.

Ertürk, İ., van Dommelen, J.A.W., Geers, M.G.D., 2009. Energetic dislocation interactions and thermodynamical aspects of strain gradient crystal plasticity theories. Journal of the Mechanics and Physics of Solids 57, 1801-1814.

Espinosa, H.D., 2005. An interpretation of size-scale plasticity in geometrically confined systems. Proceedings of the National Academy of Sciences 102, 16933-16938.

Evans, A.G., Hutchinson, J.W., 2009. A critical assessment of theories of strain gradient plasticity. Acta Materialia 57, 1675-1688.

Evers, L.P., Brekelmans, W., Geers, M.G.D., 2004. Non-local crystal plasticity model with intrinsic SSD and GND effects. Journal of the Mechanics and Physics of Solids 52, 2379-2401.

Fivel, M.C., Gosling, T.J., Canova, G.R., 1996. Implementing image stresses in a 3D dislocation simulation. Modelling and Simulation in Materials Science and Engineering 4, 581-596.

Fleck, N., Ashby, M.F., Hutchinson, J., 2003. The role of geometrically necessary dislocations in giving material strenghening. Scripta Materialia 48, 179-183.

Fleck, N., Hutchinson, J., 1997. Strain Gradient Plasticity. Advances in Applied Mechanics 33, 295-361.

Fleck, N.A., Hutchinson, J.W., 1993. A phenomenological theory for strain gradient effects in plasticity. Journal of the Mechanics and Physics of Solids 41, 1825-1857.

Fleck, N.A., Hutchinson, J.W., 2001. A reformulation of strain gradient plasticity. Journal of Mechanics and Physics of Solids 49, 2245-2271.

Fleck, N.A., Hutchonson, J.W., 1993. A phenomenological theory for strain gradient effects in plasticity. Journal of Mechanics and Physics of Solids 41, 1825-1857.

Fleck, N.A., Muller, G.M., Ashby, M.F., Hutchinson, J.W., 1994. Strain gradient plasticity: Theory and Expriment. Acta Metallurgica et Materialia 42, 475-487.

Forest, S., 2008. Some links between Cosserat, strain gradient crystal plasticity and the statistical theory of dislocations. Philosophical Magazine 88, 3549-3563.

Forest, S., Aifantis, E.C., 2010. Some links between recent gradient thermo-elasto-plasticity theories and the thermomechanics of generalized continua. International Journal of Solids and Structures 47, 3367-3376.

Fotuhi, a., Fariborz, S., 2008. Stress analysis in a cracked strip. International Journal of Mechanical Sciences 50, 132-142.

Fratzl, P.W., R., 2007. Nature's hierarchical materials. Progress in Materials Science 52, 1263-1334.

Frederick, C.O., Armstrong, P.J., 2007. A mathematical representation of the multiaxial Bauschinger effect. Materials at High Temperatures, 24, 1-26.

Fredriksson, P., Gudmundson, P., Mikkelsen, L.P., 2009. Finite element implementation and numerical issues of strain gradient plasticity with application to metal matrix composites. International Journal of Solids and Structures 46, 3977-3987.

Frick, C.P., Clark, B.G., Orso, S., Schneider, A.S., Arzt, E., 2008. Size effect on strength and strain hardening of small-scale [1 1 1] nickel compression pillars. Materials Science and Engineering A 489, 319-329.

Gao, H., 2001. Taylor-based nonlocal theory of plasticity. International Journal of Solids and Structures 38, 2615-2637.

Gao, H., Huang, H., Nix, W., Hutchinson, J., 1999. Mechanism-based strain gradient plasticity- I.Theory. Journal of Mechanics and Physics of Solids 47, 1239-1263.

Gao, H., Huang, Y., 2003. Geometrically necessary dislocation and size-dependent plasticity. Scripta Materialia 48, 113-118.

Gao, H., Ji, B., Jager, I.L., Arzt, E., Fratzl, P., 2003. Materials become insensitive to flaws at nanoscale: lessons from nature. Proceedings of the National Academy of Sciences 100, 5597-5600.

Geers, M.G.D., Brekelmans, W.A.M., Bayley, C.J., 2007. Second-order crystal plasticity: internal stress effects and cyclic loading. Modelling and Simulation in Materials Science and Engineering 15, S133-S145.

Gerken, J., Dawson, P., 2008. A crystal plasticity model that incorporates stresses and strains due to slip gradients. Journal of the Mechanics and Physics of Solids 56, 1651-1672.

Gianola, D.S., Petegem, S.V., Legros, M., Brandstetter, S., Swygenhoven, H.V., Hemker, K.J., 2006. Stress-assisted discontinuous grain growth and its effect on the deformation behavior of nanocrystalline aluminum thin films. Acta Materialia 54, 2253-2263.

Giessen, E.V.D., Needleman, A., 1995. Discrete dislocation plasticity : a simple planar model. Engineering 689.

Greer, J.R., Hosson, J.T.M., 2011. Plasticity in small-sized metallic systems: Intrinsic versus extrinsic sizeeffect. Progress in Materials Science 56, 654-724.

Greer, J.R., Nix, W.D., 2006. Nanoscale gold pillars strengthened through dislocation starvation. Physical Review B 73, 245410.

Greer, J.R., Oliver, W.C., Nix, W.D., 2005. Size dependence of mechanical properties of gold at the micron scale in the absence of strain gradients. Acta Materialia 53, 1821-1830.

Groma, I., 1997. Link between the microscopic and mesoscopic length-scale description of the collective behavior of dislocations. Physical Review B 56, 5807-5813.

Groma, I., 2003. Spatial correlations and higher-order gradient terms in a continuum description of dislocation dynamics. Acta Materialia 51, 1271-1281.

Groma, I., Bako, B., 2000. Dislocation patterning: from micro- to mesoscale description. Physical Review Letters 84, 1487-1490.

Groma, I., Bakó, B., 1998. Probability distribution of internal stresses in parallel straight dislocation systems. Physical Review B 58, 2969-2974.

Gudmundson, P., 2004. A unified treatment of strain gradient plasticity. Journal of the Mechanics and Physics of Solids 52, 1379-1406.

Gurtin, M.E., 2000. On the plasticity of single crystals: free energy, microforces, plastic-strain gradients. Journal of the Mechanics and Physics of Solids 48, 989-1036.

Gurtin, M.E., 2002. A gradient theory of single-crystal viscoplasticity that accounts for geometrically necessary dislocations. Journal of the Mechanics and Physics of Solids 50, 5-32.

Gurtin, M.E., 2010. A finite-deformation, gradient theory of single-crystal plasticity with free energy dependent on the accumulation of geometrically necessary dislocations. International Journal of Plasticity 26, 1073-1096.

Gurtin, M.E., Anand, L., 2005. A theory of strain-gradient plasticity for isotropic, plastically irrotational materials. Part I: Small deformations. Journal of the Mechanics and Physics of Solids 53, 1624-1649.

Gurtin, M.E., Anand, L., Lele, S.P., 2007. Gradient single-crystal plasticity with free energy dependent on dislocation densities. Journal of the Mechanics and Physics of Solids 55, 1853-1878.

Guruprasad, P., Benzerga, A., 2008. Size effects under homogeneous deformation of single crystals: A discrete dislocation analysis☆. Journal of the Mechanics and Physics of Solids 56, 132-156.

Habibi, M.K., Joshi, S.P., Gupta, M., 2010. Hierarchical magnesium nano-composites for enhanced mechanical response. Acta Materialia 58, 6104-6114.

Hahner, P., Zaiser, M., 1997. From mesoscopic heterogeneity of slip to macroscopic fluctuations of stress and strain. Acta Materialia 45, 1067-1075.

Han, C.-S., Gao, H., Huang, Y., Nix, W.D., 2005a. Mechanism-based strain gradient crystal plasticity—I. Theory. Journal of the Mechanics and Physics of Solids 53, 1188-1203.

Han, C.-S., Gao, H., Huang, Y., Nix, W.D., 2005b. Mechanism-based strain gradient crystal plasticity—II. Analysis. Journal of the Mechanics and Physics of Solids 53, 1204-1222.

Haque, M.A., Saif, M.T.A., 2003. Strain gradient effect in nanoscale thin films. Acta Materialia 51, 3053-3061.

Haque, M.A.S., M. T. A., 2004. Deformation mechanisms in free-standing nanoscale thin films: A quantitative in situ transmission electron microscope study. Proceedings of the National Academy of Sciences 101, 6335-6340.

Hartmaier, A., Fivel, M.C., Canova, G, R., Gumbsch, P., 1999. Image stresses in a free-standing thin film. Modelling and Simulation in Materials Science and Engineering 7, 781.

Hayashi, I., Sato, M., Kuroda, M., 2011. Strain hardening in bent copper foils. Journal of Mechanics and Physics of Solids 59, 1731-1751.

Head, a.K., 1953. Edge Dislocations in Inhomogeneous Media. Proceedings of the Physical Society. Section B 66, 793-801.

Hill, R., Rice, J., 1972. Constitutive analysis of elastic-plastic crystals at arbitrary strain. Journal of the Mechanics and Physics of Solids 20, 401-413.

Hommel, M., Kraft, O., 2001. Deformation behavior of thin copper films on deformable substrates. Acta Mater. 49, 3935-3947.

Hou, C., Li, Z., Huang, M., Ouyang, C., 2008. Discrete dislocation plasticity analysis of single crystalline thin beam under combined cyclic tension and bending. Acta Materialia 56, 1435-1446.

Huang, Y., 1991. A User-material subroutine incorporating single crystal plasticity in the ABAQUS finite element program. Division of Applied Sciences, Harvard University Cambridge, Massachusetts.

Huang, Y., Qu, S., Hwang, K.C., Li, M., Gao, H., 2004. A conventional theory of mechanism-based strain gradient plasticity. International Journal of Plasticity 20, 753-782.

Huber, N., Nix, W.D., Gao, H., 2002. Identification of Elastic-Plastic Material Parameters from Pyramidal Indentation of Thin Films. Proceedings of the Royal Society of London Series A 458, 1593-1620.

Hull, D., Bacon, D.J., 2001. Introduction to dislocations, 4th ed. Butterworth Heinemann.

Jagannadham, K., Marcinkowski, M.J., 1978. Comparison of the image and surface dislocation models. physica status solidi (a) 50, 293-302.

Jagannadham, K., Marcinkowski, M.J., 1979. Behaviour of an edge dislocation in a semi-infinite solid with surface energy effects. Journal of Materials Science 14, 1052-1070.

Jagannadham, K., Marcinkowski, M.J., 1980. Surface dislocation model of a dislocation in a two-phase medium. Journal of Materials Science 15, 309-326.

Joshi, S.P., Ramesh, K.T., 2007. An enriched continuum model for the design of a hierarchical composite. Scripta Materialia 57, 877-880.

Khan, A.S., Huang, S., 1995. Continuum Theory of Plasticity. John Wiley & Sons Inc.

Khanikar, P., Kumar, A., Subramaniam, A., 2011. Image forces on edge dislocations: a revisit of the fundamental concept with special regard to nanocrystals. Philosophical Magazine 91, 730-750.

Kiener, D., Minor, A.M., 2011. Source Truncation and Exhaustion: Insights from Quantitative in situ TEM Tensile Testing. Nano Letters 11, 3816-3820.

Kiener, D., Motz, C., Grosinger, W., Weygand, D., Pippan, R., 2010. Cyclic response of copper single crystal micro-beams. Scripta Materialia 63, 500-503.

Kiser, M.T., Zok, F.W., Wilkinson, D.S., 1996. Plastic flow and fracture of a particulate metal matrix composite. Acta Materialia 44, 3465-3476.

Kouzeli, M., Mortensen, A., 2002. Size dependent strengthening in particle reinforced aluminium. Acta Mater. 50, 39-51.

Kröner, E., 1953. Das Fundamentalintegral der anisotropen elastischen Differentialgleichungen. Z. Phys. 136, 402-410.

Kröner, E., 1955. Die Spannungsfunktionen der dreidiminsionalan anisotropen Elastizitatstheorie. Z. Phys. 141, 386.

Kröner, E., 1959. Allgemeine Kontinuumstheorie der Versetzungen und Eigenspannungen. Archive for Rational Mechanics and Analysis 4, 273-334.

Kröner, E., 1967. Elasticity Theory of Materials with Long Range Cohesive Forces. international Journal of Solids and Structures 24, 581-597.

Kuroda, M., Tvergaard, V., 2006. Studies of scale dependent crystal viscoplasticity models. Journal of the Mechanics and Physics of Solids 54, 1789-1810.

Kuroda, M., Tvergaard, V., 2008a. A finite deformation theory of higher-order gradient crystal plasticity. Journal of Mechanics and Physics of Solids 56, 2573-2584.

Kuroda, M., Tvergaard, V., 2008b. On the formulations of higher-order strain gradient crystal plasticity models. Journal of Mechanics and Physics of Solids 56, 1591-1608.

Kuroda, M., Tvergaard, V., 2009. Effects of microscopic boundary conditions on plastic deformations of small-sized single crystals. international Journal of Solids and Structures 46, 4396-4408.

Lee, M., Dundurs, J., 1973. Edge dislocation in a surface layer. International Journal of Engineering Science 11, 87–94.

Legros, M., Cabié, M., Gianola, D.S., 2009. In situ deformation of thin films on substrates. Microscopy Research and Technique 72, 270-283.

Leutz, R., Bauer, R., 1976. Computation of the anisotropic cubic elastic green's tensor function and the elastic energy coefficients of point defects in crystals. Computer Physics Communications 11, 339-351.

Li, X., Wei, Y., Lu, L., Lu, K., Gao, H., 2010. Dislocation nucleation governed softening and maximum strength in nano-twinned metals. Nature 464, 877-880.

Li, Y., Ramesh, K.T., 1998. Influence of particle volume fraction, shape, and aspect ratio on the behavior of particle-reinforced metal-matrix composites at high rates of strain. Acta Materialia 46, 5633-5646.

Llorca, J., Suresh, S., Needleman, A., 1991. An experimental and numerical study of cyclic deformation in metal-matrix composites. Metallurgical and Materials Transactions A 23, 919-934.

Lloyd, D.J., 1994. Particle Reinforced Aluminum and Magnesium Matrix Composites. International Materials Reviews 39, 1-23.

Lu, L., Chen, X., Huang, X., Lu, K., 2009. Revealing the Maximum Strength in Nanotwinned Copper. Science 232, 607-610.

Lubarda, V.A., 2006. Dislocation equilibrium conditions revisited. international Journal of Solids and Structures 43, 3444-3458.

Lubarda, V.A., Blume, J.A., Needleman, A., 1993. An analysis of equilibrium dislocation distributions. Acta Metallurgica et Materialia 41, 625-642.

Lubarda, V.A., Kouris, D.A., 1996a. Stress fields due to dislocation arrays at interfaces. Mechanics of Materials 23, 191-203.

Lubarda, V.A., Kouris, D.A., 1996b. Stress fields due to dislocation walls in infinite and semi-infinite bodies. Mechanics of Materials 23, 169-189.

Ma, a., Roters, F., Raabe, D., 2005. A Dislocation Density Based Constitutive Model for Crystal Plasticity FEM. Materials Science Forum 495-497, 1007-1012.

Ma, C.C., Lin, R.L., 2001. Image Singularities of Green's Functions for an Isotropic Elastic Half-Plane Subjected to Forces and Dislocations. Mathematics and Mechanics of Solids 6, 503-524.

Ma, Q., Clarke, D.R., 1995. Size dependent hardness of silver single crystals. Journal of Materials Research 10, 853-863.

Maaß, R., Van Petegem, S., Ma, D., Zimmermann, J., Grolimund, D., Roters, F., Van Swygenhoven, H., Raabe, D., 2009. Smaller is stronger: The effect of strain hardening. Acta Materialia 57, 5996-6005.

McDowell, D.L., 2008. Viscoplasticity of heterogeneous metallic materials. Materials Science and Engineering R: Reports 62, 67-123.

McElhaney, K.W., Valssak, J.J., Nix, W.D., 1998. Determination of Indenter Tip Geometry and Indentation Contact Area for Depth Sensing Indentation Experiments. Journal of Materials Research 13, 1300-1306.

Meijer, G., 2000. Aspects of residual thermal stress/strain in particle reinforced metal matrix composites. Composites Part B: Engineering 31, 29-37.

Mesarovic, S., 2005. Energy, configurational forces and characteristic lengths associated with the continuum description of geometrically necessary dislocations. International Journal of Plasticity 21, 1855-1889.

Mesarovic, S.D., Baskaran, R., Panchenko, A., 2010. Thermodynamic coarsening of dislocation mechanics and the size-dependent continuum crystal plasticity. Journal of the Mechanics and Physics of Solids 58, 311-329.

Meyers, M., 2008. Mechanical strength of abalone nacre: Role of the soft organic layer. Journal of the Mechanical Behavior of Biomedical Materials 1, 76-85.

Michelitsch, T., Wunderlin, A., 1996. Stress function and internal stress in linear three-dimensional anisotropic elasticity. Z. Phys. 100.

Moss, W.C., Hoover, W.G., 1978. Edge-dislocation displacements in an elastic strip. Journal of Applied Physics 49.

Motz, C., Schoberl, T., Pippan, R., 2005. Mechanical properties of micro-sized copper bending beams machined by the focused ion beam technique. Acta Materialia 53, 4269-4279.

Motz, C., Weygand, D., Senger, J., Gumbsch, P., 2008. Micro-bending tests: A comparison between three-dimensional discrete dislocation dynamics simulations and experiments. Acta Materialia 56, 1942-1955.

Mughrabi, H., 1975. Constitutive Equations in Plasticity. MIT Press, Cambridge, MA.

Mughrabi, H., 1983. Dislocation wall and cell structures and long-range internal stresses in deformed metal crystals. Acta Metallurgica et Materialia 31, 1367-1379.

Mughrabi, H., 2001. On the role of strain gradients and long-range internal stresses in the composite model of crystal plasticity. Materials science and Engineering A 317, 171-180.

Mukherjee, S., Garmestani, H., Chandra, N., 1995. Experimental Investigation of Thermally Induced Plastic Deformation of MMCs Using Backscattered Kikuchi Method. Scripta Metallurgica et Materialia 33, 93-99.

Nabarro, F.R.K., J, 1978. The stress field of a dislocation lying in a plate. Journal of Applied Physics 49.

Nan, C.W., Clarke, D.R., 1996. The Influence of Particle Size and Particle Fracture on the Elastic/Plastic Deformation of Metal Matrix Composites. Acta Materialia 44, 3801-3811.

Nicola, L., Van der Giessen, E., Needleman, A., 2005. Size effects in polycrystalline thin films analyzed by discrete dislocation plasticity. Thin Solid Films 479, 329-338.

Niordson, C., 2003a. On lower order strain gradient plasticity theories. European Journal of Mechanics - A/Solids 22, 771-778.

Niordson, C., 2003b. Strain gradient plasticity effects in whisker-reinforced metals. Journal of mechanics and physics of solids 51, 1863-1883.

Nix, W.D., 1989. Mechanical properties of thin films. Metallurgical Transactions A 20, 2217-2245.

Nix, W.D., Gao, H., 1998. Indentation size effects in crystalline materials: a law for strain gradient plasticity. Journal of Mechanics and Physics of Solids 46, 411-425.

Nix, W.D., Greer, J.R., Feng, G., Lilleodden, E., 2007. Deformation at the nanometer and micrometer length scales: Effects of strain gradients and dislocation starvation. Thin Solid Films 515, 3152-3157.

Nye, J.F., 1953. Some geometrical relations in dislocated crystals. Acta Metallurgica 1, 153-162.

Ohno, N., Okumura, D., 2007. Higher-order stress and grain size effects due to self-energy of geometrically necessary dislocations. Journal of the Mechanics and Physics of Solids 55, 1879-1898.

P. Franciosi, M. Berveiller, Zaoui, A., 1980. Latent hardening in copper and aluminium single crystals. Acta Materialia 28, 273-283.

Parthasarathy, T., Rao, S., Dimiduk, D., Uchic, M., Trinkle, D., 2007. Contribution to size effect of yield strength from the stochastics of dislocation source lengths in finite samples. Scripta Materialia 56, 313-316.

Parthasarathya, T.A., Raoa, S.I., Dimiduk, D., Uchic, M., Trinkleb, D.R., 2007. Contribution to size effect of yield strength from the stochastics of dislocation source lengths in finite samples. Scripta Materialia 56, 313-316.

Peirce, D., Asaro, R., Needleman, a., 1983. Material rate dependence and localized deformation in crystalline solids. Acta Metallurgica 31, 1951-1976.

Polizzotto, C., 2009. A nonlocal strain gradient plasticity theory for finite deformations. International Journal of Plasticity 25, 1280-1300.

Press, W.H., Teukolsky, S.A., Vetterling, W.T., Flannery, B.P., 1992. Numerical Recipes in FORTRAN: The Art of Scientific Computing. Cambridge University Press, Cambridge.

Prinz, F.B., Argon, A.S., 1984. The evolution of plastic resistance in large strain plastic flow of single phase subgrain forming metals. Acta Materialia 32, 1021-1028.

Qiu, Y.P., Weng, G.J., 1991. The influence of inclusion shape on the overall elastoplastic behavior of a two-phase isotropic composite. International Journal of Solids and Structures 27, 1535-1550.

Reddy, J.N., 2006. An introduction to the finite element method. McGraw-Hill Higher Education.

Roh, J.W., Jang, S.Y., Kang, J., Lee, S., Noh, J.S.K., W., Park, J., Lee, W., 2010. Size-dependent thermal conductivity of individual single-crystalline PbTe nanowires. Applied Physics Letters 96.

Roters, F., Raabe, D., Gottstein, G., 2000. Work hardening in heterogeneous alloys--a microstructural approach based on three internal state variables. Acta Materialia 48.

Saada, G., 2008. Planar Dislocation Arrays and Crystal Plasticity, Science and Technology. Elsevier Ltd., pp. 1-18.

Sadd, M.H., 2005. Elasticity - Theory, applications and numerics. Elsevier, New York.

Schmid, E., 1924. Yield point of crystals. Critical shear stress law, Proceedings of the International Congress for applied mechanics, Delft.

Schwarz, C., Sedlacek, R., Werner, E., 2008. Refined short-range interactions in the continuum dislocation-based model of plasticity at the microscale. Acta Materialia 56, 341-350.

Sekine, H., Chent, R., 1995. A combined microstructure strengthening analysis of SiCp/Al metal matrix composites. Composites 26, 183-188.

Shan, Z.W., Mishra, R.K., Syed Asif, S.A., Warren, O.L., Minor, A.M., 2007. Mechanical annealing and source-limited deformation in submicrometre-diameter Ni crystals. Nature materials 7, 115-119.

Shao, J.C., Xiao, B.L., Wang, Q.Z., Ma, Z.Y., Yang, K., 2011. An enhanced FEM model for particle size dependent flow strengthening and interface damage in particle reinforced metal matrix composites. . Composites Science and Technology 71, 39-45.

Shen, Y.-L., Finot, M., Needleman, A., Suresh, S., 1995. Effective plastic response of two-phase composites. Acta Metallurgica et Materialia 43, 1701-1722.

Shi, M.X., Huang, Y., Li, M., Hwang, K.C., 2004. On Source-Limited Dislocations in Nanoindentation. Journal of Applied Mechanics 71, 433-435.

Sholl, D.S., Steckel, J.A., 2009. Density functional theory: a practical introduction. John Wiley and Sons.

Shu, J., 2000. Strain gradient effects on microscopic strain field in a metal matrix composite. International Journal of Plasticity 16, 563-591.

Shu, J., 2001. Boundary layers in constrained plastic flow: comparison of nonlocal and discrete dislocation plasticity. Journal of the Mechanics and Physics of Solids 49, 1361-1395.

Sinclair, C.W., Poole, W.J., Bréchet, Y., 2006. A model for the grain size dependent work hardening of copper. Scr Mater. 55, 739-742.

Steeds, J.W., Willis, J.R., 1979. Dislocations in Anisotropic Media in Dislocations in Solids, North-Holland Amsterdam.

Stolken, J.S., Evans, A.G., 1998. A microbend test method for measuring the plasticity length scale. Acta Materialia 46, 5109-5115.

Suh, Y.S., Joshi, P.S., Ramesh, K., 2009. An enhanced continuum model for size-dependent strengthening and failure of particle-reinforced composites. Acta Materialia 57, 5848-5861.

Taya, M., Lulay, K.E., Lloyd, D.J., 1991. Strengthening of a particulate metal matrix composite by quenching. Acta Metallurgica et Materialia 39, 73-87.

Taylor, G.I., 1934. The mechanism of plastic deformation of crystals. Part I. Theoretical. Proceedings of the Royal Society A 165, 362.

Taylor, G.I., Elam, C.F., 1923. The Distortion of an Aluminium Crystal during a Tensile Test. Proceedings of the Royal Society A 102, 643-667.

Ting, T.C.T., 2008. Green's Functions for a Half-Space and Two Half-Spaces Bonded to a Thin Anisotropic Elastic Layer. Journal of Applied Mechanics 75, 051103-051103.

Uchic, M., Dimiduk, D., Florando, J.F., Nix, W., 2004. Sample Dimensions Influence Strength and Crystal Plasticity. Science 305, 986-989.

Uchic, M.D., Shade, P.A., Dimiduk, D.M., 2009. Plasticity of Micrometer-Scale Single Crystals in Compression. Annual Review of Materials Research 39, 361-386.

Van der Giessen, E., Needleman, A., 1995. Discrete dislocation plasticity: a simple planar model. Modelling and Simulation in Materials Science and Engineering 3, 689-735.

Venkatraman, R., Bravman, J.C., 1992. Separation of film thickness and grain boundary strengthening effects in Al thin films on Si. J. Mater. Res. 7, 2040-2048.

Vinogradov, V., Willis, J.R., 2008. The pair distribution function for an array of screw dislocations. international Journal of Solids and Structures 45, 3726-3738.

Vollrath, F., 2000. Strength and structure of spiders' silks. Reviews in Molecular Biotechnology 74, 67-83.

von Blanckenhagen, B., Arzt, E., Gumbsch, P., 2004. Discrete dislocation simulation of plastic deformation in metal thin films. Acta Materialia 52, 773-784.

Voyiadjis, G., Huang, W., 1996. A modeling of single crystal plasticity with backstress evolution. European Journal of Mechanics - A/Solids, 36-73.

Voyiadjis, G.Z., Al-Rub, R.K.A., 2005. Gradient plasticity theory with a variable length scale parameter. International Journal of Solids and Structures 42, 3998-4029.

Voyiadjis, G.Z., Deliktas, B., 2009. Mechanics of strain gradient plasticity with particular reference to decomposition of the state variables into energetic and dissipative components. International Journal of Engineering Science 47, 1405-1423.

Weinberger, C., Cai, W., 2007. Computing image stress in an elastic cylinder. Journal of the Mechanics and Physics of Solids 55, 2027-2054.

Weiss, J., Montagnat, M., 2007. Long-range spatial correlations and scaling in dislocation and slip patterns. Philosophical Magazine 87, 1161-1174.

Wong, E.W., Sheehan, P.E., Lieber, C.M., 1997. Nanobeam Mechanics: Elasticity, Strength, and Toughness of Nanorods and Nanotubes. Science 277, 1971-1975.

Wu, B., Heidelberg, A., Boland, J.J., 2005. Mechanical properties of ultrahigh-strength gold nanowires. Nature materials 4, 525-529.

Xiang, Y., Vlassak, J.J., 2006. Bauschinger and size effects in thin-film plasticity. Acta Materialia 54, 5449-5460.

Xu, B., Jiang, Y., 2004. A cyclic plasticity model for single crystals. International Journal of Plasticity 20, 2161-2178.

Xue, Z., Huang, Y., Li, M., 2002. Particle size effect in metallic materials: a study by the theory of mechanism-based strain gradient plasticity. Acta Materialia 50, 149-160.

Yan, L., Khraishi, T.A., Shen, Y.-L., Horstemeyer, M.F., 2004. A distributed-dislocation methof for treating free-surface image stresses in three-dimensional dislocation

dynamics simulations. Modelling and Simulation in Materials Science and Engineering 12, 289-301.

Ye, J., Han, B.Q., Lee, Z., Ahn, B., Nutt, S.R., Schoenung, J.M., 2005. A tri-modal aluminum based composite with super-high strength. Scripta Materialia 53, 481-486.

Yefimov, S., Giessen, E.V.D., Groma, I., 2004a. Bending of a single crystal: discrete dislocation and nonlocal crystal plasticity simulations. Modelling and Simulation in Materials Science and Engineering 12, 1069-1086.

Yefimov, S., Groma, I., Giessen, c.d., 2004b. A comparison of a statistical-mechanics based plasticity model with discrete dislocation plasticity calculations. Journal of the Mechanics and Physics of Solids 52, 279-300.

Zaiser, M., Aifantis, E.C., 2003. Geometrically necessary dislocations and strain gradient plasticity––a dislocation dynamics point of view. Scripta Materialia 48, 133-139.

Zaiser, M., Miguel, M.C., Groma, I., 2001. Statistical dynamics of dislocation systems: The influence of dislocation-dislocation correlations. Physical Review B 64, 1-9.

Zaiser, M., Seeger, A., 2002. Long-range Internal Stresses , Dislocation Patterning and Work-hardening in Crystal Plasticity. In: Dislocations in Solids Vol. 11, Eds. F.R.N. Nabarro, M. S. Duesbery und J. Hirth, North-Holland, Amsterdam 2002, Chapter 56, p. 1-99.

Zhang, F., Huang, Y., Hwang, K.C., Qu, S., Liu, C., 2007. A Three-Dimensional Strain Gradient Plasticity Analysis of Particle Size Effect in Composite Materials. Materials and Manufacturing Processes 22, 140-148.

Zhang, H., Ye, J., Joshi, S.P., Schoenung, J.M., Chin, E.S.C., Ramesh, K.T., 2008. Rate-dependent behavior of hierarchical Al matrix composites. Scripta Materialia 59, 1139-1142.

Zhang, Z.F., Wang, Z.G., 2008. Grain boundary effects on cyclic deformation and fatigue damage. Progress in Materials Science 53, 1025-1099.

Zhou, C., Biner, S.B., LeSar, R., 2010. Discrete dislocation dynamics simulations of plasticity at small scales. Acta Materialia 58, 1565-1577.

Zhou, L., Li, S., Huang, S., 2011. Simulation of effects of particle size and volume fraction on Al alloy strength, elongation, and toughness by using strain gradient plasticity concept. Materials & Design 32, 353-360.

Zhu, T., Li, J., 2010. Ultra-strength materials. Progress in Materials Science 55, 710-757.

Appendix A. A Note on Continuum Descriptions of GND Density Tensor

Strain gradient (nonlocal) theories invoke the existence of excess dislocations commonly referred to as the geometrically necessary dislocations (GNDs) that are necessary to maintain geometric compatibility during plastic deformation (Ashby, 1970; Nye, 1953). Hence a continuum description of dislocations is necessary to explicitly account their effects into continuum theories. Here, we make a comparison between different continuum descriptions of GNDs corresponding to the different basis which researchers used in this field.

(Nye, 1953) first presented the tensorial form of the GND density in continuum framework, now commonly referred to as Nye dislocation density tensor. This dislocation density tensor is written in terms of scalar dislocation density as

$$\mathbf{A}_N = \sum_{\alpha} b\left(\rho_{\perp}^{\alpha}\mathbf{b}^{\alpha} \otimes \mathbf{l}^{\alpha} + \rho_{\odot}^{\alpha}\mathbf{b}^{\alpha} \otimes \mathbf{b}^{\alpha}\right) \tag{A.1}$$

where the subscript N indicates Nye's definition. $\rho_{\perp}^{\alpha}$ and $\rho_{\odot}^{\alpha}$ are the scalar edge and screw GND density on slip system α respectively, b is the Burgers vector magnitude and $\mathbf{b}^{\alpha}$ and $\mathbf{l}^{\alpha}$ are unit vectors in the direction of Burgers vector and dislocation line for slip system α, respectively. Note that this expansion depends on the choice of basis as we show later, but for any prescribed basis the scalar densities are unique.

Since the continuum description of the screw dislocations is the same in different conventions, without loss of generality, we only consider edge GNDs in remaining part of this article for only one slip system. Clearly, the discussion can be generalized for multiple slip as well.

Assuming a local coordinate on a dislocation shown in Figure A.1 associated with slip system with slip in $x-$ direction and normal in $y-$ direction.

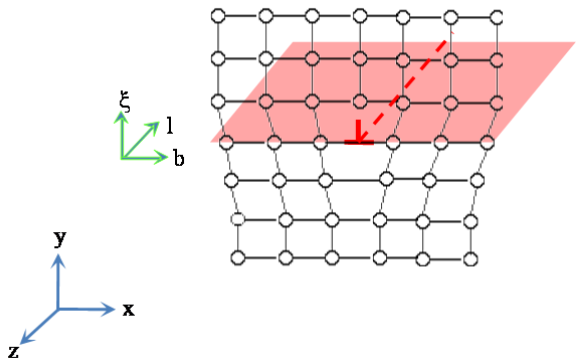

Figure A.1 Edge dislocation in local and global coordinates based on Nye definition

For a dislocation shown in Figure A.1, Eq. (A.1) is written in terms of the global coordinates as

$$\mathbf{A}_N = b\rho_\perp \, \mathbf{e_x} \otimes (-\mathbf{e_z}) \qquad \text{(A.2)}\ ^{24}$$

where b is the Burgers magnitudes. The only non-zero component of GND density tensor is obtained as $(A_N)_{xz} = -b\rho_\perp$.

Nye's definition of positive and negative edge dislocations under plane strain assumption where dislocation lines are in plane are shown in Fig. A.2 (Nye, 1953)

[24] For a single edge dislocation, $\rho_\perp = \delta(x,y)$ where $\delta(x,y)$ is two dimensional Dirac delta function.

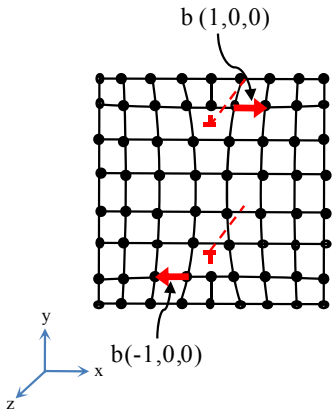

Figure A.2. Positive and negative edge dislocations according to Nye's definition (Nye, 1953)

Based on this definition of dislocation density tensor, the relation between the dislocation density and lattice curvature is obtained as

$$\mathbf{K} = \mathbf{A}_N - \frac{1}{2} tr(\mathbf{A}_N) \tag{A.3}$$

where **K** is the incompatible plastic lattice curvature. Note that elastic lattice curvature is not considered in Eq. (A.3) as initially derived by (Nye, 1953).

In chapter 3 we decomposed the total lattice curvature in terms of compatible and incompatible terms. For example, consider plane strain bending of a crystalline lattice shown in Fig. A3. Nye relation is written as $K_{xz} = (A_N)_{xz}$ (Eq. (A.3)) where both K_{xz} and $(A_N)_{xz}$ are negative continuum quantities while corresponding Burgers vector is positive (Figure A.2).

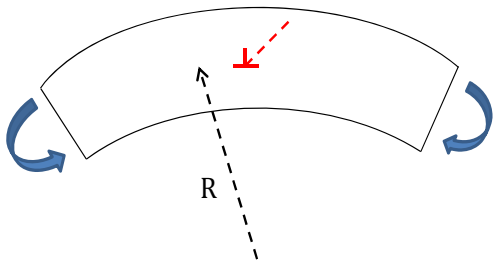

Figure A.3. Nye's definition of edge dislocation under plane strain assumption

The GND density tensor generally can be related to the strain gradient. Consider a smooth surface S bounded by a closed curve C. The net Burger's vector $\mathbf{b}$ of the dislocations piercing through S is defined by (using Stokes formula)

$$\mathbf{b} = \oint_C (\mathbf{F}^e)^{-1} d\mathbf{x} = -\int_S (curl\,(\mathbf{F}^e)^{-1})^T \cdot \boldsymbol{n}\, dS \tag{A.4}$$

where $\mathbf{n}$ is unit normal to S and $\mathbf{F}^e$ is elastic deformation gradient. Using Stokes formula, the GND dislocation density tensor is obtained as

$$(\mathbf{A}_N)^T = -curl\,(\mathbf{F}^e)^{-1} \tag{A.5}$$

In the case of small deformation theory, the elastic deformation gradient is written in terms of displacement gradient as $\mathbf{F}^e = \mathbf{I} + \mathbf{H}^e$. Then, Eq. (A.5) may be approximated by

$$(\mathbf{A}_N)^T = curl\,(\mathbf{H}^e) = -curl\,(\mathbf{H}^p) \tag{A.6}$$

This convention for GND density description is used by (Ashby, 1970) and (Forest, 2008) as well. Arsenlis and Park (1999) adopted a similar notation, but with the small difference that the dislocation line is defined in the opposite sense to that of the Nye definition. They rewrote Eq. (A.2) as $\mathbf{A}_{AP} = \rho_\perp\, b\mathbf{e}_\mathbf{x} \otimes (\mathbf{e}_\mathbf{z})$**,** which results in the non-zero components given as $(A_{AP})_{xz} = \rho_\perp\, b$. Similarly, lattice curvature - GND density relation where elastic lattice curvature is neglected is rewritten as

$$\mathbf{K} = -\mathbf{A}_{AP} + \frac{1}{2} tr(\mathbf{A}_{AP}) \tag{A.7}$$

and the GND density tensor is defined as

$$(\mathbf{A}_{AP})^T = curl\,(\mathbf{F}^e)^{-1} \tag{A.8}$$

In the small deformation theory, we obtain

$$(\mathbf{A}_{AP})^T = -curl\,(\mathbf{H}^e) = curl\,(\mathbf{H}^p) \tag{A.9}$$

In short, the continuum descriptions of GND density tensor provided by Nye (1953) and Arsenlis and Parks (1999) can be related as

$$\mathbf{A}_{AP} = -\mathbf{A}_N \tag{A.10}$$

where the negative sign is simply due to the difference in the directions of dislocation line in these two description (Figure A.2 and Figure A.3).

Another continuum description of the GND density tensor is used extensively by Gurtin and coworkers (Cermellia and Gurtin, 2000; Gurtin, 2002) and Gao and coworkers (Gao, 2001; Han et al., 2005b; Nix and Gao, 1998)

$$\mathbf{A}_{GG} = \sum_{\alpha} b\left(\rho_{\perp}^{\alpha}\mathbf{l}^{\alpha} \otimes \mathbf{b}^{\alpha} + \rho_{\odot}^{\alpha}\mathbf{b}^{\alpha} \otimes \mathbf{b}^{\alpha}\right) \tag{A.11}$$

which is the transpose of Nye's definition of the GND density tensor. Then, for dislocation shown in Figure A.1, the only nonzero component of $\mathbf{A}_{GG}$ is $(A_{GG})_{zx} = b\rho_{\perp}$. Using this notation, the lattice curvature-GND density relation is written as

$$\mathbf{K} = -(\mathbf{A}_{GG})^T + \frac{1}{2}tr(\mathbf{A}_{GG})^T \tag{A.12}$$

As a summary, we obtain

$$(\mathbf{A}_{GG})^T = \mathbf{A}_{AP} = -\mathbf{A}_N \tag{A.13}$$

This dissertation follows the GND density description that has been promoted by Gurtin, Gao and coworkers.

Appendix B. Kernel functions

As shown in chapter 3, internal residual stress for elastically isotropic medium under plane strain condition can be written as

$$T(\boldsymbol{r})_{ij}^{*} = -\varepsilon_{ipz}\varepsilon_{jqz}\int_{V} \varepsilon_{mnz}\chi_{mpq}A^{T}(\boldsymbol{r}')_{zn}dV \qquad i,j,p,q,m,n = (x,y) \qquad \text{(B.1)}$$

where χ is the kernel function, which depends on the dimensionality, geometry of the problem and the elastic properties of the material. Note that first indices in χ associated with the Burger vector direction while last two indices prescribes the stress components.

B-1 Elastically isotropic infinite medium solution

The kernel function corresponding to the elastically isotropic infinite medium can be obtained from infinite Green function solution as

$$\tilde{\chi}_{mpq} = \tilde{G}_{,mpq} \qquad \text{(B.2)}$$

where the infinite Green function for infinite medium has been proposed by (Kröner, 1959) as

$$\tilde{G} = -D\frac{(\xi^2+\eta^2)}{2}\ln(\sqrt{\xi^2+\eta^2}) \qquad \text{(B.3)}$$

where (ξ,η) is the local Cartesian coordinate system and $D = \mu/(2\pi(1-\nu))$ is the effective stiffness with shear modulus μ and Poisson's ratio ν. Substituting Eq. (A.3) in Eq. (A.2), we obtain conventional kernel functions akin to the Volterra solution, which represents the stress field of an edge dislocation with unit Burgers vector in an infinite medium (Hirth and Lothe, 1982) as

$$\tilde{\chi}_{xxx} = -\frac{D}{h}\frac{M(M^2+3N^2)}{(M^2+N^2)^2}, \qquad \tilde{\chi}_{yxx} = \frac{D}{h}\frac{N(M^2-N^2)}{(M^2+N^2)^2}$$
$$\tilde{\chi}_{xyy} = \frac{D}{h}\frac{M(N^2-M^2)}{(M^2+N^2)^2}, \qquad \tilde{\chi}_{yyy} = -\frac{D}{h}\frac{N(3M^2+N^2)}{(M^2+N^2)^2} \tag{B.4}$$

where $D = \mu/2\pi(1-\nu)$ is the effective stiffness with shear modulus μ and Poisson's ratio ν and 2h is the specimen thickness.

B-2 Elastically isotropic finite medium solution

Generally the explicit formulations for dislocation kernel functions in the presence of finite boundaries are significantly complicated. For the problem studied in this work, stress function based approach using complex Fourier transform is adapted from (Fotuhi and Fariborz, 2008). For completeness, we describe these finite kernel functions for a structure with edge dislocations of unit Burgers vectors in x and y directions, but with a somewhat modified notations. We introduce a local coordinate system (ξ, η) at the point where the internal stress is required, while the origin for the global coordinates (x, y) is placed at the neutral axes (fig. 2). Since infinity assumption is made in x direction, the kernel function are independent of global x coordinate.

$$\hat{\chi}_{mpq}(M,N,Y,h) = \frac{\mu}{h}\int_0^\infty \left[f_{mpq}(M,N,Y,\alpha) - g_{mpq}(M,N,\alpha)\right] d\alpha$$
$$m,p,q = (x,y) \tag{B.5}$$

where α is a transform variable in the complex Fourier transformation approach representing non-dimensional spatial frequency and

$$f_{mpq} = \begin{cases} f^1_{mpq}(M,N,Y,\alpha) & 0 \le N \le 1-Y \\ f^2_{mpq}(M,N,Y,\alpha) & -1-Y \le N \le 0 \end{cases}$$
$$g_{mpq} = \begin{cases} g^1_{mpq}(M,N,Y,\alpha) & 0 \le N \le 1-Y \\ g^2_{mpq}(M,N,Y,\alpha) & -1-Y \le N \le 0 \end{cases} \tag{B.6}$$

$$g^1_{yyy} = \frac{1}{2\pi(1-\nu)}(2+\alpha N)e^{+\alpha N}\cdot\cos(\alpha M)\,, \quad g^1_{xyy} = -\frac{1}{2\pi(1-\nu)}(1+\alpha N)e^{\alpha N}\cdot\sin(\alpha M)$$

$$g^2_{yyy} = -\frac{1}{2\pi(1-\nu)}(2-\alpha N)e^{-\alpha N}\cdot\cos(\alpha M), \quad g^2_{xyy} = +\frac{1}{2\pi(1-\nu)}(1-\alpha N)e^{-\alpha N}\cdot\sin(\alpha M)$$

$$g^1_{yxx} = -\frac{1}{2\pi(1-\nu)}\alpha N e^{\alpha N}\cdot\cos(\alpha M)\,, \quad g^1_{xxx} = -\frac{1}{2\pi(1-\nu)}(1-\alpha N)e^{\alpha N}\cdot\sin(\alpha M)$$

$$g^2_{yxx} = -\frac{1}{2\pi(1-\nu)}\alpha N e^{-\alpha N}\cdot\cos(\alpha M)\,, \quad g^2_{xxx} = -\frac{1}{2\pi(1-\nu)}(1+\alpha N)e^{-\alpha N}\cdot\sin(\alpha M) \tag{B.7}$$

$$g^1_{yxy} = -\frac{1}{2\pi(1-\nu)}(1+\alpha N)e^{\alpha N}\cdot\sin(\alpha M)\,, \quad g^1_{xxy} = -\frac{1}{2\pi(1-\nu)}\alpha N e^{\alpha N}\cdot\cos(\alpha M)$$

$$g^2_{yxy} = -\frac{1}{2\pi(1-\nu)}(1-\alpha N)e^{-\alpha N}\cdot\sin(\alpha M)\,, \quad g^2_{xxy} = -\frac{1}{2\pi(1-\nu)}\alpha N e^{-\alpha N}\cdot\cos(\alpha M)$$

$$\begin{bmatrix} f^1_{yyy} \\ f^1_{xyy} \end{bmatrix} = \frac{4}{\pi\Delta}\Bigg(\begin{bmatrix} \mathrm{A}^{\mathrm{x}}_1\cdot\cos(\alpha M) \\ \mathrm{A}^{\mathrm{y}}_1\cdot\sin(\alpha M) \end{bmatrix} \Big(-\big(1+\alpha(Y-1)\big)e^{\alpha(Y-1)} + \big(1-\alpha(Y-1)\big)e^{-\alpha(Y-1)}\Big) + \begin{bmatrix} \mathrm{C}^{\mathrm{x}}_1\cdot\cos(\alpha M) \\ \mathrm{C}^{\mathrm{y}}_1\cdot\sin(\alpha M) \end{bmatrix} \Big(\big(2+\alpha(Y-1)\big)e^{\alpha(Y-1)} + \big(2-\alpha(Y-1)\big)e^{-\alpha(Y-1)}\Big)\Bigg)$$

$$\begin{bmatrix} f^2_{yyy} \\ f^2_{xyy} \end{bmatrix} = \frac{4}{\pi\Delta}\Bigg(\begin{bmatrix} \mathrm{A}^{\mathrm{x}}_2\cdot\cos(\alpha M) \\ \mathrm{A}^{\mathrm{y}}_2\cdot\sin(\alpha M) \end{bmatrix} \Big(-\big(1+\alpha(Y+1)\big)e^{\alpha(Y+1)} + \big(1-\alpha(Y+1)\big)e^{-\alpha(Y+1)}\Big) + \begin{bmatrix} \mathrm{C}^{\mathrm{x}}_2\cdot\cos(\alpha M) \\ \mathrm{C}^{\mathrm{y}}_2\cdot\sin(\alpha M) \end{bmatrix} \Big(\big(2+\alpha(Y+1)\big)e^{\alpha(Y+1)} + \big(2-\alpha(Y+1)\big)e^{-\alpha(Y+1)}\Big)\Bigg) \tag{B.8}$$

$$\begin{bmatrix} f^1_{yxx} \\ f^1_{xxx} \end{bmatrix} = \frac{4}{\pi\Delta}\Bigg(\begin{bmatrix} \mathrm{A}^{\mathrm{x}}_1\cdot\cos(\alpha M) \\ \mathrm{A}^{\mathrm{y}}_1\cdot\sin(\alpha M) \end{bmatrix} \Big(\big(1-\alpha(Y-1)\big)e^{\alpha(Y-1)} - \big(1+\alpha(Y-1)\big)e^{-\alpha(Y-1)}\Big) + \begin{bmatrix} \mathrm{C}^{\mathrm{x}}_1\cdot\cos(\alpha M) \\ \mathrm{C}^{\mathrm{y}}_1\cdot\sin(\alpha M) \end{bmatrix} \big(\alpha(Y-1)e^{\alpha(Y-1)} - \alpha(Y-1)e^{-\alpha(Y-1)}\big)\Bigg)$$

$$\begin{bmatrix} f_{yxx}^{2} \\ f_{xxx}^{2} \end{bmatrix} = \frac{4}{\pi\Delta}\Bigg(\begin{bmatrix} \mathrm{A}_2^{\mathrm{x}} \cdot \cos(\alpha M) \\ \mathrm{A}_2^{\mathrm{y}} \cdot \sin(\alpha M) \end{bmatrix}\Big(\big(1-\alpha(Y+1)\big)e^{\alpha(Y+1)} - \big(1+\alpha(Y+1)\big)e^{-\alpha(Y+1)}\Big) + \begin{bmatrix} \mathrm{C}_2^{\mathrm{x}} \cdot \cos(\alpha M) \\ \mathrm{C}_2^{\mathrm{y}} \cdot \sin(\alpha M) \end{bmatrix}\Big(\alpha(Y+1)e^{\alpha(Y+1)} - \alpha(Y+1)e^{-\alpha(Y+1)}\Big)\Bigg)$$

$$\begin{bmatrix} f_{yyx}^{1} \\ f_{xyx}^{1} \end{bmatrix} = -\frac{4}{\pi\Delta}\Bigg(\begin{bmatrix} \mathrm{A}_1^{\mathrm{x}} \cdot \sin(\alpha M) \\ \mathrm{A}_1^{\mathrm{y}} \cdot \cos(\alpha M) \end{bmatrix}\Big(\big(-\alpha(Y-1)\big)e^{\alpha(Y-1)} + \big(\alpha(Y-1)\big)e^{-\alpha(Y-1)}\Big) + \begin{bmatrix} \mathrm{C}_1^{\mathrm{x}} \cdot \sin(\alpha M) \\ \mathrm{C}_1^{\mathrm{y}} \cdot \cos(\alpha M) \end{bmatrix}\Big(\big(1+\alpha(Y-1)\big)e^{\alpha(Y-1)} + \big(-1+\alpha(Y-1)\big)e^{-\alpha(Y-1)}\Big)\Bigg)$$

$$\begin{bmatrix} f_{yyx}^{2} \\ f_{xyx}^{2} \end{bmatrix} = -\frac{4}{\pi\Delta}\Bigg(\begin{bmatrix} \mathrm{A}_2^{\mathrm{x}} \cdot \sin(\alpha M) \\ \mathrm{A}_2^{\mathrm{y}} \cdot \cos(\alpha M) \end{bmatrix}\Big(\big(-\alpha(Y+1)\big)e^{\alpha(Y+1)} + \big(\alpha(Y+1)\big)e^{-\alpha(Y+1)}\Big) + \begin{bmatrix} \mathrm{C}_2^{\mathrm{x}} \cdot \sin(\alpha M) \\ \mathrm{C}_2^{\mathrm{y}} \cdot \cos(\alpha M) \end{bmatrix}\Big(\big(1+\alpha(Y+1)\big)e^{\alpha(Y+1)} + (-1 + \alpha(Y+1))e^{-\alpha(Y+1)}\Big)\Bigg)$$

The coefficients are defined as

$$\begin{aligned}
&A_1^x = L_5(L_2S_6 + L_5S_7 + L_4S_8), \qquad A_2^x = -L_5(L_1S_6 + L_5S_5 + L_3S_8)\\
&A_1^y = -L_5(L_2S_2 + L_5S_3 + L_4S_4), \qquad A_2^y = L_5(L_1S_2 + L_5S_1 + L_3S_4)\\
&C_1^x = L_5L_1S_7 + L_1L_4S_8 - L_5L_2S_5 - L_2L_3S_8, \quad C_2^x\\
&\qquad = L_5L_3S_7 + L_3L_2S_6 - L_5L_4S_5 - L_4L_1S_6\\
&C_1^y = L_5L_2S_1 + L_2L_3S_4 - L_5L_1S_3 - L_1L_4S_4, \quad C_2^y\\
&\qquad = L_5L_4S_1 + L_4L_1S_2 - L_5L_3S_3 - L_3L_2S_2\\
&\Delta = (L_1S_2 + L_5S_1 + L_3S_4)(L_2S_6 + L_5S_7 + L_4S_8) - (L_2S_2 + L_5S_3 + L_4S_4)(L_1S_6\\
&\qquad + L_5S_5 + L_3S_8)
\end{aligned} \tag{B.9}$$

$$
\begin{aligned}
L_1 &= -(1 + 2\alpha(Y+N) - 2\alpha^2\big((1-Y)-N\big)\big((1+Y)+N\big)e^{2\alpha} - (1 \\
&\quad - 2\alpha(Y+N) - 2\alpha^2\big((1-Y)-N\big)\big((1+Y)+N\big)e^{-2\alpha} \\
&\quad + (1+2\alpha)e^{2\alpha(Y+N)} + (1-2\alpha)e^{-2\alpha(Y+N)} \\
L_2 &= -e^{2\alpha\left((1+Y)+N\right)} - e^{-2\alpha\left((1+Y)+N\right)} + 2 + 4\alpha^2\big((1+Y)+N\big)^2 \\
L_3 &= e^{2\alpha\left((1-Y)-N\right)} - e^{-2\alpha\left((1-Y)-N\right)} + 2 + 4\alpha^2\big((1-Y)-N\big)^2 \\
L_4 &= (1 - 2\alpha(Y+N) - 2\alpha^2\big((1-Y)-N\big)\big((1+Y)+N\big)e^{2\alpha} + (1 + 2\alpha(Y+N) \\
&\quad - 2\alpha^2\big((1-Y)-N\big)\big((1+Y)+N\big)e^{-2\alpha} - (1-2\alpha)e^{2\alpha(Y+N)} \\
&\quad - (1+2\alpha)e^{-2\alpha(Y+N)} \\
L_5 &= -\alpha\left(2 + 2\alpha\big((1-Y)-N\big)\big((1+Y)+N\big)\right)e^{2\alpha} \\
&\quad - \alpha\left(2 - 2\alpha\big((1-Y)-N\big)\big((1+Y)+N\big)\right)e^{-2\alpha} \\
&\quad + 2\alpha\left(e^{2\alpha(Y+N)} + e^{-2\alpha(Y+N)}\right) \\
S_1 &= \left(2 - 4\nu + 2\alpha\big((1-Y)-N\big)\right)e^{\alpha\left((1-Y)-N\right)} \\
&\quad + \left(-2 + 4\nu + 2\alpha\big((1-Y)-N\big)\right)e^{-\alpha\left((1-Y)-N\right)} \\
S_2 &= \left(4 - 4\nu + 2\alpha\big((1-Y)-N\big)\right)e^{\alpha\left((1-Y)-N\right)} \\
&\quad + \left(4 - 4\nu - 2\alpha\big((1-Y)-N\big)\right)e^{-\alpha\left((1-Y)-N\right)} \\
S_3 &= \left(2 - 4\nu + 2\alpha\big((1+Y)+N\big)\right)e^{\alpha\left((1+Y)+N\right)} \\
&\quad + \left(-2 + 4\nu + 2\alpha\big((1+Y)+N\big)\right)e^{-\alpha\left((1+Y)+N\right)} \\
S_4 &= \left(-4 + 4\nu - 2\alpha\big((1+Y)+N\big)\right)e^{\alpha\left((1+Y)+N\right)} \\
&\quad + \left(-4 + 4\nu + 2\alpha\big((1+Y)+N\big)\right)e^{-\alpha\left((1+Y)+N\right)} \\
S_5 &= \left(-4 + 4\nu + 2\alpha\big((1-Y)-N\big)\right)e^{\alpha\left((1-Y)-N\right)} \\
&\quad + \left(-4 + 4\nu - 2\alpha\big((1-Y)-N\big)\right)e^{-\alpha\left((1-Y)-N\right)}
\end{aligned}
\tag{B.10}
$$

$$S_6 = \left(-2 + 4\nu + 2\alpha\left((1 - Y) - N\right)\right) e^{\alpha\left((1-Y)-N\right)} + \left(2 - 4\nu + 2\alpha\left((1 - Y) - N\right)\right) e^{-\alpha\left((1-Y)-N\right)}$$

$$S_7 = \left(4 - 4\nu - 2\alpha\left((1 + Y) + N\right)\right) e^{\alpha\left((1+Y)+N\right)} + \left(4 - 4\nu + 2\alpha\left((1 + Y) + N\right)\right) e^{-\alpha\left((1+Y)+N\right)}$$

$$S_8 = \left(-2 + 4\nu + 2\alpha\left((1 + Y) + N\right)\right) e^{\alpha\left((1+Y)+N\right)} + \left(-2 + 4\nu + 2\alpha\left((1 + Y) + N\right)\right) e^{-\alpha\left((1+Y)+N\right)}$$

Noting the components of kernel function $\hat{\chi}_{mpq}$ associated with finite medium, it can be seen that interchanging the indices do not change the functionality of the kernel function (e.g. $\hat{\chi}_{xyx} = \hat{\chi}_{yxx}$). This suggests that it may also be possible to write a finite kernel function in terms of a corresponding Green's function $\hat{G}$ such that $\hat{\chi}_{mpq} = \hat{G}_{,mpq}$.

Appendix C. Numerical integration convergence study

To evaluate internal stress arising from interaction between GNDs and free surfaces (See Eqs. 4.8 and 4.9), we need to numerically integrate the kernel function for isotropic finite medium provided in appendix B. In this appendix, we briefly study the integration procedure and convergence. We only show the integration procedure for Eq. 4.9 while similar procedure with same results has been done for Eq. 4.9 which does not present here.

For setup the problem, first we rewrite Eq. 4.9 as

$$\hat{T}_{xx} = \mu A_{zx} h \overbrace{\underbrace{\int_{-L}^{L} \int_{-1-Y}^{1-Y} \overbrace{\int_{0}^{\infty} \underbrace{[f_{xx}^{x}(M,N,Y,\alpha) - g_{xx}^{x}(M,N,\alpha)]}_{P1} \, d\alpha}^{P2} \, dN}_{P3} \, dM}^{\hat{\Gamma}_{xx}} \tag{C.1}$$

To begin with, we investigate the variation of P1 with α and normalized variables M($=\xi/h$), N($=\eta/h$) and Y($=y/h$). Figure C.1 shows in detail the variation of the term P1 with respect to α and N for different values of M and Y. Generally it can be seen that independent of other parameters, P1 is a continuous and decay function of α which ensure convergence of infinite integration in expression P2. Note that decaying distance on α does not change with variation of M however it increases when Y approaches to 1. To perform numerical integration in P2, we used Gauss-Laguerre quadrature method (Press et al., 1992) where

$$\int_{0}^{+\infty} e^{-x} f(x) \, dx = \sum_{i=1}^{n} w_i f(x_i) \tag{C.2}$$

where x_i is the i-th root of Laguerre polynomial $L_n(x)$, n is number of integration points and $w_i = \frac{x_i}{(n+1)^2[L_{n+1}(x_i)]^2}$.

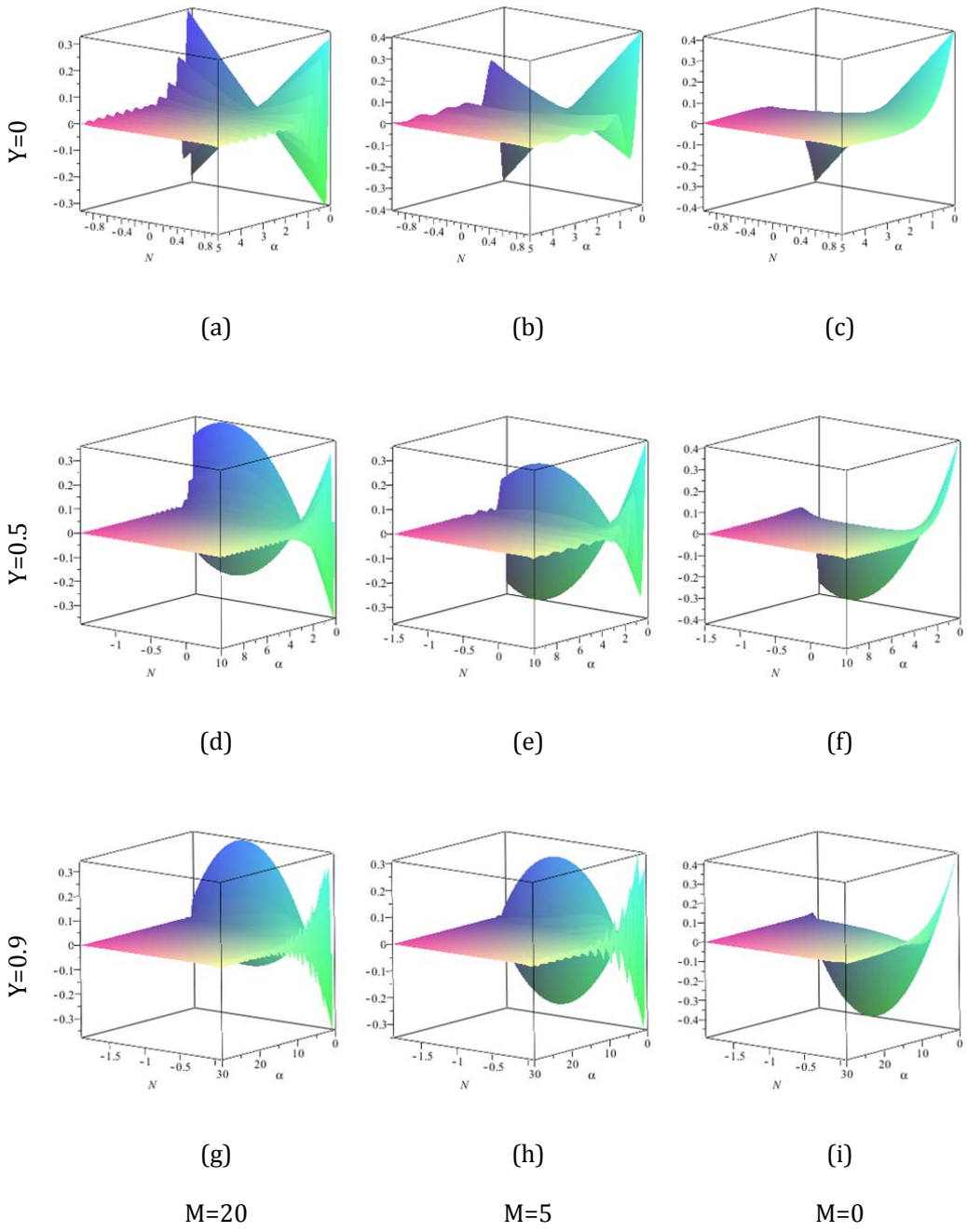

Figure C.1. Variation of P1 expression with respect to the α and N for different value of M and Y.

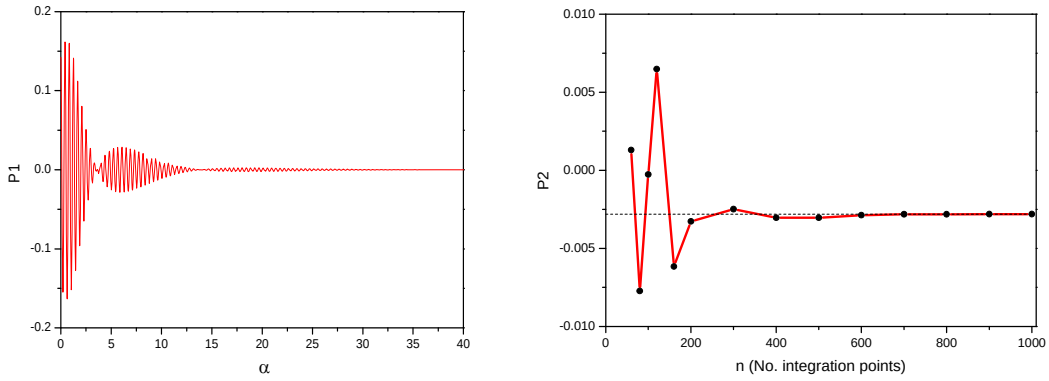

(a) (b)

Figure C.2. (a) variation of P1 versus α (b) P2 integration convergence by increasing the number of integration points (Y=0.9, M=5, N=-0.1)

The convergence of expression P2 is investigated in Fig. C2 a and b with variable used in case (h) in figure C.1 and N=-0.1. It can be seen that for the certain value used, expression P2 converges for $n > 600$. Note that expression P2 gives us non dimensional stress exerted on the point at position Y by a dislocation with distance of (N, M) from the point (figure C.3a).

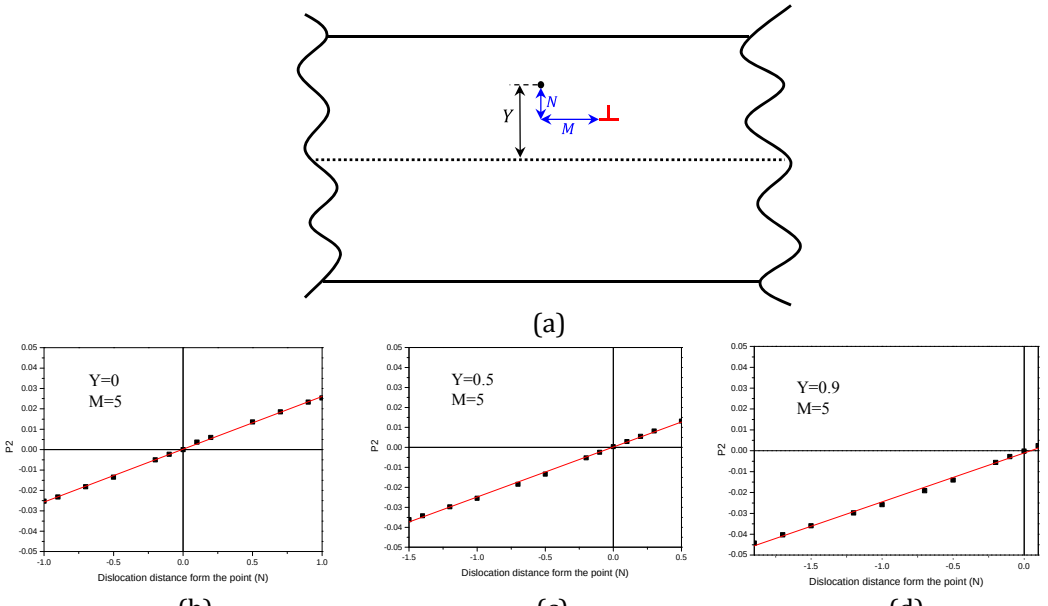

(a)

(b) (c) (d)

Figure C.3. (a) Illustration of dislocation in thin film, Normalized image stress exerted at point (b) Y=0, (b) Y=0.5, (c) Y=0.9 by a dislocation at position (M,N) from that point calculated form expression P2.

In Fig. C3b-d, the variation of expression P2 is shown as a function of the vertical distance N of the dislocation from the point keeping the horizontal distance M fixed for different points across the beam thickness. It can be seen that P2 is a linear function of N.

Integration of expression P2 over entire beam thickness (expression P3) provides the non-dimensional image stress at a point Y by a continuous finite dislocation wall with distance of M from the point (Fig. C4a). This non-dimensional stress is equal to area under the surfaces shown in Fig. C1. The non-dimensional image stress field of a finite dislocation wall in a thin film captures in Fig. C4b at different position of Y. It concluded that a finite dislocation wall in a thin film generate a linear image stress across the film thickness which is negative at top and positive at the bottom of the film. In addition, Variation of expression P3 at the film surface ($Y = 1$) versus distance M and its convergence are drawn in Fig. C4c It can be seen that the stress of dislocation wall is rapidly decay to zero by increasing the distance M. This observation is in agreement with saturation of $\hat{\Gamma}_{xx}$ with increasing L (see figure 4.7b) where integration is performed over M. The area under the curve shown in Fig. C4 from 0 to L gives the $\hat{\Gamma}_{xx}$ for specified L. Simple composite Simpson's rule is used to perform numerical integration for second and third integral in Eq. (C.1) using MAPLE software. Figure C.4c displays convergence of the P3 with the number of integration segments.

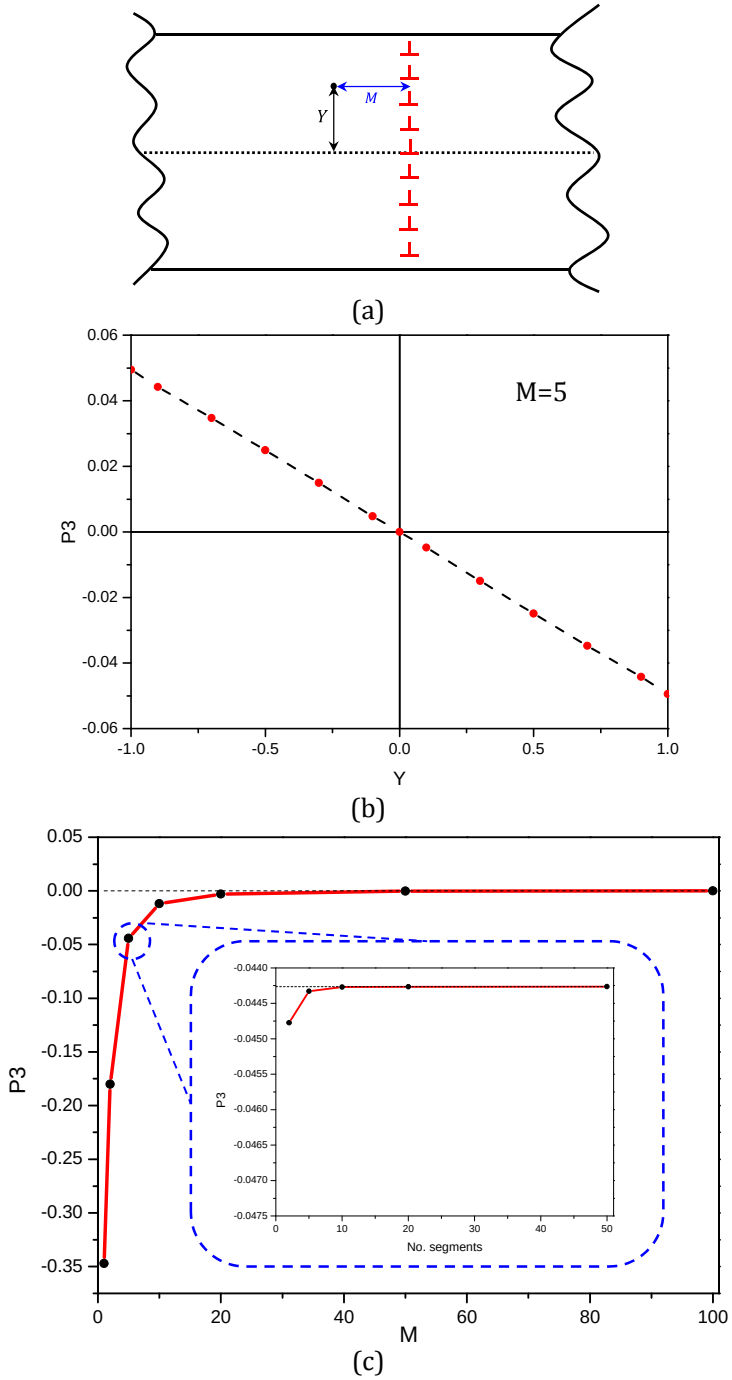

Figure C.4. (a) Illustration of finite dislocation wall in thin film, (b) Variation of P3 across film thickness for $M = 5$, (c) variation of P3 at film surface ($Y = 1$) with respect to the distance M and its convergence.